

School of Electrical Engineering, Computing and  
Mathematical Sciences

Surveillance of Space with Passive Radar using the  
Murchison Widefield Array

Brendan Hennessy

This thesis is presented for the Degree of  
Doctor of Philosophy  
of  
Curtin University of Technology

August 2023



To the best of my knowledge and belief this thesis contains no material previously published by any other person except where due acknowledgement has been made. This thesis contains no material which has been accepted for the award of any other degree or diploma in any university.

Brendan Hennessy



# Acknowledgements

I would first like to acknowledge the immense support from the Department of Defence, the last five and a half years have been a tremendous privilege.

I am incredibly grateful for the support I have received from everyone at the Curtin Institute of Radio Astronomy, as well as the MWA operations team.

They say it takes a village to raise a child, and with that in the front of my mind I would like to thank all the friends and colleagues, both current and former, at DSTO/DST Group/DSTG who have helped along the way. This list includes, but is certainly not limited to, Daniel Gustainis, Ashley Summers, Marek Dziadosz-Findlay, David Merrett, James Palmer, Travis Bessell, Stephen Howard, Roslyn Lau, Emma Heading, Paul Pincus, Nathan Misaghi, Matt Brincat, Ben Somers, Kruger White and Nick Spencer.

I have received huge help from my supervisors along the way, including Paul Hancock, Ian Morrison and Steve Prabu. Special thanks go to Rob Young and David Holdsworth for their support and guidance, and extra special thanks go to Steven Tingay and Mark Rutten without whom none of this would have been possible.

Finally, I would like to thank my incredible family for all of the love and support, including my parents Andrea and Shane, Sophie and Thomas (and both of their wonderful families) and, most of all, my amazing wife Laura. Laura, I will be forever grateful for your love, support, patience and grammatical corrections, despite all of the other things we have had going on including getting married, moving across the country, the pandemic, lockdowns and dealing with Fluffy.



# Abstract

Humans are putting more satellites into low Earth orbit (LEO) than ever before, driven by a desire for lower latency communication which, in turn, demands large constellations of thousands of satellites. Due to the high speeds of these satellites, micro-atmospheric drag, and other factors, LEO is very dynamic, and these constellation satellites are independently manoeuvrable, resulting in LEO now representing an incredibly challenging space surveillance problem. Because of this, there has never been a greater need for wide area surveillance and sensors that are able to detect objects uncued, without prior knowledge.

The underpinning technologies of radio telescope arrays are almost indistinguishable from those of radar receiver arrays, both trying to detect weak signals, often in the presence of stronger or unwanted signals. Because of this similarity, as well as a long history between the two disciplines, modern high time-resolution radio telescopes are proving to be excellent receivers for the purposes of radar.

When radio telescopes are used as radar receivers, they are most often used in conjunction with a dedicated radar transmitter. However, a different approach to radar has gained significant focus in recent years: passive radar. Passive radar uses pre-existing and non-cooperative transmitters as the radar source, namely transmitters such as for commercial radio and television broadcast. There are many challenges in running a passive radar. In particular, it is typically far more computationally demanding than traditional active radar, and the signals are often not suitable for this purpose. However, with so much television and radio entertainment being inadvertently transmitted into the space environment, there

is a large amount of ‘free’ energy that is available for radar purposes.

This thesis investigates the use of the Murchison Widefield Array (MWA) as a passive radar receiver for the surveillance of space, investigating the techniques and approaches required to achieve widefield space surveillance with a radio telescope. The MWA is a low-frequency radio telescope located in remote Western Australia. It is the low-frequency precursor to the forthcoming Square Kilometre Array. Consisting of thousands of antennas forming hundreds of subarrays distributed over a  $30 \text{ km}^2$  geographical footprint, it is a space surveillance sensor with potential.

However, there are many challenges in implementing passive radar with a sensor like the MWA, such as the incredible computational processing requirements. In order to detect small satellites at ranges exceeding 1,000 km, the radar needs to use long coherent processing intervals. However, this long integration time means the significant orbital speeds, and changing geometry, result in a near-intractable processing load.

To overcome these problems, this thesis will investigate the intersection of the orbital motion parameter space and the radar measurement parameter space, in order to find practical approaches to the passive radar challenge. These approaches are developed and demonstrated with observational campaigns. As part of these observations, other techniques and advances are required, such as the use of an external reference receiver, novel approaches to synchronisation and calibration, as well as orbital parameter matched filtering.

This work culminates in the results of a large observation campaign, with the MWA forming the receiver of a continent-spanning multistatic passive radar network. These observations produce incredibly accurate orbital estimates across a significant surveillance volume, including the detection of small objects at long ranges. The results also demonstrate the benefit of using multiple transmitters, as they provide complementary coverage in frequency, as well as geometric diversity, also multistatic orbit determination greatly improves the accuracy of orbital



parameter estimates.

In addition to space surveillance with the MWA, this thesis also includes the demonstration of techniques developed using a smaller, deployable passive radar, showing that these techniques are generally applicable to any space surveillance radar.

With the LEO space surveillance problem becoming more challenging every day, a larger number of space surveillance sensors, particularly widefield sensors, are required. However, radar processing for such a large volume is very challenging, especially since passive radar systems have no control over the illumination signals. The work here shows how practical approaches can alleviate these problems and how widefield sensors, utilising MWA-like technologies, can help overcome these space surveillance challenges.



# List of Publications

Publications directly resulting from work done for this thesis include:

**Hennessy, B.**, Tingay, S., Hancock, P., Young, R., Tremblay, S., Wayth, R.B., Morgan, J., McSweeney, S., Crosse, B., Johnston-Hollitt, M. and Kaplan, D.L., 2019, April. *Improved techniques for the surveillance of the near Earth space environment with the Murchison Widefield Array*. In 2019 IEEE Radar Conference (RadarConf19), pp.1-6. IEEE.

**Hennessy, B.**, Rutten, M., Tingay, S. and Young, R., 2020, April. *Orbit determination before detect: orbital parameter matched filtering for uncued detection*. In 2020 IEEE International Radar Conference (RADAR), pp.889-894. IEEE.

**Hennessy, B.**, Tingay, S., Young, R., Rutten, M., Crosse, B., Hancock, P., Sokolowski, M., Johnston-Hollitt, M. and Kaplan, D.L., 2021. *Uncued detection and initial orbit determination from short observations with the Murchison Widefield Array*. IEEE Aerospace and Electronic Systems Magazine, 36(10), pp.16-30.

**Hennessy, B.**, Rutten, M., Young, R., Tingay, S., Summers, A., Gustainis, D., Crosse, B. and Sokolowski, M., 2022. *Establishing the capabilities of the Murchison Widefield Array as a passive radar for the surveillance of space*. Remote Sensing, 14(11), p.2571.

**Hennessy, B.**, Gustainis, D., Misaghi, N., Young, R. and Somers, B., 2022, March. *Deployable long range passive radar for space surveillance*. In 2022 IEEE Radar Conference (RadarConf22), pp.01-06. IEEE.

Other publications not directly associated with this thesis:

**Hennesy, B.**, Holdsworth, D.A., Yardley, H., Debnam, R., Warne. G. and Jessop, M., 2023, November. *Effects of range Doppler-rate coupling on high frequency chirp radar for accelerating targets*. In 2023 IEEE International Radar Conference (RADAR), pp.1-6. IEEE.

**Hennesy, B.**, Yardley, H., Holdsworth, D.A., Debnam, R., Jessop, M. and Warne. G., 2023, November. *Velocity ambiguity resolution using opposite chirprates with LFM radar*. In 2023 IEEE International Radar Conference (RADAR), pp.1-6. IEEE.

# Contents

<b>Acknowledgements</b>	<b>v</b>
<b>Abstract</b>	<b>vii</b>
<b>List of Publications</b>	<b>xi</b>
<b>1 Background and Introduction</b>	<b>1</b>
1.1 Passive Radar . . . . .	4
1.2 Radio Astronomy . . . . .	7
1.3 Space Surveillance . . . . .	8
1.4 Keeping Up with Fast Targets . . . . .	14
1.5 Orbit Determination . . . . .	16
1.6 Space Situational Awareness with the MWA . . . . .	18
1.7 This thesis: direction and scope . . . . .	20
<b>2 Methodology, Signal Processing and Problem Formulation</b>	<b>23</b>
2.1 Passive Radar . . . . .	24
2.2 The MWA used as a Radar Receiver . . . . .	29
2.2.1 Data Collection Pipeline . . . . .	30
2.2.2 Calibration . . . . .	33
2.3 LEO Space Surveillance . . . . .	36

2.4	Signal Processing . . . . .	40
2.4.1	Radar Product Formation . . . . .	40
2.4.2	Walk across all parameter space . . . . .	44
2.5	Summary . . . . .	54
<b>3</b>	<b>Improved Techniques for the Surveillance of the Near Earth Space Environment with the Murchison Widefield Array</b>	<b>57</b>
3.1	Abstract . . . . .	58
3.2	Introduction . . . . .	58
3.3	Prior work . . . . .	59
3.4	Processing Strategies . . . . .	61
3.5	Results . . . . .	65
3.5.1	2015 Data Reprocessing . . . . .	66
3.5.2	2016 Data Collection . . . . .	68
3.5.3	Rocket Body . . . . .	70
3.5.4	Higher Order Hypotheses . . . . .	71
3.6	Future Work . . . . .	72
3.7	Conclusion . . . . .	73
3.A	Mitigating linear range-walk and linear Doppler-walk . . . . .	74
<b>4</b>	<b>Orbit Determination Before Detect: Orbital Parameter Matched Filtering for Uncued Detection</b>	<b>77</b>
4.1	Abstract . . . . .	77
4.2	Introduction . . . . .	78
4.2.1	Prior Work . . . . .	79
4.3	Problem Formulation . . . . .	80
4.3.1	Radar Product Formation . . . . .	80

4.3.2	Orbital Dynamics . . . . .	82
4.4	Orbit Determination Before Detect . . . . .	84
4.4.1	Search-Volume Constraints . . . . .	87
4.4.2	Zero Doppler Crossing . . . . .	91
4.4.3	Single Channel Orbit Detection . . . . .	92
4.5	Simulated Results . . . . .	93
4.6	Conclusion . . . . .	96
4.A	Signal Processing Computational Characteristics . . . . .	96
<b>5</b>	<b>Uncued Detection and Initial Orbit Determination from Short Observations with the Murchison Widefield Array</b>	<b>101</b>
5.1	Abstract . . . . .	101
5.2	Signal Processing for Initial Orbit Determination . . . . .	102
5.2.1	Space Surveillance Application . . . . .	102
5.2.2	Compressed Pulse Cube formation . . . . .	104
5.2.3	Orbit Determination Before Detect . . . . .	105
5.2.4	Constrained Search Space . . . . .	107
5.3	Initial Orbit Determination . . . . .	109
5.3.1	Gibbs/Herrick-Gibbs . . . . .	110
5.3.2	Direct Detection IOD . . . . .	111
5.3.3	ODBD IOD . . . . .	112
5.4	Results . . . . .	112
5.4.1	High Time Resolution Voltage Capture System . . . . .	115
5.4.2	Radar Configuration . . . . .	116
5.4.3	Surveillance Stare . . . . .	116
5.4.4	Initial Orbit Determination Example . . . . .	118

5.4.4.1	ODBD IOD . . . . .	120
5.4.4.2	Other methods . . . . .	121
5.4.5	Non-Circular Orbits . . . . .	123
5.5	Conclusion . . . . .	126
5.6	Future Work . . . . .	127
<b>6</b>	<b>Establishing the Capabilities of the Murchison Widefield Array as a Passive Radar for the Surveillance of Space</b>	<b>129</b>
6.1	Abstract . . . . .	129
6.2	Signal Processing . . . . .	130
6.3	Orbit Determination . . . . .	139
6.3.1	Multistatic Orbit Determination . . . . .	142
6.3.2	Initial Orbit Determination . . . . .	143
6.4	Continental Radar . . . . .	144
6.5	Results . . . . .	148
6.6	Conclusion . . . . .	160
<b>7</b>	<b>Discussion and Conclusions</b>	<b>163</b>
	<b>Appendices</b>	<b>165</b>
<b>A</b>	<b>Deployable Long Range Passive Radar for Space Surveillance</b>	<b>167</b>
A.1	Abstract . . . . .	167
A.2	Introduction . . . . .	168
A.3	Radar System Description . . . . .	170
A.3.1	Array Design . . . . .	170
A.3.2	Radar Configuration . . . . .	172
A.3.3	Remote Reference Collection . . . . .	174



A.4 Praxis . . . . .	175
A.5 Results . . . . .	177
A.5.1 Remote Reference Collection . . . . .	181
A.5.2 Aircraft Detection . . . . .	181
A.6 Conclusion . . . . .	183
<b>B Statement of Contributions</b>	<b>185</b>
B.1 Attribution Tables . . . . .	187
<b>Bibliography</b>	<b>193</b>



# List of Figures

1.1	Single MWA tile at Inyarrimanha Ilgari Bundara the CSIRO Murchison Radio-astronomy Observatory. Credit: Natasha Hurley-Walker ICRAR/Curtin. . . . .	3
1.2	Illustration of all the objects orbiting Earth that are currently being tracked by the Space Surveillance Network out to a range of approximately 50,000 km. At this range all the major orbital regimes, including geostationary orbit, are visible. . . . .	9
1.3	Illustration of all the objects orbiting Earth that are currently being tracked by the Space Surveillance Network out to a range of approximately 10,000 km. At this range the LEO population, and part of the medium Earth orbit population, is visible. . . . .	10
1.4	Bistatic space surveillance radar diagram with a narrow-beam transmitter and a narrow-beam receiver. The surveillance region is highlighted in the blue region. . . . .	11
1.5	Bistatic space surveillance radar diagram with a narrow-beam transmitter and a receiver array with seven notional receive beams. This configuration is referred to as a pulse chasing radar. The surveillance region is highlighted in the blue region. . . . .	13

1.6	Bistatic space surveillance staring radar diagram with a wide-beam transmitter and a receiver array with seven notional receive beams. Typically, the transmit beamwidth would extend considerably in azimuth as well (not shown). The surveillance region is highlighted in the blue region. . . . .	14
1.7	Illustration of the use of the Murchison Widefield Array (MWA) as a passive radar, showing two transmitters, one satellite and three MWA tiles. The two transmitters' elevation beampatterns (in blue) and the signal path (in green) are also shown. . . . .	18
2.1	The bistatic triangle, formed by the location of the transmitter (TX), receiver (RX), and the target. The bistatic angle, $\beta$ , is also shown. . . . .	25
2.2	A plan view of the 128 tiles for the Murchison Widefield Array's Phase I configuration. . . . .	31
2.3	A plan view of the 128 tiles for the Murchison Widefield Array's Phase II Extended configurations. . . . .	32
2.4	A plan view of the 128 tiles for the Murchison Widefield Array's Phase II Compact configurations. Note the scale is far smaller for this figure compared with Figures 2.2 and 2.3. . . . .	33
2.5	Sample calibrator output showing the calibration amplitude and phase adjustments. Wide bands are not calibrated due to the coarse channel boundaries, and the impact of RFI at 96.5 MHz is present. . . . .	34

2.6	Example output of the genetic algorithm process to update the phase corrections from the calibration solution. The figure shows the power return of six targets (Targets 1 – 4 are meteor returns, targets 5 and 6 are radio-galaxy returns), and how over 100 generations the determined phase adjustments increase the detected power of each. An individual colour scale has been used for each target. . . . .	36
2.7	Semi-major axis vs. eccentricity diagram showing the distribution of objects in the catalogue and their respective elements. RSOs with a perigee less than 2,000 km above the surface of the Earth are highlighted red. . . . .	39
2.8	The maximum speed (achieved at perigee) distribution of objects in the catalogue against their eccentricity. RSOs with a perigee less than 2,000 km above the surface of the Earth are highlighted red. . . . .	40
2.9	Example delay-Doppler map formed using MWA data. Inset (a) shows the direct path interference as well as an outgoing aircraft. Inset (b) shows an approaching International Space Station. . . .	44
2.10	Segment of a delay-Doppler map centered on an approaching ISS. Formed with a CPI of 3 s, the ISS exhibits considerable delay and Doppler walk as it moves across the CPI. . . . .	45
2.11	Four reproductions of 2.10 (utilising the same scale) with various motion mitigations applied to the pulsestack. The bottom two subfigures have had a matching Doppler-rate applied, the right two subfigures have had the Keystone transform applied. . . . .	47

2.12	Two subfigures showing a satellite moving near zero-Doppler, the left subfigure is a section of a delay-Doppler map and the right subfigure is the spatial skymap, from the horizon to zenith, resulting from the beamforming. The matching radar products were formed by implementation of (2.5). The uncompensated Doppler-rate and spatial rates produce significant smearing. . . . .	48
2.13	Identical figure as Figure 2.11, except the matching radar products were formed by implementation of (2.8). The matched Doppler-rate has dramatically improved SNR however the spatial rates still produce significant smearing. . . . .	50
2.14	Identical figure as Figures 2.11 and 2.13, except the matching radar products were formed by implementation of (2.9). The matched Doppler-rate and matched spatial have dramatically improved SNR and stopped smearing in all dimensions. Now the space station is spatially localised to a single point. . . . .	52
2.15	Spatial returns of the Hubble Space Telescope observed by the Phase II compact configuration and processed in different ways, akin to the spatial insets from Figures 2.12 – 2.14. The left figure is the result of (2.5), the middle figure implements (2.8), and the right figure is the implementation of (2.9). . . . .	54
3.1	The left section shows the Phase I array. The right section shows the Phase II compact configuration array. . . . .	61
3.2	Ambiguity surface signal power in dB of the ISS, processed with a five second CPI, along with the ISS returns processed with different dechirp hypotheses. . . . .	64
3.3	The 2015 (left) and 2016 (right) data collection configurations, overlaid on a map of Western and Central Australia. . . . .	66

3.4	The SNR (dB) of the ISS with no migration compensation applied (corresponding to initial results (Palmer et al., 2017)) through to full range and Doppler migration compensation. . . . .	67
3.5	Detected dechirp rate corresponding to the SNR in Figure 3.4. . .	68
3.6	The SNR (dB) of the ISS from the 2016 data collection with CPI lengths of one, two and three seconds. The SNR improves with CPI.	69
3.7	The SNR of the Atlas-Centaur rocket body from the 2016 data collection with CPI lengths of one, two and three seconds. The SNR improves with CPI. . . . .	71
3.8	A single snapshot in time of the SNR of the rocket body and how it varies with CPI, comparing the dechirp technique with the higher order dechirp and dechirp. . . . .	72
4.1	The orbital plane determined by orientation parameters $\Omega$ , $\omega$ , and $i$ relative to the plane of reference in the ECI coordinate frame. These parameters define the direction of the angular momentum vector $\mathbf{h}$ . The axes $\mathbf{I}$ , $\mathbf{J}$ and $\mathbf{K}$ define the ECI coordinate frame.	83
4.2	In the ECI coordinate frame the sensor is at position $\mathbf{q}$ , the celestial body at position $\mathbf{r}$ with velocity $\dot{\mathbf{r}}$ (given by (4.5) and (4.6)) and the slant range vector from the sensor to the object given by $\boldsymbol{\rho}$ . . .	84
4.3	Four valid orbital velocities given by the intersection of the sphere (given by (4.21)), parallel planes P1 and P2 (given by (4.26)), and plane P3 (given by (4.27) or (4.29)). . . . .	90
4.4	The measurement parameters of a close pass of an object in a near-circular orbit ( $e = 0.0007$ ), as well as the simulation made assuming zero eccentricity at point of closest approach. The left plot is angular space and the right is the delay-Doppler. Twenty seconds of the true pass is shown with ten seconds of the simulated path overlaid. . . . .	94

4.5	The measurement parameters of a close pass of an object in an eccentric orbit ( $e = 0.7$ ), as well as the four simulations made with the correct eccentricity and semi-major axis. The left plot is angular space and the right is the delay-Doppler. Twenty seconds of the true pass is shown with ten seconds of the simulated paths overlaid. . . . .	95
4.6	The measurement parameters of a close pass of an object in a near-circular orbit ( $e = 0.00126$ ), as well as several simulations made using different eccentricities. The left plot is angular space and the right is the delay-Doppler. Twenty seconds of the true pass is shown with ten seconds of the simulated paths overlaid. . . . .	95
5.1	An illustration of the processing strategy, for a delay cell of interest the phase is adjusted for each antenna every slow-time pulse. . . .	105
5.2	The layout of MWA the compact configuration of Phase II. . . . .	113
5.3	Near-identical plots of a single bistatic-range and Doppler slice of the sky map of the Hubble Space Telescope near zero-Doppler. 100 ms CPI. The left plot shows standard delay-Doppler processing and beamforming, the right shows ODBD methods. Data collected November 2018, with a frequency of 96.9 MHz, bandwidth of 100 kHz. . . . .	114
5.4	Single bistatic-range and Doppler slice of the sky map of the Hubble Space Telescope near zero-Doppler. Three second CPI. The left plot shows standard delay-Doppler processing and beamforming, the right shows ODBD methods. Data collected November 2018, with a frequency of 96.9 MHz, bandwidth of 100 kHz. . . . .	114
5.5	Detections from the surveillance stares, overlaid on the track data. Each detection has been associated with a NORAD (or Satellite Catalogue) Number. . . . .	117



5.6	For the WISE, a comparison of detection performance of the uncued methods against what is possible with a priori track information.	119
5.7	Aggregate detections of the WISE. The top subplot is an aggregate of the delay-Doppler maps. The next two subplots show the detection-level IOD from these detections. The left IOD subplot has no Doppler correction and the right subplot shows orbits after the detected-Doppler feedback.	121
5.8	Detection-level IOD for the WISE, propagated 60 minutes forward.	122
5.9	Detection-level IOD for the WISE, propagated 30 s forward. The left subplot shows the Doppler-corrected ODBD estimates, matching Fig. 5.8. The middle subplot shows the Herrick-Gibbs method. The right subplot shows the Doppler-analytic method.	122
5.10	Detection-level IOD for the Delta 2 rocket body, propagated 60 minutes forward.	124
5.11	For the Pegasus XL rocket body, a comparison of detection performance of the uncued methods against what is possible with a priori track information.	124
5.12	SNR of a detection when processing is extended to account for non-circular orbits. The plots show how the detection SNR varies with the size and shape of the orbital ellipse. The true values for the WISE are 0.0001 and 6,858 km and the true values for the Pegasus XL rocket body are 0.0679 and 7,284 km, both shown.	126
6.1	The bistatic radar configuration with the position of an orbital object and its velocity, $\mathbf{r}$ and $\dot{\mathbf{r}}$ , along with the positions of the transmitter and receiver, $\mathbf{r}_{rx}$ and $\mathbf{r}_{tx}$ , as well as the vectors from these sites to the object, $\boldsymbol{\rho}_{rx}$ and $\boldsymbol{\rho}_{tx}$ . The origin, $O$ , corresponds to the gravitational centre of the Earth.	132

6.2	Illustration of the signal processing steps outlined in Section 6.2. An orbital state vector is used to determine the polynomial phase signal coefficients to form a phase-matching matrix. A single range's slow-time signals are matched to the orbit, and combined using this matrix before detection. . . . .	137
6.3	Illustration of the orbit determination process, starting with a reference orbit and then estimating an orbit adjustment to best-fit the measurements. . . . .	141
6.4	A map of all the powerful (greater than 50 kW) FM radio transmitters in Australia. . . . .	145
6.5	Typical FM array's in situ measured antenna pattern via an airborne radio measurement system. . . . .	146
6.6	Incident power on an object above a receiver, for an equivalent isotropically radiated power (EIRP) of 100 kW, with a beam pattern as shown in Figure 6.5. Note that this figure is based on a spherical Earth model. . . . .	147
6.7	An example pass showing the detections of the International Space Station utilising a distant transmitter versus the elevation of the target. The blue line shows the detected signal to noise ratio and the red line shows the signal path length and the reflected range. The reflected range is given by $\rho_{rx} + \rho_{tx}$ and does not include the baseline length to give the full bistatic range, as in Equation (6.8). . . . .	148
6.8	A map showing the Murchison Widefield Array as well as the transmitters used to generate the results in Section 6.5. Details of the transmitters are given in Table 6.1. . . . .	150

6.9	Example results showing dozens of tracks' detections above the Murchison Widefield Array (MWA), with each detection's colour corresponding to its altitude. The location of the MWA is shown, denoted by an X. The transmitters are also shown, denoted by the black triangles. Additionally, rings denoting a 1000-km range (from the MWA) are included. . . . .	151
6.10	Example results, matching Figure 6.9, showing dozens of tracks' detections above the Murchison Widefield Array (MWA) with each detection's colour corresponding to its altitude. The location of the MWA is shown, denoted by an X. The transmitters are also shown, denoted by the black triangles. Additionally, a ring denoting a 1000-km range (from the MWA) is included. . . . .	152
6.11	The four measurement parameters from the detections of an out-bound COSMOS 1707 detected using an FM transmitter in Albany.	153
6.12	The resulting orbit predictions from the measurements from Figure 6.11. The top row shows the covariance of the position estimate and the velocity estimate; the bottom row shows the mean error when compared with the TLE. . . . .	154
6.13	An example pass showing the signal to noise ratio (SNR) of International Space Station detections utilising all the transmitters covered in this section. . . . .	155
6.14	The four measurement parameters from the detections of COSMOS 1707 detected using FM transmitters in both Albany and Perth. .	156
6.15	The resulting orbit predictions from the multistatic measurements from Figure 6.14. The top panels show the covariance of the position estimate and the velocity estimate. The bottom panels show the mean errors when compared with the two-line element (TLE).	156

6.16	The four measurement parameters from the detections of NADEZHDA 5 detected using FM transmitters in both Albany and Perth. . . .	157
6.17	The resulting orbit predictions from the multistatic measurements from Figure 6.16. The top panels show the covariance of the po- sition estimate and the velocity estimate. As the detections from each bistatic pair are not coincident, the combined errors will be initially identical to Perth's. The bottom panels show the mean errors when compared with the two-line element (TLE). . . . .	158
6.18	The four measurement parameters from detections of OPS 5721 de- tected using FM transmitters in Albany, Perth and Mount Gambier.	159
6.19	The resulting orbit predictions from the multistatic measurements from Figure 6.18. The top panels show the covariance of the posi- tion estimate and the velocity estimate. The bottom panels show the mean errors when compared with the two-line element (TLE).	159
A.1	The configuration of the system for the experiments covered in this paper. The passive radar receiver is utilising two transmitters, one close and one at a significant stand-off range. The receiver- to-target and transmitter-to-target paths are shown in red. The satellite trajectory (corresponding to a pass in Fig A.6) is shown in blue. . . . .	170
A.2	Sparse array configuration with the antennas directed at Zenith. Array elements configured in a hexagonal configuration with an element separation of $\lambda$ . . . . .	171
A.3	Hypersparse array configuration with the antennas directed at $30^\circ$ elevation above the horizon. Array elements configured in a hexag- onal configuration with an element separation of $2.5 \lambda$ . . . . .	172

A.4	Radar system block diagram, showing front-end amplification, calibration, gain and filtering. The chain is replicated for each polarisation. . . . .	173
A.5	Signal processing block diagram illustrating Praxis' multiple Glides for performing processing on two distinct target scenarios simultaneously. . . . .	176
A.6	Detection output of two near-identical passes of the ISS, one pass observed with the sparse array, the other pass observed with the hypersparse array. The left subplot shows the detected delay and Doppler, the right shows the detections' azimuth and elevation. . . . .	177
A.7	Spatial returns from the sparse configuration of the ISS pass in Fig. A.6, as well as the associated TLE. . . . .	178
A.8	Spatial returns from the hypersparse configuration of the ISS pass in Fig. A.6, as well as the associated TLE. . . . .	178
A.9	The left subplot is the SNR spatial response of the ISS as it passes near zenith and the right subplot shows the results when the combination of parameters are constrained to be valid orbits only. The spatial response is shown from an elevation of 30° up to zenith. The array was in the hypersparse configuration. . . . .	180
A.10	As for Figure A.9, except for a Starlink satellite. . . . .	180
A.11	Detection output of an ISS pass with the hypersparse array, processed using the reference signal from the distant transmitter in Tasmania. The left subplot shows the detected delay and Doppler, the right shows the detections' azimuth and elevation. . . . .	181

A.12 Three example long-range commercial aircraft detections are shown. The left subplot shows the aggregate delay-Doppler map of three individual highlighted detections. The right subplot is a map of the configuration with the three detections, and their iso-range ellipses, highlighting a large surveillance area. . . . . 182

# Chapter 1

## Background and Introduction

Radio telescopes, sensitive instruments designed to detect the faintest signals from the most distant cosmic objects, are proving to be capable receivers for the purpose of radar. Although radio telescope arrays have been used as imaging interferometers, recent interest in phenomena such as pulsars, fast radio bursts, and cosmic rays, is motivating the development of high time-resolution capabilities for interferometric arrays (Tremblay et al., 2015; McSweeney et al., 2020; Williamson et al., 2021). These high time-resolution modes enable the radiotelescopes to seamlessly be utilised as a radar.

The ever-increasing number of objects in Earth-centred orbit poses significant challenges for space surveillance networks, particularly with the recent rise of manoeuvring mega-constellations. Interest in lower-latency communications is seeing long-range geosynchronous satellites being replaced by a much larger number of satellites in low Earth orbit (LEO). Examples of these constellations are Starlink, OneWeb and Project Kuiper (Rossi et al., 2017; Foreman et al., 2017; McDowell, 2020). Thousands of satellites are needed to provide persistent coverage on the Earth. Because these larger number of satellites cannot be individually launched, and also due to the dynamic nature of near-Earth orbits, these megaconstellation satellites need to be far more manoeuvrable than typical satellites. The result is a LEO population that is more crowded, congested and

more dynamic than ever before.

The need for wide area surveillance sensors, in contrast to typically narrow field optical and radar space surveillance sensors, has therefore never been greater. This type of wide field radar is historically only used in large scale, billion dollar, missile defence applications. Examples of phased array scanning radars which have contributed (or continue to contribute) to the space surveillance network include the AN/FPS-85 (the world's first large phased array radar), PARCS and PAVE PAWS (Johnson, 1993; Sridharan & Pensa, 1998; Weeden et al., 2010).

A scanning radar is a large phased array which rapidly scans a coverage area with a narrow beam. The high power transmitted means the beam only needs to illuminate a direction for a very short amount of time, typically tens to hundreds of milliseconds, before scanning elsewhere. Another approach to surveillance radar is a staring radar, which utilises a (typically bistatic) transmitter to provide broad area illumination. With a large sector illuminated, a receive array is then able to form any number of receive beams (in parallel) to surveil the region of interest, sensing everything, everywhere, all at once.

Widefield surveillance with a high-powered electronically-steered scanning radar is essentially a scheduling problem in ensuring the beam scans across the sky for any new detections, whilst maintaining custody of known tracks. However, for a staring radar, the problem is more challenging. A consequence of wide area illumination is that longer integration times are required for equivalent/specific sensitivity, and the long integration necessitates a significant computational task to detect and track any fast moving objects in the wide field of regard.

This thesis investigates the use of the Murchison Widefield Array (MWA) as a passive radar receiver for the surveillance of space, specifically using commercial frequency modulation (FM) radio (88 - 108 MHz in Australia) as the illumination source. The radar configuration is a bistatic radar with a widefield staring receiver able to surveil an extensive volume of the sky, with high power transmitters at significant baseline distances, offering a significant illumination volume.



This thesis details the challenges involved with long-integration radar processing with an extremely large sensor, investigates the intersection between astrodynamic motion parameters and radar detection parameters that make surveillance feasible, and culminates in a large scale demonstration where the MWA is the receiver as part of a continent-spanning multistatic radar network.



Figure 1.1: Single MWA tile at Inyarrimanha Ilgari Bundara the CSIRO Murchison Radio-astronomy Observatory. Credit: Natasha Hurley-Walker ICRAR/Curtin.

The MWA is a low-frequency radio telescope in remote Western Australia (Tingay et al., 2013a; Wayth et al., 2018), a precursor to the forthcoming Square Kilometre Array (SKA) (McMullin et al., 2020). The MWA is a large sensor, consisting of hundreds of sub-receivers, known as tiles, distributed over a  $30 \text{ km}^2$  geographical footprint. An MWA tile is shown in Figure 1.1. The use of the MWA as a passive radar receiver for space surveillance is made possible by building on

recent understanding and technological advances across a large swathe of different fields. The areas covered in this introductory chapter are passive radar (1.1), radio astronomy (1.2), space surveillance (1.3), radar techniques for matching high velocity and manoeuvring targets (1.4), and orbit determination (1.5). The detailed history and background to these areas is outside the scope of this thesis, and only a brief discussion and overview of the most relevant aspects is included. Also covered in this chapter is the background and previous work undertaken by the MWA for space surveillance (1.6). Section 1.7 concludes the chapter with an outline of the rest of the thesis, detailing the progression from the initial results through to the results from a demonstration space surveillance campaign.

## 1.1 Passive Radar

Passive radar is a form of radar that uses existing radio frequency (RF) energy as a source of target illumination, instead of requiring a dedicated transmitter. There are many advantages to this approach, such as the radar system being electromagnetically covert and also far more cost efficient to operate. However, this comes at the disadvantage of leaving the radar at the mercy of what is being transmitted. The signals used are not guaranteed to be suitable for radar purposes. The passive radar technique as a form of radar has been long understood and in use, however, it is only in recent decades that passive radar has gained prominence, mostly due to the increase in computational power available to radar designers, and also the rise of wide-area broadcast entertainment, especially digital signals.

The origin of passive radar can be traced to the famous Daventry Experiment, conducted on the 26th of February, 1935 (Wilkins, 2011). The aim of the experiment was to validate calculations predicting the detection of an aircraft from reflections of a radio transmitter. To test this theory, two antennas were erected with their outputs combined to null the direct transmissions of the 10

kW BBC Empire broadcast<sup>1</sup>. An aircraft was then flown around the area. Any reflections from the aircraft would not be nulled and so should be detected. The experiment was a success, the aircraft was able to be detected up to a range of 8 km. Ultimately this success led to the development of the Chain Home radar system, and all Allied radar effort in the Second World War (Neale, 1985).

The Daventry Experiment also, indirectly, gave rise to the first operational passive radar, with the German Klein-Heidelberg system utilising the Chain Home transmissions to passively detect bomber aircraft. The system briefly operated during the latter stages of the Second World War before the radar sites were overrun by Allied forces (Griffiths & Willis, 2010).

In the years since the Second World War, interest in passive radar has waxed and waned (Kuschel, 2013). However, there was a significant increase in research and interest in the latter decades of the 20th Century (Griffiths & Long, 1986; Beley et al., 1995; Sahr & Lind, 1997, 1998; Ringer et al., 1999; Howland, 1999). Commercial passive radar systems were also developed during this time, most notably the Silent Sentry system, a rapidly deployable wide area early warning surveillance radar (Baniak et al., 1999).

In recent years, increased computational power and the widespread transition to digital television and radio have fuelled a resurgence in passive radar research, which continues to this day. This period of time saw the development of a number of demonstration systems and example experiments (Howland et al., 2005; Poullin, 2005; Kulpa & Misiurewicz, 2006; Yardley, 2007; O'Hagan & Baker, 2008; Palmer et al., 2008; Fabrizio et al., 2008; Coleman & Yardley, 2008; Malanowski & Kulpa, 2008; Palmer et al., 2009), including a passive radar system utilising illumination from geosynchronous orbit (Palmer et al., 2009). Other factors contributing to this renewed interest in passive radar is the increasingly congested electromagnetic spectrum and significant military interest in electromagnetically

---

<sup>1</sup>The illuminating signal was actually an unmodulated carrier, so it may potentially be more correct to refer to the experiment as cooperative bistatic rather than *truly* passive (Wilkins, 2011).

covert surveillance.

The development of FM radio based passive radar is of particular relevance to this thesis. In comparison to other digital illuminators, FM radio has typically not been favoured for passive radar because of the poor range resolution and the content-dependent radar properties (rock music yields different results to voice). However, the attributes of FM radio passive radar are ideal for long range surveillance due to the high flux density, smaller data volumes, and high powered transmitters. For that reason, FM radio passive radar has been used for long-range aircraft surveillance (Sahr & Lind, 1997; Ringer et al., 1999; Howland et al., 2005; O’Hagan & Baker, 2008; Malanowski et al., 2012, 2014; Inggs et al., 2014; Hennessy et al., 2022a).

With the expected future reduction in demand for wide broadcast entertainment such as television and radio (as opposed to more directed and individual streaming services), some have speculated that as of 2022 passive radar is at its zenith, that is “peak passive radar” (Zatman, 2022). However, beyond broadcast entertainment there is significant potential for growth in passive radar with many other potential transmitter options enabling wide area surveillance, including hitchhiking radar and space-based passive radar, as well as solar and extraterrestrial sources. Non-cooperative bistatic radar (also referred to as parasitic radar or hitchhiking radar) uses other radars as a source of illumination, and offers many advantages over entertainment-signal based passive radar as the signals are designed for radar purposes (Willis, 2005; Johnsen & Olsen, 2007; Willis & Griffiths, 2007; Strømøy, 2013; Samczynski et al., 2015; Crawshaw & Maxey, 2022).

With the significant increase in the use of space (as will be discussed further), there is growing research into space-borne and space-based passive radar (Palmer et al., 2009; Cristallini et al., 2010; Zavorotny et al., 2014; Cristallini et al., 2018; Persico et al., 2018). Finally, although there has been research into geostationary satellite based passive radar for decades, only recently has there been successful

demonstrations of solar and other extraterrestrial sources of illumination (Peters et al., 2021; Bezrukovs et al., 2023). These far-flung and distant transmission options imply large surveillance volumes illuminated by ever-present radiation sources.

## 1.2 Radio Astronomy

Radio astronomy, much like passive radar, also originated from radar in the Second World War. Many early radio astronomers worked on radar during the war and many early achievements were made with repurposed radar equipment (Lovell, 1990; Muller & Oort, 1951; Smith, 1951). This was especially true in Australia: “The Australian development can be traced to the concentration on radar development during World War II. This brought together in a well-equipped laboratory a group of able young physicists with experience of radio techniques.” (Pawsey, 1953). A large number of well-known radio astronomers contributed significantly to radar development early in their careers (Goss et al., 2023; Lovell, 1964; Goss & McGee, 2010; Kerr, 1984).

Following the war, prescient scientific radar work was undertaken with a campaign to better-understand the higher layers of the ionosphere using radar reflections from the moon (Kerr et al., 1949; Kerr & Shain, 1951). Australia was the fourth country to detect the moon with radar (Lovell, 1990). These trials consisted of large-scale bistatic radar experiments utilising a 20 MHz shortwave transmitter 600 km away, and also attempted international multistatic reception. Due to hardware requirements, the radar astronomy program was not continued in Australia. The focus was shifted to reception-only radio astronomy (Kerr, 1952, 1984). Notwithstanding this, significant radar astronomy work has been achieved throughout the 20th century (Ostro, 1993).

Early radio astronomy has been predominantly conducted with large receiver dishes, with examples such as Jodrell Bank and Parkes. These systems produced a single timeseries channel of output and were well suited to time and

frequency analysis. Large dishes are still used today but there has been a significant improvement in their capability. The majority of modern radio astronomy is conducted with arrays of individual antennas acting as interferometers, forming correlation products from which images and other data products are produced. It is only in recent years that computational processing and receiver improvements have enabled high time-resolution capabilities for large scale arrays (van Haarlem et al., 2013; Bhat et al., 2014; Tremblay et al., 2015). These high time-resolution modes enable the direct implementation of radar processing algorithms and capabilities.

### 1.3 Space Surveillance

Since the launch into orbit of Sputnik in October 1957, the use of space by humans has continued at an increasing rate. This is reflected in the recent advent of many megaconstellations, which means that there are now more human made objects in space than ever before, especially in LEO. As the launch of Sputnik took the West by surprise, one of the first space surveillance sensors that was able to detect the launching rocket body was the Jodrell Bank Mark I radio telescope used as a radar (Lovell, 1990). The need to detect and track the ever-growing number of satellites, rocket bodies, and other resident space objects (RSOs) in orbit is growing and becoming increasingly more challenging. Illustrations of the large number of RSOs in orbit around Earth are shown in Figures 1.2 and 1.3, the latter particularly highlighting the crowded nature of LEO.

In a similar vein to early radioastronomy sensors, the early space surveillance sensors were dish-based tracking radars. These dishes are excellent sensors for sensing the RSOs for tracking and predicting future locations. However, such narrow field-of-regard sensors can only track one object at a time, and are not suited for searching for new objects or lost (or even manoeuvring) objects.

Worldwide, the major space surveillance networks comprise a variety of sensor types, including optical telescopes, tracking radars, space-based sensors, and

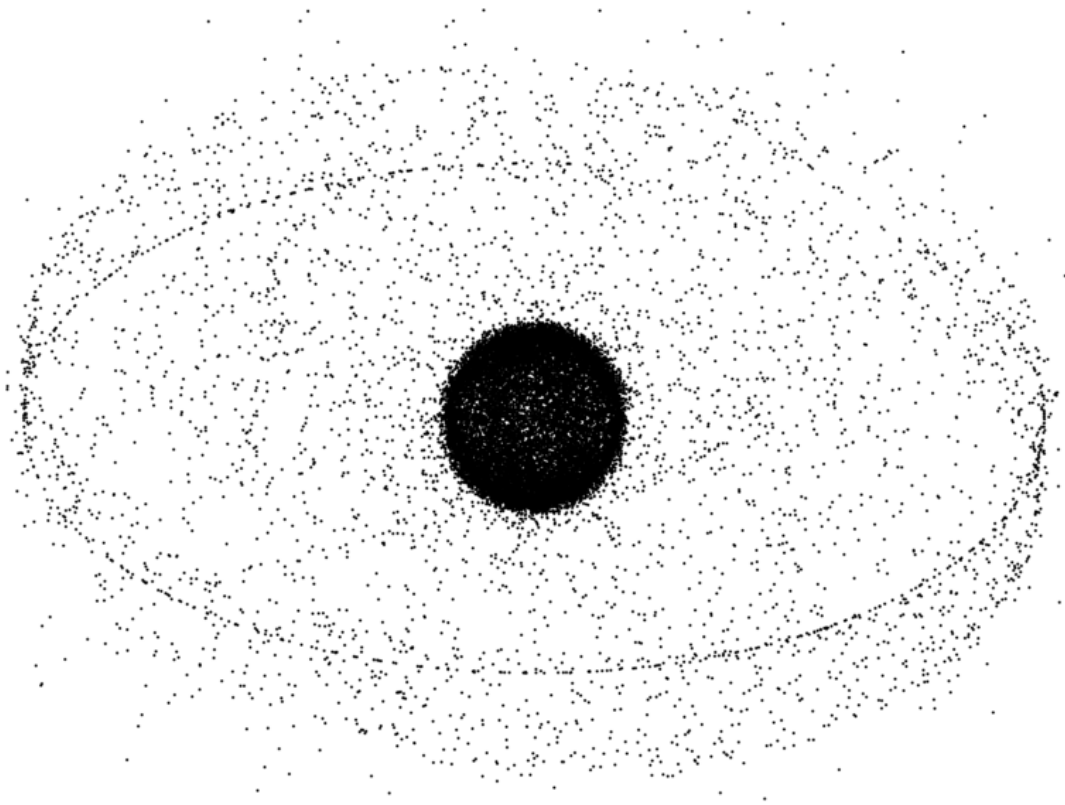


Figure 1.2: Illustration of all the objects orbiting Earth that are currently being tracked by the Space Surveillance Network out to a range of approximately 50,000 km. At this range all the major orbital regimes, including geostationary orbit, are visible.

phased array radars (Weeden et al., 2010; National Research Council, 2012; Geul et al., 2017). The narrow field sensors (e.g. telescopes and tracking radars) maintain tracks on a large number of objects using cueing information to schedule measurements of an RSO, then updating the tracks to cue subsequent sensors. However, large scale phased array radars are typically required for uncued searching and track initialisation.

Most of the phased-array systems were built for missile detection and warning purposes, and only perform a space surveillance function as a secondary role. However, there are a large number of radar array systems designed specifically for space surveillance, either scanning or staring, ranging from fully operational elements of the space surveillance network (SSN) through to research and demon-

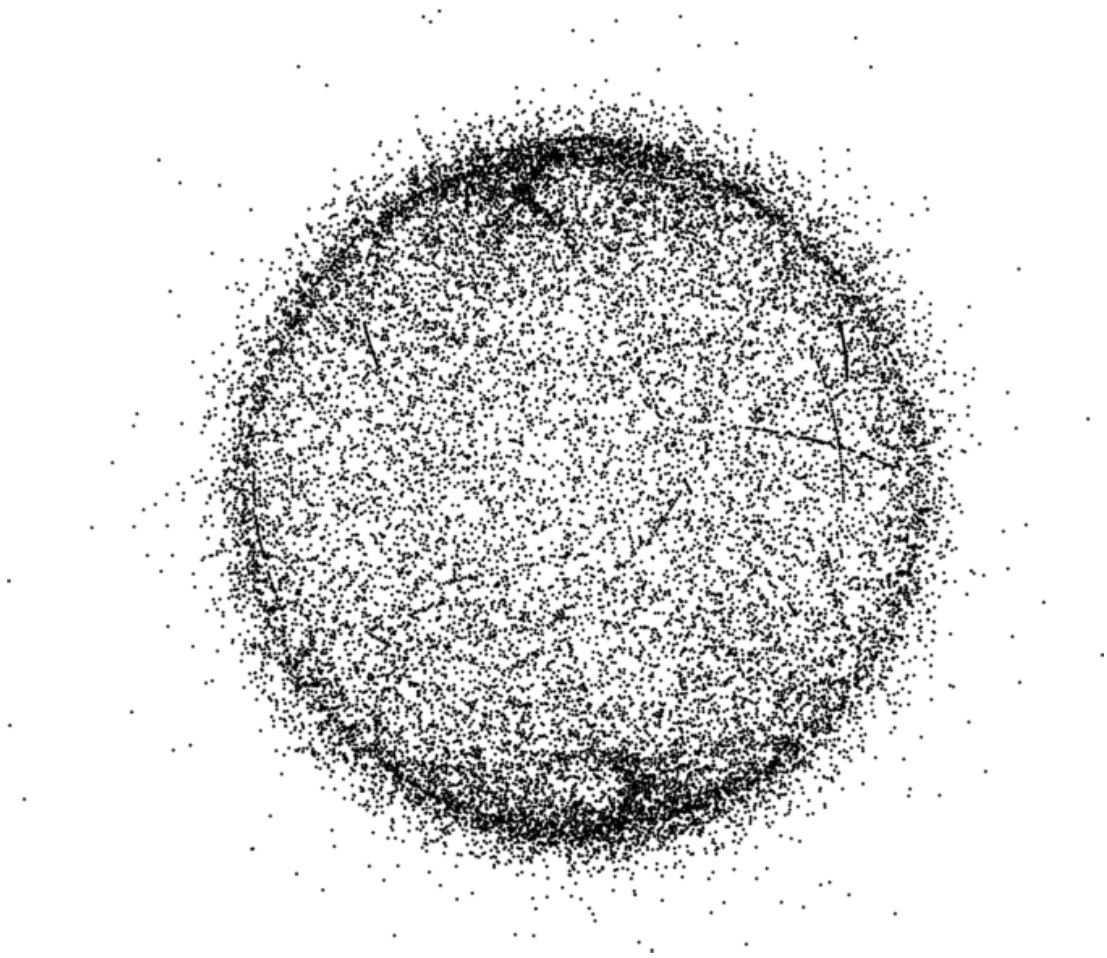


Figure 1.3: Illustration of all the objects orbiting Earth that are currently being tracked by the Space Surveillance Network out to a range of approximately 10,000 km. At this range the LEO population, and part of the medium Earth orbit population, is visible.

strator prototypes. Some examples include the operational systems of Spacefence (Haimerl & Fonder, 2015) and GRAVES (Grand Réseau Adapté à la Veille Spatiale) (Michal et al., 2005), the global network of LeoLabs' linear arrays (Rowland et al., 2021), a large number of high frequency (HF) and very high frequency (VHF) wide area surveillance radar systems (Holdsworth et al., 2020; Heading et al., 2022; Frazer et al., 2013b,a, 2016; Clarkson & Palmer, 2019; Finch et al., 2022; Hennessy et al., 2023a,b), and a large number of other higher frequency systems, including some modular designs (Saillant, 2016; Wilden et al., 2016; Gomez



et al., 2019; Wang et al., 2022; Wayth et al., 2022; Neuberger et al., 2023).

Of particular interest and relevance are the GRAVES system (Michal et al., 2005), HFLOS (Frazer et al., 2013b), Buckland Park (Holdsworth et al., 2020), and Silentium space surveillance systems (Finch et al., 2022). The key characteristic that these radars have in common is their unconventional approach (or unconventional compromises) when compared to a traditional missile approach warning / space surveillance radar. By making tradeoffs, such as using lower bandwidths, lower frequencies, or not utilising a dedicated transmitter, it is possible to achieve equivalent surveillance performance to larger systems (Frazer & Williams, 2019). A similar approach is taken with this thesis to perform a space surveillance function with the MWA using passive radar.

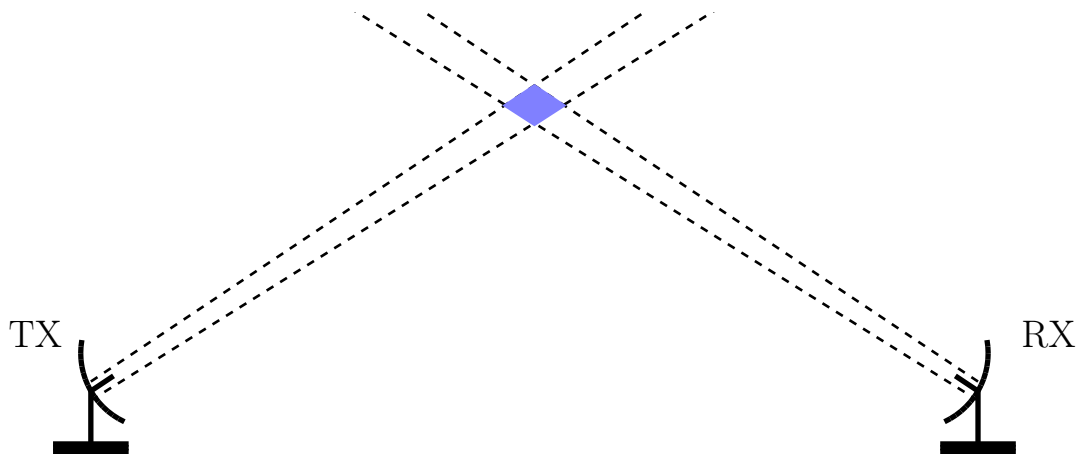


Figure 1.4: Bistatic space surveillance radar diagram with a narrow-beam transmitter and a narrow-beam receiver. The surveillance region is highlighted in the blue region.

Following the initial success of the Jodrell Bank Mark I radiotelescope in detecting rocket bodies, there has been a continual effort in undertaking the surveillance of space using radiotelescopes as radar receivers. These radiotelescopes range from operational systems through to planning simulations and include: the MWA (the focus of this thesis) (Tingay et al., 2013b; Palmer et al., 2017; Wayth et al., 2018; Hennessy et al., 2019; Prabu et al., 2020a,b; Hennessy et al., 2021; Prabu, 2021; Hennessy et al., 2022b; Prabu et al., 2022, 2023); the

Low-Frequency Array (LOFAR) (Malanowski et al., 2021a; Jędrzejewski et al., 2022a); the Australia Telescope Compact Array (ATCA) (Nosrati et al., 2022); the Green Bank Telescope (GBT) (Watts et al., 2015); the Northern Cross Radio Telescope (Losacco et al., 2019); the Sardinia Radio Telescope (SRT) (Pisanu et al., 2020; Cataldo et al., 2020; Welch et al., 2022); MeerKAT (Dhondea & Ingg, 2019); the Tianlai radio array (Li et al., 2019); and the Arecibo Telescope (Murray & Jenet, 2022).

Typically, when radio telescopes are utilised as radar receivers, the illuminating source is a cooperative radar transmitter, with a bistatic configuration generally consisting of a narrow transmit beam in conjunction with a narrow receive beam (such as from a dish, or similar), this is illustrated in Figure 1.4. The resulting surveillance volume is often highly limited, being the intersection of these two narrow beams. An advantage to this configuration is that all of the RF energy, and radar sensitivity, is concentrated in this narrow volume, meaning the radar can detect very small RSOs. However, the disadvantages are that the constrained surveillance volume limits the ability to accurately update tracks, and is potentially unable to detect objects without cueing. Another common configuration is a narrow-beam transmitter in conjunction with a receiver array, referred to as a ‘pulse-chasing’ radar, and illustrated in Figure 1.5. The use of a receiver array allows for a slightly larger surveillance volume, albeit a surveillance volume still constrained by the narrow transmit beam.

Notable exceptions to this narrow field surveillance mode of operation are the MWA and LOFAR, a northern hemisphere low frequency radiotelescope. These systems are low-frequency receive array telescopes used as a radar receiver in conjunction with wide illumination, resulting in a significant surveillance volume as illustrated by Figure 1.6. With a receive array, after the surveillance data is digitised, there is essentially no limit to the number of receive beams which can be formed. This enables a greater degree of flexibility in testing target hypotheses,

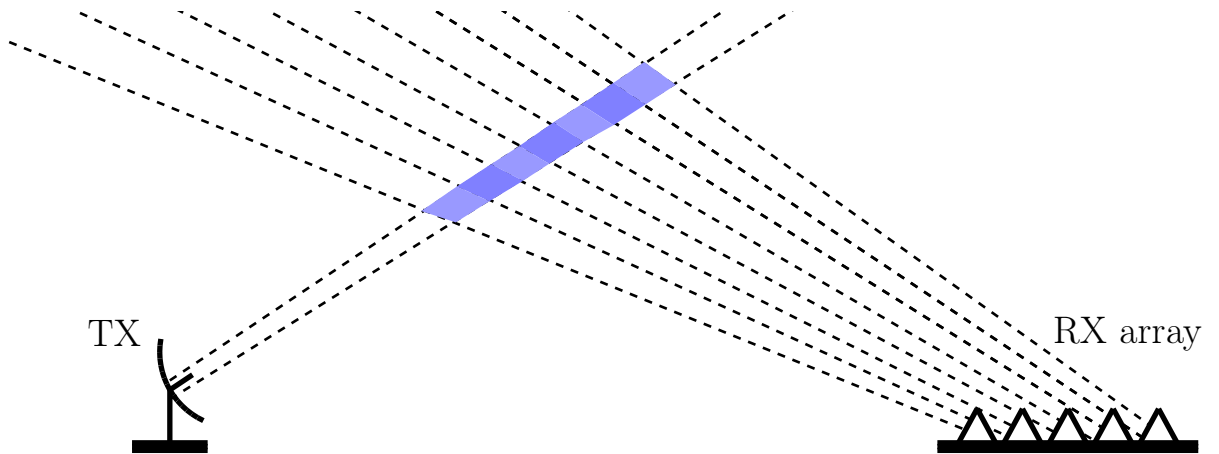


Figure 1.5: Bistatic space surveillance radar diagram with a narrow-beam transmitter and a receiver array with seven notional receive beams. This configuration is referred to as a pulse chasing radar. The surveillance region is highlighted in the blue region.

the only (receive) limit to the surveillance volume is computational processing<sup>2</sup>.

LOFAR is an extremely large receiver array consisting of a large number of subarrays, or stations. There is considerable research progressing the use of LOFAR stations as passive radar receivers with digital television as the illuminator (Kłos et al., 2020; Malanowski et al., 2021a; Droszcz et al., 2021; Jędrzejewski et al., 2021, 2022a,c,b; Malanowski et al., 2023; Jędrzejewski et al., 2023). The LOFAR system utilises digital television, specifically DVB-T, as the illumination source which is at a higher frequency and higher bandwidth than FM radio. The higher bandwidths and frequency allow for more accurate range measurements and potentially greater sensitivity to smaller objects, but also require additional processing challenges and potentially smaller transmitter beamwidths, which may reduce surveillance coverage.

With the recent advent of megaconstellations, space surveillance systems are increasingly challenged by the large number of satellites (along with all the associated launch debris) and other debris events such as collisions and anti-satellite weapons tests. This problem is compounded by the emergence of new propulsion

---

<sup>2</sup>In practice, other constraints such as receiver beam-pattern and maximum detection ranges will place limits on realistic surveillance volumes.

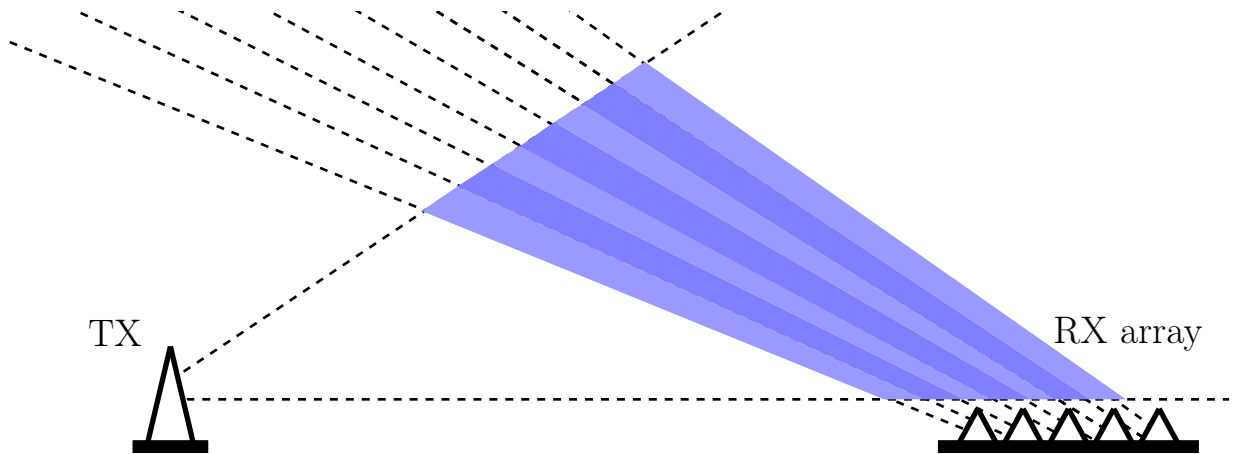


Figure 1.6: Bistatic space surveillance staring radar diagram with a wide-beam transmitter and a receiver array with seven notional receive beams. Typically, the transmit beamwidth would extend considerably in azimuth as well (not shown). The surveillance region is highlighted in the blue region.

technologies, which means these satellites are manoeuvrable in ways not previously encountered. The result is an incredibly complex and challenging space surveillance problem, demanding new and wider surveillance options.

## 1.4 Keeping Up with Fast Targets

Another challenge faced by radars is the effective detection of fast moving, and manoeuvring, targets. This is a particular challenge for radars requiring long time integration for sensitivity, as even constant motion can cause the radar and target geometry to change over the processing interval. If any of the radar measurement parameters change across the processing interval, then the target's energy returns will be divided, or *smeared*, across the measurement bins, drastically reducing sensitivity.

Radars primarily measure a transmitted signal's delay, corresponding to the reflector's radial range, as well as the transmitted signal's frequency (Doppler) shift, corresponding to radial velocity (Woodward, 1953). However, this matching process can be extended to additional motion parameters including Doppler-rate as well as an arbitrary number of subsequent derivatives (Bello, 1960; Kelly,

1961). Indeed, matching Doppler-rate, or acceleration, has been in use since the 1960s for improved detection of rockets and missiles (Jensen & McGeogh, 1963; McGeogh & Jensen, 1967). General acceleration processing has been an ongoing area of radar research (Abatzoglou & Gheen, 1998; Yasotharan & Thayaparan, 2002; Boashash, 2016; Sirianunpiboon et al., 2019; Wilden et al., 2019).

Research into the radar detection of accelerating targets (mitigating Doppler walk) is a specialised case of more general fields such as detection of polynomial-phase signals and time-frequency analysis (Abatzoglou, 1986; Boashash et al., 1990; Djuric & Kay, 1990; Peleg & Porat, 1991a; Boashash, 1992; Peleg & Friedlander, 1995; Barbarossa & Petrone, 1997; Barbarossa et al., 1998; Xia, 2000; O’shea, 2002). Such work is also directly applicable to the detection of other chirping, or accelerating, signals in other fields such as sonar or even the study of bat echolocation (Griffin et al., 1960; Altes, 1990). Just as passive radar research has flourished due to the increase in modern computational power, all of these methods are increasingly realisable.

While Doppler migration (caused by a non-zero Doppler-rate in conjunction with large processing intervals) is perhaps the most deleterious source of sensitivity loss resulting from motion, range-walk (caused by the changing delay to a reflector) is also a significant source of loss. Range-walk mitigation typically requires a form of resampling (Jin & Wu, 1984; Perry et al., 1999; Perry et al., 2007; Kulpa & Misiurewicz, 2006; Pignol et al., 2018). For that reason, it is generally far more computationally demanding to mitigate range-walk compared to Doppler-walk.

Of particular relevance is the work on passive radar research that has been undertaken at the Warsaw University of Technology, focusing on fast targets. The challenges of long integration, motion matching methods for accelerating and jerking targets, and even multistatic methods are all explored. Results include the detection of supersonic rockets (Malanowski & Kulpa, 2008; Malanowski, 2012; Rzewuski et al., 2015; Borowiec & Malanowski, 2016; Malanowski et al., 2018a,b).

Finally, a particular focus of this thesis is the investigation of the applicable intersection of radar and orbital motion parameter spaces. Simple orbits can be characterised by only six parameters, whereas the radar measurement parameter space is potentially unbounded. This is a challenge for this type of radar as the limiting factor in detection performance may in fact be computational processing. By using radar constraints to limit the orbital search space, or specific orbital aspects to limit the radar search space, significant practical results have been achieved to incorporate, or solely focus on, orbital motion and orbit determination (Markkanen et al., 2005; Kohlleppel, 2018; Hoffmann et al., 2019; Awadhiya & Vehmas, 2021; Schily et al., 2022).

## 1.5 Orbit Determination

Orbit determination is the process of taking a set, or track, of measurements to calculate the orbital parameters of an object, such that its future position can be predicted accurately in order to be detected in the future. Orbit determination dates to the 17th century and the significant interest in understanding and predicting the motion of planets, moons, and other celestial bodies. Celestial orbit determination techniques that have been developed over the centuries are just as applicable to satellites and other RSOs in LEO (Bate et al., 2020).

The standard approach for orbit determination is, given a set of measurements, to use a subset of the measurements (typically two or three) to geometrically determine an initial, or preliminary, solution. Then this initial solution is used in conjunction with the full measurement set to estimate the orbital state (Escobal, 1965; Vallado & McClain, 2001; Bate et al., 2020; Montenbruck et al., 2002). This approach first makes an approximate guess, typically referred to as initial orbit determination (IOD) or preliminary orbit determination. The IOD stage is almost exclusively a two body problem, the simplest orbital model. Other complicating factors such as the perturbations from forces such as from atmospheric drag, the gravity field of other celestial bodies, or electromagnetic forces, are not

incorporated until the full orbit determination step (Escobal, 1965).

The majority of IOD research is angles-only IOD (that is, methods to estimate an object’s position and velocity with only spatial/angular information from an observer), having regard to the historical celestial surveillance being entirely conducted with optical telescope observations. Even today, the most common space surveillance sensor is an optical telescope. Classical angles-only IOD methods are the Gauss, Laplace, and Double R methods (Escobal, 1965), although there are an increasingly large number of modern approaches (Gooding, 1993; Schaeperkoetter, 2012; Schwab et al., 2022; Gong et al., 2023).

In comparison, radar offers far more information to precisely determine the orbit of RSOs: “The introduction of radar into the implements of modern science has produced a great variation from established techniques in orbit determination schemes. For the first time, the orbit determiner could measure the distance or extension between the point of observation and the satellite, that is, the *slant range*” (Escobal, 1965). That is, rather than an angle or line of bearing, a radar detection itself provides an estimate of an object’s position. The most common IOD approaches for these data are the use of two positional estimates and a time of flight (known as Lambert’s Problem), or the use of three positional estimates (and associated times). There is a wide range of approaches for solving Lambert’s Problem (Izzo, 2015). For three positions, the common IOD methods are the Gibbs and Herrick-Gibbs methods (Escobal, 1965). However, like other IOD problems, this is still an area of ongoing research.

As IOD is typically a geometric problem, most of these methods use a set of positional estimates only. However, often radars will not be able to accurately estimate these (individual) detection positions, and this can result in a poor IOD estimate. With long-integration radars, Doppler may be a system’s most accurate measurement parameter. Because of this (as well as the fact that some radars do not measure range, such as GRAVES), there has been considerable work in recent years on IOD methods incorporating Doppler (Yanez et al., 2017; Zhang et al.,

2019; Losacco et al., 2020; Christian et al., 2022; Losacco et al., 2023; Qu et al., 2022b,a; D’Souza & Zanetti, 2023). In contrast, Doppler has always been used as a key parameter in the full orbit determination stage (Guier & Weiffenbach, 1959; Patton, 1960).

Another approach, which has created considerable recent interest, is the use of admissible regions, which can define the region of corresponding realisable orbits (Milani et al., 2004; Tommei et al., 2007; DeMars & Jah, 2014). Rather than treating detections separately (that is, IOD followed by OD), each measurement is instead used to narrow or constrain the region. This allows for the propagation of uncertainties between possible orbits, as well as a probabilistic approach to IOD (DeMars & Jah, 2014).

## 1.6 Space Situational Awareness with the MWA

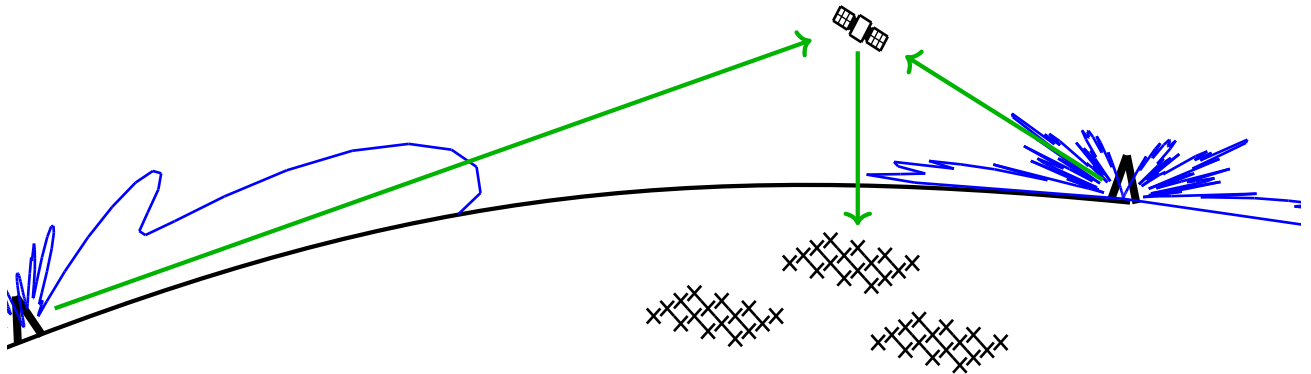


Figure 1.7: Illustration of the use of the Murchison Widefield Array (MWA) as a passive radar, showing two transmitters, one satellite and three MWA tiles. The two transmitters’ elevation beampatterns (in blue) and the signal path (in green) are also shown.

Since its inception, the MWA’s use as a passive radar receiver has been considered. As early as 2006, predictions were made that the MWA, used as a passive radar, would detect FM radio reflections from satellites and RSOs (Lind, 2006). Following these predictions, the first relevant results were published in 2012, de-



tailing the amount of terrestrial radio frequency interference (RFI), particularly FM radio, detected from moon reflections (McKinley et al., 2013). This work inferred how the Earth would appear electromagnetically to a distant sensor in the FM band. These reflections also highlighted the significant amount of energy being transmitted in the FM band into the space environment.

The first MWA results on RSO detection used reflected FM radio to detect the International Space Station (ISS) and were published in 2013 (Tingay et al., 2013b). This was achieved by using images produced using radio astronomy methods. That is, the MWA, used as an interferometer, is able to form wide area images resolving the received power in the FM band spatially, essentially an electronic support measure (ESM) product. These products are highly accurate spatially and also provide coarse frequency accuracy, although they do not provide range information. This approach is referred to as ‘incoherent’, with respect to the transmitted signal, it is transmitter agnostic as the produced images are the result of any and all received energy. This incoherent space surveillance approach has progressed significantly since the early initial results (Prabu et al., 2020a,b; Joubert & Tingay, 2021; Prabu, 2021; Prabu et al., 2022).

Both the 2012 and 2013 results were formed using an early version of the MWA, consisting of only 32 tiles. Importantly for this thesis, the initial RSO publication, (Tingay et al., 2013b), predicted that a 128 tile MWA, when used as an incoherent passive radar receiver with a time integration of 1 s and a frequency bandwidth of 50 kHz, would be able to detect an object the size of  $0.5 \text{ m}^2$  up to a range of 1,000 km.

Following these initial detections, the first ‘coherent’ results were published in 2017 (Palmer et al., 2017) and also consisted of detections of the ISS using reflected FM radio. The term ‘coherent’ refers to the radar processing with respect to the transmitted signal, where results were produced with full passive radar (that is, pulse Doppler processing) methods. In this experiment, the reference signal, the information about what was transmitted, was observed by the

MWA itself as there was sufficient sensitivity to detect diffracted FM radio over the horizon with a distance of approximately 300 km. By comparing what was transmitted to the reflected signal, it was possible to estimate the relative range and Doppler of the reflecting satellite.

The continuation of coherent passive radar work is the core focus of this thesis. This includes further development of the understanding of processes and algorithms to utilise the MWA as a passive radar for the surveillance of space, particularly confirming the initial detection predictions for small objects at a range of 1,000 km. An illustration of the use of the MWA as a passive radar receiver is shown in Figure 1.7, detailing several terrestrial transmitters illuminating a satellite with the MWA observing the reflections.

## 1.7 This thesis: direction and scope

The work presented in this thesis is the result of a confluence of recent advances in modern technology, particularly the high time resolution capabilities of modern radio telescopes, the uptake in passive radar, and increased computational processing capabilities. All of these factors are crucial to the implementation of space surveillance processing on widefield sensors that utilise MWA-like technologies.

Early chapters of this thesis present detections of larger objects, such as the Hubble Space Telescope and large rocket bodies. Subsequent chapters contain the results of targeted searches of specific smaller satellites and debris. Finally, the latter parts of the thesis contains the results from a general space surveillance campaign reporting the detection of objects meeting the initial predictions (Tingay et al., 2013b). However, beyond simply demonstrating a capacity to detect a larger number of smaller objects, the key results from this work are: the methods developed to achieve detections in wide area surveillance for matching fast targets; the accurate determination of orbital parameters; and advances in the translation of the theory to the practical implementation of these methods for a real-world sensor.

The structure of the rest of this thesis is as follows:

- Chapter 2 details the radar processing required to form a matched-product for orbital motion with a sensor like the MWA, outlining the passive radar and orbit determination challenges which are addressed in the following chapters;
- Chapter 3 (originally published as Hennessy et al. (2019)) demonstrates initial results in detecting and tracking smaller objects (in comparison to the ISS), as well as some of the advanced radar slow-time techniques required. This chapter also highlights some of the novel approaches required to realise radar functionality on a large scale system including calibration and synchronisation;
- Chapter 4 (originally published as Hennessy et al. (2020)) investigates the intersection of a two-body astrodynamics parameter space in conjunction with radar parameter space. It shows how a six-parameter orbital search space can be reduced to practically undertake blind searches for objects in orbit, especially focusing on when the most-common target types are likely to be most detectable;
- Chapter 5 (originally published as Hennessy et al. (2021)) develops and implements the novel ideas from the previous chapter, including a brief observational campaign, demonstrating uncued IOD, an extremely challenging task on a sensor like the MWA, and comparing the results against other common IOD approaches;
- Chapter 6 (originally published as Hennessy et al. (2022b)) is the culmination of the previous chapters, demonstrating the full space surveillance capabilities of the MWA, including the results from a short trans-continental observation campaign. The techniques discussed cover extreme baseline length passive radar as well as accurate orbit determination, including multistatic orbit determination, of small objects at large distances;

- Chapter 7 concludes the thesis by briefly summarising the main results and briefly exploring future research directions; and
- Finally, Appendix A (originally published as Hennessy et al. (2022a)) demonstrates how the approaches and techniques developed in this thesis (specifically, for an extremely large sensor) are broadly applicable for all passive radar space surveillance sensors, in this instance being applied to a much smaller, deployable, real-time, long-range passive radar systems for the detection of satellites.

## Chapter 2

# Methodology, Signal Processing and Problem Formulation

This chapter contains a description of the approaches and methods used to obtain and process radar data used in this thesis, as well as an outline of the challenges faced by a sensor like the Murchison Widefield Array (MWA) when used as a radar for objects in low Earth orbit (LEO).

More specifically, this chapter provides an introduction to passive radar, including the fundamental concepts of a bistatic radar system and the parameter types these systems are able to measure and sense. The chapter details the technical aspects of the MWA which are relevant to the collection and pre-processing of radar data, particularly signals at FM radio frequencies and bandwidths, including the data pipeline as well as calibration. This chapter also describes the population of objects in Earth-centered orbit, particularly LEO, and covers the simple Keplerian orbital models used, highlighting the significant speeds which are attained by objects at lower altitudes. Standard radar product formation signal processing is detailed, with examples from the MWA.

All these aspects coalesce (Section 2.4.2) to highlight the problem of wide-area space surveillance with the MWA using passive radar at FM frequencies. That is, the extreme and dynamic velocities of objects in LEO present a significant signal

processing problem. Some aspects of this problem are common to all staring space-surveillance radar systems. However, some other aspects are unique to the MWA. The signal processing challenge is so significant that any direct approach to create a matching radar product would be impossible. This outlines the challenges the rest of this thesis attempts to address and alleviate.

## 2.1 Passive Radar

An active radar will emit a high-powered, and known, signal, and then a receiver system will receive signals from a surveillance region of interest and search for reflected copies of the transmitted signal. This searching is achieved through correlation, whereby a reference copy of the known transmitted signal is shifted and contorted to match a hypothesised return, and so any correctly-matched hypothesis will form a correlation peak. The specific implementation is achieved through the incredibly efficient pulse-Doppler processing method (Stein, 1981; Palmer et al., 2011), forming a delay-Doppler map.

Detections from these delay-Doppler maps will specify the delay, in time, between the signal being transmitted and the reflected signal being received, as well as the frequency, or Doppler, shift between the transmitted signal and the reflected signal. If the radar's transmitter and receiver are at the same location, then this detected time delay will be proportional to the range to the reflector and the Doppler shift will be proportional to the reflector's radial velocity. The measured range specifies a sphere of potential locations where a reflector could be positioned, and this sphere can be combined with the knowledge of the receiver system's beam pattern (or beamformed direction) as well as the transmitter's beam pattern, to estimate the true reflector position.

The radar's ability to measure this delay is proportional to the transmitted signal's bandwidth, and the radar's ability to measure the Doppler shift is proportional to the transmitted signal's processing interval or length of correlation. Additionally, the correlation properties of the transmitted waveform are also a

determining factor.

A bistatic radar is a type of radar where the transmitter and receiver are separated. The radar system operates in the same manner, but now the measured delay is proportional to a ‘bistatic range’, and the measured Doppler shift is proportional to the rate of change of this bistatic range, referred to here as the ‘bistatic Doppler’. Instead of a sphere of potential locations, a bistatic delay measurement defines an iso-range ellipsoid of potential locations, with the transmitter and the receiver locations forming the ellipsoid’s foci. A two-dimensional cut of this ellipsoid is shown in Figure 2.1, including the locations of the transmitter, the target, and the receiver forming the ‘bistatic triangle’, with the bistatic angle being the angle subtended between the transmitter, target, and receiver (Willis, 2005; Malanowski, 2019).

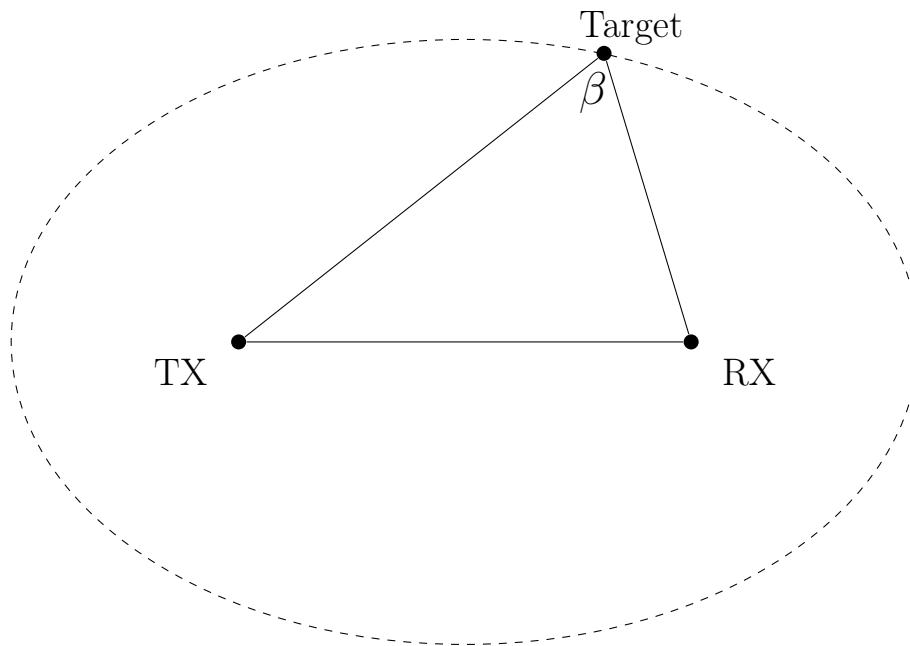


Figure 2.1: The bistatic triangle, formed by the location of the transmitter (TX), receiver (RX), and the target. The bistatic angle,  $\beta$ , is also shown.

Another difference caused by separating the transmitter and the receiver (although it should be noted that standard monostatic radar is simply a special case of bistatic radar) is with the delay resolution. The radar’s ability to mea-

sure bistatic delay is still proportional to the signal's bandwidth, but it is also inversely proportional to  $\cos\left(\frac{\beta}{2}\right)$ , and so the range resolution varies depending on where the target is relative to the bistatic geometry (Willis, 2005).

Passive radar is a form of bistatic radar which uses already existing sources of radio frequency (RF) illumination, such as commercial radio and television broadcasts, instead of a dedicated or cooperative transmitter. The operation of the passive radar is essentially identical to that of any bistatic radar. There are many advantages to using passive radar over active radar, such as reduced size, weight and power of the radar systems. Another advantage of not requiring a dedicated transmitter is that passive radars are electromagnetically covert. However, there are drawbacks, by not having control over the transmitted signal, a passive radar system is at the mercy of the characteristics of existing transmissions.

By utilising a non-cooperative transmitter, the radar system may be required to operate with sub-optimal illumination. Desired surveillance regions may not be fully covered, there may be insufficient transmit power for required sensitivity, and the transmitted waveform may not have the right radar properties. Many different radar waveforms are used, and the common metric of their efficacy is referred to as the ambiguity function.

The ambiguity function represents the ideal matched filter output with the specified waveform, across all delay and Doppler values of interest. For example, a tone signal would be indistinguishable to a delayed version of itself, and so has no range resolution. Another common waveform is the chirp, a linear frequency modulated waveform. A (repeated) chirp is ambiguous in delay and also in Doppler. A single detection could correspond to an infinite number of velocities. This type of ambiguity function is referred to as a 'bed of nails'. The advantages to such an ambiguity function are that only a small section is required to be calculated in order to sample the infinite delay and Doppler spans, and also the region between the *nails* will be zero. Conversely, a noise waveform's ambiguity function is referred to as a 'thumb-tack'. A detection will uniquely correspond to the cor-



rect delay and Doppler (with the accuracy determined by the signal bandwidth and the processing interval), the main disadvantages of a *thumb-tack* response (as opposed to a *bed of nails*, from an ambiguous waveform) is that the non-matching aspects of the cross correlation will be non-zero, and so the waveform will have a pedestal (or clutter) floor (Malanowski et al., 2020).

Passive radar signal processing is essentially the passive form of continuous wave (CW) noise radar, and allows ambiguity-free velocity and delay ranges. An often overlooked benefit of passive radar processing is this flexibility, as passive radar processing allows the coherent processing interval (CPI), and the pulse repetition frequency (PRF), to be chosen arbitrarily as these factors are not determined by transmitted signal. Received signals can be processed in multiple ways in parallel. As mentioned above, the downside is the presence of the pedestal floor. The presence of any strong signals will contribute to a floor across the entire delay Doppler space. Any potential detection will need to be stronger than this floor in order to be detected. Because of this potential to limit sensitivity, often the first step in passive radar processing is a clutter filter to remove as many unwanted strong signals as possible, prior to radar processing (Palmer & Searle, 2012; Searle et al., 2018). The process of forming delay Doppler maps, along with some examples from the MWA, is detailed in Section 2.4 below.

A major challenge in operating a passive radar is obtaining a reference copy of what was transmitted; as the transmitter is non-cooperative, the signal is not known. Typically a radar system will be located close enough to the transmitter in order to directly sample the reference, such as with an incredibly directive and high gain antenna. This approach will ensure the reference is already synchronised with the surveillance signals. However, being located so close to the transmitter is problematic as the radar will need to detect the weak target reflections in the presence of the significantly stronger signal. In addition, the direct signal, as well as strong reflections of any clutter in the region (observed in the reference collection or the surveillance), will be significant, making the clutter removal

step all the more challenging. Finally, directly sampling the reference signal will *tether* any potential radar location to be close to the transmitter, severely limiting surveillance options. It is possible to have a distributed passive radar system, so long as there is sufficient time and frequency synchronisation between the reference receiver along with the surveillance receiver.

Although there are many potential passive radar options for the illumination of objects in LEO, the focus of this thesis is on the use of FM radio. Just like any potential source, FM radio provides its own set of advantages and disadvantages. In Australia the FM band is 87.5 MHz through to 108 MHz. Although the FM band spans over 20 MHz, each individual FM station only occupies 200 kHz, and any station's instantaneous bandwidth may actually be much less. This small bandwidth at these frequencies results in quite coarse range resolution of 1.5 km<sup>1</sup>. However, the use of the FM band also results in significant flux-density, as FM transmitters are often quite powerful. Additionally, the coarse range resolution greatly reduces the size of the resulting radar product. This reduced size minimises the computational burden of radar processes. FM radio, being an analogue signal, has a highly variable ambiguity function; the radar properties vary with the signal content (Ringer et al., 1999). Different styles of music, human voice and even radio silence all have different bandwidths (and repeating patterns) which drastically change the radar-aspects.

The nearest (large) FM transmitter to the MWA is over 300 km away, and most of Australia's largest FM transmitters are thousands of kilometres away. This large standoff distance is actually beneficial for space surveillance purposes. This is due to the radiative characteristics of typical transmitters, meaning that broadcast entertainment is directed at consumers on the surface of the Earth. FM radio is typically transmitted from large towers located at significant elevation relative to the intended reception area, and the signal from these towers will

---

<sup>1</sup>The bistatic range resolution is 1.5 km but a monostatic radar with 200 kHz bandwidth has a range resolution of only 750 m. The two terms ('range resolution' and 'bistatic range resolution') are often used interchangeably.

be primarily directed to the ground (and the horizon). Notwithstanding this, at these frequencies the beamwidths are quite substantial and there will be sidelobes at higher elevation angles. This large separation between the MWA and any transmitters will help to reduce unwanted signals and RF interference (RFI), but it also ensures even narrow elevation beam FM transmitters will illuminate large volumes of space above the radio telescope receiver. Finally, there are thousands of FM transmitters around the country, ensuring that there will be a vast amount of energy above the MWA, at any potential target altitude of interest.

## 2.2 The MWA used as a Radar Receiver

The MWA is the low-frequency precursor to the square kilometre array (SKA), operating in the frequency range of 70–300 MHz (Tingay et al., 2013a; Wayth et al., 2018). The main scientific goals of the MWA are to detect radio emissions from neutral hydrogen during the Epoch of Reionisation (EoR), to study the Earth’s Sun and its heliosphere, Earth’s ionosphere, and radio transient phenomena, and to map the galactic and extragalactic radio sky (Beardsley et al., 2019).

The telescope is strategically located in a legislated radio-quiet zone, the Murchison Radio-astronomy Observatory, far from cities and other sources of electromagnetic interference. That is because the MWA, and indeed all radio telescopes, are attempting to receive and detect incredibly weak signals, and these can be swamped and masked by terrestrial transmissions.

The MWA consists of 4,096 dual-polarised wideband dipoles configured into subarrays of  $4 \times 4$  square grids, referred to as tiles. The grid spacing for each tile is 1.1 m (corresponding to a half-wavelength separation for 136 MHz), and the 16 dipoles are attached to a  $5 \text{ m} \times 5 \text{ m}$  steel mesh ground plane. These 256 tiles are distributed over  $\sim 30$  square kilometres. The current phase of the MWA, Phase II, allows for the use of half of the tiles at any one time, in compact or extended configurations (Wayth et al., 2018).

The extended array’s long and varied baselines provides extreme baseline lengths, allowing for incredibly accurate spatial measurements as well lower peak sidelobe levels. This enables the MWA to observe complex and fine detailed structures. The compact configuration is far smaller, and driven by requirements for the EoR power spectrum detection, with the majority of the baselines being shorter than 200 m. The plan view of both Phase II configurations are contained in Figures 2.3 and 2.4. The main feature of the compact configuration is the two hexagonal configurations (made up of 72 tiles). This compact configuration allows for broader beams (meaning fewer beams are required to scan a given area) but the repeated baselines of the hexagonal configurations will contribute to coherent sidelobe structure.

Additionally, some of the work included in this thesis (notably this chapter as well as Chapter 3) result from an earlier phase of the MWA, Phase I. MWA Phase I also consisted of 128 tiles, and was a large pseudo-random distribution of tiles providing excellent spatial accuracy, without some of the extreme baseline length tiles that are found in the Phase II extended configuration. The Phase I configuration is shown in Figure 2.2. Additional receivers and future MWA phases will enable the joint processing of all 256 tiles, and potentially more (Morrison et al., 2023).

### 2.2.1 Data Collection Pipeline

Each tile’s (and each polarisation’s) 16 dipole antennas are combined with an analogue beamformer to form a tile beam in a particular direction in the sky. The beamwidth is approximately  $40^\circ$  at the zenith for FM frequencies. This analogue pointing can be adjusted every 8 s.

The full frequency bandwidth for each tile, for both North-South and East-West polarisations, is directly sampled at 327.78 MHz, covering the array’s frequency range of interest. A polyphase filter bank (PFB) channelises these signals to  $256 \times 1.28$  MHz-wide critically sampled coarse channels. The MWA is

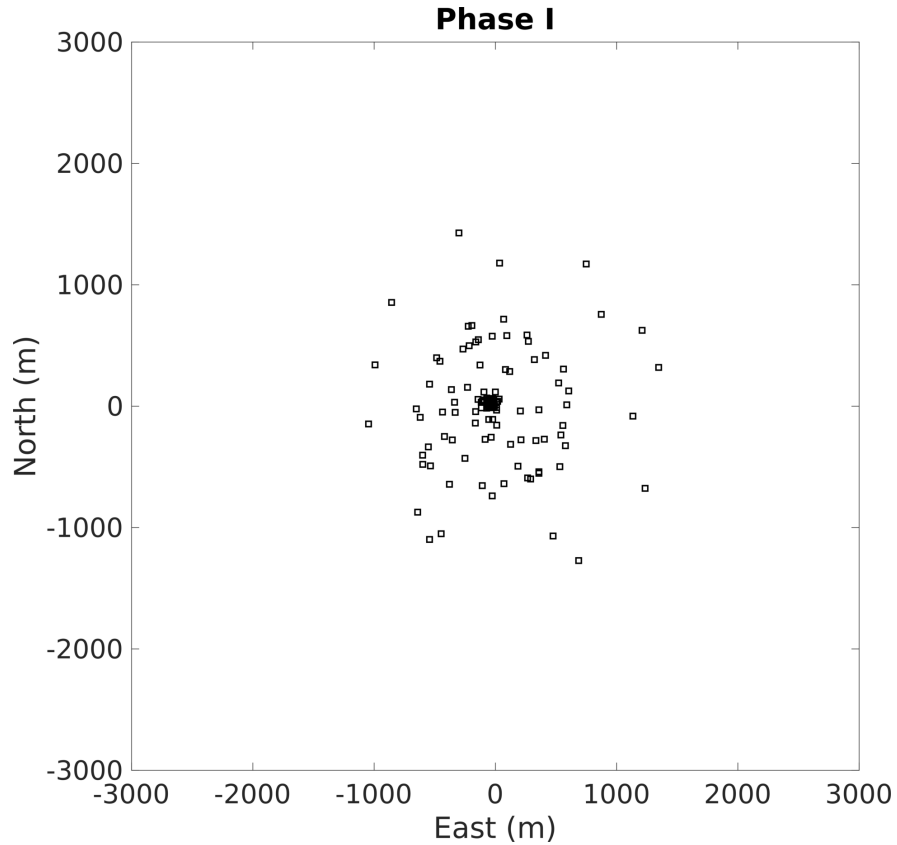


Figure 2.2: A plan view of the 128 tiles for the Murchison Widefield Array’s Phase I configuration.

able to transfer a user-defined subset of 24 of these 256 channels in real time to the high time-resolution voltage capture system (HTR-VCS), allowing for an instantaneous bandwidth of 30.72 MHz. The previous phases of the MWA only provided voltage capture modes for the fine channels, the output of a second PFB stage where each 1.28 MHz coarse channel was channelised into 128 channels of 10 kHz (Tremblay et al., 2015). For Phase I of the MWA the coarse channel needed to be reconstituted from the 128 fine channels through a PFB inversion operation (McSweeney et al., 2020).

The coarse channels, consisting of 1.28 MHz HTR-VCS data, are then further downsampled to select the various FM frequencies of interest for radar processing. For typical space surveillance applications, the standard utilisation is a (wide) beam-stare mode, with the tile’s analogue beam directed near the zenith.

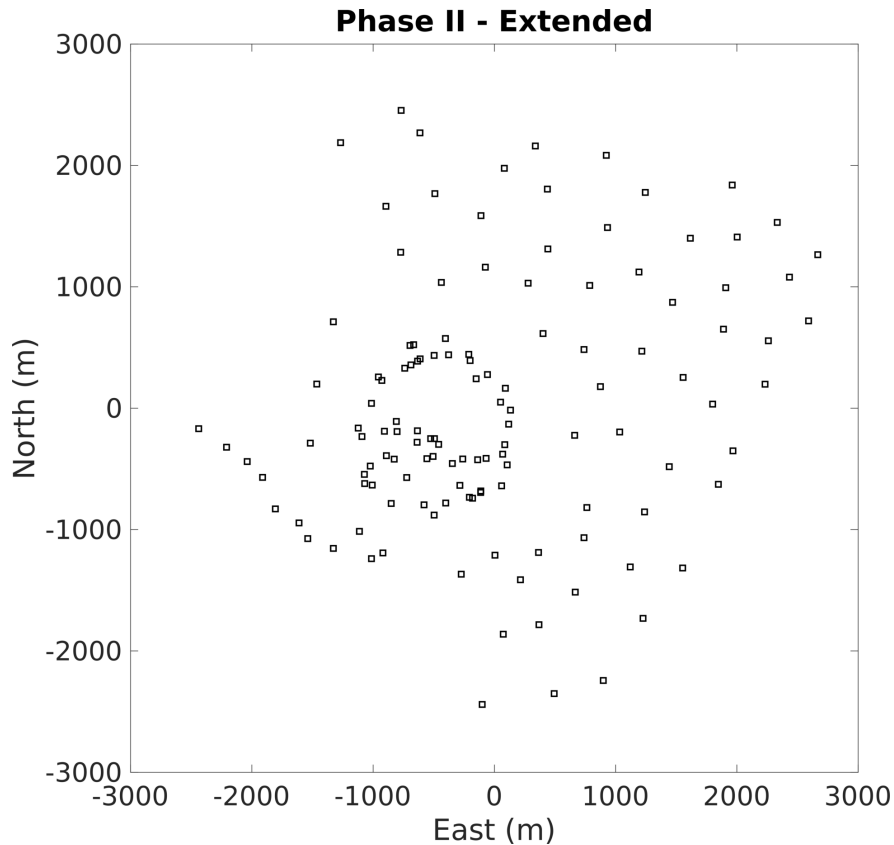


Figure 2.3: A plan view of the 128 tiles for the Murchison Widefield Array’s Phase II Extended configurations.

The net output is 128 channels with a user-defined bandwidth of (typically) 100-200 kHz. These data are then calibrated to remove any impact of the distributed array and phase-align each channel to the antenna. Once calibrated, the data are able to be used for precise electronic beamforming with the distributed array forming a large aperture providing very narrow surveillance beams.

The transmitter reference signals are collected directly at sites close to the transmitter with a small software-defined radio (SDR) system. These SDR reference systems are GPS-disciplined to allow synchronisation with the MWA’s surveillance data. Additionally, despite its location in a radio-quiet zone, the MWA is able to detect transmissions from the nearest radio transmitters 300 km away, allowing for the direct observation of nearby reference signals.

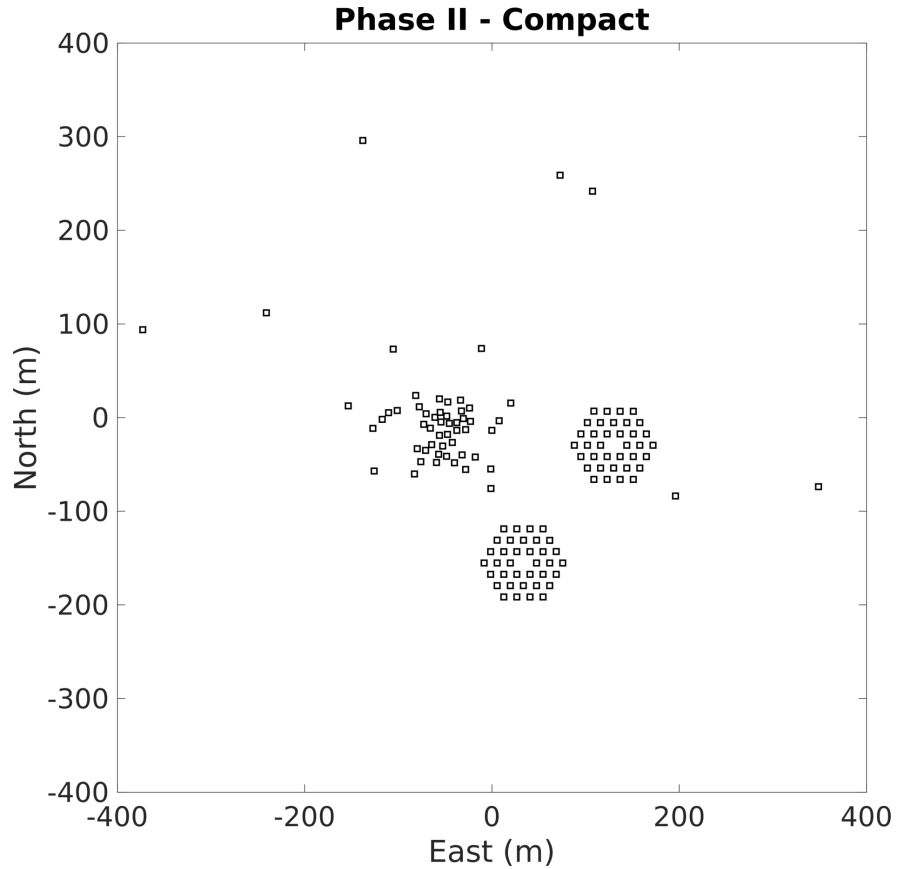


Figure 2.4: A plan view of the 128 tiles for the Murchison Widefield Array’s Phase II Compact configurations. Note the scale is far smaller for this figure compared with Figures 2.2 and 2.3.

### 2.2.2 Calibration

Because of the long cable lengths to the distant tiles and receivers, as well as the challenging environmental conditions, calibration solutions are vital to accurate tiled-array processing. Temperature variations can drastically vary the electrical length and alter impedance and loss. These variations need to be accounted for in order to phase-align the received signals to each tile’s phase centre. This requires complex gain (that is, amplitude and phase) corrections at every frequency of interest.

This calibration solution is typically achieved by processing a dedicated calibration observation that occurs close, in time, to the space surveillance observa-

tion of interest. The calibration observation is directed at a known-good calibration source (or field of sources), and knowledge of the specific source’s location and power levels, combined with the knowledge of the tile’s analogue beam-pattern, is used to generate the calibration gains (Ord et al., 2019).

A unique issue faced with calibration of the MWA for the use of passive radar, is the presence of the RFI in the frequency band of interest. Normally RFI-impacted frequencies would not be used for astronomy purposes and so calibration accuracy at these frequencies is not a typical concern. However, because passive radar processing utilises the same transmitters which cause the RFI, the calibration accuracy is of vital importance.

A sample of a typical calibrator output is shown in Figure 2.5. In this example, because of the presence of RFI, there are discontinuities at 96.5 MHz, there are also large gaps due to the frequency range spanning coarse channel boundaries. All of these issues can contribute to a poor result when attempting to interpolate across these impacted frequencies.

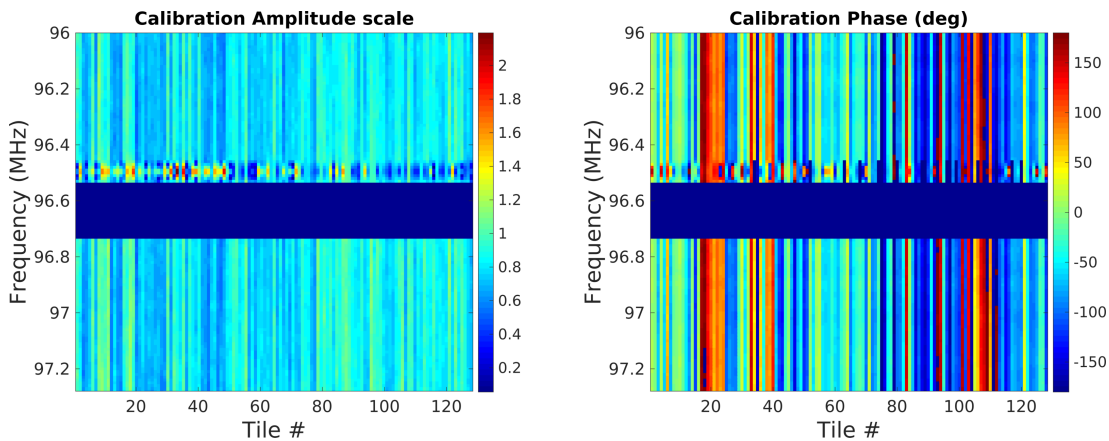


Figure 2.5: Sample calibrator output showing the calibration amplitude and phase adjustments. Wide bands are not calibrated due to the coarse channel boundaries, and the impact of RFI at 96.5 MHz is present.

Two techniques have been used throughout this thesis to refine calibration solutions so that they are usable at frequencies where RFI is present. The first is to simply interpolate across RFI-impacted frequencies, as typically there will



be nearby frequency gaps in the RFI for the calibration process to resolve a solution. Another approach taken here is a genetic algorithm process to adjust the gains and phases (at a specific frequency) to improve the returns of existing targets (Boeringer et al., 2005). These returns can be environmental targets (such as the ever-present meteor returns), or even radar detections of satellites. The process can incorporate known-true locations such as satellites with accurate ephemerides, in which the genetic algorithm will attempt to improve detected power at known directions. Alternatively, the genetic algorithm process can be direction agnostic, such as with unknown satellites or meteor returns, simply by attempting solely to maximise the detected power at (or around) the original direction. A genetic algorithm approach was chosen over other traditional numerical methods because of the sizeable problem space (amplitude and phase for every tile) compared with a relatively small number of data points. With only a small number of data points, there is insufficient information to estimate a solution gradient (Madsen et al., 2004). Genetic algorithms are a class of heuristic-based search algorithms, inspired by broad notions of natural selection and genetics. The algorithm operates by creating a large number of potential solutions, this population is updated and propagated to attempt to find solutions which maximise a given metric or heuristic (Holland, 1992; Boeringer et al., 2005).

Figure 2.6 illustrates the genetic algorithm process. An adaptive parameter process, as in Boeringer et al. (2005), was used to adjust the mutation rate, mutation range and the number of crossovers, the population size was fixed at 200 and the process ran until a steady population fitness was achieved, typically around 100 generations. Six meteor and radio-galaxy returns are used to optimise the calibration returns to maximise target power, with the resulting observation calibration solution being the one which maximises the total power from all targets. In this example only the calibration phase was adjusted, not the amplitude. The beamforming adjustments have focused the returns, and increased the power, of all six targets and the resulting phase offsets can be incorporated into the

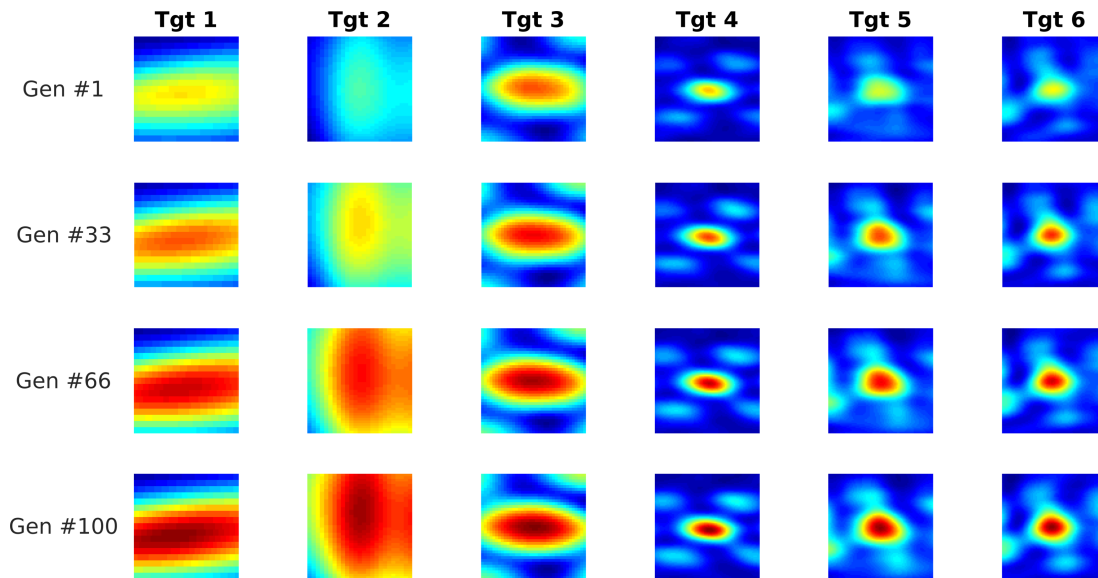


Figure 2.6: Example output of the genetic algorithm process to update the phase corrections from the calibration solution. The figure shows the power return of six targets (Targets 1 – 4 are meteor returns, targets 5 and 6 are radio-galaxy returns), and how over 100 generations the determined phase adjustments increase the detected power of each. An individual colour scale has been used for each target.

general calibration solution. This approach has consistently improved the SNR of radar detections of resident space objects (RSOs) with the observation data collected for this thesis, as any improvement in received surveillance power will have a greater impact on SNR due to correlation in the radar processing.

These calibration steps can be applied prior to any space surveillance observation, and so they do not preclude real time observation. Additionally, the environment or satellite based calibration can be implemented as a running calibration generation, that is, calibration on the fly. This would enable ongoing surveillance without the need for dedicated calibration observations.

## 2.3 LEO Space Surveillance

For RSOs in an Earth-centered orbit, there are a large number of perturbing forces determining the object’s trajectory, more than simply Earth’s gravity.

Some examples include other planetary bodies, solar wind pressure, Earth’s non-spheroidal/oblate shape, the effects of general relativity, and (particularly for LEO) microatmospheric drag. This can make orbit determination quite challenging. However, for short time periods, such as a standard radar CPI or an RSO’s pass above a radar site, a much simpler orbital motion model is more than sufficient.

The simplest orbital model is the two-body, or Keplerian, orbital model. This treats the Earth and the RSO of interest as point masses, and assumes gravity is the only force. An object in this simple orbital model will trace an ellipse, and so an advantage of the Keplerian motion model is that the RSO’s orbit is completely determined by only six parameters (and an epoch). These six parameters can be the three-dimensional cartesian position with a three-dimensional velocity. Alternatively it is common to use the Keplerian Elements. These will be covered in greater detail in Chapter 4. However they define the size and shape of the orbital ellipse (with the eccentricity and the semi-major axis), and four parameters to orient the ellipse relative to Earth. One parameter specifies the RSO’s location on the ellipse. Although an orbit is defined by an ellipse, the vast majority of objects in an Earth-centered orbit are in a circular, or near-circular, orbits.

RSOs in an Earth centered orbit can occupy altitudes from the Kármán Line<sup>2</sup> at 162 km (Imamura et al., 2021), to beyond cislunar, approximately 380,000 km away. In addition to the LEO regime, which are orbits with altitudes lower than 2,000 km, other important orbital regimes are medium Earth orbit (MEO), and geosynchronous equatorial orbit (GEO). MEO orbits have altitudes between LEO and GEO (Riebeek, 2009). MEO altitudes are typically used for navigation and other special interest satellites, and GEO is typically used by persistent Earth-observation systems and communication and entertainment satellites. However, there are many different special-case satellites in all manner of orbits, as well as

---

<sup>2</sup>The Kármán Line is the proposed boundary for where Earth’s atmosphere ends and *space* begins. There are various potential altitudes, such as 100 km, however in this thesis the lowest recorded sustained orbital altitude of 162 km is used for the Kármán Line.

rocket bodies (and other associated debris) at intermediate orbit stages between launch and the final destination orbit.

A sensor like the MWA should be able to detect RSOs to a maximum range of several thousand kilometres, depending on the object's size. These ranges are far smaller than the maximum potential Earth-centered orbital altitudes discussed. However, they represent the majority of the space surveillance population that is currently tracked. Figure 2.8 shows the semi-major axis against the eccentricity of objects that are being tracked, showing that despite circular orbits being the most common, there is a not-insignificant amount of RSOs with a considerably non-circular orbits.

The closer an RSO is to Earth, the faster it will be travelling. Geostationary satellites are at an altitude of approximately 36,000 km because that is the altitude where an RSO in a circular orbit will be slow enough to match the rotation of the Earth. RSOs in LEO travel much faster, with speeds between 7 km/s and 8 km/s being very common for circular orbits. The low-perigee (so, detectable) RSOs in non-circular orbits will have even higher speeds. Unlike a circular orbit, the speed of an RSO in an elliptic orbit changes depending on its range from Earth, and the speed will be at its greatest extent at perigee. This is shown in Figure 2.8, which details the maximum speed of all the objects currently in the space catalogue. It shows that for the objects the MWA is likely to detect, the maximum speeds will vary from 7 km/s up to almost 11 km/s. These speeds present a significant challenge to space surveillance radars due to the changing geometry and measurement parameter smearing.

Finally, with increased interest in lower-latency communications, use of LEO for communication is increasing. This requires the use of a large number of satellites in LEO instead of a smaller number of satellites in GEO. These 'megaconstellations' are the driving force behind the recent dramatic increase in LEO utilisation (Rossi et al., 2017; McDowell, 2020). Additionally, these megaconstellation satellites are far more manoeuvrable than traditional satellites and other

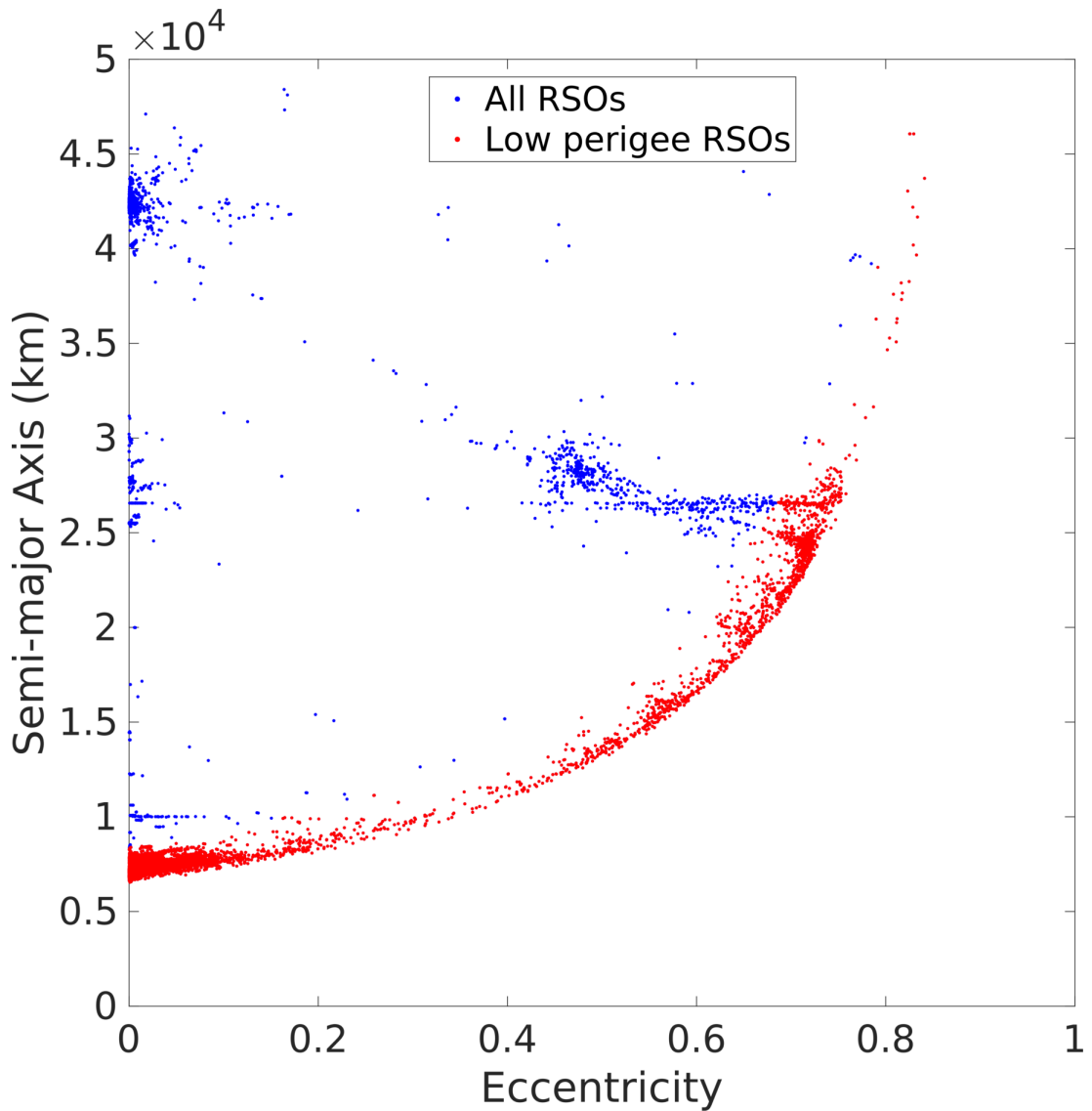


Figure 2.7: Semi-major axis vs. eccentricity diagram showing the distribution of objects in the catalogue and their respective elements. RSOs with a perigee less than 2,000 km above the surface of the Earth are highlighted red.

space debris, due to the fact that they (each individually) cannot be inserted directly at their target orbit, as well as general station-keeping requirements. The unpredictable nature of LEO perturbing forces (e.g. space weather dependent drag), the significant LEO speeds, and the recent increase in the number of manoeuvrable satellites makes LEO surveillance significantly more challenging and dynamic than it has previously been.

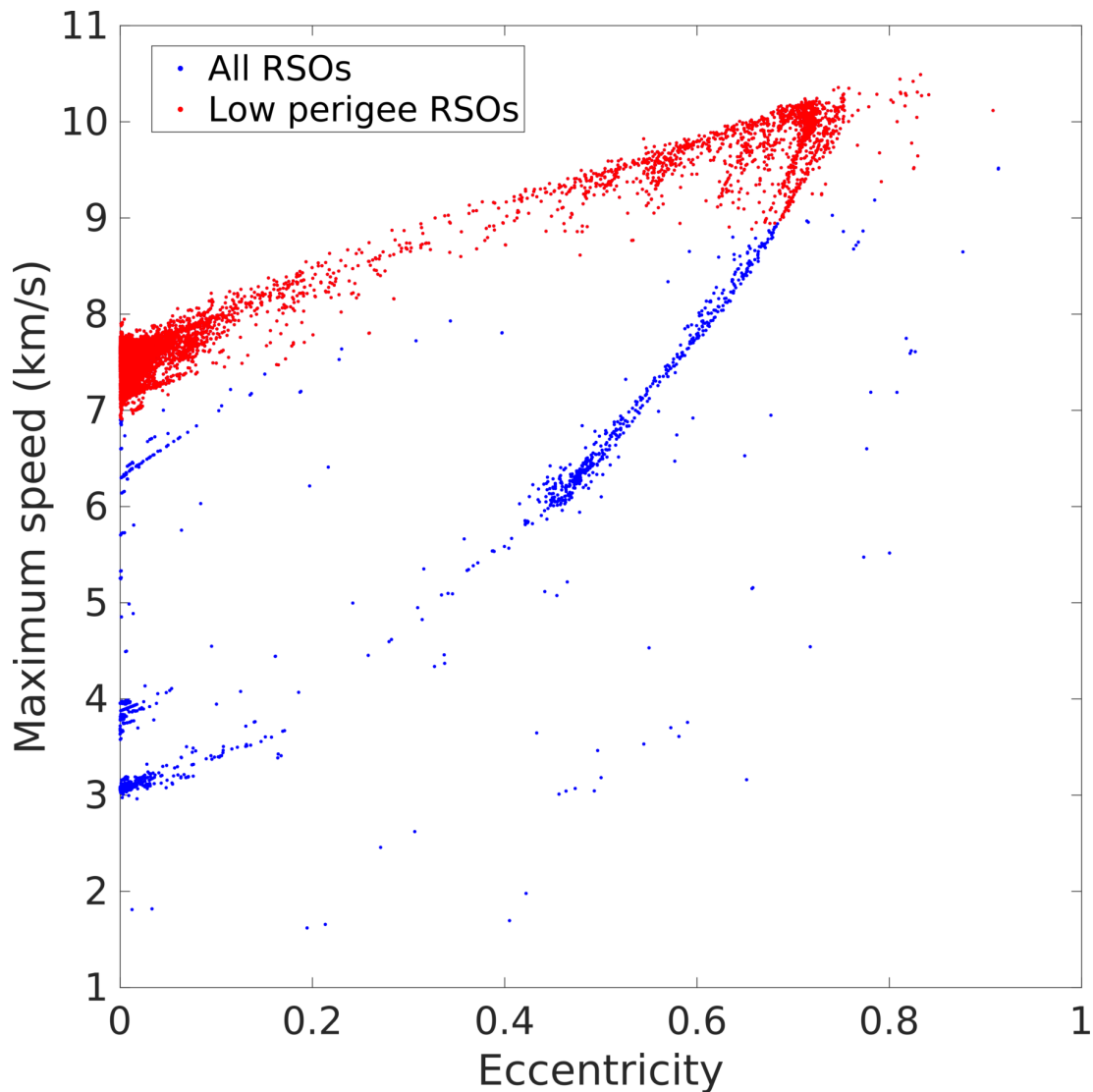


Figure 2.8: The maximum speed (achieved at perigee) distribution of objects in the catalogue against their eccentricity. RSOs with a perigee less than 2,000 km above the surface of the Earth are highlighted red.

## 2.4 Signal Processing

### 2.4.1 Radar Product Formation

The fundamental radar product used for target detection is the delay-Doppler map. This is a set of matched filter outputs, essentially correlations, provided by the Woodward Ambiguity Function (Woodward, 1953). The ambiguity function

describes a radar's ability to determine the delay and Doppler shift of a reflected signal. Given a reference copy of the transmitted signal  $r(t)$ , and a surveillance signal  $s(t)$ , both sampled at rate  $B$ , the discrete implementation of the ambiguity function for a coherent processing interval of length  $T$  of bistatic delay  $\tau$ , and bistatic-Doppler,  $f_D$ , is given by:

$$\chi[\tau, f_D] = \sum_{t=0}^{BT-1} s[t]r^*[t - \tau]e^{-j2\pi f_D \frac{t}{BT}}. \quad (2.1)$$

This essentially correlates a delayed and frequency-shifted reference signal with the surveillance signal in order to match reflections, corresponding to a hypothesised delay and Doppler frequency shift.

For a target at Cartesian position  $\mathbf{r}$ , the receiver and transmitter's positions are  $\mathbf{r}_{rx}$  and  $\mathbf{r}_{tx}$ , respectively. Then the slant range between the receiver and the target is given by  $\rho_{rx} = |\mathbf{r} - \mathbf{r}_{rx}|$ , and the slant-range velocity given by its time derivative  $\dot{\rho}_{rx}$ . Likewise the target-transmitter slant-range and slant-range velocity are  $\rho_{tx}$  and  $\dot{\rho}_{tx}$ , respectively. For a signal transmitted with wavelength  $\lambda$ , the target's parameters will correspond to a detection in the delay-Doppler map given by:

$$\tau = \frac{1}{c}(\rho_{rx} + \rho_{tx} - |\mathbf{r}_{rx} - \mathbf{r}_{tx}|), \quad (2.2)$$

$$f_D = -\frac{1}{\lambda}(\dot{\rho}_{rx} + \dot{\rho}_{tx}). \quad (2.3)$$

In practice, the ambiguity function is not estimated directly, as the need to perform a correlation the length of the CPI for every delay and Doppler hypothesis is not practical. Instead, an approximation (known as the pulse-Doppler approximation or even the Batches Algorithm in recent literature) is used (Stein, 1981). Much like in standard pulse-Doppler processing, the signal is subdivided into  $M$  pulses of length  $\tau_c$  such that each pulse is made up of  $B\tau_c$  samples. That is  $T = M\tau_c$ . Individual pulses (from the surveillance and reference signals)

are correlated together. This collection of correlated pulses is referred to as the range-compressed pulse stack, with each pulse representing a slow-time instantaneous measurement of delay, measured in fast-time. These pulses are coherently combined to resolve the target's Doppler by applying the Discrete Fourier Transform across the slow-time dimension. The expression for the discrete Batches Algorithm is:

$$\chi[\tau, f_D] = \sum_{m=-\frac{M}{2}}^{\frac{M}{2}} e^{-j2\pi\frac{f_D m}{M}} \sum_{t=0}^{B\tau_c-1} s[mB\tau_c + t]r^*[mB\tau_c + t - \tau]. \quad (2.4)$$

The key approximation of the pulse-Doppler is that the pulse length,  $\tau_c$ , is short enough that the phase variation across the pulse due to the target's motion is insignificant. Whilst the fast-time across each pulse is given by  $t$ , each pulse's slow-time is  $m\tau_c$ . Larger Doppler shifts will result in a steeper phase variation, necessitating shorter pulses (Lombardo et al., 2012). The two processing steps in the approximation is the fast-time range compression ( $t$ ), and then the pulse integration stage, coherently combining all the pulses across slow-time ( $m\tau_c$ ) by an M-point Fourier Transform. It should be noted, the correlation at all delays (the fast-time range compression) can be efficiently implemented in the Fourier domain as well.

Directional information is estimated by beamforming. Although it is possible to form a beam with the timeseries signals and then apply the delay-Doppler processing, this is very inefficient as the pulse-compression is computationally demanding. Instead, it is better to beamform on the delay-Doppler products directly (Palmer, 2015). For a receiver array consisting of  $N$  elements, each with corresponding delay-Doppler maps  $\chi_n$ , the resulting delay-Doppler map can be



formed by classical far-field beamforming<sup>3</sup> in a direction of interest, such that:

$$\chi[\tau, f_D, \theta, \phi] = \sum_{n=1}^N \chi_n[\tau, f_D] e^{-j \frac{2\pi}{\lambda} \mathbf{k} \cdot \mathbf{u}_n}, \quad (2.5)$$

where  $\chi_n[\tau, f_D]$  is the delay-Doppler map formed from the signal at the  $n^{\text{th}}$  antenna,  $\mathbf{u}_n$  is the position of the  $n^{\text{th}}$  antenna, and  $\mathbf{k}(\theta, \phi)$  is the signal wavevector for azimuth  $\theta$  and elevation  $\phi$ . For an East, North, Zenith coordinate frame<sup>4</sup>  $\mathbf{k}$  is given by:

$$\mathbf{k} = \begin{bmatrix} \sin \theta \cos \phi \\ \cos \theta \cos \phi \\ \sin \phi \end{bmatrix}. \quad (2.6)$$

Figure 2.9 is a typical delay-Doppler map as seen by the MWA. The delay-Doppler map was formed in the direction of the ISS and shows the approaching space station at a significant bistatic delay of approximately 2.25 ms. An outgoing aircraft can be seen at close range, and with relatively low speed. An interesting aspect is that despite being located in a legislated radio quiet zone, there is significant signal refracted from the transmitter (in this instance located over 300 km, and many horizons, away) such that direct-path interference is the dominant return, highlighting the great challenge radio astronomers face in dealing with RFI. The delay-Doppler map's pedestal floor, at 0 dB in the Figure, is set by the strong signal (at around 32 dB). If this 32 dB signal is removed the resulting floor would be lower, and this would increase the SNR of the satellite and aircraft. Also, any targets with peaks lower than the floor may also be revealed.

Another key aspect of Figure 2.9 occupies a large (or at least, larger than

---

<sup>3</sup>Note the far-field assumption is reasonably valid for the compact configuration of the MWA Phase II, it may not hold for the extended configuration.

<sup>4</sup>The specific coordinate used is not of any consequence, so long as the wavevector,  $\mathbf{k}$ , and each antenna location,  $\mathbf{u}_n$ , match. A topocentric coordinate frame with the topocentric right ascension and declination is used in Chapter 5 and a South, East, Zenith frame is used in Chapter 6.

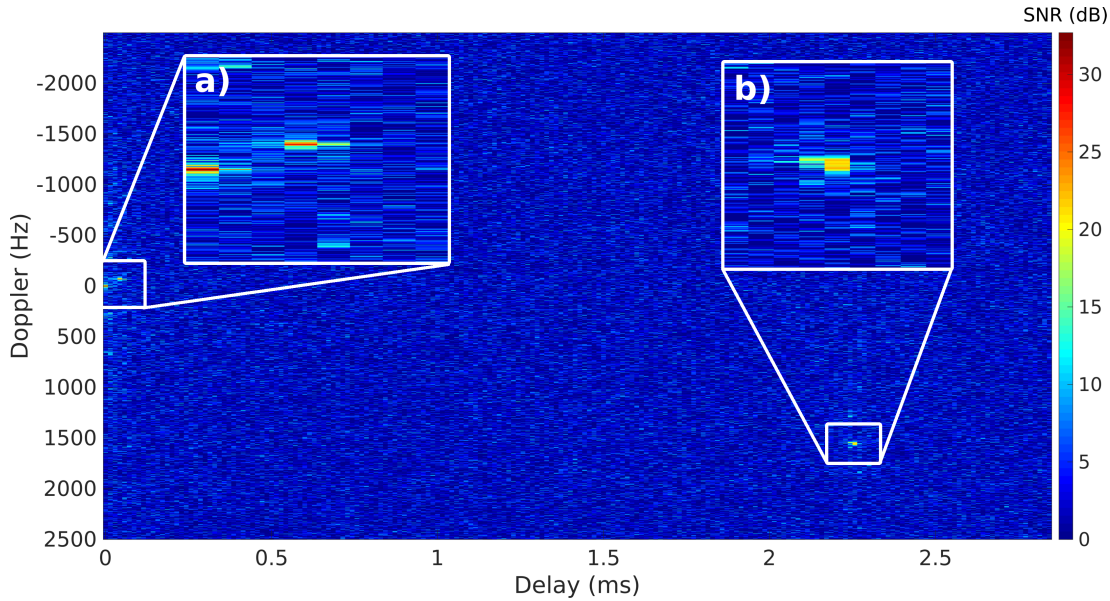


Figure 2.9: Example delay-Doppler map formed using MWA data. Inset (a) shows the direct path interference as well as an outgoing aircraft. Inset (b) shows an approaching International Space Station.

the aircraft) number of ‘cells’ in the delay-Doppler map. The processing interval used for Figure 2.9 was 1 s, and in this time the ISS has moved across the delay Doppler map, akin to motion blurring in a photograph. This blurring, referred to as delay and Doppler walk, is typically not of concern to standard surveillance radars, but it is of extreme concern for long integration space surveillance radars. The delay and Doppler walk reduces sensitivity to fast moving targets as the returned energy is spread over many cells, minimising the maximum possible energy detectable in any one cell.

## 2.4.2 Walk across all parameter space

Standard pulse-Doppler processing is described by (2.4) and (2.5), forming a delay-Doppler map for every direction of interest. It represents the approach that most radars take in forming surveillance products, although there are many improvements and efficiencies which can be achieved and implemented (opposed to the way the expressions are presented here). A common approach to improve

a radar’s sensitivity to target returns is to integrate for longer, extending the CPI to improve target SNR. However, this is problematic for fast-moving targets as any CPI increase will also mean greater target movement and delay and Doppler walk.

This is the fundamental challenge with the detection of RSOs with the MWA; the need to extend the CPI to detect smaller and more distant RSOs is balanced against the difficulty of coherently forming detection signals. Figure 2.9 was formed with a CPI of only 1 s, and the RSO already exhibited considerable delay and Doppler walk. It is not uncommon for staring radars to use CPI lengths in excess of 10 s. In order to extend the processing interval, any RSO motion through the delay-Doppler map will need to be mitigated in order to achieve meaningful detections.

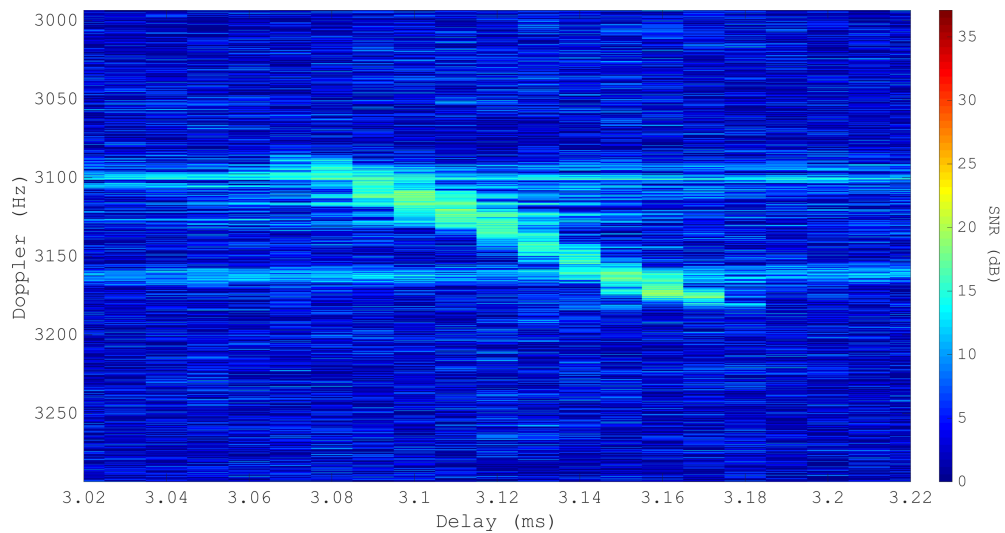


Figure 2.10: Segment of a delay-Doppler map centered on an approaching ISS. Formed with a CPI of 3 s, the ISS exhibits considerable delay and Doppler walk as it moves across the CPI.

Figure 2.10 is a cropped section of a delay-Doppler map, formed with a 3 s CPI, showing the ISS moving through range and Doppler. Throughout the CPI the ISS moves from one corner of the section to the other. Due to the Doppler-walk and the delay-walk the ISS’ returned energy is smeared across hundreds of

cells. Two horizontal spurs, or lines, are visible in the section. These are caused by the changing ambiguity function across the CPI. Within the three seconds, the FM content (music, voice, etc.) changes and so does the resulting bandwidth. Two instances of low bandwidth, and so coarse range resolution, occur, resulting in the horizontal spurs.

The two stages of (2.4) are the fast-time pulse compression, followed by the slow-time pulse-integration. As the bistatic range to the target changes across each subsequent fast-time pulse, the range compression will result in the peak forming in subsequent delay cells. Likewise, as the relative bistatic velocity changes across the CPI, the target’s bistatic Doppler shift will vary. This varying delay and Doppler causes the migration seen in Figure 2.10.

As mentioned in Chapter 1, there are many methods for combating range-walk. However, for this thesis the standard approach has been to utilise the Keystone Transform (Perry et al., 1999; Perry et al., 2007). This is a slow-time resampling which mitigates all constant radial delay-walk. It will be discussed further in Chapter 3. It should be noted that even with the narrow bandwidths offered by FM radio, delay migration is still a considerable challenge.

Similarly, there are a large number of approaches for mitigating Doppler-walk, however the optimal approach is the chirpogram. This involves matching any potential motion-induced chirp and evaluating the output. This acceleration searching is covered in subsequent chapters but as Doppler-walk is the largest source of sensitivity loss, it will be explored further here.

To mitigate the motion induced loss, a hypothesised Doppler-rate is applied across slow-time to correct for the Doppler-walk. This essentially requires forming a three dimensional delay-Doppler-Doppler-rate map. It should be noted that the inner correlation products, the range-compressed pulses, do not need to be recalculated for each Doppler-rate (or Doppler) hypothesis. Just as with the standard pulse-Doppler/batches approach, the implementation implicitly assumes the phase change across a single pulse (due to the radial acceleration) is

insignificant, and the process only matches pulse-to-pulse phase changes. Note that the pulse-integration Fourier transform needs to be implemented for each acceleration hypothesis. For a Doppler-rate  $\dot{f}_D$ , the slow-time chirp can be mitigated by the phase term,  $e^{-j\pi\dot{f}_D(m\tau_c)^2}$ .

Rewriting (2.4) to incorporate this Doppler rate,  $\dot{f}_D$  (and noting that  $M = \frac{T}{\tau_c}$ ), results in the expression for a delay-Doppler-Doppler-rate map:

$$\chi[\tau, f_D, \dot{f}_D] = \sum_{m=-\frac{M}{2}}^{\frac{M}{2}} e^{-j2\pi\left(\frac{f_D m\tau_c}{T} + \frac{\dot{f}_D (m\tau_c)^2}{2}\right)} \sum_{t=0}^{B\tau_c-1} s[mB\tau_c + t]r^*[mB\tau_c + t - \tau]. \quad (2.7)$$

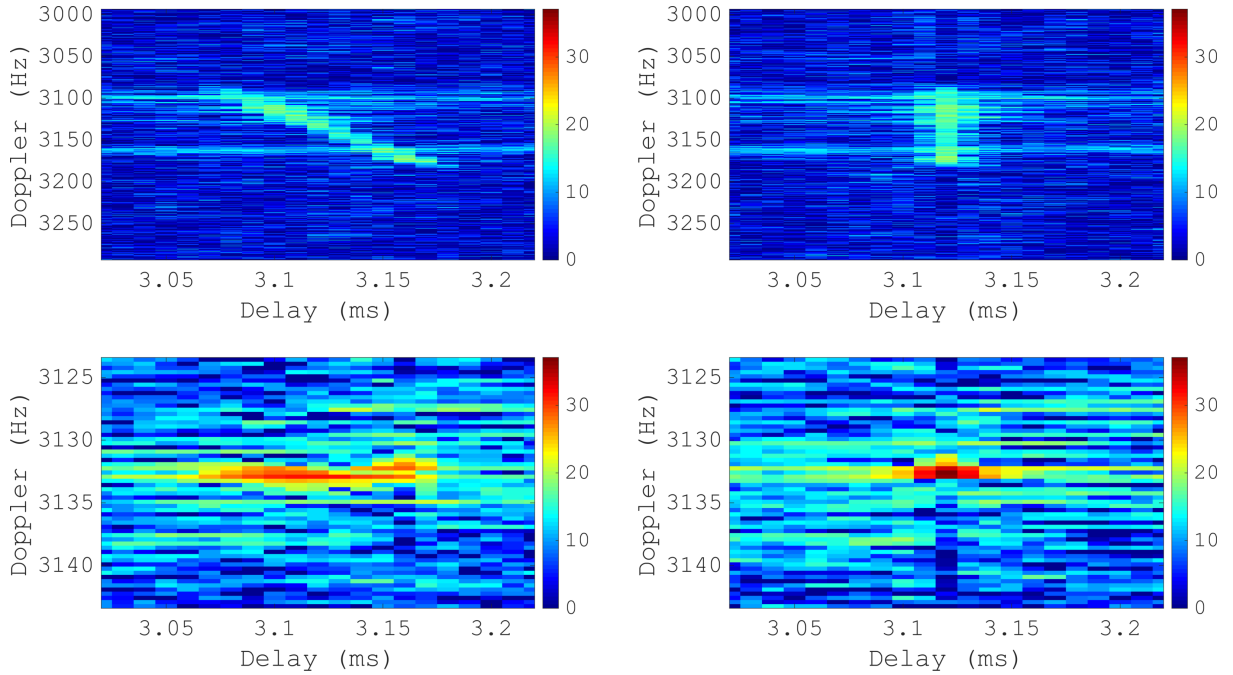


Figure 2.11: Four reproductions of 2.10 (utilising the same scale) with various motion mitigations applied to the pulsestack. The bottom two subfigures have had a matching Doppler-rate applied, the right two subfigures have had the Keystone transform applied.

Figure 2.11 is a reproduction of Figure 2.10 where the pulse stack has been processed in four different ways. The bottom two subfigures have had appropriate Doppler-rate compensation applied, and the right two subfigures have had the

Keystone Transform applied. The key aspect is that the top-left subfigure has had no motion compensation applied to the pulse stack, whereas the bottom right subfigure has had Doppler and delay migration mitigation techniques applied, with the result being a dramatic 20 dB SNR improvement.

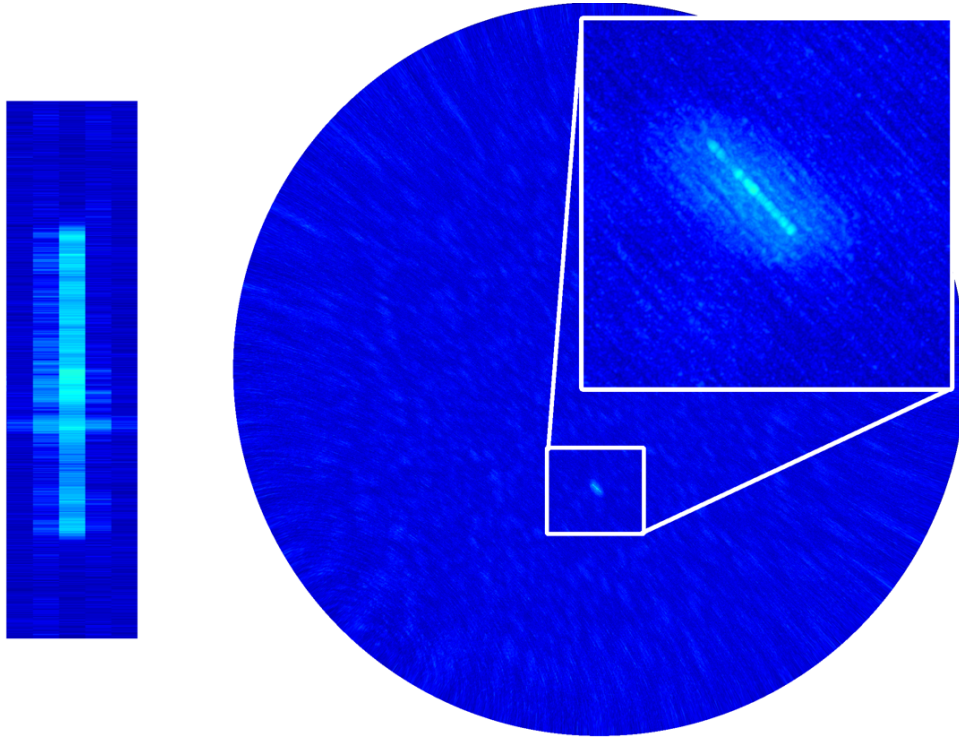


Figure 2.12: Two subfigures showing a satellite moving near zero-Doppler, the left subfigure is a section of a delay-Doppler map and the right subfigure is the spatial skymap, from the horizon to zenith, resulting from the beamforming. The matching radar products were formed by implementation of (2.5). The uncompensated Doppler-rate and spatial rates produce significant smearing.

Delay and Doppler migration is a challenging issue for any long-integration space surveillance radar. The extreme speeds of RSOs at LEO (as outlined in Section 2.3) will always result in loss in delay-Doppler map sensitivity. The MWA, used as a passive radar, is no different in these aspects. What is unique about the MWA is its sheer size. The extreme baselines (even with the Phase II compact configuration) which enable the MWA's detailed imaging capabilities also present some significant challenges to moving target detection. The incredibly fine spatial

resolution means that for even short CPIs, there will be spatial migration of the RSO. Despite orbital altitudes typically being in excess of 300 km, the large extent of the radar tiles and the extreme speeds are more than enough for spatial-walk to occur. Figure 2.12 shows the motion of the ISS through the delay-Doppler and spatial parameters. The left subfigure is a segment of a delay-Doppler map and the right subfigure is the full sky coverage, with an inset highlighting the ISS. Figure 2.12 is essentially the implementation of (2.5), and shows the significant migration in all measurement parameters. In order for the target to be fully coherently detected across the CPI, moving beams need to be incorporated in to the processing.

First, to combat the extreme parameter walk shown in Figure 2.12, Doppler-rate hypotheses are incorporated in to the spatial product forming a five-dimensional search space, with  $\dot{f}_D$ , and building on (2.7). The result is:

$$\chi[\tau, f_D, \dot{f}_D, \theta, \phi] = \sum_{n=1}^N e^{-j\frac{2\pi}{\lambda} \mathbf{k} \cdot \mathbf{u}_n} \chi_n[\tau, f_D, \dot{f}_D]. \quad (2.8)$$

The use of (2.8) is shown in Figure 2.13. It is clear the inclusion of the Doppler-rate,  $\dot{f}_D$ , has completely mitigated the Doppler-walk in the left subfigure of Figure 2.13, resulting in a significant sensitivity increase. However, the spatial migration on the right subfigure still remains. To achieve the moving beams, the wavevector needs to be changed pulse-to-pulse to move the beam across the CPI.

In order to adjust the wavevector across the CPI, angular rates (that is, azimuth rate,  $\dot{\theta}$ , and elevation rate,  $\dot{\phi}$ ) need to be incorporated into the delay-Doppler expression prior to the pulse-integration stage. This will require a pulse-integration step for every acceleration hypothesis, as well as every azimuth-rate and elevation-rate hypothesis. This will be a costly search space, as (2.8) is already a five dimensional product, and so including angular rates will grow the product to seven dimensions. The spatial and Doppler motion essentially requires a matching polynomial phase signal for every tile in order to track the hypothe-

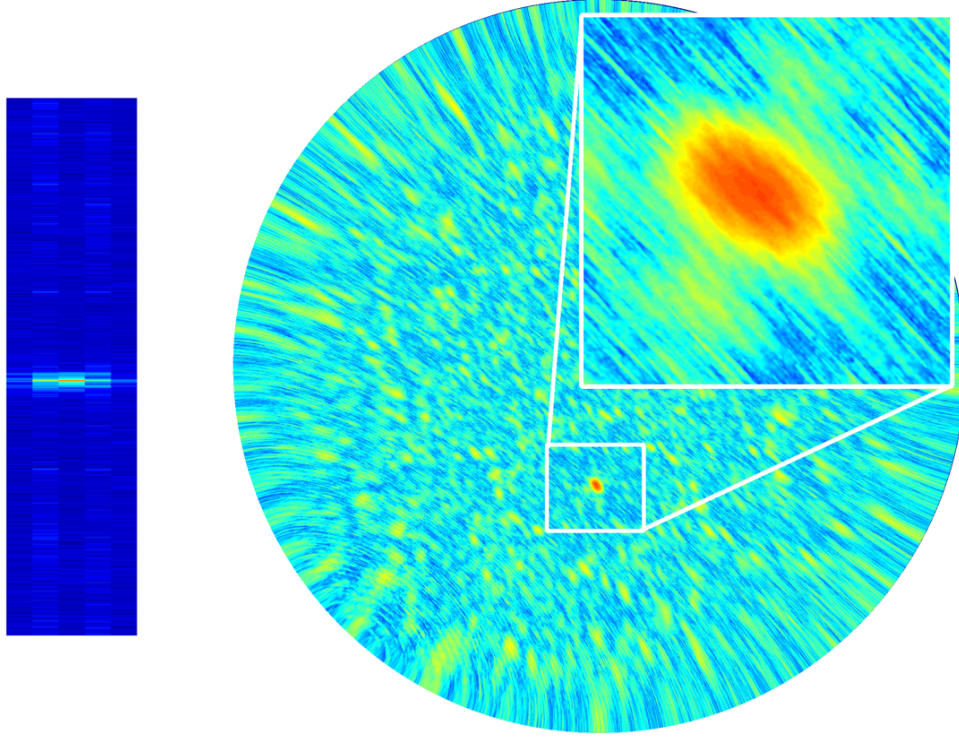


Figure 2.13: Identical figure as Figure 2.11, except the matching radar products were formed by implementation of (2.8). The matched Doppler-rate has dramatically improved SNR however the spatial rates still produce significant smearing.

sised motion. Writing the series of phase coefficients as  $w_{x,n}$  where coefficient  $x$  and antenna number  $n$ , the delay-Doppler map product is given by:

$$\chi[\tau, f_D, \dot{f}_D, \theta, \dot{\theta}, \phi, \dot{\phi}] = \sum_{n=1}^N \sum_{m=-\frac{M}{2}}^{\frac{M}{2}} e^{-j2\pi(w_{0,n} + w_{1,n}m\tau_c + \frac{1}{2}w_{2,n}(m\tau_c)^2)} \times \sum_{t=0}^{B\tau_c-1} s[mB\tau_c + t]r^*[mB\tau_c + t - \tau], \quad (2.9)$$



with

$$w_{0,n} = \frac{1}{\lambda} \mathbf{k} \cdot \mathbf{u}_n , \quad (2.10)$$

$$w_{1,n} = \frac{f_D}{T} + \frac{1}{\lambda} \dot{\mathbf{k}} \cdot \mathbf{u}_n , \quad (2.11)$$

$$w_{2,n} = \dot{f}_D , \quad (2.12)$$

$$\dot{\mathbf{k}} = \begin{bmatrix} \dot{\theta} \cos \theta \cos \phi - \dot{\phi} \sin \theta \sin \phi \\ -\dot{\theta} \sin \theta \cos \phi - \dot{\phi} \cos \theta \sin \phi \\ \dot{\phi} \cos \phi \end{bmatrix} . \quad (2.13)$$

The seven parameter delay-Doppler product, (2.9), is illustrated in Figure 2.14. When compared with Figures 2.12 and 2.13 it can be seen that both the Doppler migration **and** the spatial migration have all been completely mitigated. The peak spatial return is now a single point at the centre of the response, highlighting the accurate spatial measurement capability of the MWA.

A near-unbounded seven parameter search space is an incredibly daunting challenge. It represents a mammoth processing task that needs to be completed every CPI, and further compounding this problem, this thesis (through Chapters 3, 5 and 6) demonstrates that it is actually insufficient. For even moderate CPI lengths (e.g. 3 s), fast moving objects such as RSOs in highly eccentric orbits (travelling at speeds beyond 10 km/s), the processing needs to account for the radial-jerk, corresponding to the Doppler-acceleration as well as the spatial acceleration terms. That is, (2.9) needs to be expanded to incorporate  $\ddot{f}_D$ ,  $\ddot{\theta}$ , and  $\ddot{\phi}$  such that:

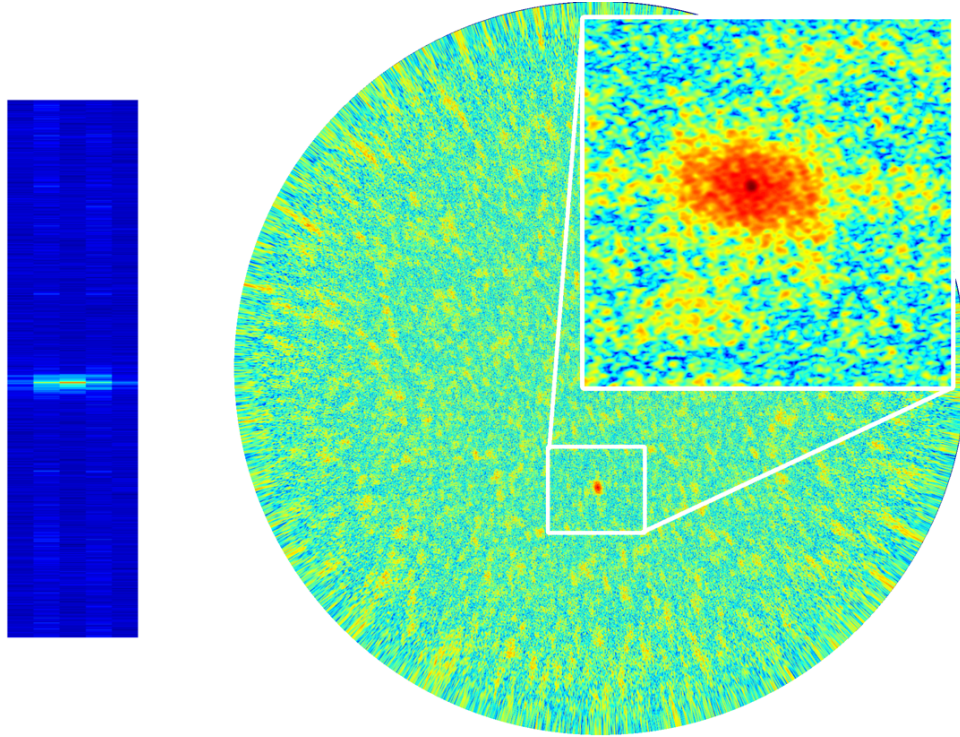


Figure 2.14: Identical figure as Figures 2.11 and 2.13, except the matching radar products were formed by implementation of (2.9). The matched Doppler-rate and matched spatial have dramatically improved SNR and stopped smearing in all dimensions. Now the space station is spatially localised to a single point.

$$\begin{aligned}
 \chi[\tau, f_D, \dot{f}_D, \ddot{f}_D, \theta, \dot{\theta}, \ddot{\theta}, \phi, \dot{\phi}, \ddot{\phi}] = & \sum_{n=1}^N \sum_{m=-\frac{M}{2}}^{\frac{M}{2}} e^{-j2\pi(w_{0,n} + w_{1,n}m\tau_c + \frac{1}{2}w_{2,n}(m\tau_c)^2 + \frac{1}{6}w_{3,n}(m\tau_c)^3)} \\
 & \times \sum_{t=0}^{B\tau_c-1} s[mB\tau_c + t]r^*[mB\tau_c + t - \tau] ,
 \end{aligned} \tag{2.14}$$

with  $w_{0,n}$ ,  $w_{1,n}$ , and  $\dot{\mathbf{k}}$  as before, and

$$w_{2,n} = \dot{f}_D + \frac{1}{\lambda} \dot{\mathbf{k}} \cdot \mathbf{u}_n , \quad (2.15)$$

$$w_{3,n} = \ddot{f}_D , \quad (2.16)$$

$$\ddot{\mathbf{k}} = \begin{bmatrix} -(\dot{\theta}^2 + \dot{\phi}^2) \sin \theta \cos \phi + \ddot{\theta} \cos \theta \cos \phi - \ddot{\phi} \sin \theta \sin \phi - 2\dot{\theta}\dot{\phi} \cos \theta \sin \phi \\ -(\dot{\theta}^2 + \dot{\phi}^2) \cos \theta \cos \phi - \ddot{\theta} \sin \theta \cos \phi - \ddot{\phi} \cos \theta \sin \phi + 2\dot{\theta}\dot{\phi} \sin \theta \sin \phi \\ \ddot{\phi} \cos \phi - \dot{\phi} \sin \phi \end{bmatrix} . \quad (2.17)$$

It should be noted that this ten-parameter motion matching pulse integration function is required even when utilising the compact configuration of the MWA. This is shown in Figure 2.15. Figure 2.15 shows the spatial returns of the Hubble Space Telescope (HST) observed with the Phase II MWA compact configuration, in a similar vein to the spatial insets of Figures 2.12 – 2.14<sup>5</sup>. The left subfigure does not match any of the Doppler or spatial motion (implementing (2.5)) and the HST is not detectable. The middle subfigure has matched the Doppler-rate (implementing (2.8)) which has improved the sensitivity. The third subfigure has matched the Doppler-rate and the spatial-rate motion (implementing (2.9)) improving sensitivity and also reducing spatial smear. In Figure 2.14 the ISS' spatial returns are concentrated to a narrow point, whereas in Figure 2.15, the HST is concentrated to a broader point with significant sidelobe structure. The broader point is the result of the shorter baselines of the Phase II compact configuration, and the ‘flower’ sidelobe structure is a result of the repeated baselines of the two hexagonal subarrays (Wayth et al., 2018).

---

<sup>5</sup>Similar examples, resulting from a smaller passive radar system, are presented in Appendix A.

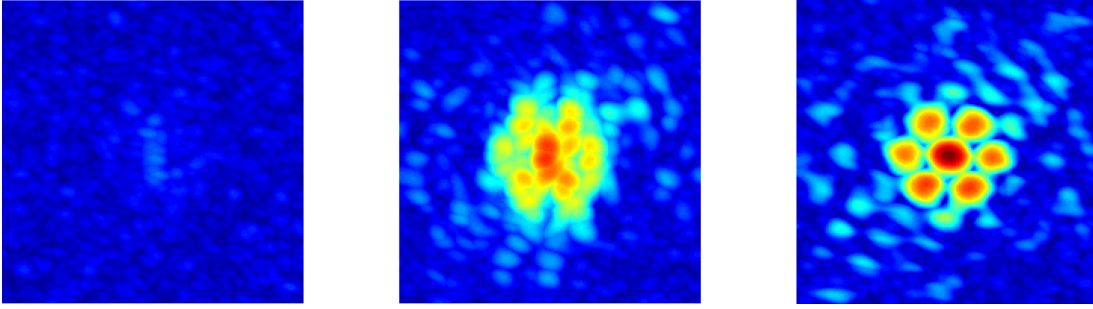


Figure 2.15: Spatial returns of the Hubble Space Telescope observed by the Phase II compact configuration and processed in different ways, akin to the spatial insets from Figures 2.12 – 2.14. The left figure is the result of (2.5), the middle figure implements (2.8), and the right figure is the implementation of (2.9).

## 2.5 Summary

Given the large speeds of RSOs in LEO (outlined in Section 2.3), any attempt to implement the required ten parameter search space, that is (2.14), would be unrealistic. Even with supercomputing capabilities, such a process would not be feasible for any long-integration space-surveillance staring radar, let alone a sensor like the MWA with its large aperture and incredibly accurate spatial resolution.

A potential response to this challenge would be to use the MWA solely as a tracking radar, that is, a sensor which takes known tracks and cues from other sources, and uses this information to form detections and update tracks. However, this approach would discard one of the advantages of a widefield staring radar in being able to detect and track unknown and uncatalogued objects, and so would not assist the challenging problem of modern LEO space surveillance.

Instead, this thesis aims to investigate practical and applied methods to overcome this problem, primarily through exploring the intersection and overlap between the radar parameter space and the orbital parameter space with the ultimate goal of taking uncued detections through to precise and accurate orbit determination. These ideas will be developed and demonstrated through a series of experimental observation campaigns with the MWA, illustrating how novel space surveillance sensors, such as radiotelescopes, can assist with the challenging

problems ahead.



## Chapter 3

# Improved Techniques for the Surveillance of the Near Earth Space Environment with the Murchison Widefield Array

The initial approach is to revisit previously collected data, and overcome the difficulties raised by these data, in order to investigate methods to extend processing intervals to detect smaller objects. This chapter is a faithful reproduction of the author's publication (Hennessy et al., 2019), as per Curtin University's policy. It differs from the original in only minor respects, including the formatting of both the text and the images, and the numbering of the equations and figures. Additionally, an appendix has been included, based on a section of the author's publication (Hennessy et al., 2023a), which covers range-walk and Doppler-walk mitigation measures in greater detail. In both this and subsequent chapters, the end matter (Acknowledgements, References) of the original papers have been shifted to the relevant sections of this dissertation. The reader will encounter some repetition of material in the introductory sections.

## 3.1 Abstract

In this paper we demonstrate improved techniques to extend coherent processing intervals for passive radar processing, with the Murchison Widefield Array. Specifically, we apply a two stage linear range and Doppler migration compensation by utilising Keystone Formatting and a recent dechirping method. These methods are used to further demonstrate the potential for the surveillance of space with the Murchison Widefield Array using passive radar, by detecting objects orders of magnitude smaller than previous work. This paper also demonstrates how the linear Doppler migration methods can be extended to higher order compensation to further increase potential processing intervals.

## 3.2 Introduction

The Murchison Widefield Array (MWA) is a radio telescope located in Western Australia (Tingay et al., 2013a). It is the low frequency precursor to the upcoming Square Kilometre Array (Braun, 2015). Operating in the frequency range 70 – 300 MHz, the main scientific goals of the MWA are to detect radio emission from neutral hydrogen during the so-called Epoch of Reionisation (EoR), to study our Sun and heliosphere, the Earth’s ionosphere, and radio transient phenomena, as well as map the Galactic and extragalactic radio sky (Bowman et al., 2013). The MWA is sensitive to, as a source of radio interference, terrestrial transmissions, such as FM radio and digital TV, reflected by objects in low Earth orbit (Tingay et al., 2013b), but as far as the Moon in the case of a global ensemble of transmitters (McKinley et al., 2013). Recently, it has been shown that passive radar techniques using the MWA can detect and range these objects in low Earth orbit (LEO), allowing orbits to be generated (Palmer et al., 2017).

With the ever increasing number of human-made objects in Earth orbit, the reduction in barriers and costs of putting an object in orbit, and the rapid uptake of small-satellite technology, the surveillance of space is an increasingly important



area of interest. This is highlighted by the increasing fears over the Kessler Syndrome, a scenario in which the density of debris in LEO is high enough that a collision causes a chain reaction of subsequent collisions, potentially rendering near-Earth space inaccessible (Patel, 2015).

Typically, the radars employed for the surveillance of space are very narrowly focused tracking radars, and are only able to surveil a small solid angle at any one time (National Research Council, 2012). The MWA has many beneficial characteristics for passive radar: the wide-area field of view (100s to 1,000s of square degrees); its location at the Murchison Radio-astronomy Observatory (MRO), a designated radio quiet zone (subject to very low levels of interference); and the MWA’s high sensitivity across a wide frequency range coinciding with numerous terrestrial transmitters.

Recent publications detailing space debris detection with radar, both passive and active, highlight the need to incorporate the object’s trajectory into the processing in order to enable longer coherent processing intervals in order to detect smaller objects (Laghezza et al., 2010; Benson, 2014; Mahmud et al., 2016).

In this paper we build upon previous work to further develop processing strategies using the MWA as an element in a passive radar system, particularly, in extending coherent processing intervals. In Section 3.3 prior work is detailed, including recent work in upgrading the MWA. Section 3.4 covers the processing strategies generally used in extending processing intervals in passive radar, as well as the specific techniques used in this paper. Section 3.5 covers a 2016 observational campaign and details some results demonstrating improvements in the detection of space debris. Last, Section 3.6 details future directions in this area and includes plans for future observational campaigns.

### 3.3 Prior work

The MWA originally consisted of 128 ‘tiles’, with each tile made up of 16 dual-polarised wide-band dipoles in a 4x4 configuration. The MWA covers a frequency

range of 70 MHz to 300 MHz, with an instantaneous bandwidth of 30.72 MHz.

The MWA has previously been used to demonstrate non-coherent<sup>1</sup> detections of the Moon as well as the International Space Station (ISS) using reflected FM radio (McKinley et al., 2013; Tingay et al., 2013b). This work went further to present simulated results predicting that the MWA is capable of detecting much smaller debris-sized objects<sup>2</sup>.

Following the non-coherent detection of the ISS, a data collection was undertaken in 2015 in order to demonstrate the use of the MWA with passive radar, focusing on the ISS. The MWA, despite being in the MRO, was able to directly receive the reference signal from Geraldton, the FM signal diffracting the three hundred kilometres. By comparing the directly transmitted signal, observed at the horizon, and the reflected surveillance signal, passive radar techniques were used to detect aircraft, ionised meteor trails and the ISS (Palmer et al., 2017).

This work proceeded to show that including the bistatic-range and Doppler measurements of the ISS greatly improves the ability to generate an orbit, in this case from a single pass. This is especially notable as this was achieved with a single 10 kW radio station, at an elevation of over 60° at the point of closest approach, well outside of the primary beam of the transmitter.

The MWA has recently undergone an upgrade, from Phase I to Phase II, doubling the number of tiles, allowing the array to be reconfigured between ‘extended’ and ‘compact’ configurations (Wayth et al., 2018). Figure 3.1 shows both the Phase I array layout as well as the Phase II compact configuration array layout, including the two compact hexagons.

Observation data are collected through the Voltage Capture System for recording high time and frequency resolution data (Tremblay et al., 2015). These voltages are collected after two polyphase filter bank (PFB) stages which critically sample the data into coarse 1.28 MHz channels and then 10 kHz fine channels. These data are phase-adjusted to account for the cable delays and then a further

---

<sup>1</sup>That is, without reference to the transmitted signal.

<sup>2</sup>Debris radius of  $> 0.5m$  to  $\sim 1,000 km$  altitude (Tingay et al., 2013b).

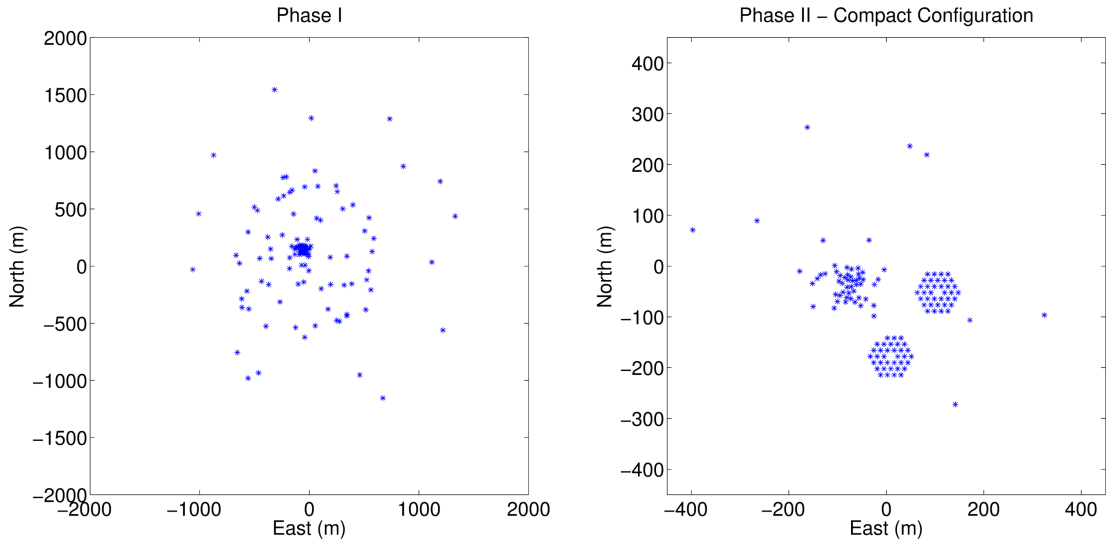


Figure 3.1: The left section shows the Phase I array. The right section shows the Phase II compact configuration array.

calibration solution is applied to remove instrumental and atmospheric effects. The calibration solutions are produced by recursively accounting for residuals after removing the visibilities from known strong compact sources (Tingay et al., 2013a).

The second PFB stage is then inverted to combine the 10kHz sub-channels into timeseries data, reconstituting the FM band for beamforming and delay-Doppler processing.

### 3.4 Processing Strategies

Space debris radar research consistently highlights the need for much longer processing intervals in order to improve system sensitivity; this mirrors similar considerations in passive radar. With the increase in computing power and available memory, extending processing intervals is far more achievable. This raises challenges for high-speed and manoeuvring targets as increasing the coherent processing interval (CPI) will lead to range and Doppler migration. That is, the target may be moving sufficiently fast to ‘smear’ returns across multiple delay

and Doppler bins during a single CPI, thereby reducing the target's power in each delay and Doppler bin. Traditionally, this has meant constraining CPIs to small values. Doppler migration is further exacerbated by increasing CPIs, as the Doppler resolution is proportional to the CPI length.

Mirroring the need to incorporate debris trajectory to improve performance, as in Section 3.2 above, incorporating target trajectory to avoid range and Doppler migration is a consistent theme in general passive radar research (Christiansen et al., 2014; Kulpa & Misiurewicz, 2006).

The classic solution for handling range migration is the Keystone Transform. The Keystone Transform is a frequency dependant slow time resampling, to decouple range and Doppler, removing all linear range migration (Perry et al., 1999). In order

to extend CPIs for detecting high-speed and manoeuvring targets, ambiguity surface processing has been extended to incorporate acceleration (Malanowski & Kulpa, 2008; Borowiec & Malanowski, 2016). As shown in (3.1), given a surveillance signal  $s(t)$  and reference signal  $r(t)$ , the narrowband ambiguity function is a matched filter over CPI  $T$  to delay  $\tau$  and Doppler  $v$ , but also extended to include the Doppler rate  $w$ . The rate of Doppler change is analogous to target acceleration.

$$\chi(\tau, v, w) = \int_T s(t)r^*(t - \tau)e^{-j2\pi(vt + \frac{1}{2}wt^2)} dt \quad (3.1)$$

This processing only removes Doppler migration due to acceleration. Range migration caused by accelerating targets will not be compensated as the delay term  $\tau$  is not adjusted. This method also requires the delay Doppler map to be recomputed for each acceleration hypothesis. Because evaluating the complete ambiguity function is computationally very expensive, approximations to these methods are used (Howland et al., 2005; Palmer et al., 2011).

These involve producing a range-compressed pulse stack and resolving Doppler with a Fourier transform. As well as being far more efficient to produce, they

also enable more efficient methods of detecting accelerating targets.

In recent years the most common method for detecting accelerating targets is the Fractional Fourier Transform (Melino & Tran, 2011). The Fractional Fourier transform is a generalisation of the classic Fourier transform to an arbitrary order, or ‘angle’, in the time and frequency plane, with the Fourier transform representing a  $\frac{\pi}{2}$  order transform. For a target undergoing linear acceleration, the Doppler returns will be smeared when extracted with the Fourier transform. However, with a suitably chosen angle, the returns will be localised to a single bin with the Fractional Fourier Transform.

A novel, and simple, improvement has come from noting that a target undergoing linear acceleration will produce a linear frequency modulation response in slow-time.

The Fractional Fourier transform decouples the frequency-time dependence in the signal to produce a tone. This leads to a great simplification. Rather than using the Fractional Fourier transform, a non-linear phase correction can be applied to dechirp the motion-induced chirp, and then the Fourier transform can be used to resolve Doppler as before (Tran et al., 2014).

The non-linear phase correction, across slow-time, is given by:

$$e^{-2j\pi c_r t^2}, \tag{3.2}$$

where the dechirp rate  $c_r$  is given by  $\frac{a}{\lambda}$ ,  $a$  is the acceleration hypothesis and  $\lambda$  the wavelength.

This is a much more efficient method for detecting accelerating targets. Not only can it be incorporated into approximations to the complete ambiguity surface, but significantly, the delay-Doppler map does not need to be recomputed for acceleration hypotheses. The compressed pulse stack can be computed once, and then only the Doppler-resolving Fourier transform needs to be repeated for each acceleration value.

An example of this is shown in Figure 3.2, showing the results of a five second

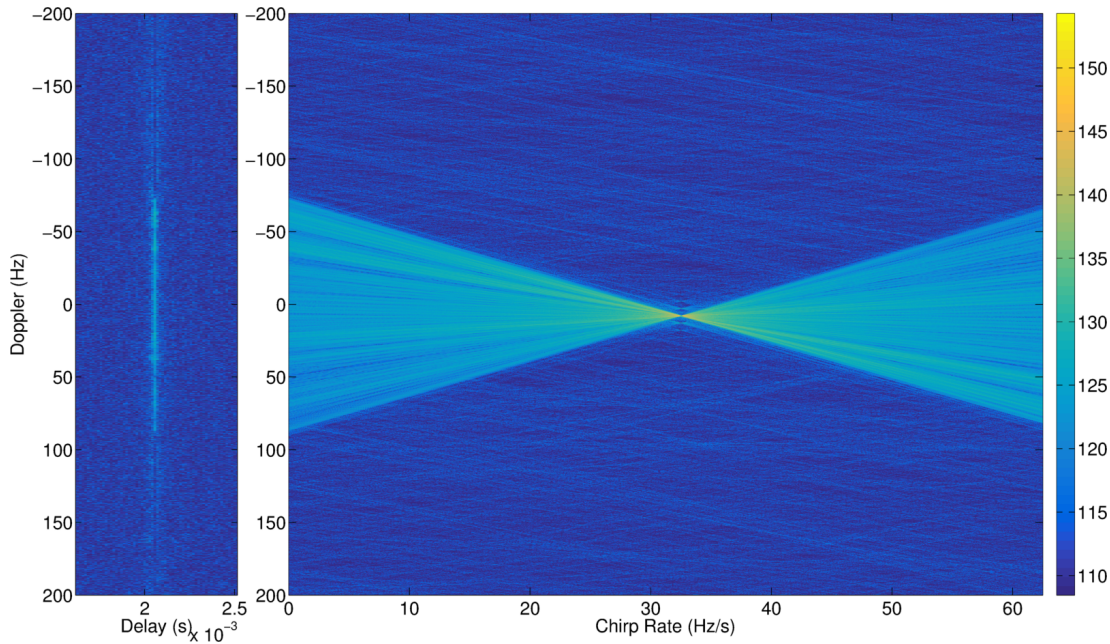


Figure 3.2: Ambiguity surface signal power in dB of the ISS, processed with a five second CPI, along with the ISS returns processed with different dechirp hypotheses.

CPI for the ISS moving through zero Doppler. The left panel shows a region of the delay Doppler map with the ISS manifesting as a vertical line, smeared across hundreds of Doppler bins, the result of Doppler migration. The right shows a single range bin reprocessed for a range of dechirp hypotheses. The target SNR is increased when the target is localised to a single Doppler frequency, with the appropriate dechirp rate.

A common approach is to handle range and Doppler migration separately, rather than attempting to compensate for both in one transform (Kodituwakku & Melino, 2014; Li et al., 2017). Traditionally, this is achieved by processing to remove linear range migration and then processing to remove Doppler migration due to linear acceleration. The efficacy of extending processing intervals is limited in this case, as a target undergoing acceleration will result in non-linear range migration.

Orbital kinematics, however, are ideal for this type of extended integration processing, as orbital object motion is very stable and reliable. In the space

situational awareness (SSA) case, the acceleration that is detected is primarily due to apparent radial acceleration caused by the changing bistatic geometry.

For an object in orbit, the major contribution to acceleration is Earth's gravity, combined with other much smaller forces such as atmospheric drag and space weather effects. The bistatic acceleration, rather Doppler rate, detected in bistatic radar processing will be dominated by the relative geometry, as the Doppler rapidly changes as the object passes overhead. This is incredibly beneficial to extended processing, as the range and Doppler migration effects are quite separate. The rate of Doppler change will be highest when the Doppler is zero, at the object's closest point, transitioning from positive to negative Doppler. Therefore Doppler migration is greatest when the range migration is zero. Conversely the range migration will be at its maximum at larger ranges, at which the Doppler magnitude is at a maximum, and Doppler rate is approaching zero.

This only applies to objects in relatively stable orbits; if an object was falling directly toward the radar then the true acceleration, due to gravity, would dominate the Doppler rate, and these methods would not be suitable. Two stage linear range and Doppler-rate methods will tend to defocus returns of non-orbital objects, as seen in returns from meteors and aircraft.

### 3.5 Results

Previously reported detections of the ISS with passive radar using the MWA were achieved by measuring range, Doppler, azimuth, and elevation and then inferring azimuth, and elevation rates (Palmer et al., 2017). The results included in this paper also measure Doppler rates using the dechirping method, mentioned earlier. However, azimuth and elevation rates are also directly measured by constructing the surveillance signal based on ephemerides. The surveillance signal is constructed by adjusting the beamforming weights during the CPI so that the target is tracked throughout. This sub-CPI beamforming adjustment, whilst suitable for demonstrating improved detection performance, is not tractable for

wide-field, blind searches as it is essentially adding extra dimensions to the ambiguity function.

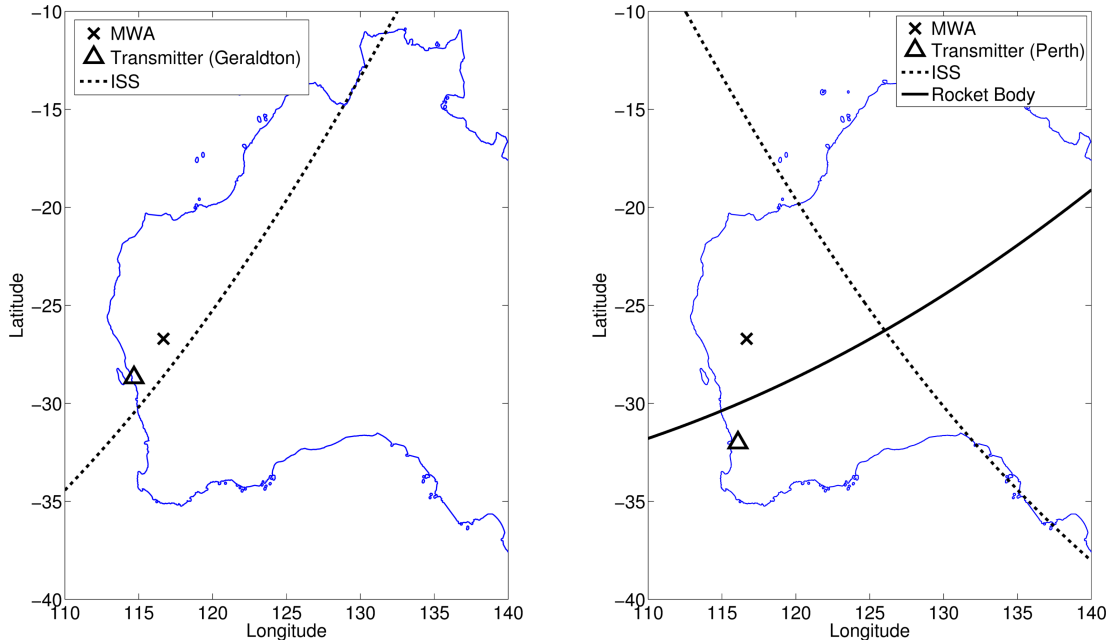


Figure 3.3: The 2015 (left) and 2016 (right) data collection configurations, overlaid on a map of Western and Central Australia.

### 3.5.1 2015 Data Reprocessing

The first passive radar detections of an object in orbit, were generated from a dedicated MWA observation collected in 2015 (Palmer et al., 2017). In this 2015 dataset the ISS passes almost directly above the MWA<sup>3</sup>, providing ideal conditions for detection. However, a significant issue with this earlier work was the ISS’ SNR, or detectability, decreasing with longer processing intervals.

This was due to the ISS’ return smearing through the ambiguity surface and search parameters. As well as the Doppler and range smearing, additional migration occurred in beamforming direction and direction rates. This is due to the high angular resolution achievable with the MWA, particularly with the long baselines in the initial configuration. With an angular resolution less than one

<sup>3</sup>Rather, passing at a maximum elevation of 70° from the MWA.



tenth of a degree, our standard processing could not coherently follow the ISS as it subtends almost three degrees per second at the point of its closest approach.

Another issue was that the reference signal was formed directly from the MWA observation data. This had the result of limiting potential baseline lengths; with Geraldton being 300 km away the elevation of the ISS from the transmitter was large enough that the ISS was not in the primary transmitter beam. The reference signal is likely to have suffered from multipath effects, diffracting over such a distance, which may raise the clutter floor or cause destructive interference. The map of the collection geometry with the transmitter in Geraldton, the MWA and the ISS path is shown in Figure 3.3. The MWA was in its Phase I configuration, as shown in Figure 3.1.

Figure 3.4 shows the reprocessing of the ISS' pass from the 2015 data using the Keystone Transform to mitigate range migration as well as dechirping to mitigate Doppler migration; for comparison it also shows the SNR from the original publication, without any migration compensation.

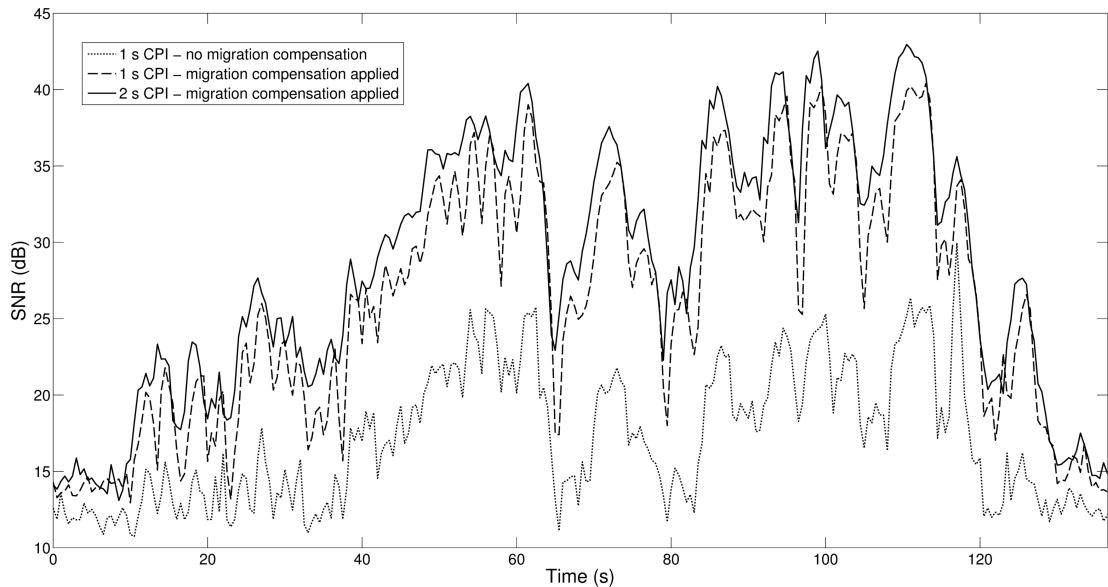


Figure 3.4: The SNR (dB) of the ISS with no migration compensation applied (corresponding to initial results (Palmer et al., 2017)) through to full range and Doppler migration compensation.

The migration compensation methods result in a dramatic increase in the SNR

due to the improved processing gain. In this instance the ISS is now initially detected at a slant range of over 1,000 km from the MWA. More importantly, however, the SNR of the ISS increases with the CPI, with Figure 3.4 showing an expected  $\sim 3\text{dB}$  increase changing from a one second CPI to a two second CPI.

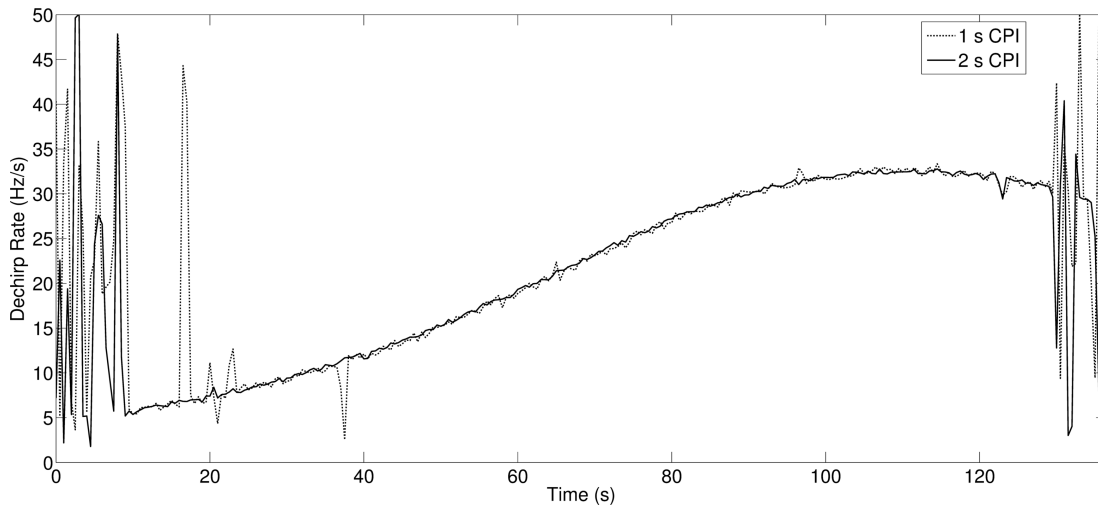


Figure 3.5: Detected dechirp rate corresponding to the SNR in Figure 3.4.

Figure 3.5 shows the associated chirp rates for the SNR returns in Figure 3.4. It shows a very clear trackable curve, and again, results improve as the CPI increases.

### 3.5.2 2016 Data Collection

As part of a broader demonstration campaign, FM band collections were undertaken by the MWA in late 2016, targeting the ISS again, and also some lower Radar Cross-Section (RCS) objects (Morreale et al., 2017). Specifically, the MWA focused on a rocket body, a large piece of debris in LEO. For this collection, a reference signal was recorded separately in Perth, 600 km away from the MWA. The reference collection recorded the entire FM band; the main focus was three 100 kW omnidirectional, mixed polarisation stations from the Bickley transmitters. There was no direct-path FM signal present in the MWA collections, due to the specific ducting/propagation conditions for the particular analogue beamforming

configuration. The particular collection geometry, shown in Figure 3.3, was far from ideal, being so far from the MWA. The MWA was in the Phase II compact configuration, as shown in Figure 3.1.

Figure 3.6 shows the SNR of the ISS for three different CPI lengths, with the migration compensation techniques applied. It shows the ISS being detected with significant SNR despite being so far from Perth and the MWA. The closest approach was at a bistatic range of 1,436 km, with a total reflected path distance never less than 2,000 km. The ISS was almost certainly in the main beam of the transmitter, being less than  $15^\circ$  elevation from Perth for the duration of the observation.

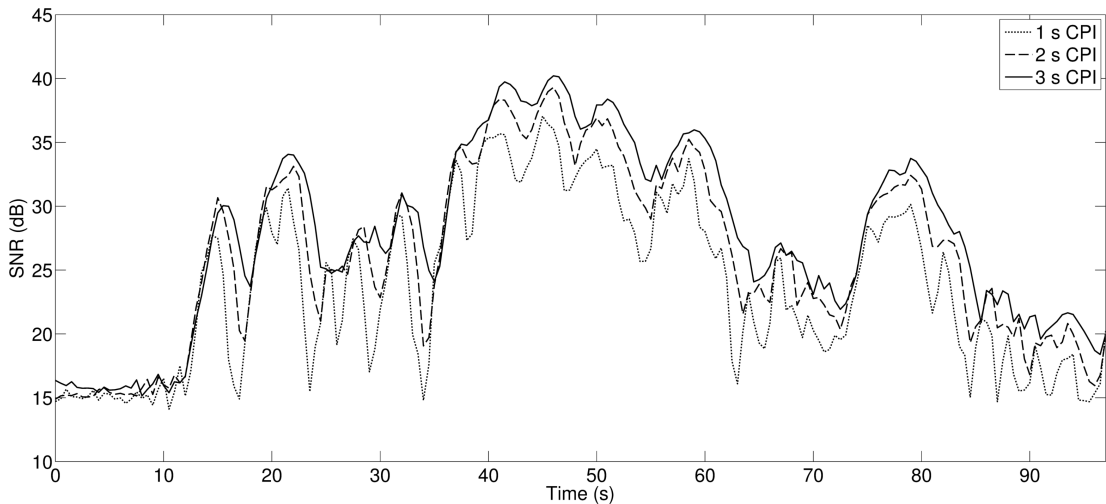


Figure 3.6: The SNR (dB) of the ISS from the 2016 data collection with CPI lengths of one, two and three seconds. The SNR improves with CPI.

An interesting aspect of these passes was that the reference signal was inadvertently recorded without any clock synchronisation. In order for the reference signal to be used for coherent processing, it needed to be synchronised, both in time and frequency. Bright meteor returns were used for coarse time-synchronisation, and then the returns of the ISS itself were used for fine time and frequency alignment. That is, reflections from meteor trails are sufficiently large that they are easily detected incoherently, such that a time-aligned MWA surveillance signal, known to contain meteor returns, can be formed. This meteor reflection is cor-

related across the reference signal until the coherent meteor return is detected, providing a coarse time alignment (as the exact location of the meteor return is not known). This coarse time alignment then allows a surveillance beam to be formed towards the ISS, so that coherent ISS detections, in delay and Doppler, can then be compared to expected returns from ephemerides to provide fine time and frequency offsets, which are corrected. This time and frequency alignment was sufficient to be able to detect the other target from this collection, a rocket body.

### 3.5.3 Rocket Body

The rocket body was a stage from the Atlas-Centaur launch system, launched in August 1972. The object is 9 m long with a diameter of 3.05 m. Based on a perfectly conducting cylinder of the same dimensions, the RCS at 100 MHz is estimated to be between  $10m^2$  and  $100m^2$ , an order of magnitude or more smaller than the ISS (Frazer et al., 2013b).

As shown in Figure 3.3, this pass is sub-optimal for passive radar processing, as the object passes much closer to the transmitter than the receiver. At the point of closest approach, at a bistatic range of 894 km, the rocket body was at an elevation of  $73^\circ$  from the transmitter; well outside the transmitter's main beam. Figure 3.7 shows the SNR of the rocket body for this pass when processed using the migration compensation techniques. Unlike the ISS, the rocket body is not detectable without accounting for the range and Doppler smearing. These migration techniques allowed coherent improvements in detectability with CPIs up to 10 s, at some points in its trajectory.

These results, as well as the sub-optimal geometry, both suggest that much smaller targets will be readily detectable. The best SSA results will be achieved when surveilling the wide area directly above the MWA, when the objects are illuminated by the main beam of FM radio transmitters.

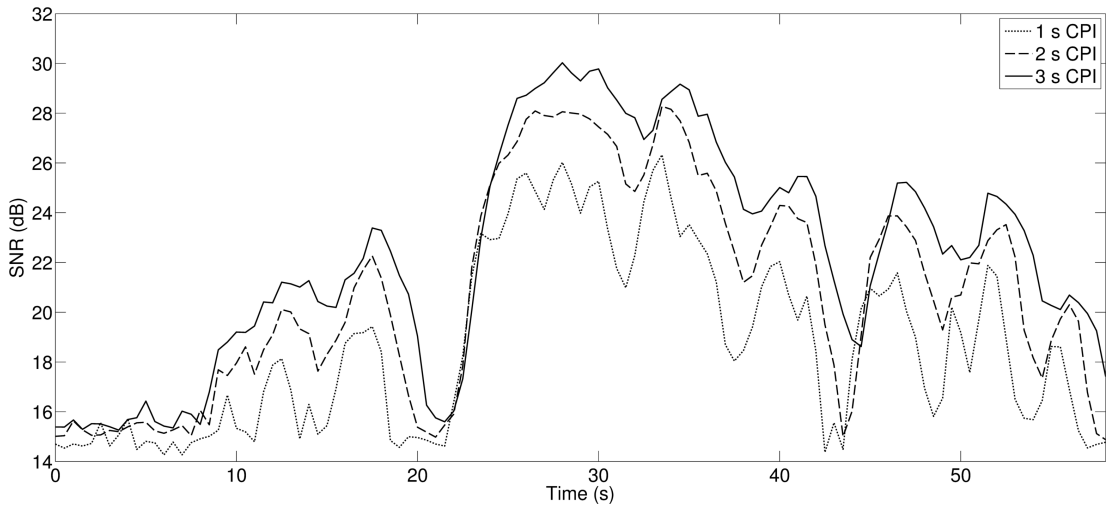


Figure 3.7: The SNR of the Atlas-Centaur rocket body from the 2016 data collection with CPI lengths of one, two and three seconds. The SNR improves with CPI.

### 3.5.4 Higher Order Hypotheses

The modified narrowband ambiguity function (3.1) has previously been extended to incorporate higher order Doppler migration compensation terms (Malanowski & Kulpa, 2008). This still requires recomputation of the ambiguity surface, so is very computationally expensive. Similarly, the dechirp processing (3.2), can be extended to include non-linear and higher order frequency modulation terms. With this extension the non-linear phase adjustment can be applied to dechirp and dejerk the target's Doppler migration.

$$e^{-2j\pi(ct^2+c_jt^3)} \quad (3.3)$$

The chirp rate, now varying over time, is given by  $c_r + c_j t$ , to include  $c_j$ , the rate of change of the chirp rate. This rate is here referred to as the 'jerk', as it is analogous to the rate of change of bistatic acceleration.

Figure 3.8 shows a single snapshot in time of the SNR of the rocket body and how it varies with CPI. It shows that by incorporating the higher order motion compensation term, at least in Doppler, a modest improvement in maximum CPI length is achieved. However, like previous methods mentioned, higher order

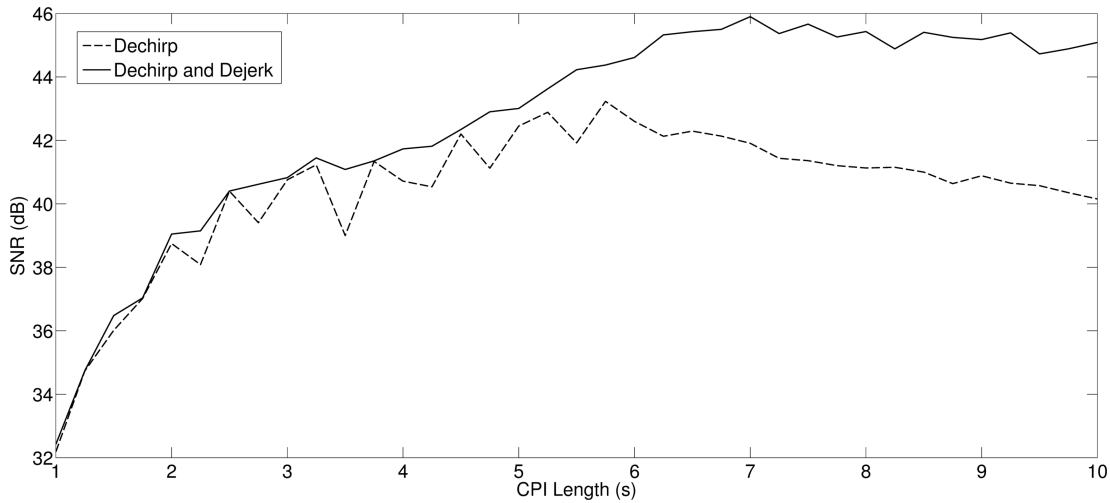


Figure 3.8: A single snapshot in time of the SNR of the rocket body and how it varies with CPI, comparing the dechirp technique with the higher order dechirp and dejerk.

compensation means further extending the search space processing, as required for the detection of unknown targets.

### 3.6 Future Work

In order to conduct surveillance processing with the MWA, more tractable processing strategies will need to be developed. The methods in Sections 3.4 and 3.5 demonstrate improvements in the performance of passive radar using the MWA. However, applied naively they would result in a 10-dimensional ambiguity surface to search over. An improvement would be to work backwards from the orbital parameters of interest, as an object’s orbit will largely constrain and define most of the other search parameters (Kohlleppel, 2018). Incorporating orbital kinematics, even including highly eccentric orbits, will greatly reduce the subspace of possible values for other parameters, including range and Doppler migration factors, as well as pointing directions and their associated rates.

Further improvements to these methods would benefit from additional data collections targeting even smaller RCS objects, including space debris, passing

above the MWA. These data collections are planned for the near future and will be reported in future publications.

### 3.7 Conclusion

This paper covers improved techniques for extending coherent processing intervals with passive radar for space surveillance using the MWA. Specifically, applying a two stage linear range and Doppler migration compensation by utilising Keystone Formatting and a recent dechirping method.

These methods have limitations for accelerating targets, but work well for objects in orbit by handling migration due to apparent radial acceleration due to the bistatic geometry.

These methods are then used to further demonstrate the potential for the surveillance of space with the Murchison Widefield Array using passive radar, by detecting objects at least an order of magnitude smaller than previous work. Notably, the detection conditions were difficult, including the sub-optimal bistatic geometry and the separately recorded and unsynchronised reference signal.

This paper also demonstrates how linear Doppler migration methods can be extended with higher order compensation to further increase potential processing intervals.

Finally, this paper outlines approaches that may improve these techniques, by directly incorporating orbital parameters into the ambiguity surface formation. Planned future collections will further improve space debris detection and tracking with the MWA.

### 3.A Mitigating linear range-walk and linear Doppler-walk

The Woodward Ambiguity Function, essentially (3.1), represents the optimal method for matching delayed and frequency shifted narrowband signals. However, in practice it is not implemented directly due to the computational requirements of having to perform a long correlation for every delay and Doppler hypothesis. This is further complicated by incorporating Doppler-rate, as in (3.1).

As detailed in Section 2.4.1, instead of evaluating the Woodward Ambiguity Function directly, it is approximated by forming a series of short correlation pulses, and then integrating these pulses through the Fourier Transform (FT), as shown in (2.4). Each matched pulse represents a snapshot in slow-time, and the full product is referred to as the slow-time fast-time pulse stack. The resulting ambiguity function, the delay Doppler map, is essentially the fast-time slow-frequency product.

This appendix illustrates how this approach is affected by target motion, and how linear range-walk and Doppler-walk occur. It then details methods for mitigating these deleterious terms, specifically with the Keystone transform for the range-walk and the chirpogram for the Doppler-walk.

If a target's motion over a CPI is described by the bistatic-delay  $d(t)$ , expressions for the slow-time fast-time response can be generated with the assumption that the target motion  $d$  only varies from pulse to pulse and any intra-pulse motion is negligible. If the the output of the match-filtered response, described in (2.4), at slow-time index  $m$  is given by  $p_m(t)$ , then fast-time slow-time is approximated by:

$$S(t, t_m) = Ap_m(t - c^{-1}d(t_m))e^{-j\frac{2\pi}{c}f_c d(t_m)} , \quad (3.4)$$

where  $t_m$  is the slow time for return index  $m$  such that  $t_m = mB\tau_c$  in (2.4),  $d(t_m)$  is the bistatic delay to the target for time instance  $t_m$  and  $f_c$  is the transmitted centre frequency. Also,  $A$  is a constant that depends on the target radar cross



section and the target range and  $c$  is the speed of light.

By taking the FT over fast-time, the received signal in fast-frequency slow-time is:

$$S(f, t_m) = AP_m(f)e^{-j\frac{2\pi}{c}(f+f_c)d(t_m)} , \quad (3.5)$$

where  $P_m(f)$  is the FT of  $p_m(t)$ .

With a constant bistatic velocity motion model across the CIT,  $d(t_m)$  is given by  $d(t_m) = d + vt_m$ , and so (3.5) is now:

$$S(f, t_m) = AP_m(f)e^{-j\frac{2\pi}{c}((f+f_c)d)}e^{-j\frac{4\pi}{c}((f+f_c)vt_m)} , \quad (3.6)$$

where the coupled term  $fv_t_m$  term represents the linear range migration during the CIT.

There are many methods for mitigating range walk however the primary one used in this thesis is the Keystone Transform. The Keystone Transform is a method which can be applied to the slow-time fast-frequency expression to eliminate linear range walk by resampling slow-time as  $t_m = \frac{f_c}{f+f_c}t'_m$ , where the resulting fast-frequency slow-time expression is:

$$S(f, t'_m) = AP_m(f)e^{-j\frac{2\pi}{c}((f+f_c)d+fv't'_m)} , \quad (3.7)$$

which no longer contains the coupling between the fast-frequency,  $f$ , and slow-time  $t_m$  (Perry et al., 1999; Perry et al., 2007)

For accelerating motion, if a quadratic motion model is used with radial acceleration  $a$  such that  $d(t_m) = d + vt_m + \frac{1}{2}at_m^2$ , then (3.5) is now given by:

$$S(f, t_m) = AP_m(f)e^{-j\frac{2\pi}{c}((f+f_c)d+(f+f_c)vt_m+(f+f_c)\frac{1}{2}at_m^2)} . \quad (3.8)$$

Mitigating all range-walk is now challenging because of the inclusion of both linear and non-linear terms ( $fv_t_m$  and  $fat_m^2$  respectively). These terms cannot be mitigated with a single slow-time resampling, although there are methods

which partially reduce the impact of both (Zhou et al., 2007; Scott et al., 2015). However, given that the Doppler walk resulting from accelerating targets is almost always a far more significant degrading factor than for non-accelerating targets, the non-linear range-walk term is typically less of a concern. This is especially true for space surveillance, where the radial acceleration will be at its greatest when the satellite is at its closest approach and the radial range-rate will be zero.

The Doppler-walk term is the acceleration-induced slow-time chirp in (3.8) of  $e^{-j\frac{2\pi}{c}f_c a t_m^2}$ . There are many methods applicable to estimating this radial-acceleration, including time-frequency methods, which are crucial for removing this significant source of loss (Kay & Boudreaux-Bartels, 1985; Peleg & Porat, 1991b; O'shea, 2002; Boashash, 2016; Sirianunpiboon et al., 2019). However, the optimal method is the chirpogram which requires searching through acceleration hypotheses and matching with a slow-time dechirp, allowing an unperturbed Doppler term,  $e^{-j\frac{2\pi}{c}f_c v t_m}$ , to be matched by the FT through the coherent integration. That is, when the matching non-linear phase term  $c_r$  from (3.2) is applied to (3.8), all linear Doppler-walk is mitigated as described in 3.4.

## Chapter 4

# Orbit Determination Before Detect: Orbital Parameter Matched Filtering for Uncued Detection

With the daunting prospect of forming matching products with a large number of measurement parameters, this chapter delves into astrodynamics and investigates the application of orbital motion to the radar measurement space in order to achieved uncued detection. Similar to previous chapters, this chapter is reproduced from the author’s publication (Hennessy et al., 2020), an additional appendix discussing the computational characteristics has been included here. The reader will encounter some repetition of material in the introductory sections.

### 4.1 Abstract

This paper presents a novel algorithm to incorporate orbital parameters into radar ambiguity function expressions by extending the standard ambiguity function to match Keplerian two-body orbits. A coherent orbital matched-filter will maximise a radar’s sensitivity to objects in orbit, as well as provide rapid initial

orbit determination from a single detection. This paper then shows how uncued detection searches can be practically achieved by incorporating radar parameters into the orbital search-space, especially for circular orbits. Simulated results are compared to results obtained from ephemeris data, showing that the orbital path determined by the proposed method, and the associated radar parameters that would be observed, match those derived from the ephemeris data.

## 4.2 Introduction

Modern radar systems are able to generate optimal filters matched to increasingly complex target motion, resulting in increased sensitivity to targets exhibiting these motion at the cost of significant processing load. This problem is most difficult for sensors targeting objects in low Earth orbit (LEO), especially sensors with a significant field of regard. This is due to the observation time required to detect smaller targets, combined with significant orbital velocities and large search volumes, increasing the parameter space to impractical levels.

Extending radar processing integration times in order to increase detection sensitivity requires mitigation against range migration, Doppler migration, and angular migration. The correction of these migrations is further complicated by the motion of the Earth, and hence the sensor located on the Earth. The direct implementation of a matched filter in this radar search space may lead to the incorporation of many parameters.

The nominal trajectory of orbits is well understood and is generally deterministic. The motion of a two-body Keplerian orbit, an idealised case of an object of insignificant mass orbiting around a much larger central body<sup>1</sup>, can be expressed entirely by six parameters. Matching the processing to this well-defined orbital motion for the purpose of improved radar detection and space situational awareness is therefore a natural extension.

Whilst the primary aim of this general method is to increase a radar's sen-

---

<sup>1</sup>Treated as a single point mass.

sitivity to objects in orbit, detections from a filter matched to a target’s orbital trajectory will additionally provide coarse initial orbit determination. Traditionally, performing initial orbit determination requires many radar detections of a pass of an object in space.

After briefly covering prior work, Section 4.3 details the problem formulation, specifically in terms of ambiguity function expressions and Keplerian orbital dynamics. In Section 4.4, Orbit Determination Before Detect (ODBD) methods are discussed, including matched processing to orbital parameters, constraining the search volume, and constraining the orbit in radar measurement space, particularly for uncued detections. Some specific applications, including single-channel object detection and orbit determination are also discussed. Section 4.5 presents simulated results, with comparison against ephemerides. Section 4.6 concludes with a description of future work.

### 4.2.1 Prior Work

The motivation for this paper is to further develop techniques for the surveillance of space with the Murchison Widefield Array (MWA) using passive radar. The paper is particularly concerned with developing techniques for uncued detection over a wide field of regard. The MWA is a low frequency (70 - 300 MHz), wide field-of-view, radio telescope located in Western Australia (Tingay et al., 2013a). The MWA has demonstrated the incoherent detection of the International Space Station (ISS) (Tingay et al., 2013b) and other, smaller, objects in orbit (Prabu et al., 2020b). However, for coherent processing, methods compensating for all aspects of motion migration are required in order to detect smaller satellites and space debris (Hennessy et al., 2019). As passive radar systems have no control over the transmitter used for detection, improving processing gain through extended Coherent Processing Intervals (CPIs) is a method used to achieve the required sensitivity (Malanowski & Kulpa, 2008). Orbital trajectories are ideal targets for such techniques, as stable and predictable relative motion allows for simpler

measurement models. Such techniques have also been used with active radar, for improved sensitivity and processing gain (Markkanen et al., 2005) (Zhang et al., 2019).

Consisting of 256 tiles spread across many square kilometres, the MWA’s sparse layout<sup>2</sup> provides high angular resolution. Objects in orbit will therefore transit many beamwidths per second at the point of closest approach. Because of this, high angular resolution (normally a desirable attribute) can result in significant angular migration. Highly eccentric orbits will transit significantly faster. This is particularly challenging for the uncued detection of small objects, where longer integration times are needed to achieve sufficient sensitivity.

Individual radar detections consisting of a single measurement of range, Doppler, azimuth and elevation, only define a broad region of potential orbital parameters (Tommei et al., 2007). This region may be constrained by incorporating angular rates (DeMars & Jah, 2014), and even further by including radial acceleration and jerk (Zhang et al., 2019). Usually, many radar detections are required to perform initial orbit determination. The mapping between radar measurement space and orbital parameters is an ongoing area of research (Kohlleppel, 2018).

## 4.3 Problem Formulation

### 4.3.1 Radar Product Formation

A standard timeseries matched filter is a function to detect reflected copies of a reference signal  $d(t)$  in the surveillance signal  $s(t)$ , specifically copies delayed by  $\tau$  and frequency shifted by  $f_D$ :

$$\chi(\tau, f_D) = \int_T s(t)d^*(t - \tau)e^{-j2\pi f_D t} dt. \quad (4.1)$$

---

<sup>2</sup>At FM radio frequencies, even the compact configuration of MWA Phase II is sparse (Wayth et al., 2018).

This matched filter can be extended to more complicated motions by *dechirping* (or even applying higher order corrections to) the motion-induced frequency shift. For example, instead of matching to the radial velocity with a Doppler shift of  $f_D$ , higher order motions could be matched with a time varying frequency (that can be represented as a polynomial phase signal) given by  $f_D + f_C t$ , where  $f_C$  is proportional to the radial acceleration. This can be extended to an arbitrary number of parameters at the cost of adding extra dimensions to the matched filter outputs. To account for any range migration, the delay term  $\tau$  will also need to be a function of time to match the radial motion.

For a receiver array consisting of  $N$  elements, the surveillance signal  $s(t)$  can be formed by classical far-field beamforming in a direction of interest such that:

$$s(t) = \sum_{n=1}^N s_n(t) e^{-j\mathbf{k}(\theta, \phi) \cdot \mathbf{u}_n}, \quad (4.2)$$

where  $s_n(t)$  is the received signal at the  $n^{\text{th}}$  antenna,  $\mathbf{u}_n$  is the position of the  $n^{\text{th}}$  antenna, and  $\mathbf{k}(\theta, \phi)$  is the signal wavevector for azimuth  $\theta$  and elevation  $\phi$ . Time varying adjustments can be made to every measurement parameter to create a filter,  $\chi$ , matched to the exact motion of an object with range  $\rho(t)$  and slant range-rate  $\dot{\rho}(t)$ , in time-varying directions given by azimuth  $\theta(t)$  and elevation  $\phi(t)$ :

$$\chi(\theta(t), \phi(t), \rho(t), \dot{\rho}(t)) = \int_T \left[ \sum_{n=1}^N e^{j\mathbf{k}(\theta(t), \phi(t)) \cdot \mathbf{u}_n} s_n(t) \right] d^*(t - 2c^{-1}\rho(t)) e^{-j\frac{4\pi}{\lambda}\dot{\rho}(t)t} dt, \quad (4.3)$$

where the delay to the target is now given by the total path distance scaled by  $\frac{1}{c}$ , and the Doppler shift is given by  $\frac{2\dot{\rho}}{\lambda}$ .

### 4.3.2 Orbital Dynamics

The most common elements used to parameterise an orbit are the Keplerian, or *classical*, orbital elements. These elements directly describe the size, shape, and orientation of an orbital ellipse (with one focus being at the centre of the central body), and the position of an object on this ellipse at some epoch, in the Earth-Centered Inertial (ECI) coordinate frame (Vallado & McClain, 2001). The ECI coordinate frame has its origin at the centre of the Earth, but it does not rotate with the Earth. It is also worth noting that a Keplerian orbit can, in fact, be any conic section. However, in this paper, it is assumed that orbits describe Earth-captured closed orbits.

The Keplerian orbital parameters are: the semi-major axis,  $a$ , and eccentricity,  $e$ , defining the size and shape of the ellipse; the right-ascension of the ascending node,  $\Omega$ , and inclination,  $i$ , which define the orientation of the elliptical plane to the Earth's equatorial plane; the argument of periapsis,  $w$ , defining the orientation/rotation of the ellipse in the orbital plane; and finally, the true anomaly,  $\nu$ , defining the position of the object on the ellipse (refer to Figure 4.1).

It is also assumed that the only force acting on the object in orbit is due to the gravity of the dominant mass<sup>3</sup>, with the acceleration due to the Earth's gravity  $\ddot{\mathbf{r}}$ , given by:

$$\ddot{\mathbf{r}} = -\frac{\mu}{|\mathbf{r}|^3}\mathbf{r}, \quad (4.4)$$

where  $\mu$  is the standard gravitational parameter for the Earth.

Given the orbital parameters, and the acceleration due to the Earth's gravity, the Cartesian position  $\mathbf{r}$ , and velocity  $\dot{\mathbf{r}}$ , for an object in Earth orbit is completely

---

<sup>3</sup>Uniform acceleration does not take into account the ellipsoidal/oblate nature of the Earth or other forces, such as micro-atmospheric drag, solar weather, and gravity due to other celestial bodies. For the short duration of a single CPI, these factors are generally negligible.



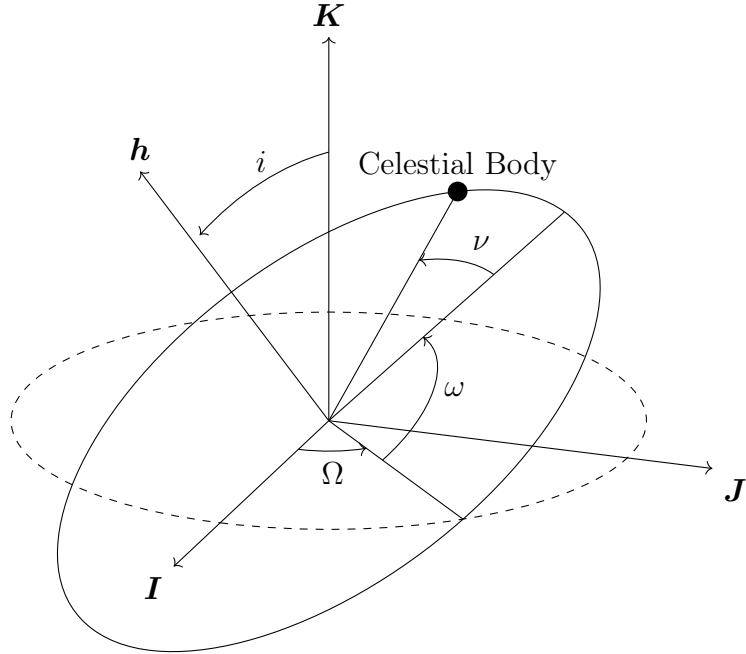


Figure 4.1: The orbital plane determined by orientation parameters  $\Omega$ ,  $\omega$ , and  $i$  relative to the plane of reference in the ECI coordinate frame. These parameters define the direction of the angular momentum vector  $\mathbf{h}$ . The axes  $\mathbf{I}$ ,  $\mathbf{J}$  and  $\mathbf{K}$  define the ECI coordinate frame.

deterministic and is given by:

$$\mathbf{r} = \frac{a(1 - e^2)}{1 + e \cos \nu} (\cos \nu \mathbf{P} + \sin \nu \mathbf{Q}) ; \quad (4.5)$$

$$\dot{\mathbf{r}} = \sqrt{\frac{\mu}{a(1 - e^2)}} (-\sin \nu \mathbf{P} + (e + \cos \nu) \mathbf{Q}) , \quad (4.6)$$

where  $\mathbf{P}$  and  $\mathbf{Q}$  represent axes of a coordinate system co-planar with the orbital plane in the Cartesian ECI coordinate frame (given by axes  $\mathbf{I}$ ,  $\mathbf{J}$ , and  $\mathbf{K}$ ). The third axis,  $\mathbf{W}$ , is perpendicular to the orbital plane (Vallado & McClain, 2001). These vectors are described by:

$$\mathbf{P} = \begin{bmatrix} \cos \Omega \cos \omega - \sin \Omega \cos i \sin \omega \\ \sin \Omega \cos \omega + \cos \Omega \cos i \sin \omega \\ \sin i \sin \omega \end{bmatrix} ; \quad (4.7)$$

$$\mathbf{Q} = \begin{bmatrix} -\cos \Omega \sin \omega - \sin \Omega \cos i \cos \omega \\ -\sin \Omega \sin \omega + \cos \Omega \cos i \cos \omega \\ \sin i \cos \omega \end{bmatrix} ; \quad (4.8)$$

$$\mathbf{W} = \begin{bmatrix} \sin i \sin \Omega \\ -\sin i \cos \Omega \\ \cos i \end{bmatrix} . \quad (4.9)$$

Note that a complicating factor with the ECI reference frame is that a nominally stationary position on the surface of the Earth, such as a fixed radar sensor, will have significant motion.

## 4.4 Orbit Determination Before Detect

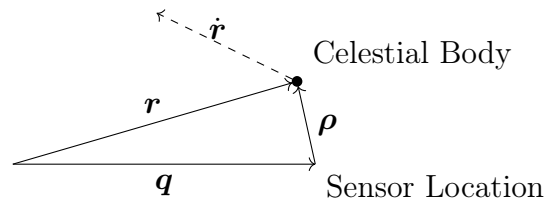


Figure 4.2: In the ECI coordinate frame the sensor is at position  $\mathbf{q}$ , the celestial body at position  $\mathbf{r}$  with velocity  $\dot{\mathbf{r}}$  (given by (4.5) and (4.6)) and the slant range vector from the sensor to the object given by  $\boldsymbol{\rho}$ .

For a two-body Keplerian orbit, the time-varying terms  $\rho(t)$ ,  $\dot{\rho}(t)$ ,  $\phi(t)$ , and  $\theta(t)$  (4.3) can be completely described by an orbit's six independent parameters. Although the position of an object in orbit is given by (4.5), there are no closed form solutions for the time varying position  $\mathbf{r}(t)$ . Instead, a Taylor series approxi-

mation can be used to calculate an expression for the object's position throughout a CPI such that  $\mathbf{r}(t) = \sum_{n=0}^{\infty} \frac{\mathbf{r}^{(n)}(0)t^n}{n!}$  (where  $\mathbf{r}^{(n)}(x)$  denotes the  $n^{\text{th}}$  derivative of  $\mathbf{r}$  evaluated at the point  $x$ ), with  $t$  being the time through the CPI of length  $T$ ,  $t \in [-\frac{T}{2}, \frac{T}{2}]$ . With knowledge of the sensor's location,  $\mathbf{q}(t)$  (as in Figure 4.2), and  $\dot{\mathbf{q}}(t)$  giving the slant range vector from the sensor to the object, as well as the slant-range rate, as  $\boldsymbol{\rho}(t) = \mathbf{r}(t) - \mathbf{q}(t)$  and  $\dot{\boldsymbol{\rho}}(t) = \dot{\mathbf{r}}(t) - \dot{\mathbf{q}}(t)$ , a polynomial expression for the slant-range and slant-range rate equations of motion over the CPI is possible:

$$\rho(t) = |\boldsymbol{\rho}(t)| = \left| \sum_{n=0}^{\infty} \frac{\mathbf{r}^{(n)}(0)t^n}{n!} - \mathbf{q}(t) \right| ; \quad (4.10)$$

$$\dot{\rho}(t) = |\dot{\boldsymbol{\rho}}(t)| = \left| \sum_{n=1}^{\infty} \frac{\mathbf{r}^{(n)}(0)t^{n-1}}{(n-1)!} - \dot{\mathbf{q}}(t) \right| . \quad (4.11)$$

These expressions can be extended (or truncated) to arbitrary accuracy.

The directional angles are now calculated as topocentric right ascension and declination, that is right ascension and declination relative to the sensor location, given by  $\alpha$  and  $\delta$ , respectively:

$$\alpha(t) = \tan^{-1} \left( \frac{\rho_{\mathbf{J}}(t)}{\rho_{\mathbf{I}}(t)} \right) ; \quad (4.12)$$

$$\delta(t) = \tan^{-1} \left( \frac{\rho_{\mathbf{K}}(t)}{\sqrt{\rho_{\mathbf{I}}(t)^2 + \rho_{\mathbf{J}}(t)^2}} \right) , \quad (4.13)$$

noting that these expressions depend on the individual elements of  $\boldsymbol{\rho}$  such that  $\boldsymbol{\rho}(t) = [\rho_{\mathbf{I}}(t), \rho_{\mathbf{J}}(t), \rho_{\mathbf{K}}(t)]^T$ .

Using the expressions in this section, it is possible to form a matched filter to the orbital elements themselves, essentially creating  $\chi(e, a, i, \Omega, \omega, \nu)$  at a given epoch (4.3). This enables arbitrarily long CPIs by tracking an orbit throughout the CPI. Additionally, instead of calculating a Taylor Series expression for the

orbital position  $\mathbf{r}(t)$ , and deriving the parameters of interest, it is far more efficient to directly calculate a Taylor Series expression for the parameters of interest. For a sensor at known Cartesian position  $\mathbf{q}$ , with known instantaneous velocity, acceleration and jerk, given by  $\dot{\mathbf{q}}$ ,  $\ddot{\mathbf{q}}$ , and  $\dddot{\mathbf{q}}$ , respectively, and given the slant range vector  $\boldsymbol{\rho} = \mathbf{r} - \mathbf{q}$ , the slant range and its instantaneous derivatives are given by:

$$\rho = |\boldsymbol{\rho}| ; \quad (4.14)$$

$$\dot{\rho} = \frac{\boldsymbol{\rho} \cdot \dot{\boldsymbol{\rho}}}{\rho} ; \quad (4.15)$$

$$\ddot{\rho} = -\frac{(\boldsymbol{\rho} \cdot \dot{\boldsymbol{\rho}})^2}{\rho^3} + \frac{|\dot{\boldsymbol{\rho}}|^2 + \boldsymbol{\rho} \cdot \ddot{\boldsymbol{\rho}}}{\rho} ; \quad (4.16)$$

$$\begin{aligned} \dddot{\rho} = & 3\frac{(\boldsymbol{\rho} \cdot \dot{\boldsymbol{\rho}})^3}{\rho^5} \quad (4.17) \\ & - 3\frac{(\boldsymbol{\rho} \cdot \dot{\boldsymbol{\rho}})(|\dot{\boldsymbol{\rho}}|^2 + \boldsymbol{\rho} \cdot \ddot{\boldsymbol{\rho}})}{\rho^3} \\ & + \frac{3\dot{\boldsymbol{\rho}} \cdot \ddot{\boldsymbol{\rho}} + \boldsymbol{\rho} \cdot \dddot{\boldsymbol{\rho}}}{\rho} , \end{aligned}$$

where  $\dddot{\mathbf{r}}$  is from the derivative of (4.4) and is given by:

$$\dddot{\mathbf{r}} = \frac{3\mu\mathbf{r} \cdot \dot{\mathbf{r}}}{|\mathbf{r}|^5}\mathbf{r} - \frac{\mu}{|\mathbf{r}|^3}\dot{\mathbf{r}} . \quad (4.18)$$

Now, (4.15), (4.16), and (4.17) can be used to directly specify the target's Doppler, chirp rate, and radial jerk. This leads to more efficient expressions (when compared to (4.10) and (4.11)) for the slant-range, and also slant-range rate, throughout the CPI of length  $T$  such that  $t \in [-\frac{T}{2}, \frac{T}{2}]$ :

$$\rho(t) = \rho + \dot{\rho}t + \frac{1}{2}\ddot{\rho}t^2 + \frac{1}{6}\dddot{\rho}t^3 ; \quad (4.19)$$

$$\dot{\rho}(t) = \dot{\rho} + \ddot{\rho}t + \frac{1}{2}\dddot{\rho}t^2 . \quad (4.20)$$

A fourth-order Taylor Series approximation to the slant-range,  $\rho(t)$ , was cho-

sen due to previous work, which demonstrated that a third order polynomial phase signal may be required in order to coherently match orbits for CPIs of duration up to 10 seconds (Hennessy et al., 2019).

Similarly, equivalent approximations can be formed for the angular measurement parameters  $\alpha(t)$  (4.12) and  $\delta(t)$  (4.13).

#### 4.4.1 Search-Volume Constraints

The methods described above enable coherent processing that matches orbital parameters; however, they are not suitable for searching to perform uncued detections. The parameter space is far too large to be practically searched, and the vast majority of orbits will not correspond to passes within a region of interest above the sensor. Although, as stated earlier in Section 4.3.2, alternatives to the Keplerian parameter set are available. In fact, it is possible to parameterise a Keplerian orbit with the Cartesian position and velocity to constitute the six elements (Vallado & McClain, 2001). It is also possible to utilise combinations of both sets of elements in other formulations.

Instead of searching through classical orbital parameters, three parameters can be expressed as a hypothesised ECI position within a search volume of interest. This ensures any hypothesised orbit, determined from these initial parameters, will be within the search volume. Given this potential orbital position,  $\mathbf{r}$ , only three more additional parameters are needed to fully define an elliptical orbit. Although the three elements forming the orbital velocity could be treated as free variables, the majority of possible velocities would not correspond to valid Earth-captured orbits. Instead, given position  $\mathbf{r}$  and semi-major axis  $a$ , the magnitude of the velocity of the corresponding orbit is given by the Vis-Viva equation (Vallado & McClain, 2001):

$$|\dot{\mathbf{r}}|^2 = \mu \left( \frac{2}{|\mathbf{r}|} - \frac{1}{a} \right). \quad (4.21)$$

Furthermore, given position  $\mathbf{r}$  and eccentricity  $e$ , the semi major axis length will itself be constrained between the potential limits of the orbit's apogee and perigee ranges:

$$\frac{|\mathbf{r}|}{1+e} \leq a \leq \frac{|\mathbf{r}|}{1-e}. \quad (4.22)$$

The semi-major axis is also constrained by realistic limits on an orbit's range, as well as a sensor's maximum detection range, represented by minimum and maximum allowable periapsides,  $rp_{min}$  and  $rp_{max}$ :

$$\frac{rp_{min}}{1-e} \leq a \leq \frac{rp_{max}}{1-e}. \quad (4.23)$$

Another constraint is the constant angular momentum of the orbit,  $\mathbf{h}$ . This vector is perpendicular to the orbital plane, parallel to  $\mathbf{W}$ , with a magnitude depending on the size and shape of the ellipse:

$$\mathbf{h} = \sqrt{\mu a(1-e^2)}\mathbf{W} = \mathbf{r} \times \dot{\mathbf{r}}. \quad (4.24)$$

This cross-product may be rewritten to form an expression for the inner product between the position and velocity:

$$\mathbf{r} \cdot \dot{\mathbf{r}} = \pm \sqrt{|\mathbf{r}|^2 |\dot{\mathbf{r}}|^2 - |\mathbf{h}|^2}. \quad (4.25)$$

Combined with the magnitude of the velocity, from the Vis-Viva equation (4.21), as well as the magnitude of the constant angular momentum (4.24), an expression for this inner product can be formed which depends solely on the position  $\mathbf{r}$  and the size and shape of the orbital ellipse:

$$\mathbf{r} \cdot \dot{\mathbf{r}} = \pm \sqrt{|\mathbf{r}|^2 \mu \left( \frac{2}{|\mathbf{r}|} - \frac{1}{a} \right) - \mu a(1-e^2)}. \quad (4.26)$$

Additionally, the specific relative angular momentum vector,  $\mathbf{h}$ , is perpen-

dicular to both the orbital position  $\mathbf{r}$  and orbital velocity  $\dot{\mathbf{r}}$ . This leads to the expressions  $\mathbf{r} \cdot \mathbf{h} = 0$  and  $\dot{\mathbf{r}} \cdot \mathbf{h} = 0$ , which result in another constraint on the velocity, dependant on the right ascension of the ascending node,  $\Omega$ :

$$\begin{bmatrix} r_K \sin \Omega \\ -r_K \cos \Omega \\ r_J \cos \Omega - r_I \sin \Omega \end{bmatrix} \cdot \dot{\mathbf{r}} = 0 . \quad (4.27)$$

These expressions lead to a simple geometric solution for determining orbits when  $\mathbf{r}$  (and other parameters) are known, and  $\dot{\mathbf{r}}$  is unknown. For determining  $\dot{\mathbf{r}}$ , (4.21) defines a sphere of radius  $\sqrt{\mu(\frac{2}{|\mathbf{r}|} - \frac{1}{a})}$ , representing valid orbits in the velocity vector's element space. Additionally, (4.26) defines two parallel planes of valid orbits, which intersect with (4.21) to define two circles. Finally, intersecting these two circles with the plane defined by the position and the right ascension of the ascending node,  $\Omega$ , (4.27) will result in a maximum of four intersection points, that is, four velocities, each corresponding to a valid orbit. An example diagram is shown in Figure 4.3. Although this means that a choice of six orbital parameters will result in up to four potential orbital matched filters, this approach will be far more efficient than methods outlined earlier in this section, as the orbit will be within the search volume, and each parameter choice restricts the range of subsequent parameters.

Therefore, given an orbital position,  $\mathbf{r}$ , a choice of eccentricity,  $e$ , semi-major axis,  $a$ , and right ascension of the ascending node,  $\Omega$ , four potential orbital velocities,  $\dot{\mathbf{r}}$ , are calculated, which leads to an expression for the complete matched filter:

$$\chi(\mathbf{r}, \dot{\mathbf{r}}) = \int_{-\frac{T}{2}}^{\frac{T}{2}} \left[ \sum_{n=1}^N e^{j\mathbf{k}(\delta(\mathbf{r}, \dot{\mathbf{r}}, t), \alpha(\mathbf{r}, \dot{\mathbf{r}}, t)) \cdot \mathbf{u}_n} s_n(t) \right] d^*(t - 2c^{-1}\rho(\mathbf{r}, \dot{\mathbf{r}}, t)) e^{-j\frac{2\pi}{\lambda}\dot{\rho}(\mathbf{r}, \dot{\mathbf{r}}, t)t} dt . \quad (4.28)$$

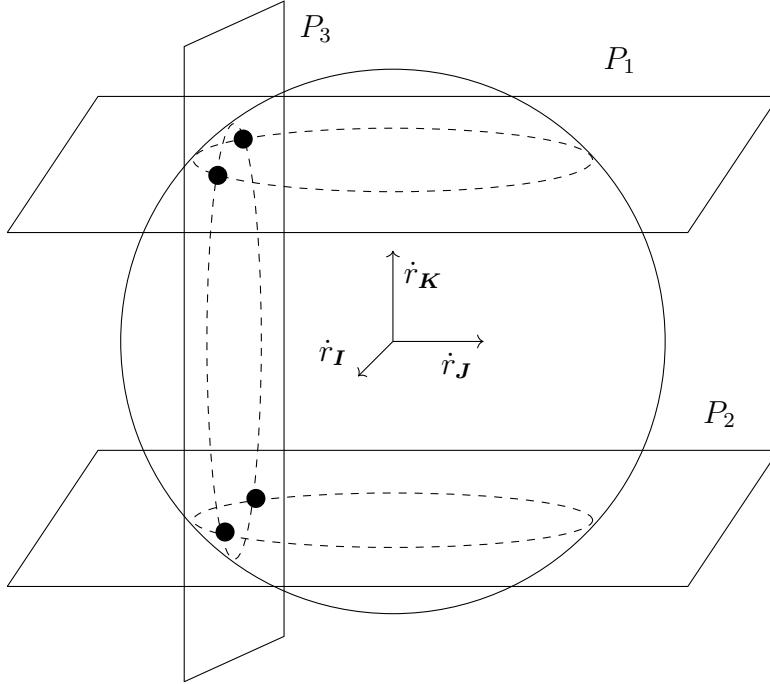


Figure 4.3: Four valid orbital velocities given by the intersection of the sphere (given by (4.21)), parallel planes  $P_1$  and  $P_2$  (given by (4.26)), and plane  $P_3$  (given by (4.27) or (4.29)).

The proposed method tests for only realistic orbits in a given search region. Also, given a set of orbit parameters, this matched filter should maximise a radar's sensitivity to that orbit. Additionally, a detection in this matched filter corresponds to a detection in the orbital element space, providing initial orbit determination from a single detection.

This style of trajectory-match approach, has several advantages beyond just maximising sensitivity to motion models. Coupling measurement parameters together through a trajectory model can improve achievable resolution compared with using separate independent measurement parameters. As an example, a radar's range resolution is determined solely by the signal bandwidth, but its Doppler and Doppler-rate resolution improve with the CPI length. Through coupling the measurement parameters with the trajectory model, as a radar can resolve finer Doppler and Doppler rate measurements it can essentially resolve



finer trajectory states. This can potentially improve target localisation as increasingly accurate state measurements could localise a target within a single range bin.

#### 4.4.2 Zero Doppler Crossing

The flexibility of the geometric formulation in Section 4.4.1 allows radar parameters to be used alongside, and in place of, other orbital parameters to constrain the search space. A Doppler shift  $f_D$  will define another plane in  $\dot{\mathbf{r}}$  space, given by:

$$\frac{\boldsymbol{\rho}}{\rho} \cdot \dot{\mathbf{r}} = -\frac{\lambda f_D}{2} + \frac{\boldsymbol{\rho} \cdot \dot{\mathbf{q}}}{\rho} . \quad (4.29)$$

Equation (4.29) can be used to search for a particular Doppler shift instead of one of the orbital parameters. This is useful because it allows a blind search to constrain the search-space solely for objects in orbit at their point of closest approach to the sensor. As an object is passing overhead, its point of closest approach will correspond exactly with it being at zero Doppler, which is when it is most detectable<sup>4</sup>. If a radar is unable to detect an object at its point of closest approach, at its minimum range, there is little value trying to detect it as it moves further away, towards the horizon.

Another benefit to applying this constraint is that, as Doppler is proportional to the range-rate, this constraint will also restrict the orbit search-space to a point of minimal (or zero) range migration, which greatly simplifies matched-processing<sup>5</sup>.

The vast majority of the objects in an Earth-captured orbit are in a circular, or near-circular, orbit. Searching solely for objects in a circular orbit greatly decreases the potential orbital search space. A circular orbit means the eccentricity of the orbital ellipse is zero,  $e = 0$ , and so (4.22) becomes  $a = |\mathbf{r}|$ . In a circular orbit, the position and velocity vectors will always be perpendicular, so (4.26)

---

<sup>4</sup>This may not necessarily hold in all instances, depending on particular beampattern and radar cross section factors.

<sup>5</sup>Depending on the CPI length, it may be possible to make  $\rho(t) \approx \rho$ .

simplifies to  $\mathbf{r} \cdot \dot{\mathbf{r}} = 0$ , a single plane instead of two parallel planes. The result is that a three-parameter search, within a region of interest, provides sufficient information to match the closest approach of objects in a circular orbit. For a given position in a search-region, there will be at most two possible orbits to match against (determined from the intersection of (4.21), (4.26), and (4.29)). This type of search approach, attempting uncued detection of the most common types of orbit when they are most detectable, is a far more realisable and practical approach than a completely unbounded search through measurement parameters. Additionally, for an eccentric orbit, the orbital velocity and position are perpendicular at perigee (Vallado & McClain, 2001). For typical radar detection ranges, an object in a highly eccentric orbit is likely to be within a radar’s field of regard solely at, or near, perigee. Because of this, the same simplification of  $\mathbf{r} \cdot \dot{\mathbf{r}} = 0$  could be used to reduce the number of potential orbits.

### 4.4.3 Single Channel Orbit Detection

Coupling together measurement parameters is not necessarily new; however, incorporating such techniques into the detection stage offers some significant advantages. By coupling together the measurement parameters using these ODBD methods, it is possible to apply this matched filtering to single beam radar systems. This could be a post-beamformed surveillance signal from an array or even a classic narrowbeam tracking radar. Because the trajectory model determines all measurement parameters, a particular polynomial phase signal which results in a detection is coupled to a particular location and orbit. This is shown in (4.28). The beamforming parameters do not determine the location; rather the (hypothesised) location determines the beamforming parameters. Removing the array processing, as in (4.30), does not remove the ability to localise a target using the algorithm.

$$\chi(\mathbf{r}, \dot{\mathbf{r}}) = \int_{-\frac{T}{2}}^{\frac{T}{2}} s(t) d^*(t - 2c^{-1}\rho(\mathbf{r}, \dot{\mathbf{r}}, t)) e^{-j\frac{2\pi}{\lambda}\dot{\rho}(\mathbf{r}, \dot{\mathbf{r}}, t)t} dt \quad (4.30)$$

In the case of a narrow beam radar, the pointing of the beam will be incorporated into the algorithm by determining the search region that is used. Because it handles sensor motion, this type of processing would be ideal for a satellite-based sensor, with the sensor location term  $\mathbf{q}(t)$  (or its instantaneous components  $\mathbf{q}, \dot{\mathbf{q}}, \ddot{\mathbf{q}}$ , etc.) themselves determined by a known orbit rather than the motion of the Earth.

## 4.5 Simulated Results

These methods have been verified by comparing ODBD-derived measurement parameters, described in section 4.4, of an object in orbit, against measurement parameters propagated from available ephemerides. These ephemeris tracks consist of the six Keplerian orbital elements, as well as several additional parameters describing drag and orbital decay. These tracks are propagated with the standard SGP-4 propagator used by the USSPACECOM two-line element sets (USSPACECOM, 2023).

The configuration used for these simulations, matching (Hennessy et al., 2019), is a sensor located at the MWA (at a latitude of 27° south) in a bistatic configuration with a transmitter in Perth, approximately 600 km further south. This transmitter is taken to be transmitting an FM radio signal at a centre frequency of 100 MHz.

Figure 4.4 shows the path of an object in a near circular orbit at closest approach. The simulated measurement parameters match very well in both angular and delay-Doppler space despite being based on a perfectly circular orbit. Likewise, Figure 4.5 also matches with the prediction, noting that the simulation used

the matching eccentricity and semi-major axis.

Figure 4.6 shows the path of an object in a near circular orbit, but slightly more eccentric than Figure 4.4 ( $e = 0.00126$ ) at point of closest approach. The simulated circular path matches well in the delay-Doppler space but diverges in the angular space. Additionally, several other simulated close eccentricities are shown, resulting in changes to the direction of travel but little difference in the delay-Doppler space. The delay-Doppler results suggest good tolerance to small eccentricity changes, however the sensor’s angular resolution may limit potential processing intervals.

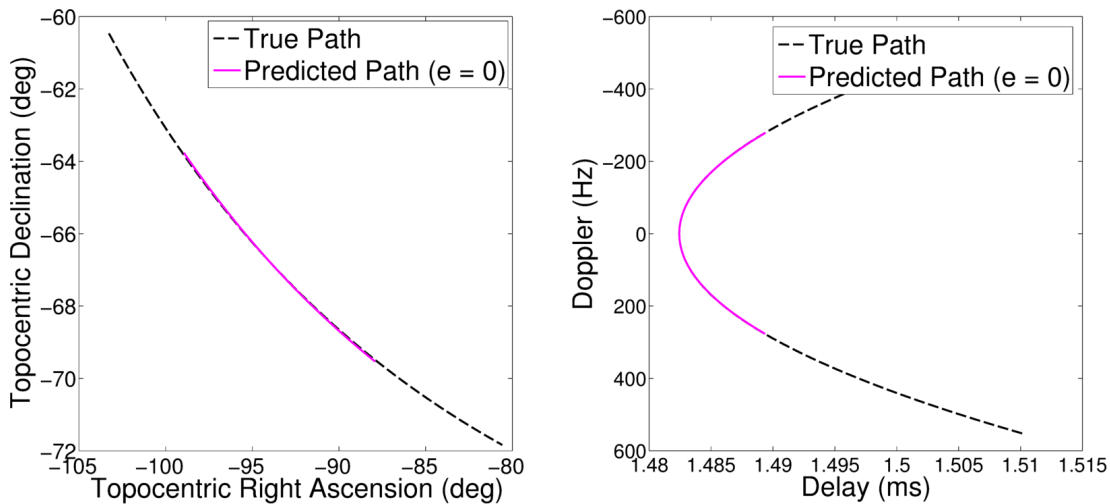


Figure 4.4: The measurement parameters of a close pass of an object in a near-circular orbit ( $e = 0.0007$ ), as well as the simulation made assuming zero eccentricity at point of closest approach. The left plot is angular space and the right is the delay-Doppler. Twenty seconds of the true pass is shown with ten seconds of the simulated path overlaid.

The good agreement between the parameters derived from methods described in this paper, when compared with ephemeris derived parameters, suggests that earlier results, (Hennessy et al., 2019), can be practically achieved without requiring a priori information.

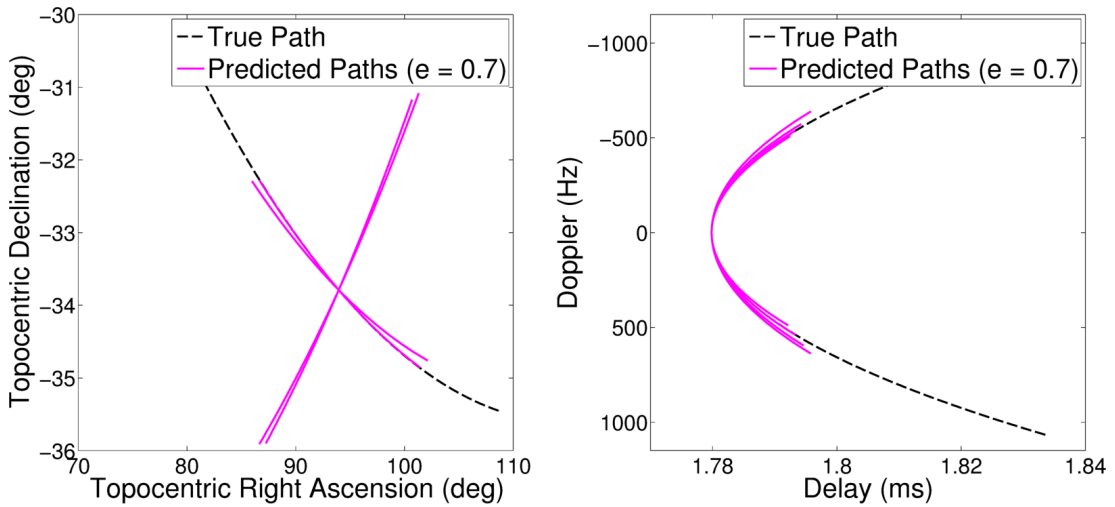


Figure 4.5: The measurement parameters of a close pass of an object in an eccentric orbit ( $e = 0.7$ ), as well as the four simulations made with the correct eccentricity and semi-major axis. The left plot is angular space and the right is the delay-Doppler. Twenty seconds of the true pass is shown with ten seconds of the simulated paths overlaid.

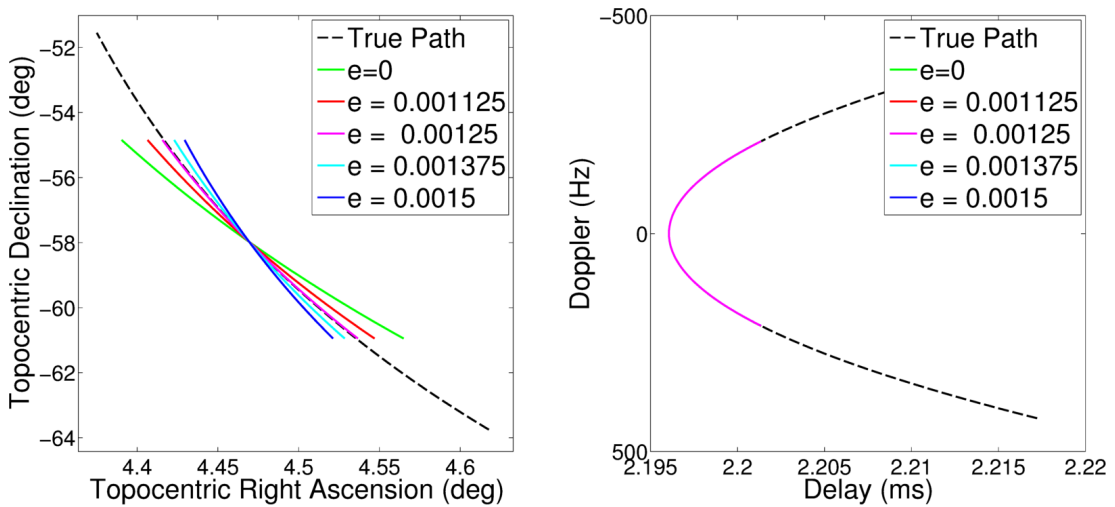


Figure 4.6: The measurement parameters of a close pass of an object in a near-circular orbit ( $e = 0.00126$ ), as well as several simulations made using different eccentricities. The left plot is angular space and the right is the delay-Doppler. Twenty seconds of the true pass is shown with ten seconds of the simulated paths overlaid.

## 4.6 Conclusion

Modern radars are able to form matched-filter products with significant numbers of measurement parameters, especially with digital beamforming and extended processing intervals. Conversely, the motion of an object in a Keplerian orbit is defined by only six parameters. Mapping radar measurement parameters from orbital motion parameters constrains the search space for uncued detection, it additionally allows for other constraints to be applied to further reduce the search-space, most notably when searching for objects in a circular orbit at their point of closest approach to the sensor. For a hypothesised orbit of this type, all range, Doppler, and angular motion parameters can be derived entirely from a three-dimensional position. Detections from this matched filter will correspond to the hypothesised orbit. This means that initial orbit determination can be potentially achieved from a single radar detection.

In future work, these algorithms will be experimentally validated with MWA observations. Noting that although these methods have been developed for the MWA, these methods also apply to conventional active space surveillance radar or even to satellite-based sensors. Additionally, it is planned to investigate the sensitivity of these techniques, characterising their variance by calculating the Cramér-Rao lower bound (CRLB) on the variance of the initial orbital estimates.

## 4.A Signal Processing Computational Characteristics

This appendix discusses the signal processing computational aspects of the methods discussed in this chapter and used throughout this thesis. The intent is to bridge a gap between Section 2.4.2, which discusses the computational requirements in terms of number of parameter spaces, and Section 6.2 which discusses computational requirements in terms of the number of orbits to be matched. Here,

the orbital search space methods for initial orbit determination, which are first described in this chapter and then implemented and demonstrated in Chapter 5, are detailed in terms of signal processing requirements.

There are many actions a radar needs to perform each CPI, however, a simple way to describe a radar's computational requirements is to say the number of computational operations a radar performs each CPI is proportional to the number of pulse integration stages multiplied by the length of each pulse integration step. That is, essentially the number of Fourier Transforms (FTs) multiplied by the length of each FT. A standard approach would be to form a number of surveillance beam to cover a region of interest, and for each beam, form a delay Doppler map of sufficient range to cover a volume of interest. Then, for each beam, and for each range bin, perform a single pulse-integrating FT to cover a velocity-extent of interest. There are alternative approaches to reduce computational load, such as forming a delay-Doppler map for each receive channel and beamforming on these (as detailed in Section 2.4.1), however these approaches are not easily applicable to space surveillance systems because of the need to match Doppler-rate and other higher order parameters prior to pulse integration.

A simple LEO space surveillance mission can hypothesised to further detail the processing requirements. A region of interest may be described by, say, a  $20^\circ \times 20^\circ$  area of the sky, with a range extent of 1000 km, and a velocity range of interest spanning  $\pm 5000$  m/s. The number of pulse integration FTs can be expressed in terms of these mission requirements, along with a radar's angular resolution  $\Delta\theta$  and the range resolution, which depends on the bandwidth  $f_b$ . The size of each FT can be expressed in terms of the mission requirements and the CPI length  $T$ , along with the radar's operating frequency  $f_c$ . The combination of all these space surveillance requirements, along with radar's parameters, allows us to form an expression for the number of operations required to form a beam in every direction of interest and then form a pulse stack large enough for the range extent and the velocity extent. This number is given by the number of beams

times the number of range bins times the size of the FT:

$$\left(\frac{20}{\Delta\theta}\right)^2 \times \frac{1000f_b}{2c} \times 2\frac{5000f_cT}{c}, \quad (4.31)$$

with  $c$  being the speed of light.

An MWA-like radar can be said to operate at a frequency of 100 MHz, a bandwidth of 100 kHz, a CPI of 3 s and an angular resolution of  $0.1^\circ$ . Such a system would need to form 40,000 beams, the range resolution would be 1500 m and the Doppler resolution would be  $\frac{1}{3}$  Hz. The number of operations required to form a sufficiently large delay-Doppler map in every region of interest is proportional to the result of (4.31), which is approximately  $6.68 \times 10^7$ .

Such a system would not be able to detect satellites and other fast-moving objects as there is no processing for mitigating the extreme motion of satellites. The metric of  $6.68 \times 10^7$  would in reality need to be multiplied by the number of acceleration hypotheses, the number of acceleration-rate hypotheses as well as the number of spatial-rate and spatial-acceleration hypotheses as given by (2.14). However the metric of  $6.68 \times 10^7$  is a useful one as it represents a standard radar approach to the large surveillance volume (including large velocity extent) required.

For space objects, the large number of acceleration, jerk, and spatial hypotheses are not necessary, as most parameter sets will not correspond to a valid LEO. Instead, these radar measurement parameters can be derived from the orbital parameters of interest, a smaller dimension parameter space. A full search would instead only require further searching through a number of eccentricity hypotheses  $N_e$ , a number of semi major axis hypotheses  $N_a$  and number of orbital plane orientation hypotheses  $N_\nu$ . These numbers are not easy to estimate, as the ‘resolution’ of these parameters vary depending on the specific value of the other parameters. Additionally, the eccentricity and semi-major axis search spaces are bounded, the potential span of these values changes depending on other parameters as well, as outlined in Section 5.4.5. However, the number of operations



required for a full orbital search is proportional to every three-dimensional point in the search space (given by the number of beams times the number of range bins), for every point there are three more orbital parameters, and for each orbit a large pulse integration step. The final number is approximately  $6.68 \times 10^7 N_e N_a N_\nu$ .

The first step that reduce this search space, is to only consider circular orbits. By only matching circularly orbits we reduce this six dimensional search space to four parameters, with  $N_e = N_a = 1$ , the only other remaining parameter is  $N_\nu$ . This orbital plane parameter now represents the azimuthal direction of travel of the object.

Another step to reduce this search space is to only consider objects at their point of closest approach, as this represents a point objects are likely to be most detectable. This constraint has two impacts on the number of operations on the search space. First, it significantly reduces the number of potential orbits, for a given point of interest there are only two possible orbits, secondly, it also reduces the size of the pulse integration stage as now it is only required to match for an object near zero Doppler. If now say we are interested in velocities between  $\pm 50$  m/s then the number of operations required to detect an object in a circular orbit near its point of closest approach is given by:

$$\left(\frac{20}{\Delta\theta}\right)^2 \times \frac{1000f_b}{2c} \times 2 \frac{50f_c T}{c} \times 2 . \quad (4.32)$$

That is, the number of computational operations are proportional to the number of beams, the number of range bins, the two orbital hypotheses and the much smaller pulse integration stage. For the MWA-like numbers used above the result is approximately  $1.34 \times 10^6$ . Not only is this an order of magnitude smaller than the number of operations required to form a standard radar's coverage, it is many orders of magnitude smaller than the operations required for a full orbital search of the surveillance volume.



# Chapter 5

## Uncued Detection and Initial Orbit Determination from Short Observations with the Murchison Widefield Array

Having developed techniques to attempt initial orbit determination, data can be collected with new observation modes in order to verify these new uncued approaches (comparing with other traditional methods) as well as detecting smaller objects. Similar to previous chapters, this chapter is reproduced from the author's publication (Hennessy et al., 2021), albeit with the removal of some aspects of the introductory sections, which were incorporated into Chapter 2.

### 5.1 Abstract

This paper details the latest developments in the use of the Murchison Widefield Array as a passive radar receiver for the surveillance of space. We cover methods developed to incorporate orbital parameters into matched-filter processing to achieve uncued detection without a prior track, and generate accurate

detection-level initial orbit estimates. We present the results from a short collection campaign conducting broad surveillance stares, using FM transmitters as an illuminator with a significantly large bistatic baseline length of 600 km. Initial results demonstrate improved performance in the Murchison Widefield Array’s detection of objects in typical low-Earth orbital regimes, detecting objects with a radar cross section of  $1 \text{ m}^2$ , as well as the generation of accurate initial orbital estimates using very short arc detections spanning less than half a degree.

## 5.2 Signal Processing for Initial Orbit Determination

### 5.2.1 Space Surveillance Application

Many aspects of standard delay-Doppler map formation are poorly suited to the detection of objects in LEO. The large orbital velocity leads to rapidly changing bistatic geometry, which results in a target which is not stationary in any measurement space during the measurement period. Untreated range-walk, Doppler-walk, and angular-walk will severely limit the potential integration time. Some of these issues can be addressed independently. For example, the Keystone Transform removes all range-walk due to linear range migration (Perry et al., 1999). However, Doppler and angular-walk can only be mitigated with a specific motion hypothesis.

Rather than being a simple Doppler *shift* (as in (2.1) and (2.4)), orbital motion imparts a time-varying phase adjustment on the reflected signal. This phase adjustment varies across the CPI due to the rapidly changing bistatic geometry. For extended processing intervals, this varying phase signal needs to be accurately matched in order to ensure sensitivity is increased along with the processing interval.

These phase matching methods have been used for extended CPI lengths in

previous work in order to detect objects in orbit (Hennessy et al., 2019). The Doppler shift throughout the CPI is modelled by a polynomial phase signal with coefficients determined by the instantaneous velocity, acceleration, and subsequent rates. As Doppler is proportional to radial velocity, the Doppler rate is proportional to radial acceleration and the Doppler acceleration is proportional to the radial jerk (Borowiec & Malanowski, 2016). That is, rather than forming a matched filter to a constant radial-velocity, products of a larger dimension can be formed instead (Kelly, 1961; Stein, 1981). To extend a delay-Doppler map to match Doppler-rate and Doppler-acceleration, a four dimensional matched filter is required, e.g.  $\chi[\tau, f_D, \dot{f}_D, \ddot{f}_D]$  (Hennessy et al., 2019).

Finally, angular migration is particularly pernicious. Similar to range and Doppler walk, angular migration results in reduced sensitivity due to the target smearing across angular bins, determined by the sensor’s angular resolution. However, there is an additional impact. Unaccounted phase variations, which are not matched by beamforming, will result in a slow-time frequency shift of the signal. These time-varying phase residuals will be perceived as an antenna-dependant Doppler shift. This will, at best, result in an overall Doppler error for a detected target, or at worst, smear the target such that it is not detected. Unaccounted higher-order phase variations will also have a similar impact on higher-order Doppler measurements. To overcome this, the wavevector in (2.5) will need to be updated to follow any potential targets throughout the CPI. Much like the extra Doppler dimensions above, these issues can be mitigated by adding extra search dimensions to the beamforming space. Rather than forming delay-Doppler products at a fixed direction, the signal wavevector expression (2.5) can be extended to incorporate directional rates and directional accelerations. However, this will extend a two-dimensional azimuth and elevation search space to a four, or six, dimensional spatial search space. In fact, a 10 dimensional search space would be needed in order to achieve the same sensitivity as previously published results, which utilised the known track (Hennessy et al., 2019).

## 5.2.2 Compressed Pulse Cube formation

Matching these additional measurement parameters requires a shift in processing strategy. In order to match spatial and Doppler rates, these parameters need to be included in the processing prior to the Doppler-resolving Fourier Transform in (2.4). Instead of forming delay-Doppler maps for each antenna, this rapidly changing bistatic geometry requires processing with individual pulse stacks at each antenna. Instantaneous Doppler and signal-wavevector phase adjustments are now applied on a pulse-by-pulse basis, with the phase adjustments determined by the hypothesised spatial and Doppler rates.

Fig. 5.1 is an illustration of the processing strategy. To implement the sub-CPI beamforming, the phase of a given delay cell of interest is updated for each pulse to spatially track the time varying wavevector. Once a single range-compressed pulse stack has been formed to match a specified direction and directional rates, the higher order phase terms can be adjusted to allow the Doppler-resolving Fourier transform to best match the radial velocity. That is, a polynomial phase adjustment is applied to remove the effect introduced by the target's Doppler rates (due to radial bistatic acceleration, jerk, and higher order motions) leaving only the linear phase adjustment caused by the target's Doppler. This is then resolved with the Fourier Transform resulting in a delay-Doppler map specifically matched to a given direction, directional rates, and Doppler profile.

Note that it is possible to form such a delay-Doppler map by applying the sub-CPI beamforming and Doppler rates to entire pulses, rather than a single delay bin as in Fig. 5.1. However, this is not done in practice because there is an intrinsic coupling between all parameters. A target's hypothesised Doppler and spatial profile will determine (at least in part) its potential valid ranges. Combinations of individually realistic measurement parameters in range, Doppler and direction may not be physically realisable. Instead, only a subset of potential combinations will correspond to a physically-possible target motion, and only a subset of these will correspond to a realistic orbital motion. Fig. 5.1 highlights

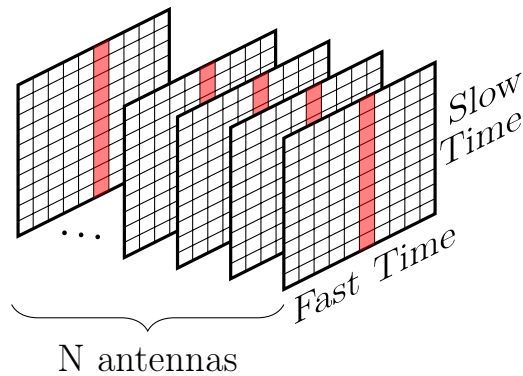


Figure 5.1: An illustration of the processing strategy, for a delay cell of interest the phase is adjusted for each antenna every slow-time pulse.

only one delay cell, because for a given delay only correspondingly valid Doppler, and directional parameters are required to form the resulting delay-Doppler map. This coupling between measurement parameters and target motion is covered in more detail in the next section. It is also a focus of the planned signal processing approach for the GESTRA space surveillance radar (Wilden et al., 2019).

### 5.2.3 Orbit Determination Before Detect

As outlined in Section 5.2.1, radar products need to be formed in larger measurement dimensions to detect objects in orbit. This has been demonstrated previously utilising a priori information to track orbital objects throughout the CPI (by adjusting the beamforming for each compressed pulse) and then searching in Doppler-rate and Doppler-acceleration (Hennessy et al., 2019). This is effective for the detection of space objects because although the velocity is significant, and the rate at which the geometry changes is significant, the trajectory itself is stable and predictable. This is a common approach used by other space surveillance radars, particularly incorporating Doppler-rate, or chirp, adjustments to match radial acceleration (Vierinen et al., 2019; Holdsworth et al., 2020).

However, previous results with the MWA searching through these Doppler-rates were all based on a priori information to determine the beamforming. De-

spite using truth information for the beamforming, these detections still required a search in delay, Doppler, Doppler-rate, and Doppler-acceleration to form detections. Naively extending these methods for uncued searching would be problematic, with the four-dimensional search space needing to be extended significantly to search in directional and directional rate parameters.

Instead of forming a matched filter from a significant number of measurement search parameters, it is possible to limit the search space to realistic trajectories. As detailed in earlier work (Hennessy et al., 2020), this Orbit Determination before Detect (ODBD) approach can be achieved by searching through hypothesised target position and velocity and then deriving the measurement parameters. In this way, the search space is limited in dimension, and the measurement space can be completely unconstrained.

This type of approach is well suited to space surveillance as orbital trajectories have very defined and predictable motions, and are generally not manoeuvring. In fact, the simplest form of an orbit is a two-body, or *Keplerian*, orbit which is completely determined by only six parameters. This treats the Earth and the object of interest as point masses, and assumes gravity is the only force, with the acceleration experienced given by the object's position,  $\mathbf{r}$  and the standard gravitational parameter for Earth,  $\mu$ :

$$\ddot{\mathbf{r}} = -\frac{\mu}{|\mathbf{r}|^3}\mathbf{r}, \quad (5.1)$$

From this, given a cartesian position  $\mathbf{r}$  and velocity  $\dot{\mathbf{r}}$  an object's trajectory can be determined for all time. With a Keplerian system, orbits form conics with one focal point being at the (gravitational) centre of the Earth; however, in this work we are only interested in elliptical orbits. It should be noted that the orbits are only elliptical in the Earth-Centered Inertial (ECI) coordinate frame. The ECI coordinate system has an origin at the centre of the Earth, however the coordinate system does not rotate with the Earth. A six-tuple position and velocity will sufficiently define an orbit for all time.



Because there is no closed-form solution to Kepler's equation, numerical methods must be used to calculate the parameters of interest over the CPI. We use Taylor series approximations for the measurement parameters of interest - Doppler and its subsequent rates as well as the directions and their subsequent rates. Essentially, this determines the motion-induced polynomial phase signal coefficients from the position, velocity, equation (5.1), and its instantaneous derivatives. (2.3) can be rewritten as:

$$f_D = -\frac{1}{\lambda} \left( \frac{\boldsymbol{\rho}_{rx} \cdot \dot{\boldsymbol{\rho}}_{rx}}{\rho_{rx}} + \frac{\boldsymbol{\rho}_{tx} \cdot \dot{\boldsymbol{\rho}}_{tx}}{\rho_{tx}} \right) \quad (5.2)$$

with expressions for  $\dot{f}_D$ ,  $\ddot{f}_D$ , and any number of subsequent derivatives of the Doppler frequency easily determined in a similar manner. Likewise, the expression for the topocentric right-ascension and declination,  $\alpha$  and  $\delta$  respectively, are derived from the ECI coordinate frame. These are the directional parameters used in place of azimuth and elevation, and are determined from the slant-range vector from the target to the receiver  $\boldsymbol{\rho}_{rx} = \mathbf{r} - \mathbf{r}_{rx} = [\rho_{rx_X}, \rho_{rx_Y}, \rho_{rx_Z}]^T$ .

$$\alpha = \tan^{-1} \left( \frac{\rho_{rx_Y}}{\rho_{rx_X}} \right) \quad (5.3)$$

$$\delta = \tan^{-1} \left( \frac{\rho_{rx_Z}}{\sqrt{\rho_{rx_X}^2 + \rho_{rx_Y}^2}} \right) \quad (5.4)$$

Although (5.1) is specific to Keplerian orbital trajectories, any motion model could be applied to determine the measurement parameters; taking  $\ddot{\mathbf{r}} = 0$  would result in matching linear velocity.

## 5.2.4 Constrained Search Space

The work in the previous section (Section 5.2.3) limits the search space for uncued detection to the six parameters required to define the orbit, the initial position, and velocity. This enables searches to be limited to only the sets of measurement

parameters corresponding to orbits of realistic Earth-captured Keplerian orbits. This is still a significant search space. Not only is it six dimensional, a given cartesian position will still leave three slack variables in the velocity vector. However, for a given position it is possible to further restrict the extent of potential orbital velocities.

A method to significantly constrain this search is to limit the search to solely match circular orbits. This ensures that any resulting orbit will be realistic, it drastically limits the potential range of resulting velocities, and most importantly it will not be overly restrictive. The vast majority of objects in an Earth-captured orbit are in circular, or near-circular, orbits. This is especially true away from the equator.

The circular orbit assumption is implemented by the Vis-Viva equation (with orbit eccentricity set to zero) in (5.5) and also noting that the orbital position and velocity must be perpendicular, (5.6) (Vallado & McClain, 2001).

$$|\dot{\mathbf{r}}|^2 = \frac{\mu}{|\mathbf{r}|} \quad (5.5)$$

$$\mathbf{r} \cdot \dot{\mathbf{r}} = 0 \quad (5.6)$$

For a given position, (5.5) and (5.6) leave only one slack variable, as (5.5) limits the magnitude of any velocity and (5.6) defines the plane it lies on. Only one variable is needed to define the direction of the orbital velocity on this plane.

A final constraint which can be placed upon the orbital velocity is limiting the search space to only those orbits with favourable geometry for uncued detection. This is achieved by defining the velocity to correspond to an object at its point of closest bistatic approach to the MWA. An object will be most detectable at minimum range, as long as there are no mitigating factors such as unfavourable bistatic radar cross section (RCS) or transmitter beampattern. This is achieved

by expressing (5.2) in terms of the orbital velocity:

$$\left( \frac{\rho_{rx}}{\rho_{rx}} + \frac{\rho_{tx}}{\rho_{tx}} \right) \cdot \dot{\mathbf{r}} = -\lambda f_D + \frac{\rho_{rx} \cdot \dot{\mathbf{r}}_{rx}}{\rho_{rx}} + \frac{\rho_{tx} \cdot \dot{\mathbf{r}}_{tx}}{\rho_{tx}} \quad (5.7)$$

Choosing an (instantaneous) bistatic Doppler shift of  $f_D = 0$  in (5.7), and solving for orbital velocity with (5.5) and (5.6), will ensure that the orbit for object at position  $\mathbf{r}$  will be circular and at minimum range.

The result is that for an uncued search only the three parameters, the cartesian position, are needed to determine every measurement parameter necessary to form matched radar products in order to detect an orbital object at this position. This allows effective processing limited to a surveillance volume of interest.

It should be noted that there are two solutions to the intersections of (5.5), (5.6) and (5.7), necessitating two matched filters per cartesian position; however, this is still a significant improvement in limiting the scope of a blind search.

### 5.3 Initial Orbit Determination

Orbit determination is traditionally performed with a preliminary, or initial, orbit determination step which is then refined with subsequent measurements, often in a batch process (Montenbruck et al., 2002). That is, a number of detections are used to perform an IOD step to provide an initial orbit, then this initial orbit is used with the remaining detections to perform the OD step. This form of splitting up the IOD and OD steps is useful as many space surveillance sensors, such as narrowbeam or optical sensors, are not able to natively perform the IOD stage and rely on an a priori track to update and refine. With radar measurements, the most common IOD steps are the Gibbs and Herrick-Gibbs methods (Section 5.3.1 below).

Recently, there has been interest in harmonising the IOD and OD use of measurements into a single step, through the use of admissible regions. Rather than arbitrarily using some measurements for the IOD step and others for the OD

refinement phase, instead a radar measurement will define a region of potential orbits to which the detection could correspond, which is refined with subsequent measurements. Individual radar detections consisting of a single measurement of range, Doppler, azimuth, and elevation, define a broad region of potential orbital parameters (Tommei et al., 2007). This region may be constrained by incorporating angular rates (DeMars & Jah, 2014). In this approach, the OD step is completely unified with every measurement incorporated identically, as a single radar detection does not consist of enough information to define an orbit.

However, the classic approach of using an IOD step to generate an initial orbit, which is used for follow on tracking, is well suited for processing with the MWA. From Section 5.2.1 earlier, the measurement parameter space goes well beyond traditional radar systems, and so it is not feasible to provide uncued detections in measurement space from which to define an admissible region. Further, a detection consisting of so many additional measurement parameters would go a long way to defining an orbit. Instead, if the uncued search methods are employed and are able to provide enough information to form an initial orbital estimate, the standard track methods (normally used with a priori information) may be sufficient to detect the object, and to confirm the orbit to a sufficient quality (Section 5.2.4). Detections of the type outlined in Section 5.2.4 will naturally be very short arcs, as they are specifically matched to a single Doppler value and the relative velocity will be changing rapidly.

### 5.3.1 Gibbs/Herrick-Gibbs

The Gibbs and Herrick-Gibbs methods are two methods to define an orbit, a six-tuple position and velocity, given three position measurements. From three successive positions  $\mathbf{r}_1$ ,  $\mathbf{r}_2$  and  $\mathbf{r}_3$  the Gibbs method determines the velocity, and so an orbit, at the middle measurement  $\dot{\mathbf{r}}_2$ . The Gibbs method needs at least  $5^\circ$  separation (in the orbital plane) between detections (Vallado & McClain, 2001). An object would need to be tracked for a considerable amount of time in order to

have detections spanning a  $5^\circ$  arc, for a typical object in LEO, this would exceed one minute. For uncued detections, with the MWA, shorter arc IOD is necessary.

The Herrick-Gibbs method is an approximation of the Gibbs method, which is far better suited to short-arc measurements. The Herrick-Gibbs method further incorporates the time of each of the measurements to better estimate the velocity  $\dot{\mathbf{r}}_2$ . If  $t_1$ ,  $t_2$ , and  $t_3$  are the times of position measurements  $\mathbf{r}_1$ ,  $\mathbf{r}_2$  and  $\mathbf{r}_3$  respectively, and if  $t_{ij}$  denotes the time between measurements  $i$  and  $j$  such that  $t_{ij} = t_i - t_j$ , then the velocity at the middle point is given by:

$$\begin{aligned} \dot{\mathbf{r}}_2 = & -t_{32}\left(\frac{1}{t_{21}t_{31}} + \frac{\mu}{12|\mathbf{r}_1|^3}\right)\mathbf{r}_1 + \\ & (t_{32} - t_{21})\left(\frac{1}{t_{21}t_{32}} + \frac{\mu}{12|\mathbf{r}_2|^3}\right)\mathbf{r}_2 + \\ & t_{21}\left(\frac{1}{t_{32}t_{31}} + \frac{\mu}{12|\mathbf{r}_3|^3}\right)\mathbf{r}_3 \end{aligned} \quad (5.8)$$

with  $\mathbf{r}_2$  and  $\dot{\mathbf{r}}_2$  now constituting a six-tuple Keplerian orbit estimate. The three position vectors need to be coplanar for the Gibbs and Herrick-Gibbs methods to provide an accurate estimate.

### 5.3.2 Direct Detection IOD

As discussed earlier, the simplest form of an orbit is completely defined by six parameters (and an epoch) meaning that technically only six measurement parameters are required to generate an orbit. Given a detection consisting of an azimuth, elevation, and a range (determining the orbital position) and Doppler, Doppler-rate, and Doppler-acceleration it is analytically possible to determine an orbital velocity (Zhang et al., 2019). However, the accuracy of this orbit would be tremendously dependent on a radar's ability to measure the subsequent Doppler-rates.

### 5.3.3 ODBD IOD

As well as Doppler and its rates, it is anticipated that by adding further measurement parameters, particularly the spatial parameters, detections from the MWA will contain enough information to determine an orbit. This is naturally incorporated into the methods outlined in Section 5.2.3. By hypothesising an orbit to determine the measurement parameters, any subsequent detection generated from these parameters would intrinsically be associated with the hypothesised orbit. Because of the narrow beamwidths and the extended CPI lengths, any ODBD-like detection will require the array to track the object spatially (and in Doppler) throughout the CPI. Any detection will then be associated with the implicit knowledge that the detection has been *tracked*, which provides a level of confidence in the orbit used to define the track.

## 5.4 Results

To evaluate and verify these methods, the MWA conducted broad surveillance stares tuned to FM radio frequencies. Results in this section are formed utilising a single FM station transmitting from Perth, some 600 km to the South. This constitutes a significant bistatic baseline length. For these observations, the MWA was in the compact configuration of Phase II (Wayth et al., 2018).

The compact configuration is best suited for LEO space surveillance as some of the baselines in the extended configuration are so long that orbital ranges are not actually in the far-field of the array. Also, the larger beamwidths of the compact configuration ensure the angular search space is not overly restrictive. It should be noted that even in the compact configuration, at FM frequencies the array is still considerably sparse. As shown in Fig. 5.2, the distinct feature of the compact configuration is its two dense hexagonal cores. These identical baselines are favourable for the EoR power spectrum experiment, however, they do introduce significant grating lobes (Wayth et al., 2018). Although it is possible

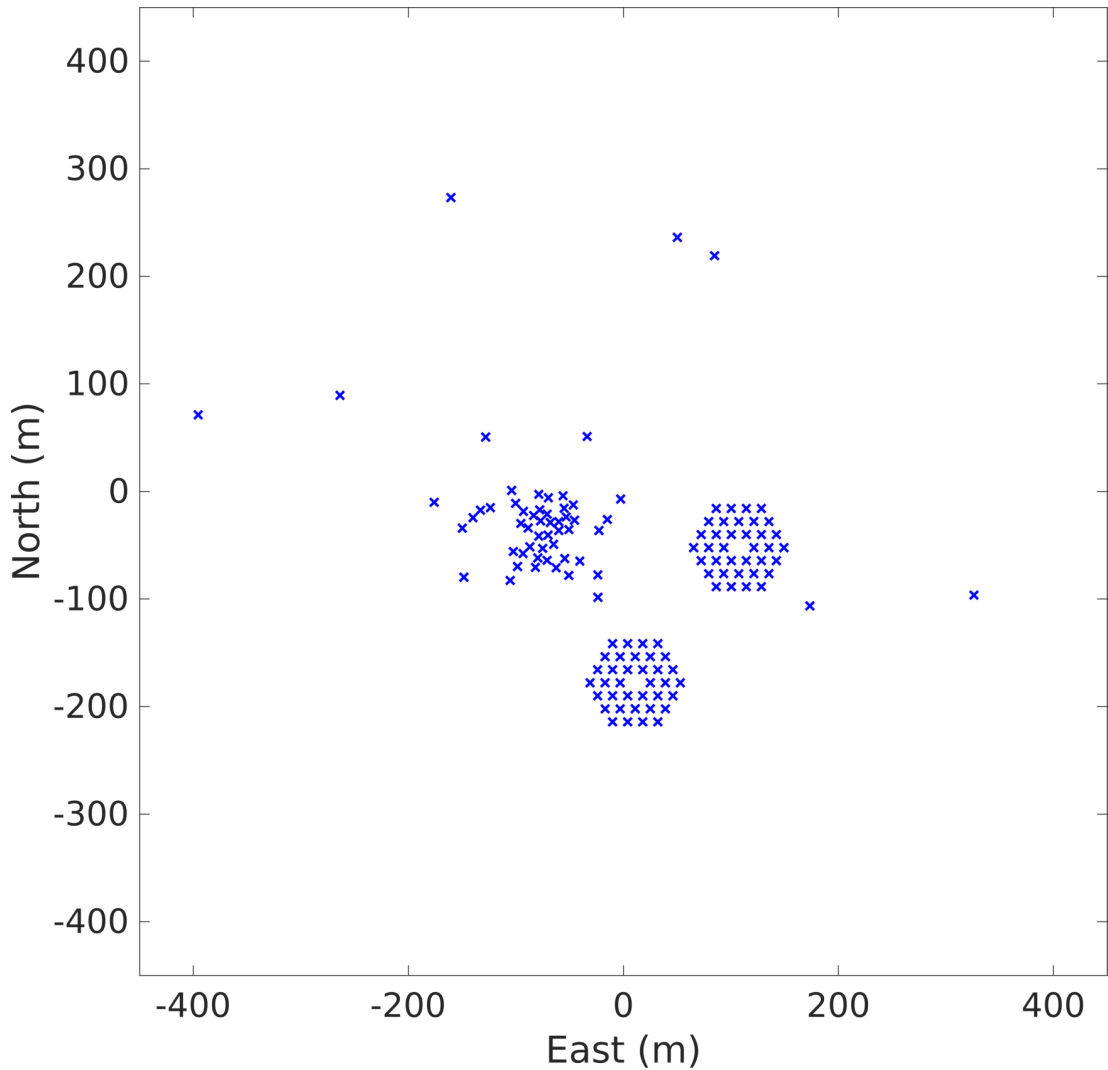


Figure 5.2: The layout of MWA the compact configuration of Phase II.

to apply a weighting to the array returns in order to reduce the grating lobes, this will reduce sensitivity. Instead, orbital matched filtering techniques can provide some level of discrimination by constraining the radar parameters used for each beam.

Fig. 5.3 shows a single range and Doppler slice of the skymap of the Hubble Space Telescope (HST) passing at point of closest approach. The left subplot is created with standard delay-Doppler processing and the right is formed with ODBD methods. However, with the short CPI length of only 100 ms the two plots

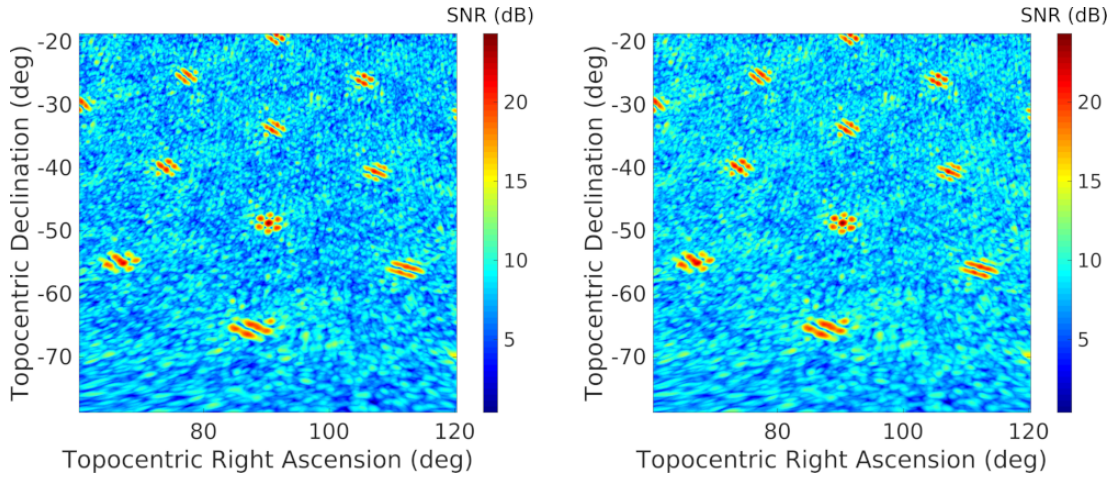


Figure 5.3: Near-identical plots of a single bistatic-range and Doppler slice of the sky map of the Hubble Space Telescope near zero-Doppler. 100 ms CPI. The left plot shows standard delay-Doppler processing and beamforming, the right shows ODBD methods. Data collected November 2018, with a frequency of 96.9 MHz, bandwidth of 100 kHz.

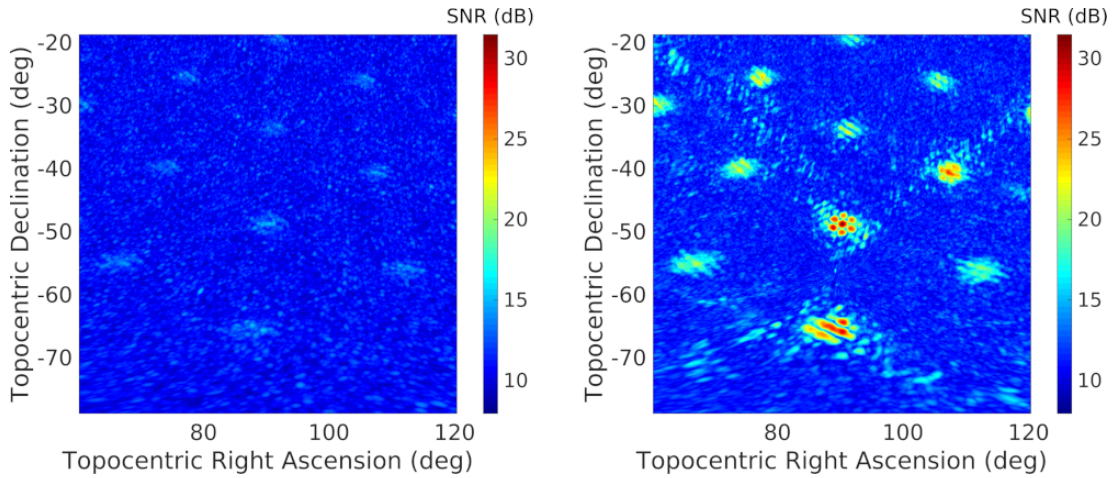


Figure 5.4: Single bistatic-range and Doppler slice of the sky map of the Hubble Space Telescope near zero-Doppler. Three second CPI. The left plot shows standard delay-Doppler processing and beamforming, the right shows ODBD methods. Data collected November 2018, with a frequency of 96.9 MHz, bandwidth of 100 kHz.

are indistinguishable. The HST is located in the centre and is clearly visible with the ‘flower’-like spatial structure which is associated with the Phase II compact configuration, and significant grating lobes are clearly visible. In contrast, Fig.



5.4 is from the same data but with the CPI extended to three seconds. Of interest in this figure is that on the left subplot the object is now smeared spatially, and will have also smeared in the other measurement domains. The right subplot shows the ODBD processing has achieved greater coherence through the integration period, with the flower structure retained and the SNR considerably higher. The grating lobes have also been attenuated with most being significantly attenuated<sup>1</sup>. This is because the orbital parameters for an object in a circular orbit at point of closest approach will vary depending on the object’s true location, meaning most of the grating lobes are significantly reduced. Of course, the HST is a comparatively large target and these now-reduced grating lobes will be far less apparent with smaller targets.

#### 5.4.1 High Time Resolution Voltage Capture System

The MWA has previously supported high-time resolution radioastronomy through the Voltage Capture System (VCS), with fine channels being recorded at 10 kHz (Tremblay et al., 2015). These 10 kHz channels can be combined together by inverting a second polyphase filter bank (PFB) stage to reconstitute the FM band. This has been used for earlier work in order to correlate MWA-collected timeseries surveillance data against a separate reference channel (Hennessy et al., 2019). However, recent improvements have included the High Time Resolution VCS mode, allowing sampling of the coarse channels (1.28 MHz bandwidth) directly. This enables direct correlation of the MWA surveillance data with external reference signals without the need to perform a fine-channel PFB inversion stage, which avoids loss from the fine channelisation as well as artefacts introduced by the inversion and reduces the overall computational load.

---

<sup>1</sup>Similar examples, resulting from a smaller passive radar system, are presented in Appendix A.

## 5.4.2 Radar Configuration

The processing for the following results used a CPI length of 3 s, with a 0.5 s staggered offset between CPIs. We used the SBS Radio 96.9 MHz FM radio station, from Perth, transmitting at 100 kW<sup>2</sup>. The data were downsampled to 100 kHz. For passive radar purposes, there is a general preference for high bandwidth analogue signals, like rock music, however the MWA provides sufficient spatial resolution for precise localisation rather than relying on somewhat improved range resolution. Instead, the generally lower-bandwidth signal of SBS offers a better signal for long CPI integration.

## 5.4.3 Surveillance Stare

The data for this section were collected in November 2018 and were processed using the methods outlined in Section 5.2.4. That is, only searching through cartesian position and constructing matched filters for an object in a circular orbit at its point of closest approach. There was an analogue beamforming pointing change during the observation. It should be noted that to generate results in this section, we constrained the search volume to be 50 km cubes around known objects of interest. Moving forward we will be preparing efficient implementations of these methods in order to perform genuine uncued searches.

For the processing we used a simple threshold detector with a 16 dB SNR cutoff to declare detections. This cutoff being sufficiently high to mitigate any false detections with a very low probability of false alarm (Skolnik, 1970). The trade-off, from using such a conservative threshold, is that any weak returns will not be detected.

Fig. 5.5 shows the detection results from processing the data spanning eight minutes and ten seconds. All of the detections correspond with known targets, which have been manually associated. The detections occur over a wide area of the

---

<sup>2</sup>Note this is the maximum licensed transmit power; actual transmitted power may be lower than this.

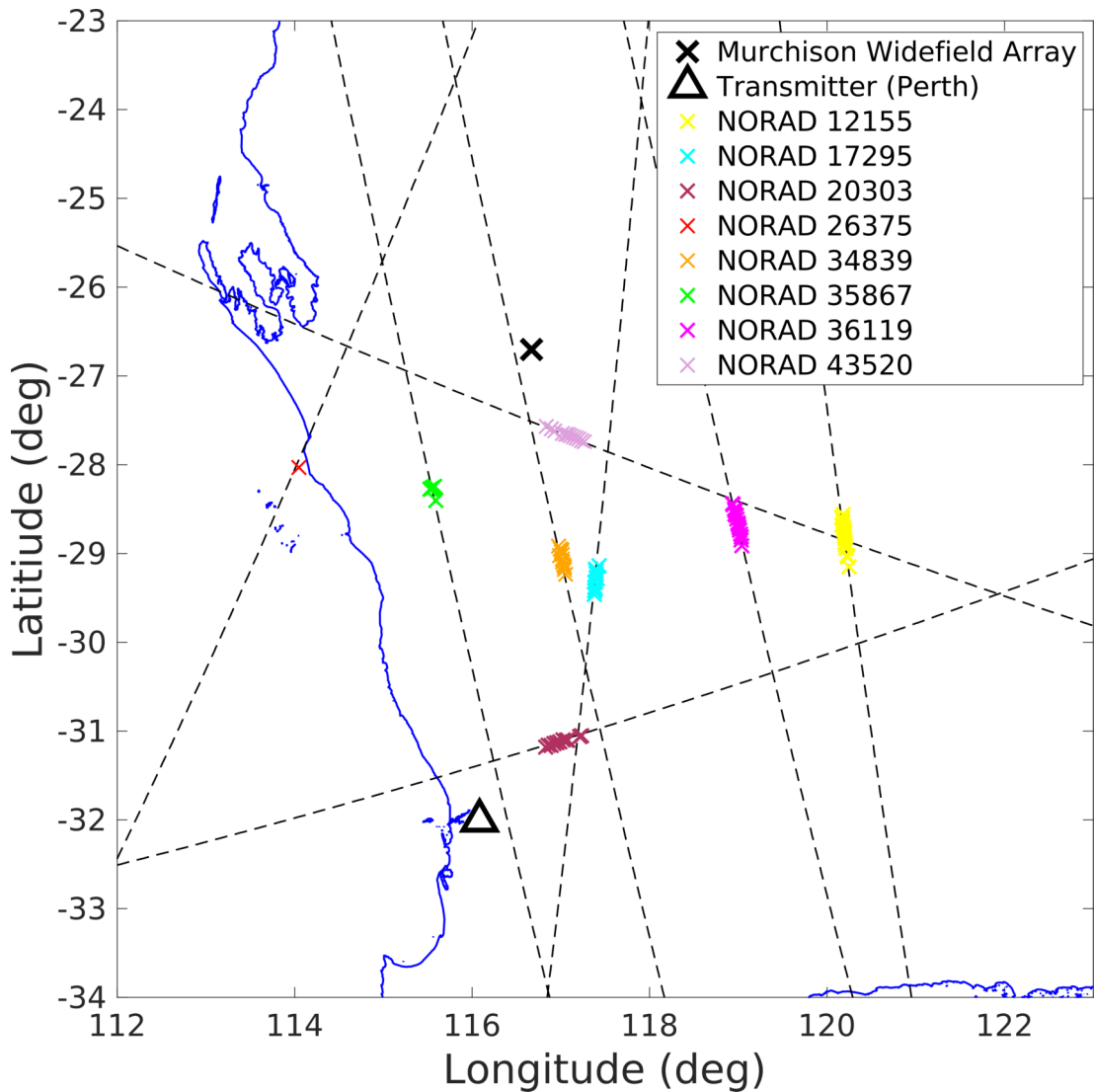


Figure 5.5: Detections from the surveillance stares, overlaid on the track data. Each detection has been associated with a NORAD (or Satellite Catalogue) Number.

sky. The detections all occur at significant elevation angles from the transmitter, with the lowest transmitter-target elevation being  $30^\circ$ ; all targets would certainly be outside the transmitter’s main lobe (O’Hagan et al., 2017). The figure lists the satellite catalogue numbers, also known as the NORAD numbers, associated with the detections.

Table 5.1 lists the detected objects. Although all the objects are classified as

Table 5.1: Detected objects and the detection’s respective ranges. Eccentricity values taken from truth data.

NORAD	Name	TX Range	RX Range	Eccentricity
12155	SL-3 R/B	746 km	661 km	0.0030
17295	COSMOS 1812	630 km	624 km	0.0005
20303	DELTA 2 R/B	556 km	743 km	0.0098
26375	PEGASUS R/B	675 km	549 km	0.0679
34839	YAOGAN 6	596 km	548 km	0.0027
35867	FREGAT/IRIS	566 km	426 km	0.0006
36119	WISE	686 km	587 km	0.0001
43520	CZ-2C DEB	698 km	495 km	0.0007

large<sup>3</sup> by the USSPACECOM (USSPACECOM, 2023), the objects are considerably smaller than any previously detected by the MWA.

The smallest objects in Table 5.1 are likely to be the Widefield Infrared Survey Explorer (WISE) and the Pegasus XL rocket body (R/B)<sup>4</sup>, NORAD numbers 36119 and 26375, respectively. Both objects have dimensions less than one wavelength, with the Pegasus XL Rocket Body being an Orion-38 rocket stage with length 1.3 m and diameter 0.97m. At FM radio frequencies the RCS of such an object would be close to 1 m<sup>2</sup>. Detections of objects this small are consistent with earlier performance predictions (Tingay et al., 2013b).

#### 5.4.4 Initial Orbit Determination Example

Because of the constraints applied to the search, particularly matching objects at closest approach, the detections span very short arcs. This is illustrated in Fig. 5.5. This poses a potential problem as only minimal numbers of detections will be available to form a best-estimate of the orbit for follow-on tracking.

Fig. 5.6 shows the SNR of detections from both the uncued search as well as using a priori data for tracking. The shaping caused by the Doppler mismatch is

<sup>3</sup>That is, objects with an RCS greater than or equal to 1 m<sup>2</sup>, although this would almost certainly be for a higher frequency than is being used here.

<sup>4</sup>The debris object, with NORAD 43520, would possibly be smaller, but its dimensions are unknown.

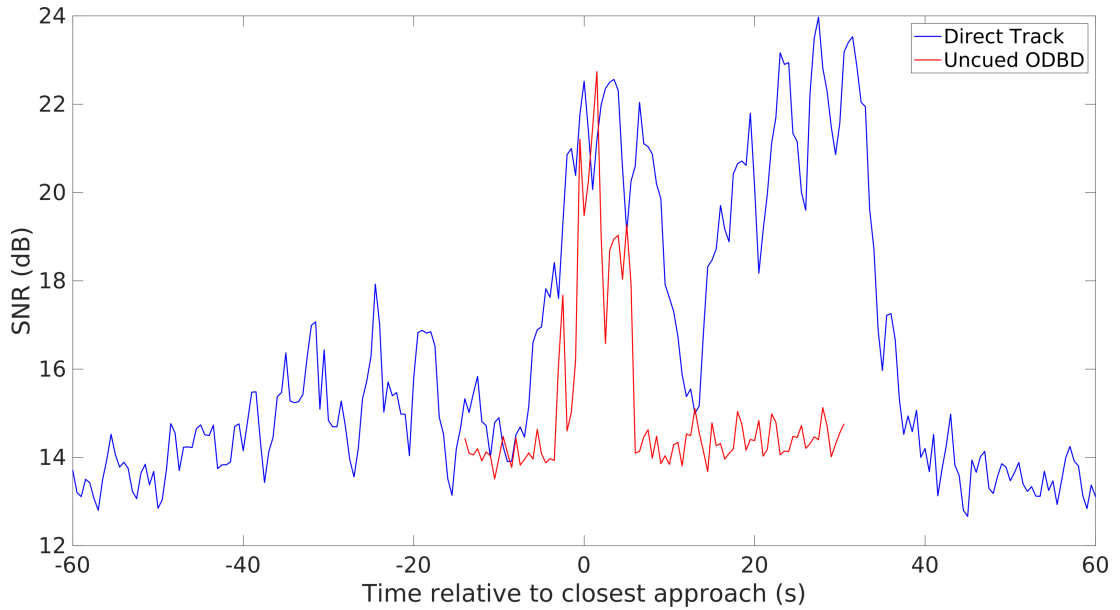


Figure 5.6: For the WISE, a comparison of detection performance of the uncued methods against what is possible with a priori track information.

clear, as the SNR decreases the further it is from its closest approach.

Interestingly, Fig. 5.6 shows that the detectability of the WISE is at its greatest at a point some 30 seconds after its closest approach. At this point its bistatic range is 70 km greater than the minimum, this is most likely due to the WISE moving into a transmit beam sidelobe. The baseline distance from the MWA to Perth is insufficient to ensure targets will be in the main beam, even with the large FM elevation beamwidths (O’Hagan et al., 2017). The vast surveillance volume above the MWA will be punctured by transmit nulls and low elevation side lobes. There will also be similar volume constraints imposed by the receiver beampattern. The intersection of these limitations along with constraining the search to only match orbital objects at minimum range may be overly restrictive for uncued detection. Limiting the search volume to match the beampatterns and increasing the parameter search space may significantly improve detection results.

#### 5.4.4.1 ODBD IOD

Fig. 5.7 details the pass of the WISE, an infrared space telescope (NORAD 36119), shown in Fig. 5.5 above. The bottom left subplot of Fig. 5.7 shows the aggregate delay-Doppler map for the detections. The orbital-derived higher order Doppler terms have coherently integrated the target motion, as the detections do not smear. The top subplot shows each detection's associated orbit propagated out 30 seconds, the wide fan in these predicted orbits (when compared to the nominal truth) because the WISE is only at its point of closest approach instantaneously, and its Doppler varies by hundreds of Hz in a manner of seconds. It is no surprise that the output of a zero-Doppler matched filter will have errors when the target is not at zero-Doppler. The bottom right subplot of Fig. 5.7 shows the same orbital predictions, except this time the orbital estimate has been updated with the detection's Doppler value. This is done by feeding back the measured Doppler shift into (5.7) to adjust the hypothesised orbit. Now, with the correct Doppler value incorporated there is a significantly improved agreement between the detected orbits and the truth.

Fig. 5.8 shows the same detection-level orbital estimates as the right subplot of Fig. 5.7, but now they are propagated forward an hour. This shows good agreement for such a considerable propagation time; after the 60 minutes there is less than  $1^\circ$  cross range error. These predictions are noteworthy because they are each generated from a single 3 s detection. Also, the orbits have only been propagated forward with two-body propagation, which itself will contribute to errors.

Of course, the goal with this work is not to try to generate an orbit from a single detection, and integrating many detections will improve any orbital estimate. However, having such a rapid IOD step, and feature-rich detections, will greatly assist ongoing tracking as well as measurement association.

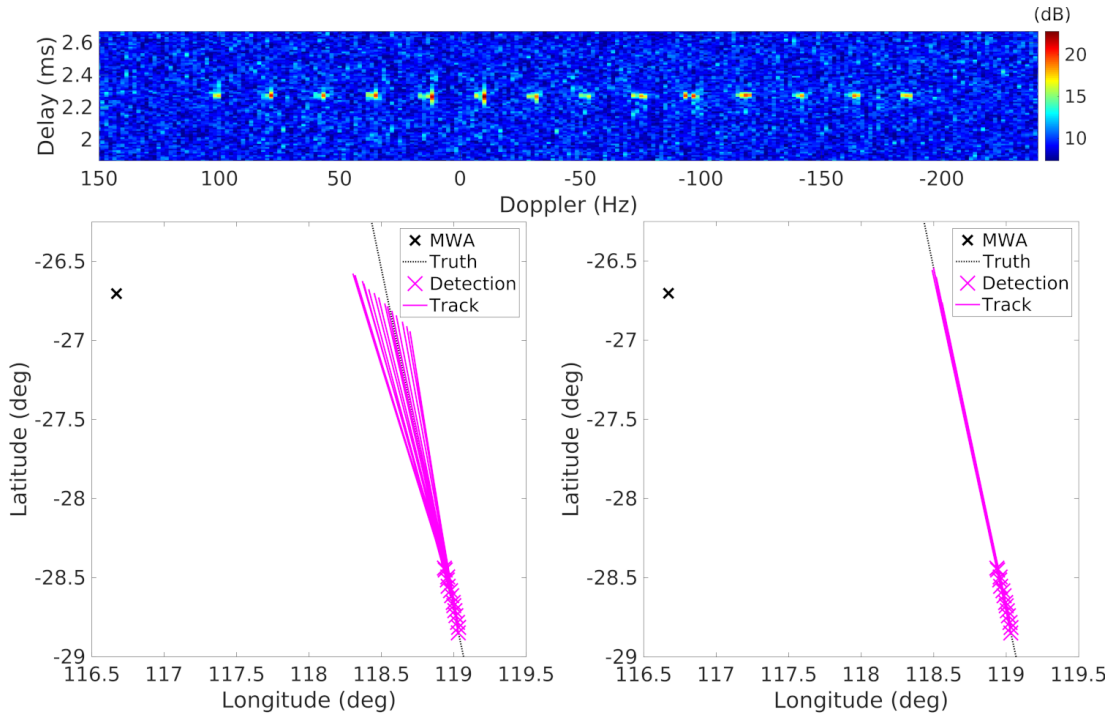


Figure 5.7: Aggregate detections of the WISE. The top subplot is an aggregate of the delay-Doppler maps. The next two subplots show the detection-level IOD from these detections. The left IOD subplot has no Doppler correction and the right subplot shows orbits after the detected-Doppler feedback.

#### 5.4.4.2 Other methods

Other IOD methods from Section 5.3 have been used with the initial detections of the WISE. Fig. 5.9 shows the results for using the Doppler-corrected ODBD detection-level estimates, the Herrick-Gibbs estimates, and also analytically calculating the orbital velocity from the Doppler, Doppler-rate, and Doppler-acceleration. For the Doppler analytic method, if we had taken the ODBD-derived parameters directly, the resulting orbit would be identical to the left subplot in Fig. 5.7. Instead, for each detection, a subsequent search was conducted through all Doppler parameters to determine those which maximised the detection SNR. These Doppler parameters were those used to determine the velocity in the Doppler analytic results in Fig. 5.9.

Fig. 5.9 shows that the Doppler-corrected orbits compare favourably against

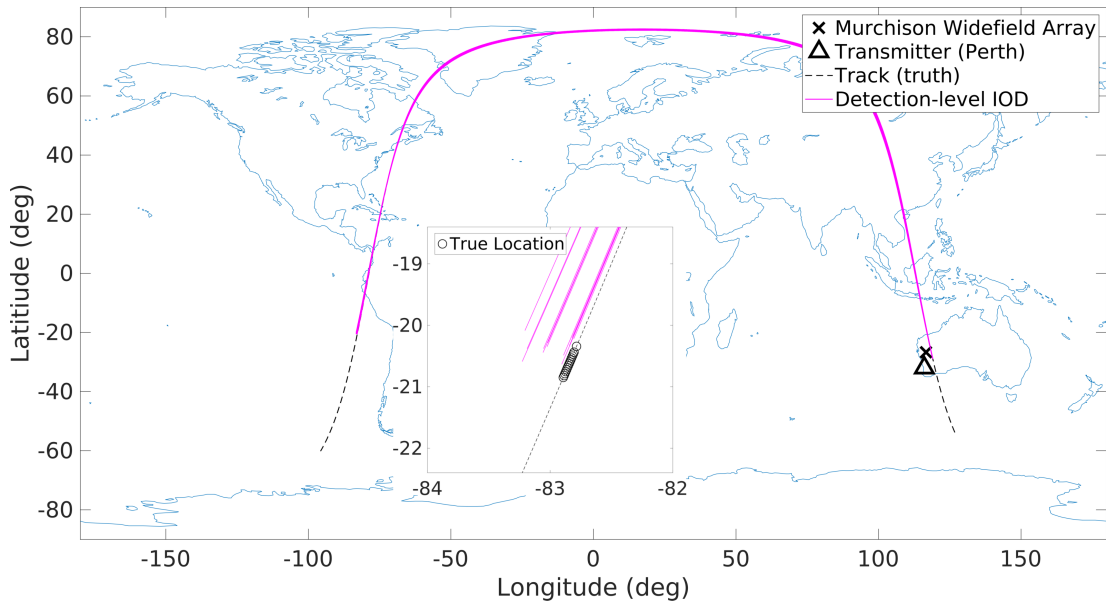


Figure 5.8: Detection-level IOD for the WISE, propagated 60 minutes forward.

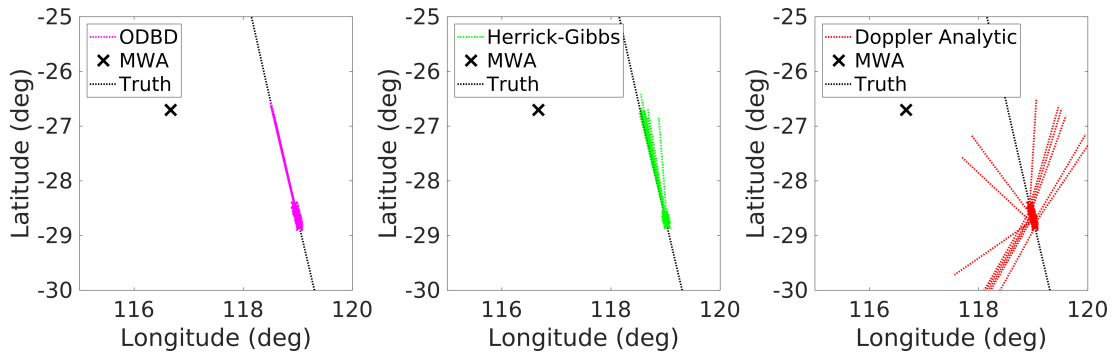


Figure 5.9: Detection-level IOD for the WISE, propagated 30 s forward. The left subplot shows the Doppler-corrected ODBD estimates, matching Fig. 5.8. The middle subplot shows the Herrick-Gibbs method. The right subplot shows the Doppler-analytic method.

other methods. This is because the IOD estimate is intrinsically incorporating every measurement parameter, whereas the Herrick-Gibbs is incorporating three positions and the Doppler analytic method only uses a position and three Doppler parameters. However, Fig. 5.9 shows that MWA detections are not necessarily well-suited to these other methods. The detections are all coplanar, however the extent of the arc is only  $0.41^\circ$  which will cause issues with the Herrick-Gibbs



solutions. Also, the direct analytic method of (Zhang et al., 2019) is very dependant on the second derivative of the Doppler, and a 3 s CPI provides insufficient resolution for estimating this. Further, this estimate will be highly susceptible to noise, clutter, and signal amplitude changes across the CPI.

### 5.4.5 Non-Circular Orbits

The methods used to form the matched filters in Section 5.4.3 matched circular orbits in order to reduce the search space. However, there were a few interesting examples of slightly eccentric detections. A Delta 2 rocket body with an eccentricity of 0.01 was detected, as well as a Pegasus XL rocket body with an eccentricity of 0.068. Whilst these orbits are still quite circular, they represent larger eccentricities than the vast majority of the catalogue.

Fig. 5.10 shows the orbits of the Delta 2 rocket body predicted out an hour. Because the detection level orbits will have an eccentricity of zero, there is now a noticeable offset between the detection-level predictions and the truth, although the cross-range error is still quite small. Unfortunately, as the detections only span a  $0.39^\circ$  arc, the Herrick-Gibbs predictions do not fare any better, however the eccentricities of the Herrick-Gibbs estimates range from 0.00091 to 0.00116, which are far more accurate.

The Delta 2 rocket body was detected 11 times, whereas the Pegasus XL rocket body was only detected once. Two contributing factors are the RCS of the Delta 2 is about ten times larger than the Pegasus XL, and the Delta 2 orbit is less eccentric.

Fig. 5.11 shows the detected SNR of the Pegasus XL rocket body with both the circular-uncued search as well as the track based on a priori truth information. Not only is the SNR attenuated past its point of closest approach (as in Fig. 5.6 above), it will also be attenuated because the eccentricity is not zero. The measurement parameters derived for a circular orbit will not match well with true parameters. The object was also near its orbital perigee, and so its velocity is

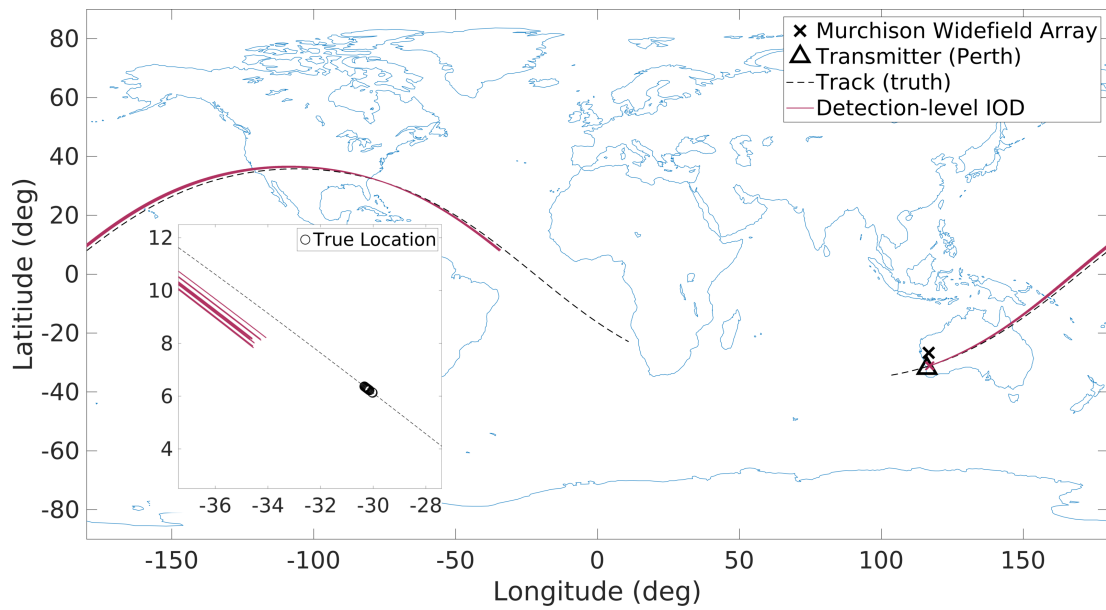


Figure 5.10: Detection-level IOD for the Delta 2 rocket body, propagated 60 minutes forward.

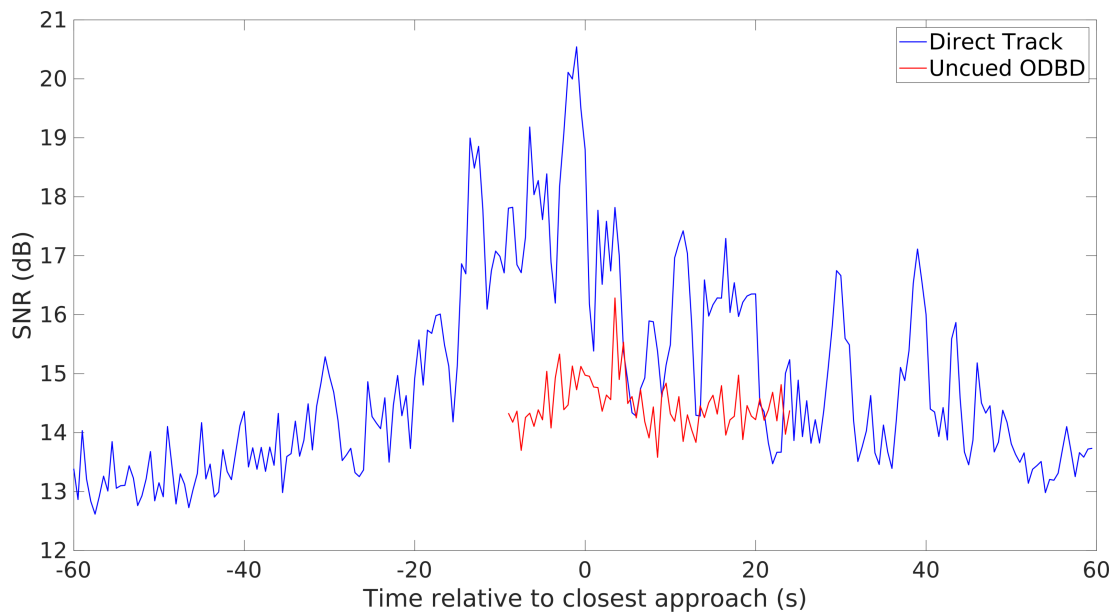


Figure 5.11: For the Pegasus XL rocket body, a comparison of detection performance of the uncued methods against what is possible with a priori track information.

considerably larger than that of an object in a circular orbit. This means that the bistatic geometry is changing faster than it would otherwise, and the 0.5

s staggered offset between CPIs may not be sufficient to ensure objects of this eccentricity will near its point of closest approach at the mid-point of the CPI.

Because of these factors, it is very fortunate that the processing was able to detect the rocket body, as mismatches attenuate the sensitivity and insufficiently regular update times may also miss the optimal conditions. Fig. 5.11 shows the object is detectable (with a simple track based detection method) for over a minute and includes SNRs greater than 20 dB.

Rather than matching solely for circular orbits, the full Vis Viva and velocity-position inner product expressions can be used instead of (5.5) and (5.6). With a circular orbit, its position would define the semi-major axis,  $a = |\mathbf{r}|$ . However for non-circular orbits the search parameter space is extended by two dimensions, to now include the orbital eccentricity and semi-major axis, which define the size and the shape of the orbital ellipse.

$$|\dot{\mathbf{r}}|^2 = \mu \left( \frac{2}{|\mathbf{r}|} - \frac{1}{a} \right) \quad (5.9)$$

$$\mathbf{r} \cdot \dot{\mathbf{r}} = \pm \sqrt{|\mathbf{r}|^2 \mu \left( \frac{2}{|\mathbf{r}|} - \frac{1}{a} \right) - \mu a (1 - e^2)} \quad (5.10)$$

These additional dimensions are not completely unconstrained, for a given target range  $|\mathbf{r}|$  must lie between the orbital apogee and perigee ranges. Additionally, the perigee must be associated with a stable orbit (otherwise the Keplerian model will not hold) so this must be greater than approximately 100 km. Fig. 5.12 shows the detections corresponding to the WISE and the Pegasus XL rocket body (from Figs. 5.6 and 5.11) reprocessed for eccentricities up to 0.1, along with the corresponding semi-major axis.

Note that now there will be four solutions, so four matched filters, for a given position combined with (5.7) , (5.9) and (5.10).

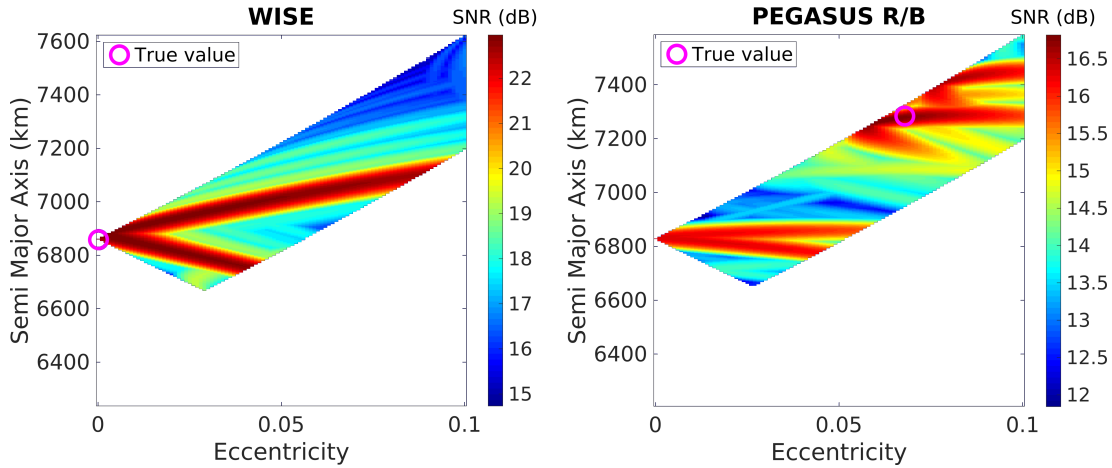


Figure 5.12: SNR of a detection when processing is extended to account for non-circular orbits. The plots show how the detection SNR varies with the size and shape of the orbital ellipse. The true values for the WISE are 0.0001 and 6,858 km and the true values for the Pegasus XL rocket body are 0.0679 and 7,284 km, both shown.

## 5.5 Conclusion

With traditional processing, the narrow beamwidth of the MWA would normally limit the CPI interval for detecting moving targets. This paper has demonstrated initial results incorporating novel methods to extend processing intervals, which are needed for detecting small objects at orbital ranges. By accounting for the target's motion through range, Doppler, and spatial parameters, processing intervals can be extended sufficiently in order to detect targets with an RCS of 1 m<sup>2</sup>.

The number of potential measurement parameters is quite large, with processing needed to account for range, Doppler and its many derivatives, and the directions and their subsequent derivatives. To account for this large space, this paper has demonstrated results by searching through orbital parameters and generating measurement parameters from these orbits. This has the advantage of limiting the search space to Keplerian orbits, ensuring detections will correspond to a hypothesised orbit, and it allows the measurement space to be constrained by orbital parameters.

These detection-level orbits are accurate, despite being formed with only three seconds of matched-processing. Additionally, having an accurate velocity estimate will greatly assist ongoing tracking and measurement association.

The majority of objects in an Earth-captured orbit are in circular, or near circular, orbits. Despite limiting the search parameters to circular orbits, small objects have been detected at a significant eccentricity, despite the attenuation caused by this mismatch.

In this paper, all objects were detected at SNRs above 20 dB, and the detection threshold was set at a very conservative 16 dB. By incorporating a different detector allowing lower, more realistic, detection limits, improved results against smaller targets could be achieved. Smaller object detection will be limited as RCS decreases exponentially as the objects move into the Rayleigh scattering region.

The initial results presented here further demonstrate the potential of the MWA for wide area space surveillance as a passive radar receiver.

## 5.6 Future Work

The IOD step is performed to construct a preliminary orbit to assist with ongoing tracking. This will be useful for the MWA as it will be able to track, confirm, and update known tracks, and then have uncued preliminary orbits feeding in to this process. Investigating orbit determination processes with the track data is a key focus of future work in order to minimise the amount of searching required to verify or reacquire tracks.

Western Australia has a low population density, and so, a low density of large transmitters, one of the reasons it is an ideal location for radio telescopes. The nearest and largest transmitter is 600 km away in Perth, however despite this distance, orbital objects above the MWA are still at a large elevation from the transmitter, being illuminated by elevation sidelobes. This means the surveillance volume above the MWA will be limited by the transmit antennas elevation pattern. If the transmit antennas sidelobes are more than 15 dB below the main lobe,

then the signal level from the main lobe of transmitters thousands of kilometres away will be stronger above the MWA than the Perth transmitter. Future observations will be conducted with reference collections situated near more distant transmitters, to investigate this potential gain.

Last, to process the data in this paper, search regions have been limited for efficient processing. As the processing requires two time-varying beams to be formed, albeit only at a single range of interest, for each detection, an optimised implementation will enable faster processing and a significantly increased detection volume.

## Chapter 6

# Establishing the Capabilities of the Murchison Widefield Array as a Passive Radar for the Surveillance of Space

With a full set of practical approaches minimising the radar search space, the Murchison Widefield Array can now be used as a full space surveillance sensor, from detection through to complete orbit determination, including multistatic orbit determination. Similar to previous chapters, this chapter is reproduced from the author's publication (Hennessy et al., 2022b), albeit with the removal of some aspects of the introductory sections, which were incorporated into Chapter [2](#).

### 6.1 Abstract

This paper describes the use of the Murchison Widefield Array, a low-frequency radio telescope at a radio-quiet Western Australian site, as a radar receiver forming part of a continent-spanning multistatic radar network for the surveillance of

space. This paper details the system geometry employed, the orbit-specific radar signal processing, and the orbit determination algorithms necessary to ensure resident space objects are detected, tracked, and propagated. Finally, the paper includes the results processed after a short collection campaign utilising several FM radio transmitters across the country, up to a maximum baseline distance of over 2500 km. The results demonstrate the Murchison Widefield Array is able to provide widefield and persistent coverage of objects in low Earth orbit.

## 6.2 Signal Processing

An issue faced when using a sensor such as the MWA as a space-surveillance radar is the tradeoff between needing to integrate for a longer amount of time for increased sensitivity, and the changing geometry that orbital motion imparts. The precise and narrow beamwidth, resulting from such a large aperture, means that RSOs in LEO will occupy a beam for only a brief instant. For even a short coherent processing interval (CPI), the object in orbit will need to be tracked spatially throughout the CPI. Similarly, the object will need to be tracked in delay and Doppler parameter space as well. This is the fundamental challenge with the detection of RSOs with the MWA; the need to extend the CPI to detect smaller and more distant RSOs is balanced against the difficulty of coherently forming detection signals. This section covers efficient and scalable methods for dealing with this problem by matching the radar-receiver parameters to the orbital motion. This type of track-processing is achievable given the a priori information on orbits, whereas for uncued detection and searches, earlier studies have detailed practical methods for forming hypothesised orbits (Hennessy et al., 2021).

Given a large number of potential orbits, either from known tracks, searching a volume of orbits around known tracks, or uncued search hypotheses, the surveillance data, and the collected reference signals, are able to be coherently matched to detect an RSO in that orbit.



Rather than directly processing across the received signals, range-compressed pulses are formed for each antenna. These pulses are then matched to the RSO motion (Stein, 1981; Palmer et al., 2011). The signals are split into  $M$  pulses, each with a duration of  $\tau$ , such that the CPI length is given by  $M\tau$ . The pulse length,  $\tau$ , needs to be sufficiently short to ensure that any change in the Doppler frequency across the pulse is insignificant (Palmer et al., 2011). Decreasing the pulse length is equivalent to increasing the maximum unambiguous velocity coverage. For a CPI length of 3 s,  $M$  will need to be in the order of 40,000 pulses in order to unambiguously span potential orbital velocities.

Given a reference signal  $s_r$  and  $N$  tiles that each have a received signal  $s_n$  ( $n$  ranging from 0 to  $N - 1$ ), the range-compressed pulses are formed by correlation. Given the sample rate  $B$ , each pulse consists of  $B\tau$  samples, and the pulse compression forming the range-compressed pulse stack is obtained with the following formula:

$$\chi_n[t, m] = \sum_{t'=0}^{B\tau-1} s_n[mB\tau + t'] s_r^*[mB\tau + t' - t], \quad (6.1)$$

where  $t$  is the fast-time (or delay) sample index,  $m$  is the slow-time pulse index, and  $t'$  is the fast-time correlation index for the two pulses. Note that the sample rate,  $B$ , is treated here as equal to the signal bandwidth, although in practice the true signal bandwidth will vary with the analogue content.

This pulse stack is formed for each tile,  $n$ , creating a compressed pulse cuboid. Typically these pulses are coherently integrated simply with a Fourier transform (FT), resolving Doppler. However, for rapidly changing geometries, this will not be sufficient, and instead the phase resulting from the target's motion needs to be matched from pulse to pulse.

Constant radial motion will result in a linear phase rate across subsequent pulses, which will be coherently matched by the FT. However, with orbital motion, the target's radial slant range changes rapidly, as will its Doppler signal. This results in a complicated signal with the Doppler changing rapidly, which

is typically treated as a polynomial phase signal. For orbital motion, matching higher-order terms in this polynomial phase signal results in significant increases in the signal-to-noise ratio (SNR) (Malanowski & Kulpa, 2008; Hennessy et al., 2019). The moving object’s phase will be different for each antenna as well, resulting in differing polynomial phase signals from each tile which need to be matched in order to be combined.

Although it is possible to form a single beam (and even a moving beam), and then search in Doppler-rate terms (or indeed vice versa), the parameter space is far too large and this approach is intractable. Instead, each tile’s matching polynomial phase signal is determined from a hypothesised orbit in order to best match the orbital motion. This essentially matches the Doppler phase signal and the spatial phase signal in one process.

The bistatic radar configuration is illustrated in Figure 6.1, with a target at position  $\mathbf{r}$ , relative to the centre of the Earth, with the velocity  $\dot{\mathbf{r}}$ . The receiver’s Cartesian location is given by  $\mathbf{r}_{rx}$  and the transmitter’s by  $\mathbf{r}_{tx}$ . The position vectors from the receiver and the transmitter to the RSO are  $\boldsymbol{\rho}_{rx}$ , and  $\boldsymbol{\rho}_{tx}$ , respectively. The polynomial phase coefficients are derived from this geometry with an orbital motion model.

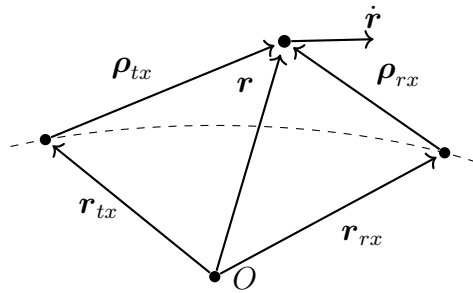


Figure 6.1: The bistatic radar configuration with the position of an orbital object and its velocity,  $\mathbf{r}$  and  $\dot{\mathbf{r}}$ , along with the positions of the transmitter and receiver,  $\mathbf{r}_{rx}$  and  $\mathbf{r}_{tx}$ , as well as the vectors from these sites to the object,  $\boldsymbol{\rho}_{rx}$  and  $\boldsymbol{\rho}_{tx}$ . The origin,  $O$ , corresponds to the gravitational centre of the Earth.

The bistatic radar configuration is illustrated in Fig. 6.1, with a target at position  $\mathbf{r}$ , relative to the centre of the Earth, with velocity  $\dot{\mathbf{r}}$ . The receiver’s

cartesian location is given by  $\mathbf{r}_{rx}$  and the transmitter's by  $\mathbf{r}_{tx}$ . The position vectors from the receiver and the transmitter to the RSO are  $\boldsymbol{\rho}_{rx}$ , and  $\boldsymbol{\rho}_{tx}$ , respectively. The polynomial phase coefficients are derived from this geometry with an orbital motion model.

For the relatively short duration of a single CPI, the motion model assumes that the only force acting on the object in orbit is Earth's gravity. The acceleration due to the Earth's gravity  $\ddot{\mathbf{r}}$ , is given by the inverse square law:

$$\ddot{\mathbf{r}} = -\frac{\mu}{|\mathbf{r}|^3}\mathbf{r}, \quad (6.2)$$

where  $\mu$  is the standard gravitational parameter for Earth.

This type of orbit, a Keplerian orbit, describes two-body motion and is the simplest orbital model. An orbit is fully determined by the state vector  $\mathbf{x} = \begin{bmatrix} \mathbf{r} & \dot{\mathbf{r}} \end{bmatrix}$ , and so every future or past motion parameter, and then the phase parameter can be determined from the state vector  $\mathbf{x}$  at a given time.

Given  $\boldsymbol{\rho}_{rx} = \mathbf{r} - \mathbf{r}_{rx}$ ,  $\dot{\boldsymbol{\rho}}_{rx} = \dot{\mathbf{r}} - \dot{\mathbf{r}}_{rx}$ , etc., the receiver range, range rate, range acceleration and range jerk are given by:

$$\rho_{rx} = |\boldsymbol{\rho}_{rx}|, \quad (6.3)$$

$$\dot{\rho}_{rx} = \frac{\boldsymbol{\rho}_{rx} \cdot \dot{\boldsymbol{\rho}}_{rx}}{\rho_{rx}}, \quad (6.4)$$

$$\ddot{\rho}_{rx} = -\frac{(\boldsymbol{\rho}_{rx} \cdot \dot{\boldsymbol{\rho}}_{rx})^2}{\rho_{rx}^3} + \frac{|\dot{\boldsymbol{\rho}}_{rx}|^2 + \boldsymbol{\rho}_{rx} \cdot \ddot{\boldsymbol{\rho}}_{rx}}{\rho_{rx}}, \quad (6.5)$$

$$\begin{aligned} \ddot{\rho}_{rx} = 3\frac{(\boldsymbol{\rho}_{rx} \cdot \dot{\boldsymbol{\rho}}_{rx})^3}{\rho_{rx}^5} & \quad (6.6) \\ - 3\frac{(\boldsymbol{\rho}_{rx} \cdot \dot{\boldsymbol{\rho}}_{rx})(|\dot{\boldsymbol{\rho}}_{rx}|^2 + \boldsymbol{\rho}_{rx} \cdot \ddot{\boldsymbol{\rho}}_{rx})}{\rho_{rx}^3} & \\ + \frac{3\dot{\boldsymbol{\rho}}_{rx} \cdot \ddot{\boldsymbol{\rho}}_{rx} + \boldsymbol{\rho}_{rx} \cdot \ddot{\ddot{\boldsymbol{\rho}}}_{rx}}{\rho_{rx}}, & \end{aligned}$$

and this is similarly the case for the transmitter's terms  $\rho_{tx}$ ,  $\dot{\rho}_{tx}$ ,  $\ddot{\rho}_{tx}$  and  $\ddot{\rho}_{tx}$ .

Additionally,  $\ddot{\mathbf{r}}$  is determined from (6.2) and is given by:

$$\ddot{\mathbf{r}} = \frac{3\mu\mathbf{r} \cdot \dot{\mathbf{r}}}{|\mathbf{r}|^5}\mathbf{r} - \frac{\mu}{|\mathbf{r}|^3}\dot{\mathbf{r}} . \quad (6.7)$$

Note that  $\dot{\mathbf{r}}_{rx}$ ,  $\ddot{\mathbf{r}}_{rx}$  and  $\ddot{\mathbf{r}}_{rx}$  are the (known) motion terms for the receiver on the Earth's surface, and this is similarly the case for  $\dot{\mathbf{r}}_{tx}$ ,  $\ddot{\mathbf{r}}_{tx}$  and  $\ddot{\mathbf{r}}_{tx}$  for the transmitter. In this reference frame with a rotating Earth, the MWA is travelling (instantaneously) 47 m/s faster than the southern-most transmitter used in Section 6.5.

The expressions for the instantaneous bistatic delay and Doppler are

$$t_D = \frac{1}{c}(\rho_{rx} + \rho_{tx} - |\mathbf{r}_{rx} - \mathbf{r}_{tx}|) , \quad (6.8)$$

$$f_D = -\frac{1}{\lambda}(\dot{\rho}_{rx} + \dot{\rho}_{tx}) . \quad (6.9)$$

The spatial parameters, azimuth and elevation, and their rates, are determined directly from the orbit as well, ensuring that any RSO is spatially tracked throughout the CPI. These parameters are determined from the receiver's slant range vector rotated from an Earth-centred inertial (ECI) geocentric equatorial reference frame to a south-east zenith (SEZ) topocentric-horizon frame. The rotated vector  $\mathbf{q}$  and its subsequent rates  $\dot{\mathbf{q}}$  and  $\ddot{\mathbf{q}}$  are given by the following formula:

$$\mathbf{q} = \mathbf{D}^{-1}\boldsymbol{\rho}_{rx} , \quad (6.10)$$

$$\dot{\mathbf{q}} = \mathbf{D}^{-1}\dot{\boldsymbol{\rho}}_{rx} , \quad (6.11)$$

$$\ddot{\mathbf{q}} = \mathbf{D}^{-1}\ddot{\boldsymbol{\rho}}_{rx} , \quad (6.12)$$

where  $\mathbf{D}$  is the SEZ to ECI rotation matrix (Vallado & McClain, 2001). Note in some publications  $\mathbf{q}$  and  $\boldsymbol{\rho}$  are instead written as  $\boldsymbol{\rho}_{sez}$  and  $\boldsymbol{\rho}_{eci}$  respectively.

From these topocentric pointings, the azimuth and elevation,  $\theta$  and  $\phi$ , respectively, and their rates, are determined. Given  $\mathbf{q} = [q_S, q_E, q_Z]^T$ , the expressions

for the spatial parameters are:

$$\theta = \frac{\pi}{2} - \tan^{-1} \left( \frac{q_E}{q_S} \right), \quad (6.13)$$

$$\dot{\theta} = \frac{\dot{q}_S q_E - \dot{q}_E q_S}{q_S^2 + q_E^2}, \quad (6.14)$$

$$\begin{aligned} \ddot{\theta} = & \frac{1}{(q_S^2 + q_E^2)^2} \left( (\ddot{q}_S q_E - \ddot{q}_E q_S)(q_S^2 + q_E^2) \right. \\ & \left. - 2(\dot{q}_S q_S + \dot{q}_E q_E)(\dot{q}_S q_E - \dot{q}_E q_S) \right), \end{aligned} \quad (6.15)$$

and

$$\phi = \tan^{-1} \left( \frac{q_Z}{\sqrt{q_S^2 + q_E^2}} \right), \quad (6.16)$$

$$\dot{\phi} = \frac{\dot{q}_Z - \dot{q} \sin \phi}{\sqrt{q_S^2 + q_E^2}}, \quad (6.17)$$

$$\begin{aligned} \ddot{\phi} = & \frac{1}{q_S^2 + q_E^2} \left( \frac{(\dot{q} \sin \phi - \dot{q}_Z)(\dot{q}_S q_S + \dot{q}_E q_E)}{\sqrt{q_S^2 + q_E^2}} \right. \\ & \left. + (\ddot{q}_Z - \ddot{q} \sin \phi - \dot{q} \dot{\phi} \cos \phi) \sqrt{q_S^2 + q_E^2} \right). \end{aligned} \quad (6.18)$$

Note that the slant ranges (and their rates) will be unchanged by the rotation,  $q = |\mathbf{q}| = \rho_{rx}$ , and again, this is also the case for the subsequent rates.

A previous study assumed that two terms for each of the spatial parameters were sufficient (Hennessy et al., 2019). However, some particularly fast moving objects, such as rocket bodies in geosynchronous transfer orbits, require additional parameters. The full angular accelerations were required to detect an SL-12 rocket body (NORAD 20082) travelling at 9.6 km/s (in the ECI reference frame).

An equivalent approach is to rotate the tile locations to the ECI frame, in which case the spatial parameters and subsequent beamforming will have a topocentric right ascension and topocentric declination (rather than the azimuth and elevation) (Hennessy et al., 2021).

Given these spatial parameters, the polynomial phase coefficients can be de-

terminated for both Doppler and spatial aspects. The Doppler phase coefficients for the first four terms are given by their respective-order Taylor series terms:

$$d_0 = -\frac{2\pi}{\lambda}(\rho_{rx} + \rho_{tx} - |\mathbf{r}_{rx} - \mathbf{r}_{tx}|) , \quad (6.19)$$

$$d_1 = -\frac{2\pi}{\lambda}(\dot{\rho}_{rx} + \dot{\rho}_{tx}) , \quad (6.20)$$

$$d_2 = -\frac{\pi}{\lambda}(\ddot{\rho}_{rx} + \ddot{\rho}_{tx}) , \quad (6.21)$$

$$d_3 = -\frac{\pi}{3\lambda}(\dddot{\rho}_{rx} + \dddot{\rho}_{tx}) . \quad (6.22)$$

Similarly, the expression for the spatial coefficients is given by:

$$b_{n,0} = -\frac{2\pi}{\lambda}(\mathbf{k} \cdot \mathbf{u}_n) , \quad (6.23)$$

$$b_{n,1} = -\frac{2\pi}{\lambda}(\dot{\mathbf{k}} \cdot \mathbf{u}_n) , \quad (6.24)$$

$$b_{n,2} = -\frac{\pi}{\lambda}(\ddot{\mathbf{k}} \cdot \mathbf{u}_n) , \quad (6.25)$$

where  $\mathbf{u}_n$  is the location of the  $n$ th tile, and  $\mathbf{k}$ ,  $\dot{\mathbf{k}}$  and  $\ddot{\mathbf{k}}$  are the wavevector and its rates determined from (6.13)–(6.18).

Finally, the resulting matched phase signal for each antenna can be formed by sampling each antenna's polynomial phase signal at time instances  $m\tau$ , for  $m \in [-\frac{M-1}{2}, \dots, \frac{M-1}{2}]$ :

$$P_n[m] = e^{-j(b_{n,0} + (b_{n,1} + d_1)m\tau + (b_{n,2} + d_2)(m\tau)^2 + d_3(m\tau)^3)} . \quad (6.26)$$

This full set of matching phase signals ensures that a potential orbit determined by the state vector  $[\mathbf{r}, \dot{\mathbf{r}}]$  will be completely tracked both spatially and in Doppler across every pulse and every tile.

This phase-matching matrix can then be applied to the data, by applying the polynomial phase signal correction to each tile by forming the Hadamard product between the two. These signals are then coherently combined by summing across each tile to form a single, fully matched, slow time-series for a single range bin,

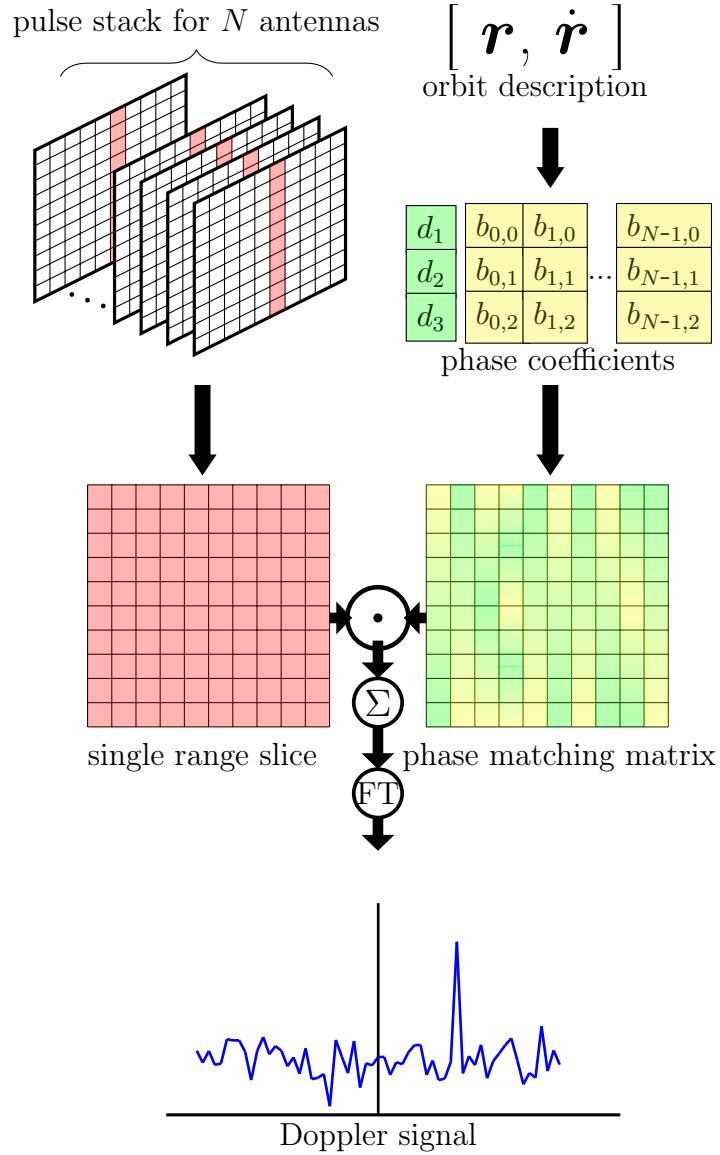


Figure 6.2: Illustration of the signal processing steps outlined in Section 6.2. An orbital state vector is used to determine the polynomial phase signal coefficients to form a phase-matching matrix. A single range's slow-time signals are matched to the orbit, and combined using this matrix before detection.

$\chi[m]$ . The range bin delay sample is determined by the time delay  $t_D$ , from (6.8), as well as the sample rate  $B$ .

$$\chi[m] = \sum_{n=0}^{N-1} (P_n[m] \odot \chi_n[t, m])|_{t=Bt_D} . \quad (6.27)$$

Finally, the Fourier transform will integrate the fully orbital-matched slow-time pulses resolving the slow frequency, or Doppler, signal. This full process is illustrated in Figure 6.2. This final signal is passed through a constant false alarm rate (CFAR) detector to produce detections of the matched orbit.

$$\chi[f] = \left| \sum_{m=-\frac{M-1}{2}}^{\frac{M-1}{2}} \chi[m] e^{-j2\pi \frac{fm}{M}} \right|^2 . \quad (6.28)$$

Note that the  $d_0$  term is not included, since the final phase is not of immediate interest; however, the inclusion of  $d_1$  ensures any matched target returns will be close to zero Doppler. This allows for a pruned FT implementation. That is, only those frequency bins sufficiently close to zero Doppler need to be determined to cover any potential orbital velocity offset, and also large enough to encompass sufficient bins allowing for accurate threshold estimation for the CFAR detector.

The process in (6.27) and Figure 6.2 only samples a single range bin; creating an entire delay–Doppler map would serve little purpose, since the orbit-derived parameters used to generate that map would only be relevant to a single range. A common pitfall with passive radar and analogue signals is that the ambiguity function is content-dependant; depending on the specific audio signal, the range resolution can be quite poor (Ringer et al., 1999). By processing a single range bin, this issue can be avoided, or at least moderated. Although signal content might result in a poor ambiguity function, by matching orbits directly, the orbit-derived parameters will vary across range bins and only one orbit will have the best-matched parameters.

By forming detections with orbit-derived parameters, every detection will be



associated with an orbital track with some confidence, since the beamforming has followed the orbit through the CPI. This associated trajectory greatly assists ongoing tracking and detection-track association. Additionally, having a known trajectory estimate is required for the OD step outlined in Section 6.3.

This process is entirely flexible and the motion model can be extended to more complicated orbital models, such as incorporating an oblate Earth or other perturbing forces. The measurement model can also be tailored, rather than applying far-field beamforming which is suitable for the MWA’s compact configuration. The matched signals are able to be readily extended to near-field beamforming. Instead of calculating beamforming coefficients as well as Doppler coefficients, Doppler coefficients ((6.19)–(6.22)) can be determined for each tile’s location and the resulting matched signal can be determined as before.

## 6.3 Orbit Determination

Given an orbital track, either from an RSO catalogue or an initial orbit hypothesis, the six dimensional positions and velocities are determined and the processing steps described in Section 6.2 are applied. The position and velocity state vectors, or indeed the orbital elements, can be adjusted to form search volumes for RSOs, either to detect manoeuvred targets or to update an old track. If an RSO is detected, a series of associated measurements will be produced, although the process utilises the six-dimensional state vectors. The measurements are produced in the standard radar measurements of azimuth, elevation, bistatic-range, and Doppler.

The number of measurement parameters is extendable in many measurement dimensions. As covered in previous sections, there is a need to account for higher-order motion parameters such as Doppler rates as well as spatial rates. These dimensions are not searched in the processing steps, as that would result in an intractable search space. Instead, only azimuth, elevation, bistatic range, and Doppler are the adjusted measurement parameters (either directly or via the

orbital elements); the first three are searched over as part of the Cartesian location and the latter, Doppler, is searched over via the FT as part of the final Doppler-resolving step. If sufficient computational resources existed, it may be possible to independently search through higher-order parameters, which would allow them to be included as part of the OD step.

Orbit determination is achieved using the batch least-squares method outlined in (Montenbruck et al., 2002). This method fits an orbit to a track (or collection) of measurements  $\mathbf{z}$ . The measurements vector  $\mathbf{z}$  consists of  $k$  measurements such that  $\mathbf{z} = [\mathbf{z}_0 \ \mathbf{z}_1 \ \dots \ \mathbf{z}_{k-1}]^T$ , each observed at times  $t_0, t_1 \dots t_{k-1}$ , with each measurement consisting of the detected delay, Doppler, azimuth and elevation such that  $\mathbf{z}_i = [t_{Di} \ f_{Di} \ \theta_i \ \phi_i]^T$ .

If the function  $\mathbf{f}$  maps a state vector  $\mathbf{x}$  to its respective measurement parameters at times  $t_0, t_1 \dots t_{k-1}$  (for a single pass, two-body orbit propagation is used such that  $\mathbf{f}$  consists of Equations (6.8), (6.9), (6.13) and (6.16); for longer-term orbit determination, more complicated models need to be used), the best orbital fit is the state vector which, when propagated, minimises the residuals between the measurements and the predicted measurements:

$$\hat{\mathbf{x}} = \underset{\mathbf{x}}{\operatorname{argmin}}(|\mathbf{z} - \mathbf{f}(\mathbf{x})|^2) . \quad (6.29)$$

As  $\mathbf{f}$  is highly non-linear, finding a general minima is not trivial and instead a solution is found by linearising all quantities around an initial state vector  $\mathbf{x}_0$ . This initial solution may be provided a priori from a source such as a previous pass or a space catalogue, or instead from the detections directly using an IOD method. The residuals,  $\boldsymbol{\epsilon}$ , can then be approximated:

$$\boldsymbol{\epsilon} = \mathbf{z} - \mathbf{f}(\mathbf{x}) , \quad (6.30)$$

$$\approx \mathbf{z} - \mathbf{f}(\mathbf{x}_0) - \frac{\partial \mathbf{f}}{\partial \mathbf{x}}(\mathbf{x} - \mathbf{x}_0) , \quad (6.31)$$

$$= \Delta \mathbf{z} - \mathbf{F} \Delta \mathbf{x} , \quad (6.32)$$

with  $\Delta \mathbf{x} = \mathbf{x} - \mathbf{x}_0$  being the difference between  $\mathbf{x}$  and the reference state vector, and  $\Delta \mathbf{z} = \mathbf{z} - \mathbf{f}(\mathbf{x}_0)$  being the difference between the actual measurements and the predicted measurements for the reference orbit. Additionally, the Jacobian  $\mathbf{F} = \frac{\partial \mathbf{f}(\mathbf{x})}{\partial \mathbf{x}}|_{\mathbf{x}=\mathbf{x}_0}$  consists of the partial derivatives of the modelled observations with respect to the state vector.

Now, the orbit determination step is achieved by solving a linear least-square problem, with Equation (6.29) simplified as:

$$\Delta \mathbf{x}_{ls} = \underset{\Delta \mathbf{x}}{\operatorname{argmin}}(|\Delta \mathbf{z} - \mathbf{F} \Delta \mathbf{x}|^2) . \quad (6.33)$$

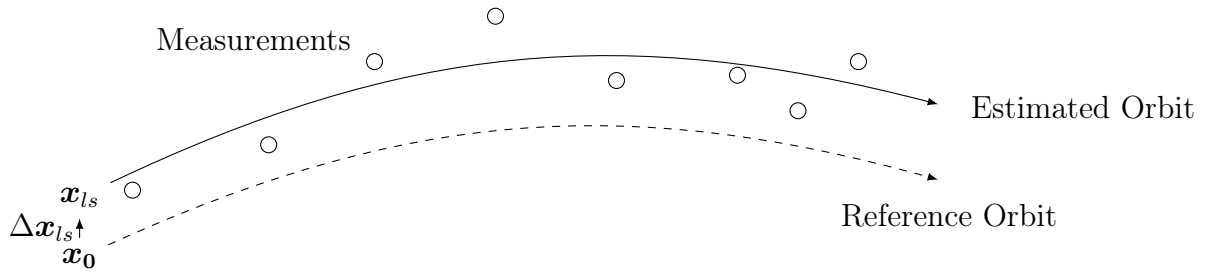


Figure 6.3: Illustration of the orbit determination process, starting with a reference orbit and then estimating an orbit adjustment to best-fit the measurements.

With each detection and track associated with a state vector,  $\mathbf{x}_0$ , a solution to Equation (6.33) is readily determined (Madsen et al., 2004). This process is illustrated in Figure 6.3.

In order to compare different measurement types equally, the residuals are normalised by scaling the measurements (and thus, the Jacobians) by the mean measurement error  $\sigma_i$ . In Equation (6.33),  $\mathbf{F}$  and  $\Delta \mathbf{z}$  are replaced by  $\mathbf{F}' = \mathbf{\Sigma} \mathbf{F}$  and  $\Delta \mathbf{z}' = \mathbf{\Sigma} \Delta \mathbf{z}$ , with  $\mathbf{\Sigma}$  being the diagonal matrix  $\mathbf{\Sigma} = \operatorname{diag}(\sigma_0^{-1}, \sigma_1^{-1}, \dots, \sigma_{k-1}^{-1})$ . The mean measurement errors in  $\mathbf{\Sigma}$  are determined experimentally and also from the measurement resolutions, with the range measurement accuracy determined by the signal bandwidth, the Doppler resolution determined by the CPI length, and the azimuth and elevation resolutions determined by the size of the array aperture.

In terms of signal processing, the only aspect that is within the system's control is the Doppler resolution through adjusting the CPI length. It is also possible to further scale the errors using each detection's SNR, such that stronger detections contribute to the orbital fit to a greater extent than the weaker detections (Vierinen et al., 2017).

With this process, the linearised error covariance matrix is now obtained with the following formula:

$$\text{cov}(\mathbf{x}_{ls}, \mathbf{x}_{ls}) = (\mathbf{F}^T \boldsymbol{\Sigma}^2 \mathbf{F})^{-1} . \quad (6.34)$$

The diagonal elements of this covariance matrix yield the standard deviation of the estimate of each element of the state vector.

### 6.3.1 Multistatic Orbit Determination

The OD approach is readily extendable to incorporate multistatic returns, with the detections from additional transmitters simply providing extra measurement parameters to fit the orbit. Having each detection associated with a state vector allows for the easy association of multistatic measurements.

A given detection's position is defined by the narrow beamwidth of the electronically steered beam and its intersection with the isorange ellipsoid defined by the time delay from Equation (6.8). However, the range resolution achievable using FM radio signals is quite poor, and although the large aperture allows spatially accurate beams, the volume of the intersection will extend radially. This segment, when intersected with subsequent ellipsoids, will not dramatically improve the estimation, as each subsequent coarse ellipsoid will still be intersected with the identical narrow beam.

Conversely, the target's velocity estimate can be dramatically improved. By expressing (6.9) in terms of the orbital velocity,  $\dot{\mathbf{r}}$ , it is clear that every Doppler

measurement  $f_D$  defines a plane of potential velocities:

$$\left( \frac{\boldsymbol{\rho}_{rx}}{\rho_{rx}} + \frac{\boldsymbol{\rho}_{tx}}{\rho_{tx}} \right) \cdot \dot{\mathbf{r}} = -\lambda f_D + \frac{\boldsymbol{\rho}_{rx} \cdot \dot{\mathbf{r}}_{rx}}{\rho_{rx}} + \frac{\boldsymbol{\rho}_{tx} \cdot \dot{\mathbf{r}}_{tx}}{\rho_{tx}} . \quad (6.35)$$

Additional Doppler returns from different sensors will drastically constrain the extent of possible velocities. Two measurements will define a line, and three or more detections will completely determine (or even overdetermine) the velocity. An accurate velocity estimate is the most important aspect of the orbital state vector estimate, as errors in the velocity estimation will produce increasingly erroneous position estimates when propagated forward. Even if multistatic detections are not coincident, the resulting orbit will be improved for having multiple Doppler measurements to constrain the region of possible velocities.

Other benefits of multistatic observations include the diversity of coverage, both spatially and in terms of signal content, as well as resilience by making the most of the vast amount of energy being radiated outward. If the bistatic configuration is relying on narrow elevation sidelobes, there will be gaps in illumination. Using multiple transmitters will help ensure any gaps are covered by at least one other sensor. Additionally, analogue FM radio is not necessarily ideal for radar due to the content-dependant nature of the ambiguity function, and diverse options (even multiple stations from the one tower) will provide resilience in the event one station's content is not suitable. FM radio signals have been shown to be well suited for distributed bistatic radar systems (Sahr, 2007).

### 6.3.2 Initial Orbit Determination

The process outlined in Section 6.2 requires an orbit to match the parameters in order to form detections. Although these orbits can come from a catalogue of tracks, there will still need to be additional work for uncued detection. The six-dimensional search space of all potential orbit state vectors is currently an unreasonably large search space. However, earlier work has shown that the appli-

cation of radar constraints can greatly simplify the process. By looking for RSOs at their point of minimum bistatic range, and constraining ranges in orbital eccentricity, this search space can be reduced further (Hennessy et al., 2020). Akin to creating a spatial fence with receiver beams, this approach only searches a narrow region in orbital parameter space. RSOs that do not pass through the right parameter space on one pass will pass through eventually. Tracked RSOs can then be treated as normal, per the general steps in this section.

There may be thousands of objects from a typical space catalogue observable from the MWA at any one point in time, and matching these tracks (and also searching a region around these tracks) would potentially require matching a hundred thousand orbits. An uncued search of a region, even including a constrained orbital search space, will potentially require matching one million orbits.

Depending on the available computer memory, a region’s hypothesised orbits and resulting parameters can be stored. The phase matrix coefficients, or indeed the full phase matrices, are applicable for all subsequent CPIs and thus, storing them saves on ongoing computation.

## 6.4 Continental Radar

The Australian continent provides a unique context for large-scale FM radio-based passive radar. The majority of the population is concentrated in cities near the coast, particularly in the south-east of the country. The FM radio transmitters are similarly located in the population centres. This is illustrated by a map of the most powerful FM transmitters in Figure 6.4. The MWA is naturally situated far away from these powerful transmitters. This isolation benefits the MWA’s astrophysics goals by reducing incident radio frequency interference (RFI). Such a location would ordinarily be less than ideal for terrestrial passive radar purposes, with most passive radar systems designed to be located within the footprint of the illuminating transmitter. However, for detecting satellites at LEO altitudes, such a separation becomes a significant advantage.

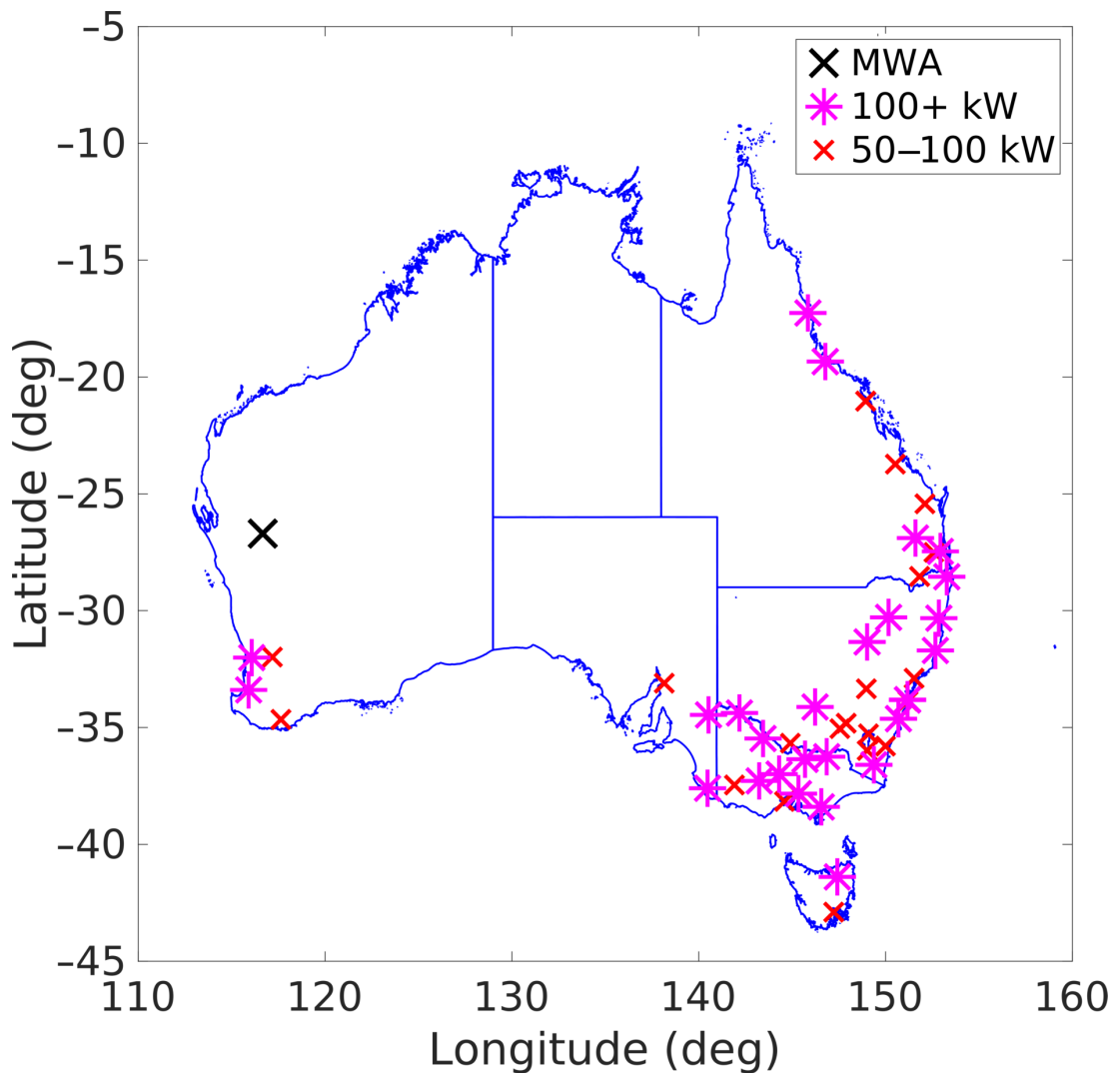


Figure 6.4: A map of all the powerful (greater than 50 kW) FM radio transmitters in Australia.

Typical FM radio transmitting antennas consist of six to eight antennas combined to form a beam. These antennas are typically angled (as well as electronically beam-steered) towards the ground in order to direct the maximum amount of energy to the population (O’Hagan et al., 2017). This can pose a challenge for satellite illumination, as every effort is made to minimise the amount of wasted energy being radiated outward from Earth, with the main elevation sidelobes being as low as  $-15$  dB compared to the main lobe (O’Hagan et al., 2017). However, these sidelobes will still provide sufficient illumination, and perhaps some

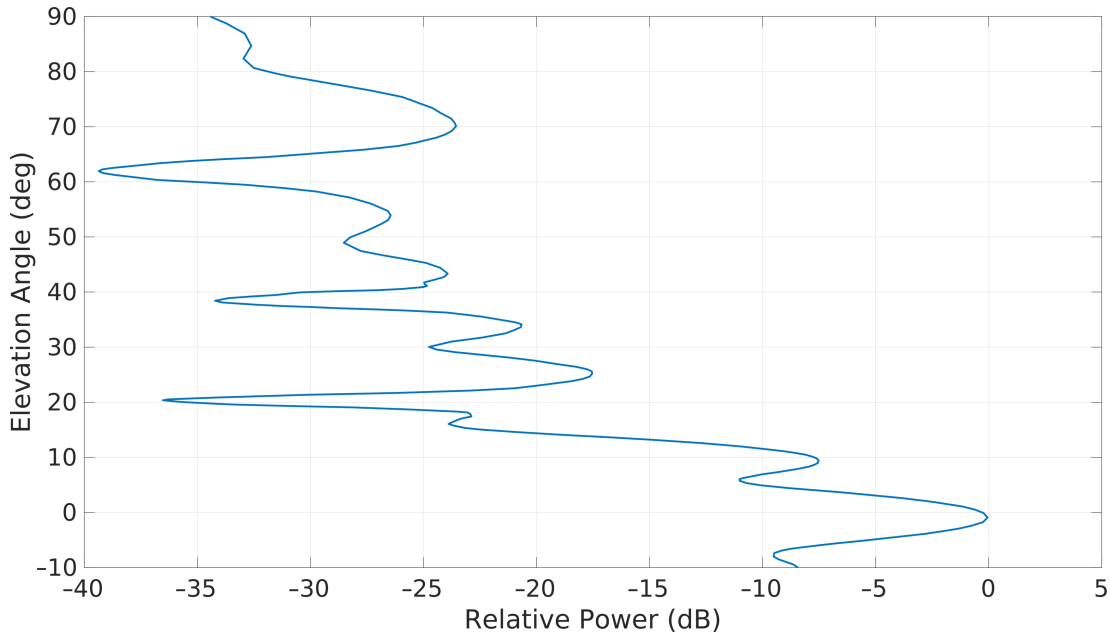


Figure 6.5: Typical FM array’s in situ measured antenna pattern via an airborne radio measurement system.

Australian transmitters are not so directive, especially given the widespread and low population density found in some rural areas. Figure 6.5 details a typical FM transmitter pattern. The main beam is directed to the ground; however, sidelobe levels are not insignificant at elevations of up to 15°. At higher elevations, considerable energy is still being radiated in some sidelobes. The patterns of other transmitters may not be so directional.

Instead of relying on sufficient sidelobes for target illumination, it is possible to make use of the main lobe for illumination. Given the number of transmitters in the south-east of Australia, and the lack of large interfering transmitters in between that region and the MWA, a target above the MWA will be illuminated by the main beam of potentially dozens of significant sources. This is illustrated in Figure 6.6, showing the incident power on an RSO at various altitudes above a receiver with a wide range of potential transmitter–receiver separation distances. It shows that the loss incurred by the increased transmitter to target distance,  $\rho_{tx}$ , is more than offset by the transmitter gain of the main lobe, from Figure



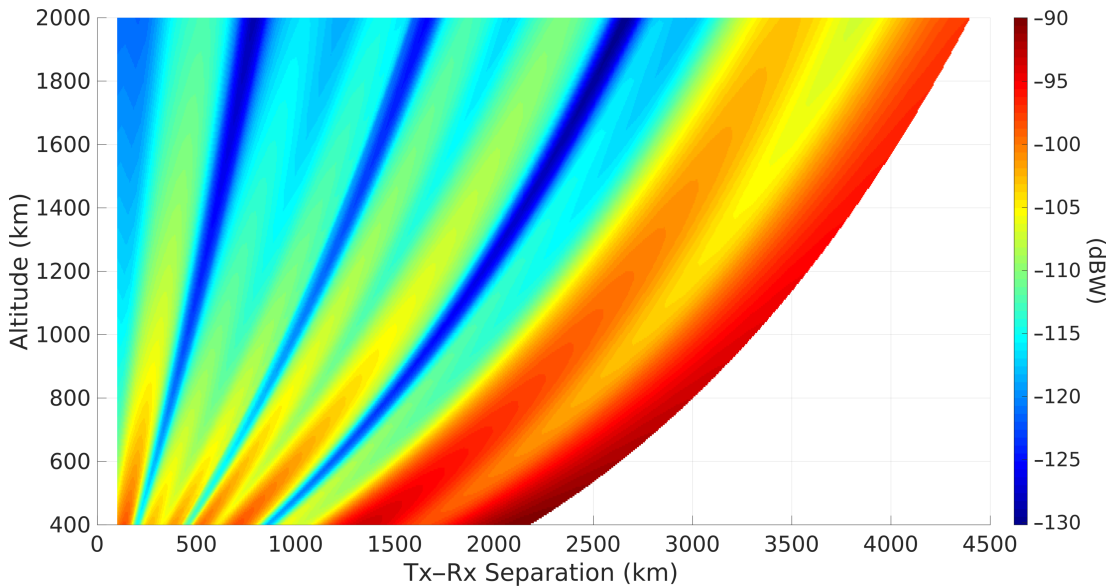


Figure 6.6: Incident power on an object above a receiver, for an equivalent isotropically radiated power (EIRP) of 100 kW, with a beam pattern as shown in Figure 6.5. Note that this figure is based on a spherical Earth model.

6.5. Indeed, the MWA has been used to detect FM radio returns from the moon, undoubtedly from transmitters half-way around the world (McKinley et al., 2013).

The use of the main lobe is illustrated in Figure 6.7, showing the SNR of the International Space Station (ISS), utilising a transmitter in Mount Gambier, over 2500 km away from the MWA. This shows that the strongest detections occur at the lowest transmitter elevation angles (despite the larger signal path loss); it even highlights the diffraction of signals along the Earth’s surface with detections occurring at transmitter elevations of almost  $2^\circ$  below the horizon.

Finally, the majority of FM transmitters transmit a vertically polarised signal, so the direction relative to the MWA will determine the best receiver polarisation. The vertical polarisation to the south will be coplanar with the MWA’s north–south polarisation, and there is a similar situation for transmitters to the east and the MWA’s east–west polarisation. However, impacts from effects such as Faraday rotation due to the ionosphere and other factors mean that the presence of matching transmitter and receiver polarisations is not necessarily a decisive

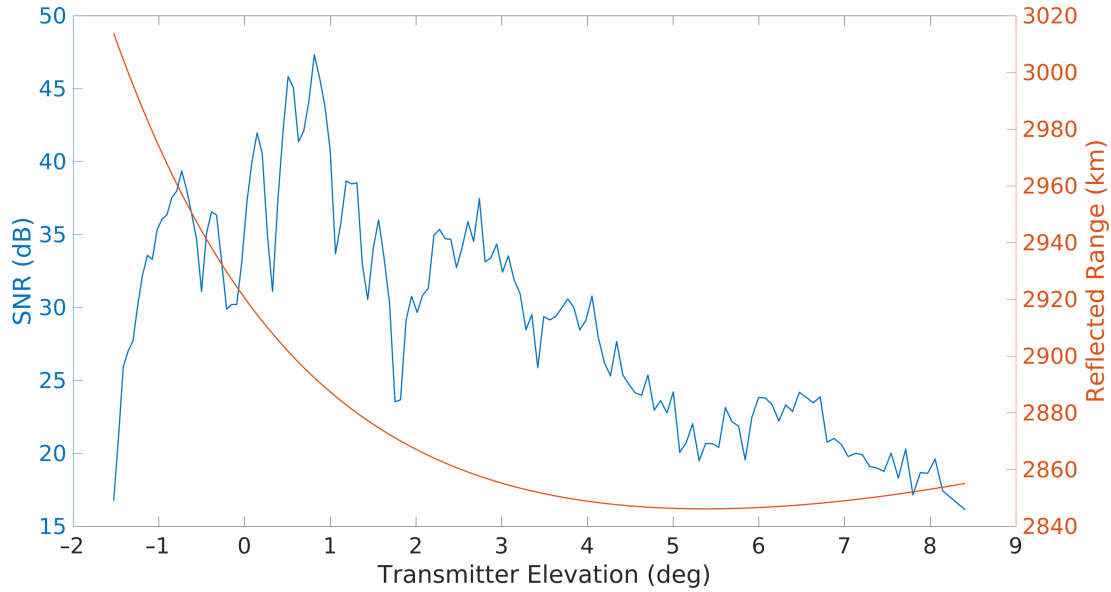


Figure 6.7: An example pass showing the detections of the International Space Station utilising a distant transmitter versus the elevation of the target. The blue line shows the detected signal to noise ratio and the red line shows the signal path length and the reflected range. The reflected range is given by  $\rho_{rx} + \rho_{tx}$  and does not include the baseline length to give the full bistatic range, as in Equation (6.8).

factor in the detected SNR.

## 6.5 Results

The results in this section are obtained from 20 min of data consisting of a series of five minute dwells collected in December 2019. These dwells were recorded and channelised in real-time and transferred to storage in Perth. Subchannels were selected such that the full national FM band of approximately 20 MHz was collected. The MWA’s analogue beamformer was directed to point at the zenith. In addition to MWA observations, several transmitter reference signals were collected from around the country. These are outlined in Table 6.1 and shown in Figure 6.8. Despite being located in a radio-quiet observatory, a sufficient signal is able to be observed from the nearby transmitters in Geraldton, some 300 km to the south-west of the MWA. Reference observations were collected in Perth

Table 6.1: Transmitters utilised in this section’s results.

Name (locale)	Maximum Power	Distance from MWA
Geraldton	30 kW	295 km
Perth	100 kW	591 km
Albany	50 kW	886 km
Mount Gambier	240 kW	2,524 km

utilising receiver hardware identical to that used in the MWA. Located at the Curtin Institute of Radio Astronomy (CIRA), this MWA-like reference receiver is synchronised with the MWA via GPS.

Transmitter reference signals were also collected at locations near Albany and Mount Gambier with a SDR setup. These remote SDR nodes are all GPS-disciplined in order to maintain synchronisation, the collections were manually triggered, and each node was able to record a reference with a bandwidth of 10 MHz. Although 10 MHz is insufficient to collect the full FM band, it is generally sufficient to collect every high-powered FM station from a single site. The transmitter near Mount Gambier, over 2500 km away from the MWA and situated in the south-east of South Australia, is one of the highest power radio transmitters in the country. It should be noted that for each transmitter there are many different FM radio stations, all potentially being broadcast at different power levels. The figures in Table 6.1 are simply the maximum licensed power level from that tower, and the true levels may, in fact, be lower.

Data from these remote SDR devices were then transferred to servers at CIRA in Perth, alongside the MWA-collected data, allowing offline space surveillance processing. This is achieved by downsampling the MWA data, as well as the SDR transmitter reference data, to narrowband signals (typically 100 kHz) matching known FM stations, and then undertaking radar processing as detailed in Section 6.2, utilising a 3 s CPI.

Figures 6.9 and 6.10 illustrate some of the aggregate detections from these observations. These detections are formed by parsing the Doppler signal data (from Equation (6.28)) through a cell-averaging CFAR detector. In passive radar

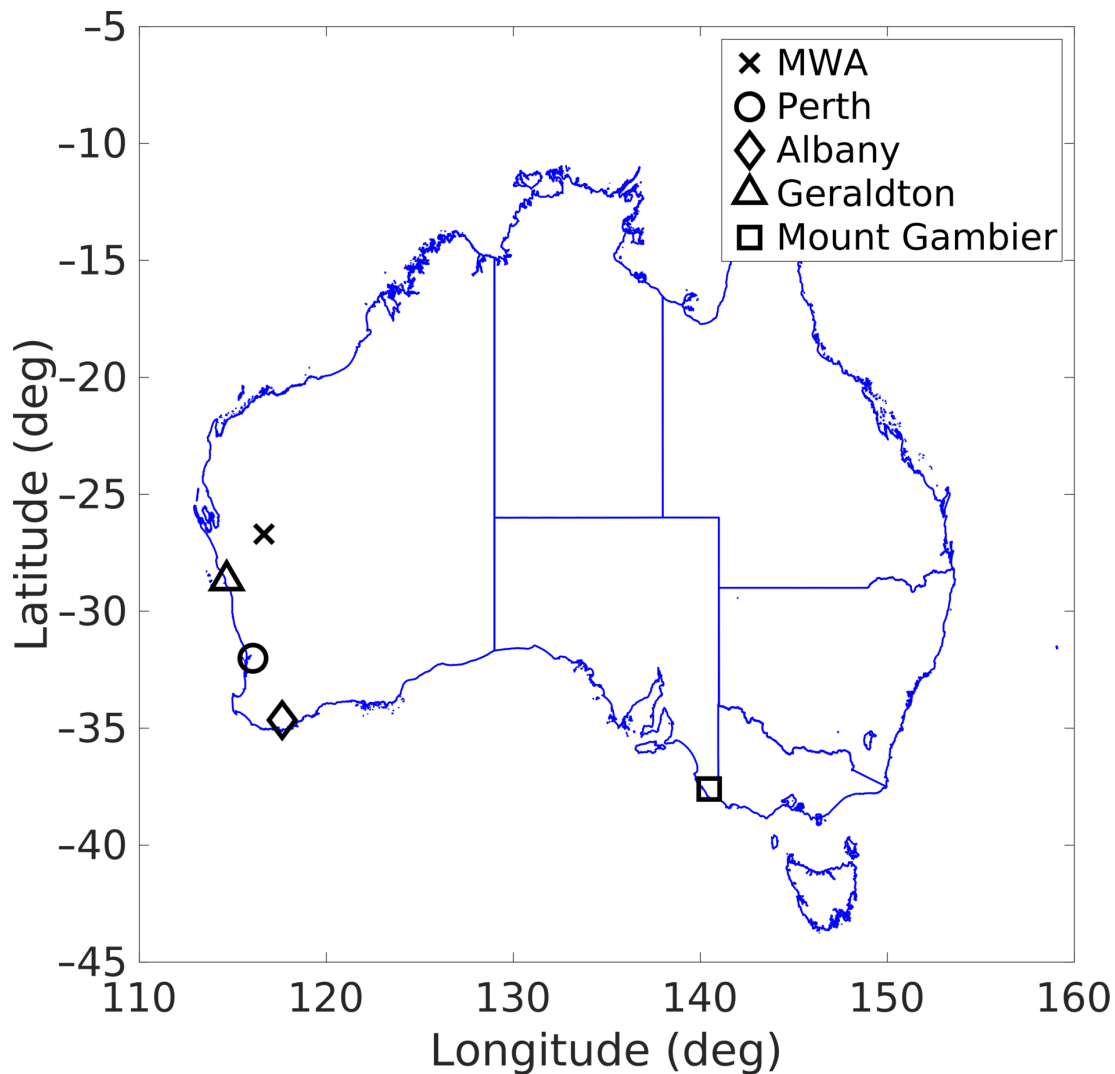


Figure 6.8: A map showing the Murchison Widefield Array as well as the transmitters used to generate the results in Section 6.5. Details of the transmitters are given in Table 6.1.

processing (and indeed, noise radar), target signals exist against a noise/clutter pedestal floor formed by the cross correlation of the reference signal against other unwanted/mismatched signals. The CFAR detector estimates this floor from a local threshold region around the cell that is being evaluated, and the SNR is determined by the peak signal against this floor. For these results, we have used a very conservative threshold of 16 dB, greatly minimising the presence of any false detections. System performance would be improved with a more realistic

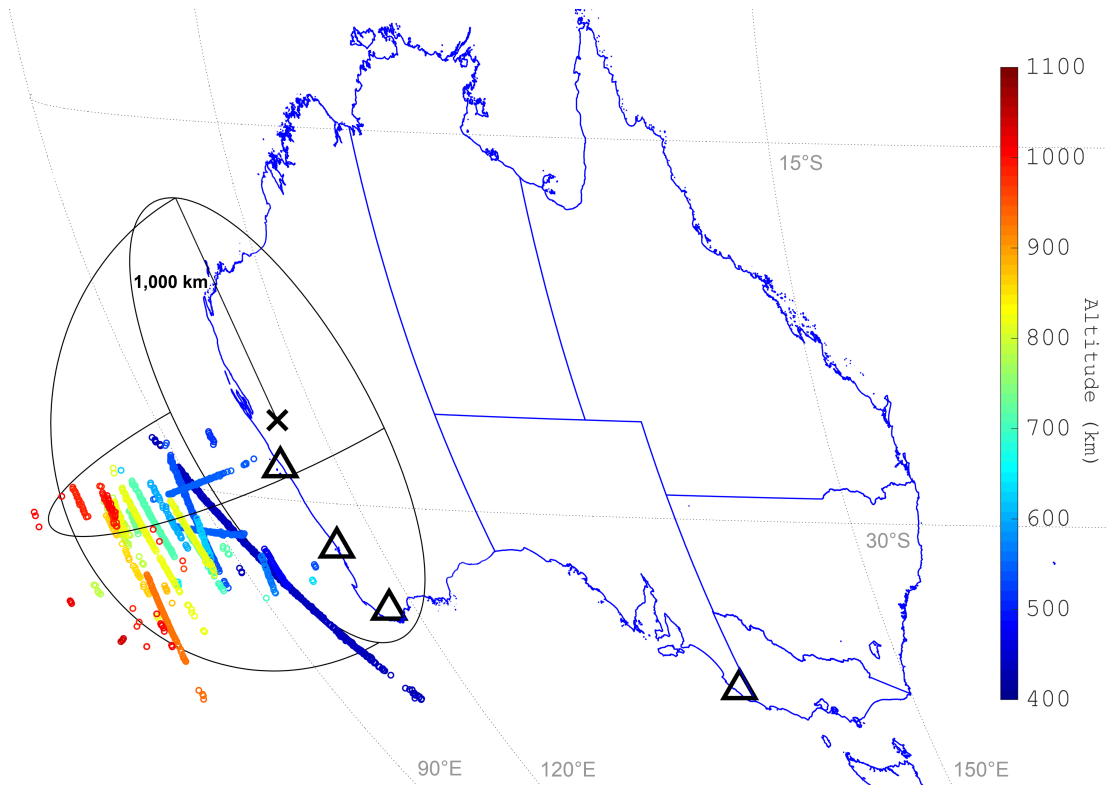


Figure 6.9: Example results showing dozens of tracks’ detections above the Murchison Widefield Array (MWA), with each detection’s colour corresponding to its altitude. The location of the MWA is shown, denoted by an X. The transmitters are also shown, denoted by the black triangles. Additionally, rings denoting a 1000-km range (from the MWA) are included.

threshold; however, care would need to be taken to ensure false detections are not incorporated into orbital estimates.

The MWA is able to maintain tracks of many targets at various ranges. During these short and targeted dwells, the MWA was able to detect every large RSO that was within the MWA’s main beam at a range of less than 1000 km. The USSPACECOM catalogue defines a large object as having a median radar cross section (RCS) of  $1 \text{ m}^2$  or greater and a medium object having a median RCS between  $0.1 \text{ m}^2$  and  $1 \text{ m}^2$ ; however, these values are for microwave frequencies which differ from those used in this paper, and should only be taken as a general indicator of size (USSPACECOM, 2023). Additionally, many detections are found outside these limits, including the detection of medium RSOs, RSOs at longer

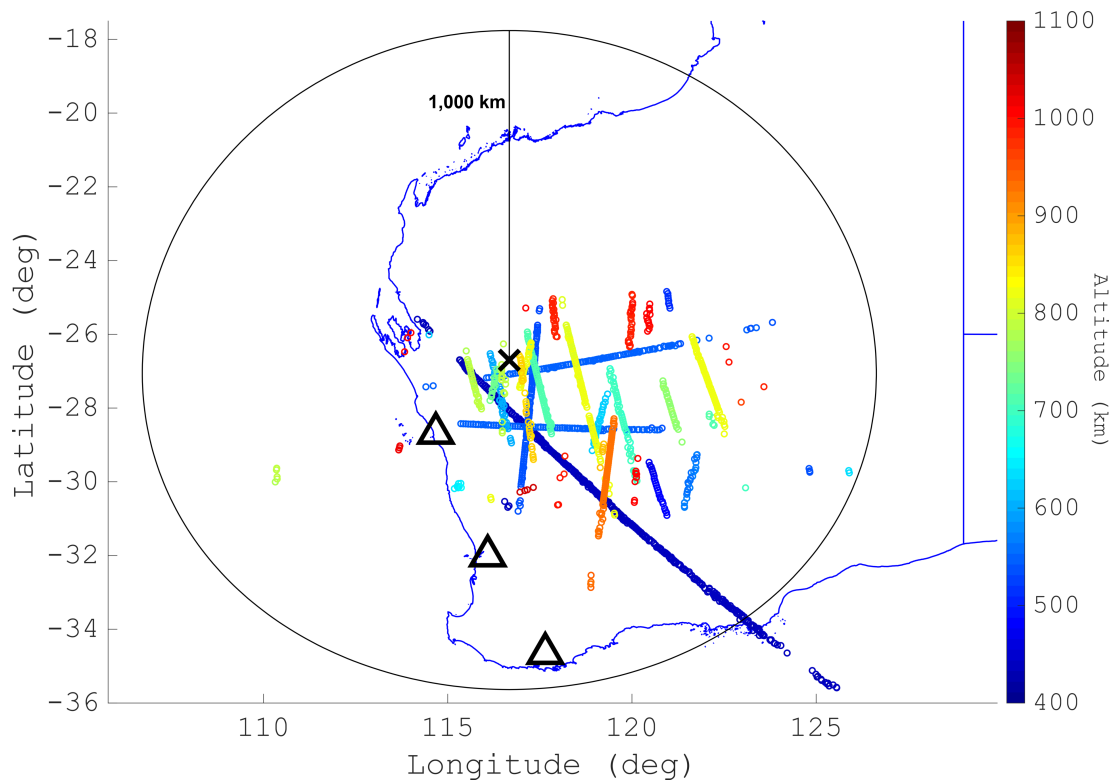


Figure 6.10: Example results, matching Figure 6.9, showing dozens of tracks' detections above the Murchison Widefield Array (MWA) with each detection's colour corresponding to its altitude. The location of the MWA is shown, denoted by an X. The transmitters are also shown, denoted by the black triangles. Additionally, a ring denoting a 1000-km range (from the MWA) is included.

ranges, and indeed RSOs well outside of the main receiver beam. This is consistent with the earlier theorised performance (Tingay et al., 2013b). Predictions of the large RSOs with a closest approach of less than 1000 km indicate the MWA would detect over 1800 RSO passes per day, when used in a beam-stare mode pointing at the zenith. However, detections outside these conservative limits, as well as the ability to rapidly adjust the analogue beamforming, suggest the true number will be larger.

Figure 6.11 shows the detections of an outbound pass of COSMOS 1707 (NO-RAD 16326), a large (now defunct) satellite. The detections were formed utilising the transmitter near Albany and show the bistatic range, bistatic Doppler, azimuth and elevation. Tracked for almost 90 s, the RSO passes the closest bistatic

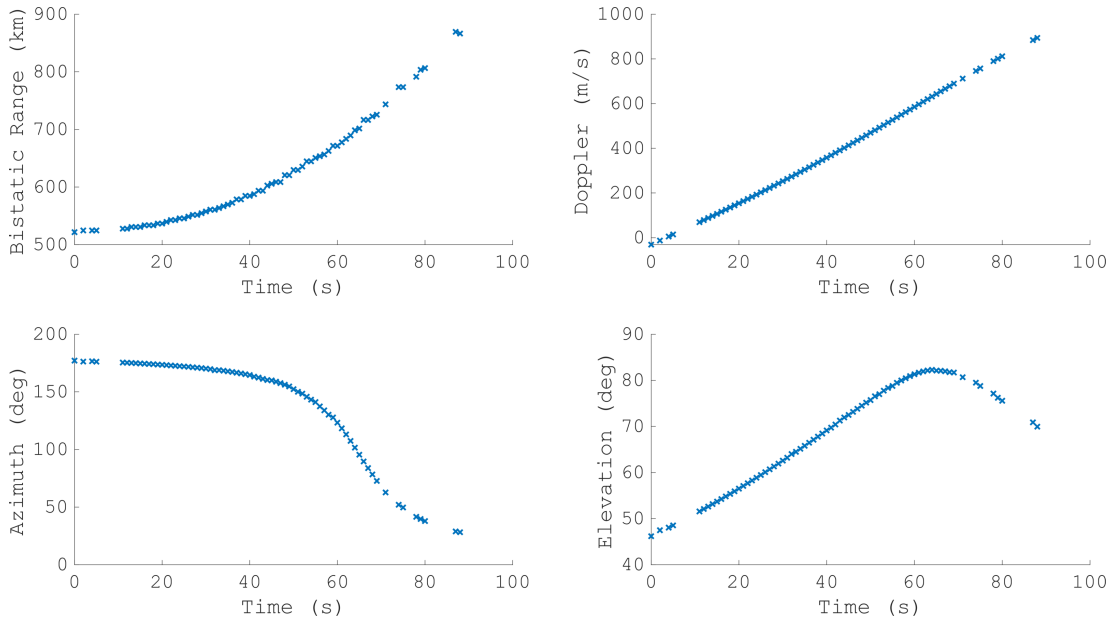


Figure 6.11: The four measurement parameters from the detections of an out-bound COSMOS 1707 detected using an FM transmitter in Albany.

approach (at zero Doppler) and moves north to the closest approach to the receiver (at its maximum elevation). Figure 6.12 shows the accuracy of the orbit generated from the COSMOS 1707 measurements. The top row shows the accuracy of the positional and the velocity covariance, from (6.34). The bottom row shows the accuracy of the position and velocity estimate in comparison to the two-line element (TLE) ephemeris. The two rows are in general agreement as to the resulting accuracy and the results are significantly improved when compared to the initial study (Palmer et al., 2017). These results are typical of most of the objects the MWA detects with a bistatic configuration.

With many more transmitters at the radar’s disposal, there is a scope for increased coverage. Figure 6.13 shows the SNR of a pass of the International Space Station for every transmitter collected in this campaign. It shows three minutes of detections with almost 50 s of complete overlap for each bistatic pair. The SNR fluctuations shown (for all transmitters) highlight the variable nature of the illuminator coverage due to changes in the transmitter beam pattern as

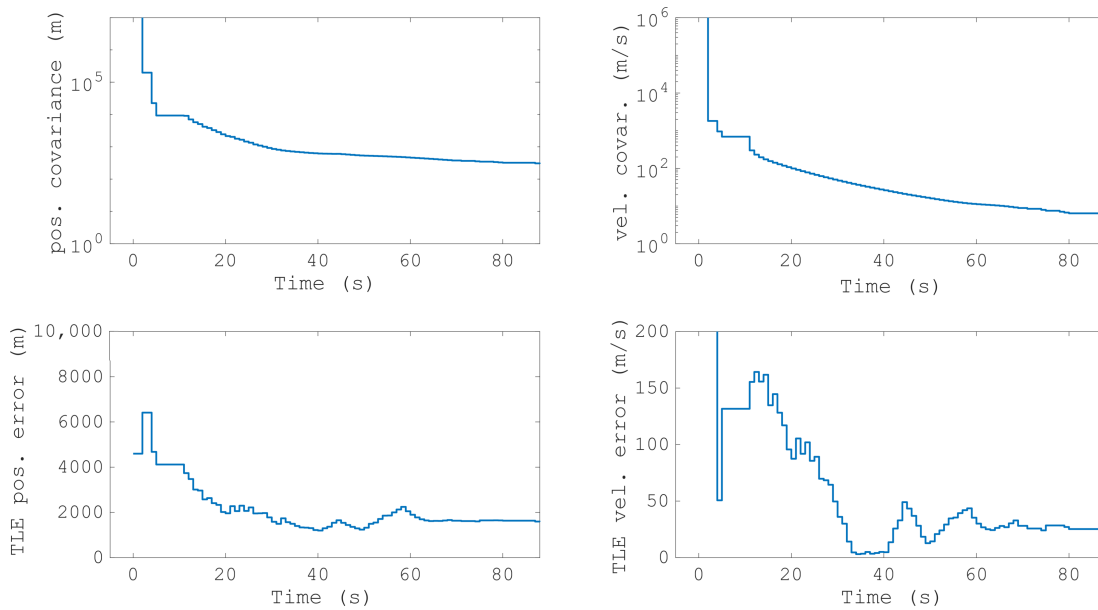


Figure 6.12: The resulting orbit predictions from the measurements from Figure 6.11. The top row shows the covariance of the position estimate and the velocity estimate; the bottom row shows the mean error when compared with the TLE.

well as variations in bistatic RCS. There may be additional contributing factors such as Faraday rotation. The ISS is detected well outside of the MWA’s receiver beam, to an elevation of as low as  $5^\circ$  above the horizon.

Although only the ISS and the Hubble Space Telescope were large enough to be detected simultaneously using all transmitters, approximately three quarters of all the detected targets had associated detections from another transmitter. Additionally, every transmitter was able to detect objects that were not detected by any other transmitter, including the comparatively weaker Geraldton site. This highlights that FM broadcast transmissions do not uniformly cover the volume above the MWA, and results will improve with more transmitters being utilised. Despite only being licensed to transmit up to a maximum of 50 kW, the particular configuration of the Albany transmitter, and its elevation sidelobes, produced the largest number of detections of all the transmitters listed in Table 6.1.

Figure 6.14 shows the detection’s measurements for the same RSO pass as in Figure 6.11; however, this time, the detections from the Perth transmitter



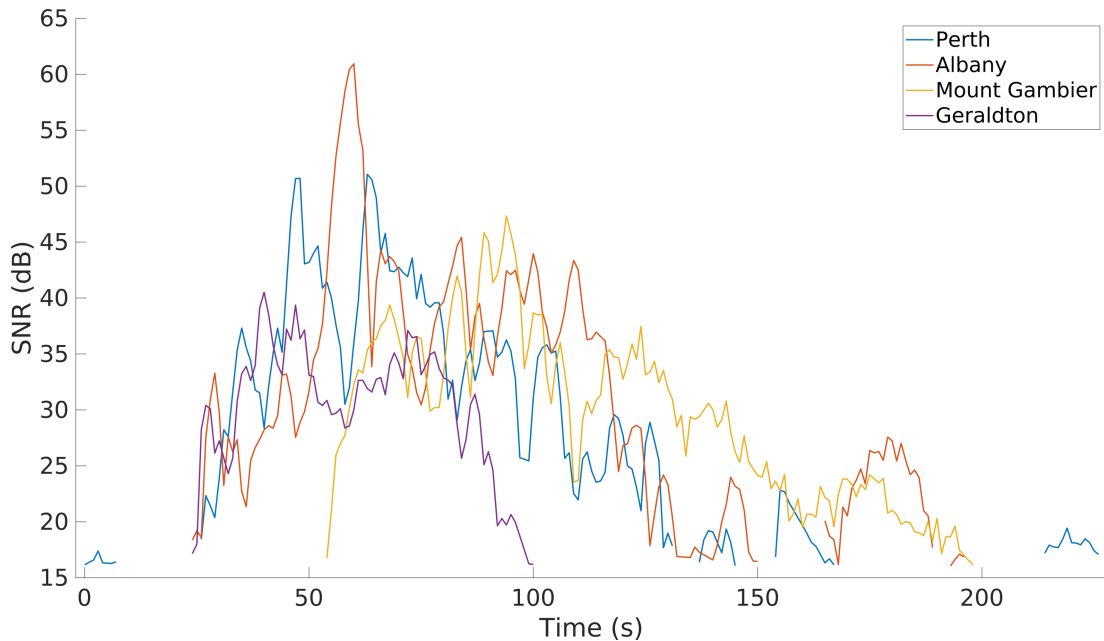


Figure 6.13: An example pass showing the signal to noise ratio (SNR) of International Space Station detections utilising all the transmitters covered in this section.

are included. The spatial parameters are near-identical as expected, with the differing geometry resulting in differing delay and Doppler tracks. When these are combined together in the OD stage, the results are significantly improved.

Figure 6.15 shows the accuracy of the combined orbit, equivalent to Figure 6.12 showing a single bistatic case. The combined orbit is significantly more accurate than either individual bistatic pairs, particularly the determined velocity. A single detection from Perth (at the 17 s mark) reduces the velocity covariance by an order of magnitude, matching the expectations outlined in Section 6.3.1.

As mentioned earlier, multistatic detections do not need to be coincident to improve the overall orbit. Figures 6.16 and 6.17 show the results from the detections of NADEZHDA 5 (NORAD 25567), a far smaller (albeit still classified as large) RSO at a range of 1000 km. The figures again show detections from both the Albany and Perth bistatic pairs, but instead of being coincident, the set of the detections are separated by over a minute. However, just as before, the multistatic detections greatly improve the accuracy of the orbit, confirmed both

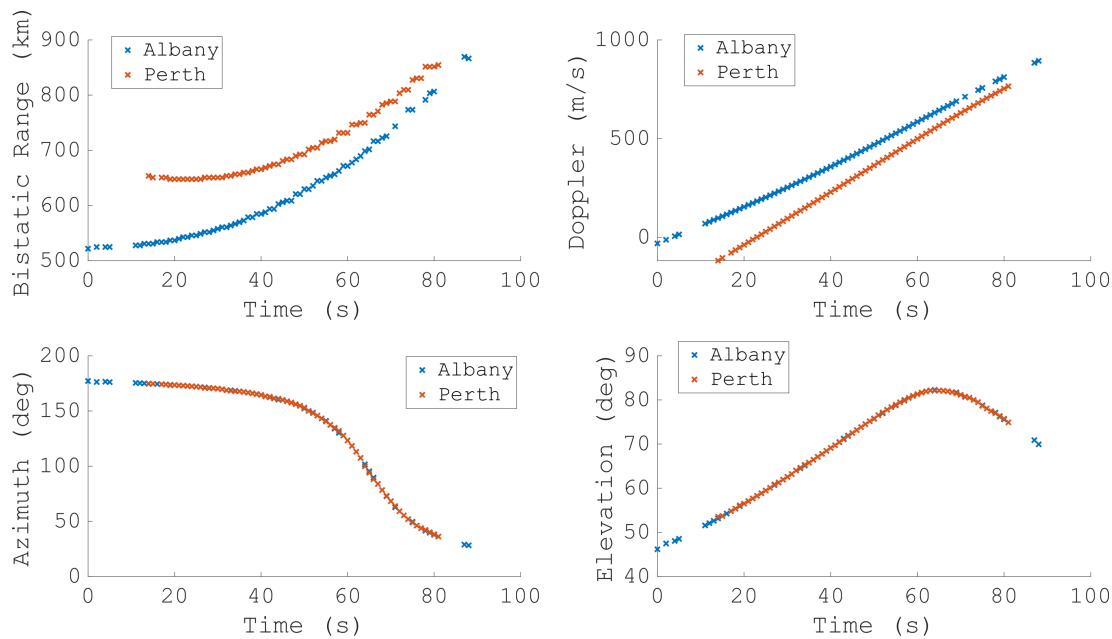


Figure 6.14: The four measurement parameters from the detections of COSMOS 1707 detected using FM transmitters in both Albany and Perth.

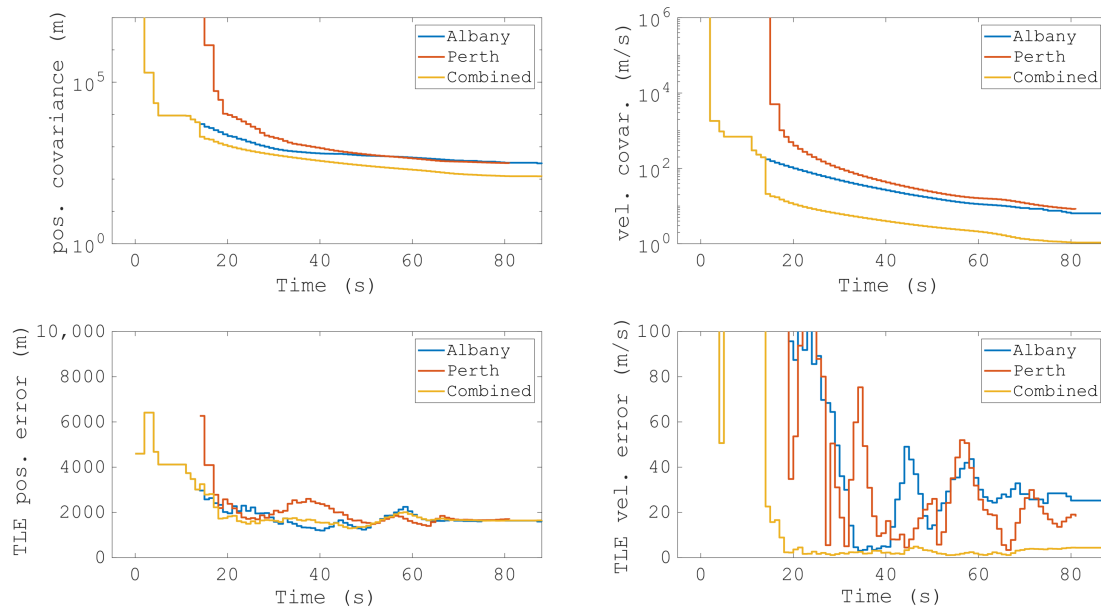


Figure 6.15: The resulting orbit predictions from the multistatic measurements from Figure 6.14. The top panels show the covariance of the position estimate and the velocity estimate. The bottom panels show the mean errors when compared with the two-line element (TLE).

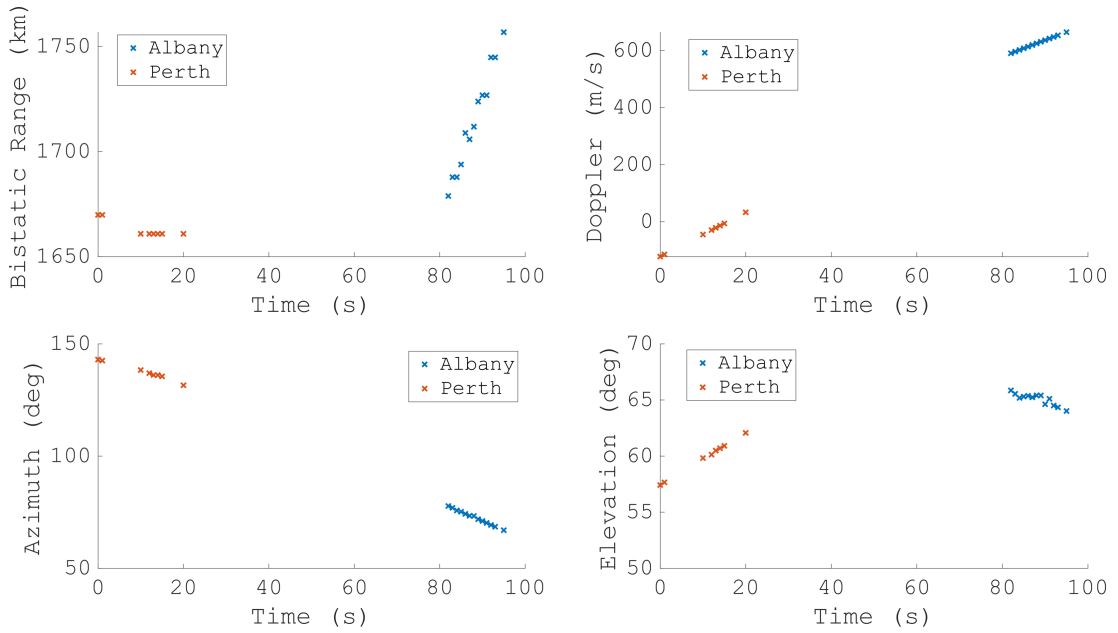


Figure 6.16: The four measurement parameters from the detections of NADEZHDA 5 detected using FM transmitters in both Albany and Perth.

by the reduced covariance as well as compared to the TLE.

An example of the three transmitters is simultaneously shown in Figures 6.18 and 6.19. In this example, the satellite OPS 5721 (NORAD 9415) is detected for approximately 20 s with the Albany illuminator; however, these detections are supplemented by a small number of detections achieved utilising the Perth and Mount Gambier illuminators. Despite the short period of detections, the resulting orbit is very accurate when compared against the TLE. Indeed, after only five seconds, the resulting orbit utilising detections across all three transmitters is very accurate.

There are complications when comparing and assessing determined orbits, especially when comparing them to the TLEs. Looking at the covariance of the multistatic results in Figure 6.15, the increasing number of detections improves the estimate, especially for velocity. However, when compared to the TLE, the error does not improve; rather, it plateaus. This could be due to many factors; however, these results are within the accuracy of the TLEs themselves, as posi-

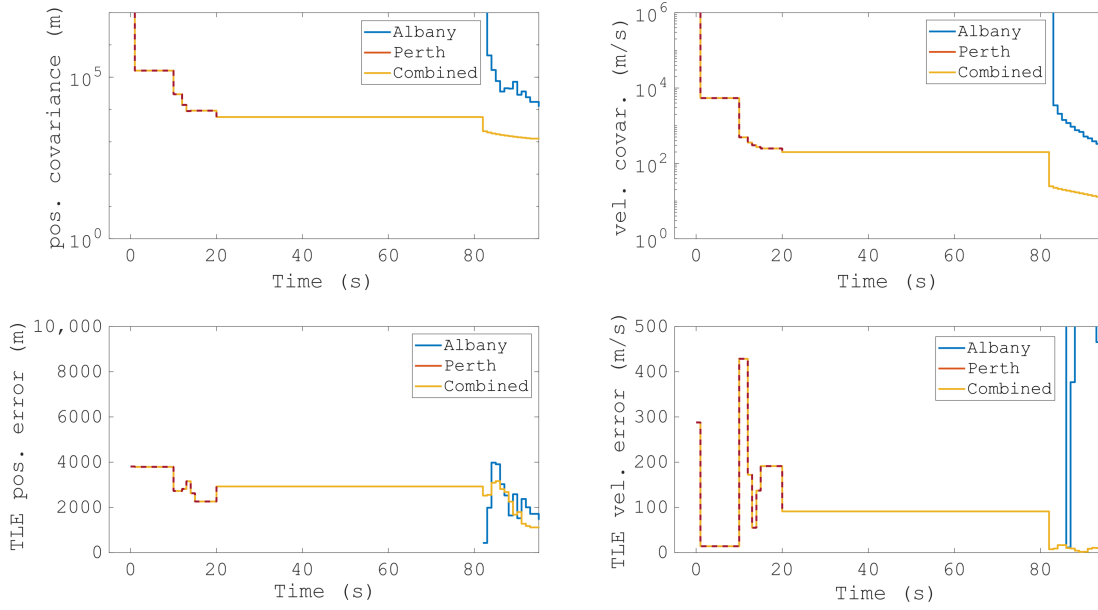


Figure 6.17: The resulting orbit predictions from the multistatic measurements from Figure 6.16. The top panels show the covariance of the position estimate and the velocity estimate. As the detections from each bistatic pair are not coincident, the combined errors will be initially identical to Perth’s. The bottom panels show the mean errors when compared with the two-line element (TLE).

tional errors generally vary from a minimum error of approximately 1 km at the TLE’s epoch up to 5 km, depending on the age of the TLE (Vallado et al., 2006; Ly et al., 2020). These uncertainties could potentially mask any systematic biases or offsets, either from the system itself or from the ionosphere (Hapgood, 2010; Holdsworth et al., 2020). Longer surveillance campaigns are needed to properly assess any potential systemic issues and to fully evaluate the accuracy of short-arc orbit determination.

The true RCS sizes of objects are challenging to estimate, particularly for a passive radar. Without knowing the precise details of transmitter characteristics, the amount of incident power is not known. Additionally, bistatic RCS is typically a complicated function and without accurate knowledge of the precise size and attitude of RSOs, the bistatic RCS is difficult to determine.

The RCS values for known RSOs can be coarsely estimated with simple shapes, such as cylinders. Comparing the estimates of the detected objects pro-

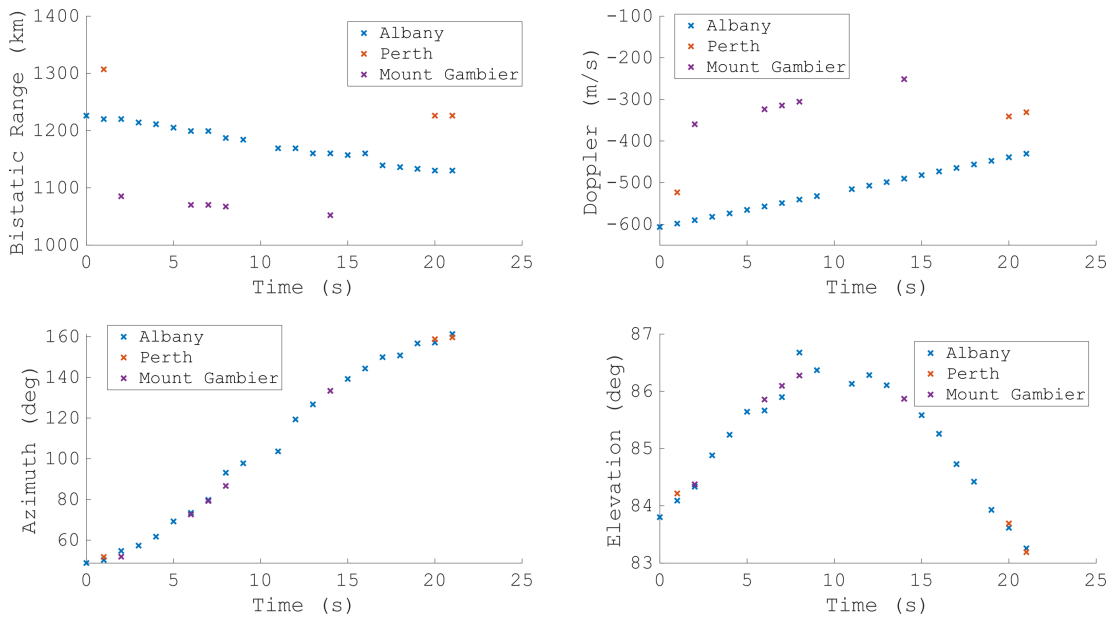


Figure 6.18: The four measurement parameters from detections of OPS 5721 detected using FM transmitters in Albany, Perth and Mount Gambier.

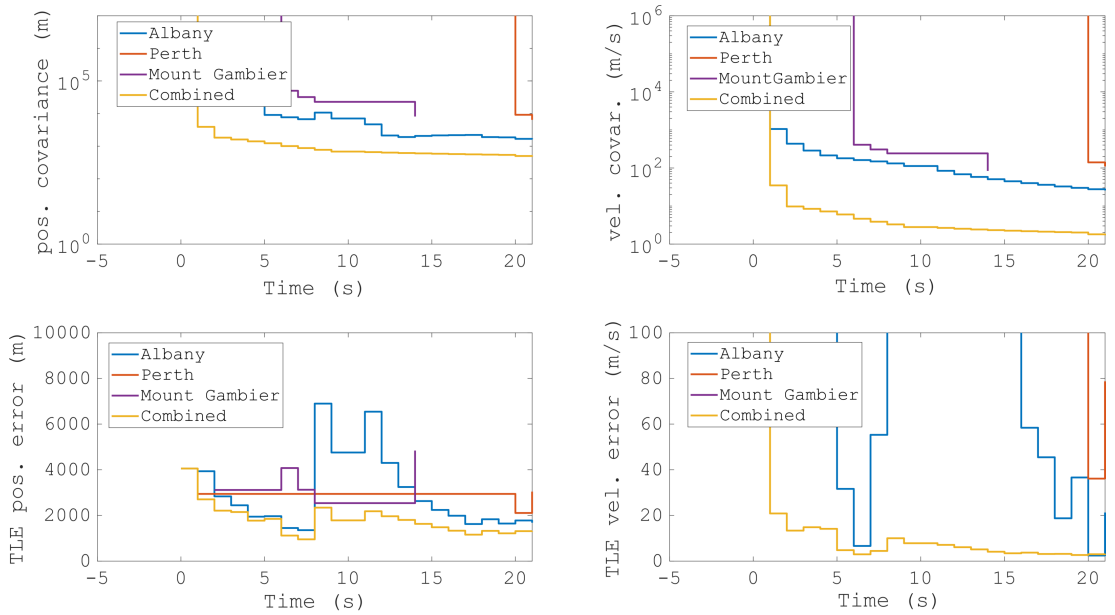


Figure 6.19: The resulting orbit predictions from the multistatic measurements from Figure 6.18. The top panels show the covariance of the position estimate and the velocity estimate. The bottom panels show the mean errors when compared with the two-line element (TLE).

vides additional data points to match against the earlier performance predictions. For example, the medium RCS satellite OV1-5 (NORAD 2122) was detected at a range of 1150 km from the MWA (the corresponding bistatic range was 1600 km) with an SNR of 21 dB. The maximum monostatic RCS of a cylinder of matching dimensions (1.387 m length and 0.69 m diameter) is approximately  $0.7 \text{ m}^2$ . For OV1-5, the RSO's length is less than half a wavelength, meaning that for smaller RSOs, the scattering will cause the RCS to decrease rapidly (Knott et al., 2004). Conversely, for RSOs that possess trailing antennas that have low RCS at high frequencies, these structures can produce a large RCS at MWA frequencies. Examples such as OV1-5 agree strongly with the initial predictions that the MWA, used as a passive radar, is able to detect objects with an RCS of  $0.5 \text{ m}^2$  to a range of 1000 km (Tingay et al., 2013b).

## 6.6 Conclusion

This paper has described the use of the MWA as a passive radar for the surveillance of space with FM radio illumination. The MWA's high time-resolution and receiving capabilities have been described, and the orbital-specific signal processing methods to form radar products have been detailed, from pulse compression through to forming detections. These orbital-specific methods are required to track an RSO's motion throughout long CPIs to increase SNR. Following detection, the paper details the orbit determination methods, and how multistatic detections can greatly improve the orbital estimate. To demonstrate and verify these methods, this paper includes the results of a short collection campaign, utilising four transmitters across the country. With the data collected during this campaign the MWA was able to detect and accurately track every large object that passed through its main beam at a range of 1000 km or less. It additionally tracked many other objects outside these limits. These results are in agreement with earlier predictions made of the space surveillance capabilities of the MWA when used as a passive radar receiver.

Multiple transmitters were used to form a multistatic radar network, with multistatic detections allowing for rapid and accurate orbit determination, with additional transmitters also providing greater coverage and resilience. By utilising these many transmitters, the MWA is able to provide persistent and widefield coverage of satellites in low Earth orbit. The MWA is able to achieve this coverage using scalable and efficient signal processing matching the radar processing to the RSO's orbit. The widefield coverage ensures that RSOs are tracked for sufficient time to accurately determine an orbit from a single pass.

Although it is not the SKA's intended purpose, using the techniques described here, the SKA will be a highly capable space surveillance sensor when used as a radar (Stove, 2013). The SKA will be significantly more sensitive than the MWA, and even a modest increase in sensitivity would enable the detection of signals from a higher altitude (for example, from 1000 km to 2000 km). As shown in Figure 6.6, higher altitudes would intrinsically allow the utilisation of transmitters at even greater distances, including along Australia's eastern seaboard. Conversely, since transmissions reflected from RSOs are a source of interference for astrophysical observations, knowledge of which RSOs are above the horizon will be important information for the removal of RSO effects from SKA observations. Incorporating a system to remove interference reflected from RSOs would be a natural extension for any radio telescope space surveillance radar.





# Chapter 7

## Discussion and Conclusions

The primary aim of this thesis has been to investigate the use of the Murchison Widefield Array (MWA) as a passive radar receiver for the surveillance of space, with a particular focus on practical measures to achieve these surveillance capabilities. These approaches have been developed and demonstrated with observations focused on signal processing improvements, initial orbit determination, and a large scale set of observations for space surveillance.

The required novel approaches and ideas which have been discussed in this thesis have included the investigation of radial acceleration and radial jerk processing for long CPI integration and the demonstration of radar functionality with separately collected reference signals. The analyses also include environmental-based synchronisation and calibration of an undisciplined reference signal. These advances have led to an improved sensitivity for the detection of smaller objects.

A key outcome for the uncued detection of space objects resulted from the investigation of the intersection between the orbital motion parameter space and the radar measurement parameter space. Following this, the thesis has shown that linking the measurement parameters and the orbital motion parameters leads directly to the most efficient implementation of the pulse-Doppler approximation algorithm for matching orbits, ensuring that every radar measurement parameter is mapped directly back to the requisite orbital elements.

The demonstration of these methods culminated in a brief observational campaign, with the MWA forming the radar receiver as part of a continental-scale multistatic network. The large aperture of the MWA, which initially caused significant processing challenges, now directly enables extremely accurate orbital estimates of satellites and other objects. The accuracy is improved by utilising multistatic orbit determination arising from multiple transmitters across the country. These detections met the initial predictions for the passive radar sensitivity of the MWA. The ultimate result is a widefield sensor able to surveil a significant volume of the low Earth orbit space above it.

More generally, the methods described in this thesis were developed for a large-aperture observatory-scale system. However, these methods have been also been demonstrated on a deployable passive radar system. This shows that any space surveillance radar can benefit from orbital-specific radar parameter matching to increase sensitivity and decrease processing requirements.

Radio astronomy is plagued by radio frequency interference from terrestrial transmitters (as well as from space-borne transmitters). This problem is exacerbated by the reflected RFI from large satellites in low-Earth orbit. As well as detecting satellites, the techniques described in this paper could be used to remove the RFI from astronomy data. Indeed, as reference signals are needed for coherent radar processing, collecting known-interfering signals directly would also enable optimal RFI clutter removal. As high time-resolution observation modes become more ubiquitous, and with improved computational processing, time-series techniques may be more applicable to radio astronomy data, and see more utility, prior to standard astronomical imaging.

Finally, the types of signals that radio telescopes are able to detect, such as solar and extra-galactic emissions, have shown great potential as radar illumination sources. Expanding passive radar processing to the concept of extreme-baseline forward scatter space surveillance could very well unlock vast surveillance possibilities.

# Appendices



# Appendix A

## Deployable Long Range Passive Radar for Space Surveillance

This thesis has focused on the development of techniques for space surveillance capabilities with the Murchison Widefield array, an incredibly unique sensor, these capabilities may be more broadly applicable and this will be addressed in this appendix. Similar to previous chapters, this appendix is reproduced from the author's publication (Hennessy et al., 2022a). The reader will encounter some repetition of material in the introductory sections.

### A.1 Abstract

A deployable long-range passive radar system has been used to observe satellites in low Earth orbit utilising distant transmitters in real time. This paper details the experimental radar's design, including its array, configuration and software. Methods to improve satellite detections and initial orbit determination are also described. The radar is capable of detecting objects the size of small rocket bodies, in real time, utilising a transmitter 300 km away. Additionally, during post-processing, satellites were detected when utilising a separately collected reference, from a transmitter 1,600 km away. Such a system enables passive long-range

detection at considerable standoff ranges from transmitters of opportunity.

## A.2 Introduction

Radio broadcast transmissions at VHF are an excellent illuminator for long range surveillance with passive radar. The large transmitter power and generally broad elevation beam ensures a significant volume is illuminated, particularly at longer distances from the transmitter. The majority of passive radar systems are located within line-of-sight of the transmitter in order to ensure the direct collection of the reference signal. Whilst this ensures a strong reference is collected, it can hamper the performance of the radar as target returns are received in the presence of the (significantly stronger) illuminating signal, with target returns needing to be separated from the reference. Further, this configuration reduces the potential locations for passive radars due to the limited transmitter footprint. This limitation is particularly challenging in a large country like Australia.

The experimental radar described in this paper is a passive radar system designed by the Defence Science and Technology Group (DSTG) to take advantage of FM radio illuminators of opportunity for long range surveillance. During a recent trial to test and evaluate this radar in the Woomera Test Range, there was an opportunity to collect data focused on the detection of satellites utilising transmitters at significant standoff ranges. The measurements of satellites are incidental to the radar's main purpose and were collected as part of system testing and calibration.

The use of FM radio for passive radar has been well studied and developed, with many systems achieving maximum aircraft detection ranges up to 350 km (Howland et al., 2005; Malanowski et al., 2012, 2014; O'Hagan & Baker, 2008; Sahr & Lind, 1997). These systems utilised baseline lengths less than 100 km, at this distance performance is often limited by the interference of the transmitted direct-path signal appearing in the surveillance receiver (O'Hagan & Baker, 2008).

Extending the transmitter-receiver baseline offers significant advantages for

long-range surveillance, notably reducing the impact of the direct signal on the receiver as well as increasing the surveillance volume by taking greater advantage of the radiative properties of the transmitter. Greater separation from the transmitter also increases the electromagnetically covert nature of a passive radar system.

DSTG has long undertaken experimental research in passive radar. DSTG’s research has focused on experiments within the large landmass of Australia, as surveilling such a large coast line and airspace is a significant challenge, and technologies such as passive radar can assist in this challenge. DSTG has previously investigated the application of passive radar with a wide variety of potential illuminators, including FM radio (Ringer et al., 1999), DAB, DVB-T (at VHF and UHF) (Palmer et al., 2008), and DVB-S (Palmer et al., 2009). Recent space surveillance radar research has investigated the use of a number of novel sensors including a High Frequency Line of Sight system (Frazer et al., 2013b,a), a radiotelescope (the Murchison Widefield Array (Tingay et al., 2013a)) used as a passive radar receiver (Palmer et al., 2017; Hennessy et al., 2019; Hennessy et al., 2021), and wind height profiling radar (Holdsworth et al., 2020).

With the ever-increasing amount of energy being radiated by terrestrial transmitters, and the wide area of illumination, space surveillance with passive radar is increasingly realisable (Sahr & Lind, 1997; Tingay et al., 2013b; Clarkson & Palmer, 2019; Malanowski et al., 2021b). This paper describes the design of a deployable radar system intended to operate in a low noise environment, including the array, radar configuration and real-time signal processing. It details detections and tracks of both aircraft as well as objects in low Earth orbit (LEO) at long ranges.

Section [A.3](#) details the system design including the array, receiver system and remote reference collection configuration. Section [A.4](#) describes the real-time signal processing software, and Section [A.5](#) includes the results of the system. This includes details of the detections of satellites with different array configurations,

description of orbit determination and orbital-specific processing to mitigate spatial ambiguities from grating lobes, detections with a remotely collected reference from a baseline of 1,600 km, and long-range aircraft detections.

### A.3 Radar System Description

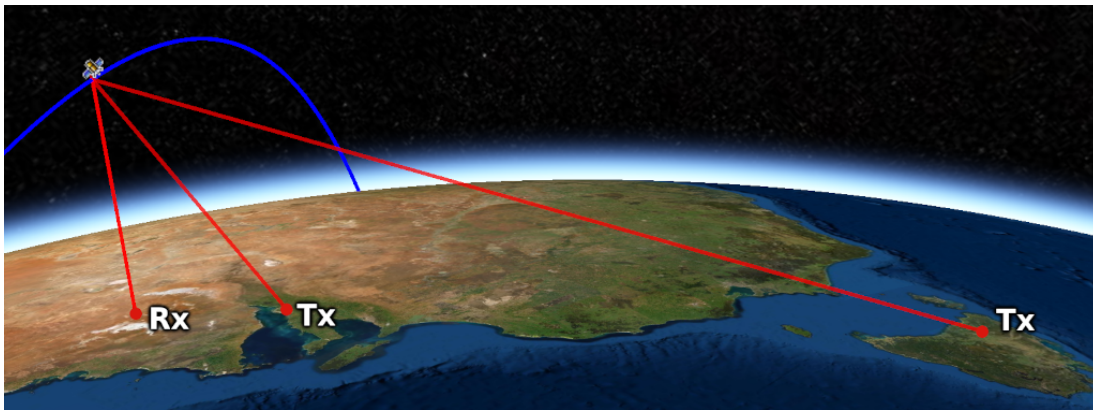


Figure A.1: The configuration of the system for the experiments covered in this paper. The passive radar receiver is utilising two transmitters, one close and one at a significant stand-off range. The receiver-to-target and transmitter-to-target paths are shown in red. The satellite trajectory (corresponding to a pass in Fig A.6) is shown in blue.

The description of the system in this section relates to the configuration used in a test deployment undertaken by DSTG during 2020. The aim of the test was to evaluate the radar in a low noise environment, trialling a variety of array configurations to observe both satellites in LEO and aircraft. The receiver system was located in the Woomera Test Range and utilised two FM radio transmitters as illuminators. The configuration is illustrated in Fig. A.1.

#### A.3.1 Array Design

A simple dipole array is ideal for all-sky surveillance, however this requires a large number of elements for spatial accuracy, with sufficient array gain to compensate for reduced element gain. Instead, the deployed system utilised a small number



of directive antennas, with beamwidths of  $50^\circ$  in each plane, and 11 dBi gain. The smaller number of elements allows the system to be more easily deployable, while providing effective coverage of a smaller, but still considerable, region of the sky.

The surveillance array consisted of seven antennas in an equispaced hexagonal configuration, with an element in the centre. The antennas are large, dual-polarised Yagis. In an effort to minimise antenna pattern distortion, the antennas are mounted on 3D printed reconfigurable mounts to adjust the antenna tilt whilst minimising the metal near the elements.



Figure A.2: Sparse array configuration with the antennas directed at Zenith. Array elements configured in a hexagonal configuration with an element separation of  $\lambda$ .

Due to the long wavelengths, as well as the large antennas, the array-element spacing was increased in order to minimise mutual coupling and other effects. The advantage of a sparse configuration is that the spatial accuracy will be significantly increased through the narrowing of the array pattern beamwidth, whereas the disadvantage is an increase in grating lobes. These are less of a concern given the directive antennas mean the system only surveils a specific region of the sky. However, great care needs to be taken to ensure ambiguous spatial detections are

handled appropriately.



Figure A.3: Hypersparse array configuration with the antennas directed at  $30^\circ$  elevation above the horizon. Array elements configured in a hexagonal configuration with an element separation of  $2.5 \lambda$ .

For this paper the two configurations discussed are a sparse configuration with an element separation of  $\lambda$  (as shown in Fig. A.2), and a hypersparse<sup>1</sup> configuration with a separation of  $2.5 \lambda$  (Fig. A.3). At these frequencies, the element separations for the two configurations were 2.86 m and 7.16 m respectively.

### A.3.2 Radar Configuration

Low-loss and phase-matched cables connect the array elements to a front-end amplification and calibration box. This includes the surveillance array and a reference antenna pointed towards the transmitter. For each antenna, both polarisations are collected. The amplification and calibration box consists of front

---

<sup>1</sup>Hypersparse being five or more times greater than the standard unambiguous element separation of  $\frac{\lambda}{2}$ .

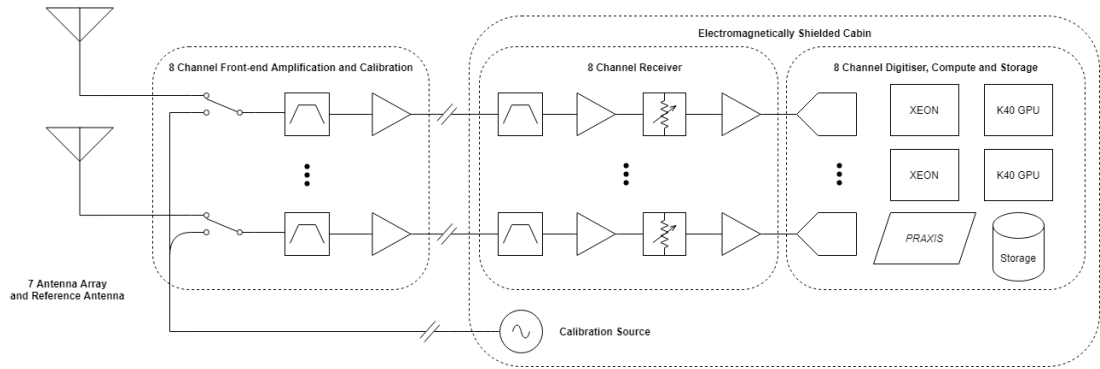


Figure A.4: Radar system block diagram, showing front-end amplification, calibration, gain and filtering. The chain is replicated for each polarisation.

end filters, significant low noise amplification, a configurable calibration-signal injection point and finally buffer-driver amplification. To maximise sensitivity to the weak reflected signals in the environment, the system is located far from the transmitter to help achieve a system that is externally noise limited.

The buffer-driver amplification is required to enable a standoff distance between the array and the EM-shielded cabin housing the receiver equipment. The EM-protection is included to shield the receiver stages inside the cabin. However in such a low noise environment, the shielding is most beneficial for preventing EM interference generated by the electronic equipment from leaking out of the container<sup>2</sup>. The radar system block diagram is illustrated in Fig. A.4.

The significant amplification and number of gain stages is required due to the extreme baseline length between the transmitter and the receiver. For this collection period the closest (large) transmitter was 300 km away. Despite this large distance, there was sufficient signal diffracted/propagated along the baseline to enable the direct collection of this reference signal, due to the favourable propagation at low frequencies and the lack of competing sources. These types of transmissions are readily received at these long distances in low noise environments across Australia (Tingay et al., 2020).

<sup>2</sup>Anecdotally, the noise floor increased by approximately 10 dB when the cabin door was opened, releasing the electronic spuria.

Calibration is achieved by switching the front-end input to a calibration source, and estimating each channel’s relative phase-delay and gain from the measurements of the calibration source.

### **A.3.3 Remote Reference Collection**

Relying on sufficient over-the-horizon propagation in order to obtain a copy of the reference signal can be problematic. Reduced signal levels, fluctuations in weather conditions and changes to the background noise can all mask the desired signal. Another issue with short baselines is the reliance on sufficient elevation sidelobe levels to illuminate objects in orbit. Even with a baseline distance of 300 km, a satellite above the radar will still be at a significant elevation above the horizon relative to the transmitter and well outside of the main beam (O’Hagan et al., 2017).

In order to make use of very distant transmitters for larger baselines, a different method is needed to obtain the reference signal. The reference signal can be obtained directly from a site closer to the transmitter, which is then relayed to the receive site for real-time processing, or recorded for offline-processing. This configuration is far better suited for satellite illumination as this allows the surveillance receiver to be located at distances significantly beyond the broadcast coverage of the transmitter, thereby allowing placement in extremely RF-quiet locations.

For the work presented in this paper, such a remote reference collection system was deployed at DSTG’s site in Tasmania, conveniently located near one of the country’s largest radio transmitters. This geometry achieved a baseline of over 1,600 km.

The remote reference collection system consisted of a software defined radio, a GPS receiver, and a laptop. The system was remotely triggered to record signals at the same time as the surveillance receiver. Comparable reference collection configurations are being utilised for similar systems requiring extended

baselines (Jędrzejewski et al., 2021; Hennessy et al., 2021). Although the full spectrum was collected at a high fidelity, FM radio reference signals are quite tolerant to downsampling, further enabling real time remote reference utilisation in future work (Sahr, 2007).

## A.4 Praxis

A real-time demonstrator software system, Praxis, has been developed to demonstrate a diverse range of passive radar signal processing algorithms. Praxis covers three features of real-time demonstration; signal acquisition from the receiver, signal processing and visualisation. The novel concept that drives Praxis' development is a real-time configurable topology of signal processing blocks, termed *Glisser*. Glisser permits simultaneous processing of different target scenarios with different signal processing requirements, termed *Glides*. For this experiment Glisser was configured for a low-elevation air traffic scenario consisting of range migration compensation and low-elevation direction-of-arrival (DOA) estimation, and a high-elevation space target scenario consisting of Doppler migration compensation and zenith-elevation DOA estimation. Each signal processing scenario requires Direct Path Interference (DPI) clutter suppression (Palmer & Searle, 2012), pulse compression (Palmer et al., 2011) and range-migration mitigation (Perry et al., 2007). Following this common processing the chain is split into two separate but parallel processed Glides where the scenario dependent processing is performed as shown in Fig. A.5. A DOA scheme similar to that described in (Palmer, 2015) was used in order to digitally form beams in the delay-Doppler domain rather than the time domain. Both scenarios require direct path interference cancellation. For this experiment, Praxis was running on consumer-grade dual-CPU workstations with pairs of NVIDIA GPGPUs for parallelisation of signal processing algorithms.

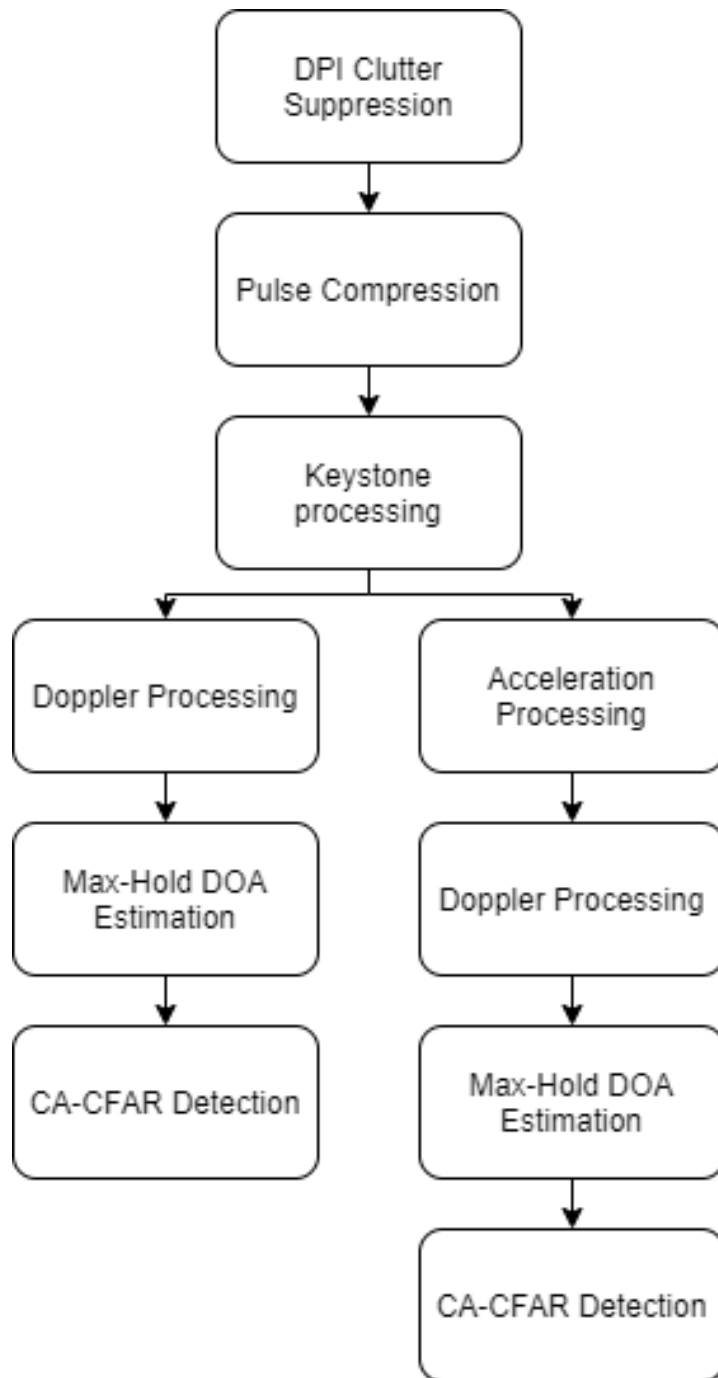


Figure A.5: Signal processing block diagram illustrating Praxis' multiple Glides for performing processing on two distinct target scenarios simultaneously.

## A.5 Results

For the satellite detection processing, Delay-Doppler maps are formed by searching through azimuth, elevation and Doppler-rate (radial acceleration) and these radar products are passed through a CFAR detector. The resulting detections are associated with satellites, specified by a catalogue of orbital tracks, typically characterised by two-line element set (TLE) descriptors (Vallado & McClain, 2001). The processing in this section utilised a CPI length of 3 s, and sample rate of 100 kHz. In real time, the system was able to detect many large satellites in orbit, including the International Space Station (ISS), smaller objects such as rocket bodies, as well as Starlink satellites at their operational orbit altitude.

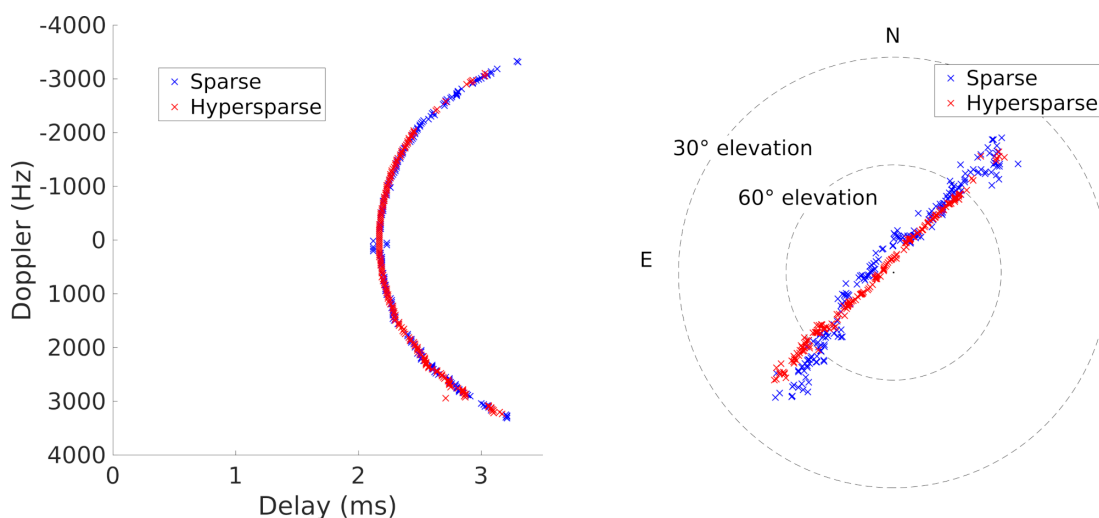


Figure A.6: Detection output of two near-identical passes of the ISS, one pass observed with the sparse array, the other pass observed with the hypersparse array. The left subplot shows the detected delay and Doppler, the right shows the detections' azimuth and elevation.

The common approach for detection and tracking undertaken by space surveillance sensors is to perform an initial orbit determination (IOD) step and then to refine and improve this initial estimate with subsequent orbit determination (OD) (Vallado & McClain, 2001). For detections which are able to be associated to a known track, the IOD step is not required. The separation of approaches is

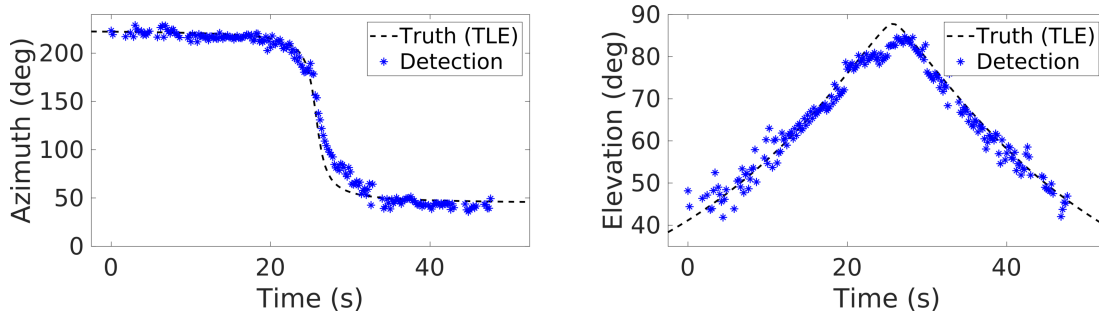


Figure A.7: Spatial returns from the sparse configuration of the ISS pass in Fig. A.6, as well as the associated TLE.

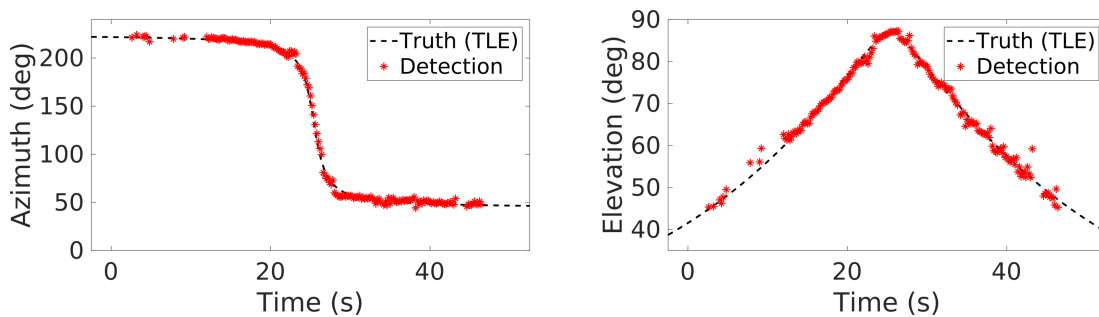


Figure A.8: Spatial returns from the hypersparse configuration of the ISS pass in Fig. A.6, as well as the associated TLE.

beneficial for space domain awareness generally, as many narrow-field sensors are unable to perform the IOD step and instead require *a priori* tracks. However, a wide-field passive radar system is able to perform the full uncued detection and track objects throughout the pass.

The array configuration choices detailed in Sec. A.3.1 lead to interesting implications for the IOD and OD steps. Increasing the element separation greatly improves the spatial resolution, and so improves the accuracy of the orbit. However, the spatial ambiguities which are introduced by a separated array makes IOD increasingly challenging.

This is illustrated in Fig. A.6, showing two near-identical passes of the ISS observed by the two array configurations. It is clear that whilst the detections are similar in delay and Doppler space, the spatial accuracy of the increased



Table A.1: Errors of the generated orbits from the single ISS passes from Fig. A.6, when compared to respective TLEs.

Array Configuration	TLE position error	TLE velocity error
Sparse	16.1 km	147.7 m/s
Hypersparse	5.6 km	74.3 m/s

separation is noticeable. This is particularly highlighted by Figures A.7 and A.8, showing the spatial parameters of the two passes, compared with the truth. The angular mean-square errors for the sparse array pass (Fig. A.7) was  $6.7^\circ$  azimuth and  $2.2^\circ$  elevation, and for the hypersparse array pass (Fig. A.8) the errors were  $2.1^\circ$  azimuth and  $0.8^\circ$  elevation. The increased accuracy of the larger aperture will greatly improve the quality and accuracy of any resulting orbit.

The OD step is achieved by finding the set of orbital elements given by a cartesian position and velocity that, when propagated to match the detections, minimise the residual differences between the detections and the predictions (Montenbruck et al., 2002). Table A.1 shows the results of this process on the two ISS passes shown in Fig. A.6, comparing the generated elements against the TLE. The extent of the errors, especially for the hypersparse configuration, are approaching the magnitude of the errors of the TLEs themselves, and will certainly be improved by incorporating subsequent passes (Flohrer et al., 2008).

Although the residual errors from the OD step are greatly reduced, the ambiguous spatial returns resulting from the increased separation makes direct IOD quite difficult. Figures A.9 and A.10 show the spatial returns of a single range of a near-zenith pass of the ISS and a Starlink satellite, respectively. The left subplot shows the standard array response, with processing only in the spatial, range, Doppler and Doppler-rate parameters. The grating lobes of the array results in the large number of peaks in the map. However, because of the constrained nature of orbital motion, only a small subset of potential spatial returns can correspond to the delay and Doppler returns. As shown in other work (Hennessy et al., 2021; Hennessy et al., 2020), by limiting the processing to only search through viable

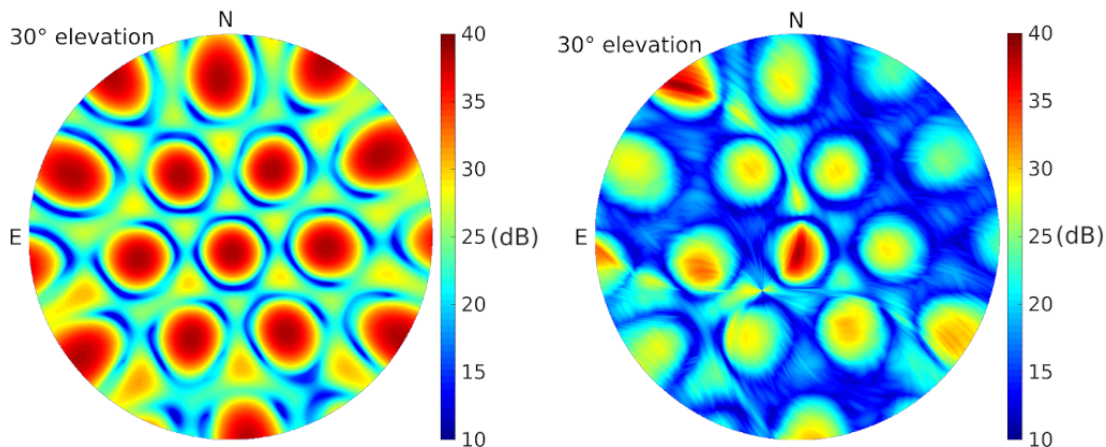


Figure A.9: The left subplot is the SNR spatial response of the ISS as it passes near zenith and the right subplot shows the results when the combination of parameters are constrained to be valid orbits only. The spatial response is shown from an elevation of  $30^\circ$  up to zenith. The array was in the hypersparse configuration.

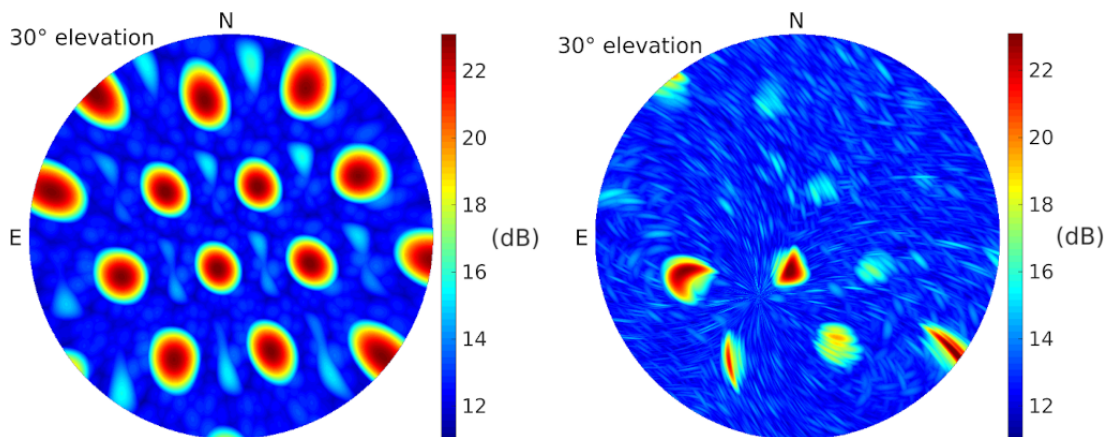


Figure A.10: As for Figure A.9, except for a Starlink satellite.

Doppler-rates (dependent on the Doppler and the direction), it is possible to reduce, or eliminate, a large number of these grating lobes. This is highlighted by the right subplots of Figures A.9 and A.10. Note, any resulting ambiguities will need to be handled with other methods, such as temporal filtering by comparing IOD outputs against the resulting tracks.

### A.5.1 Remote Reference Collection

The signal from the distant transmitter was also used for the detection of satellites. Fig. A.11 shows detections of an ISS pass, with the target tracked for a large duration of the pass at a suitable signal-to-noise ratio (SNR). When the ISS was directly above the receiver, it was still at an elevation of  $8^\circ$  relative to the transmitter despite the baseline distance being 1,600 km, possibly limiting the illumination of the target. A longer transmitter-receiver separation is required to ensure targets at these orbital altitudes will be at sufficiently low elevations, relative to the transmitter, for main beam illumination.

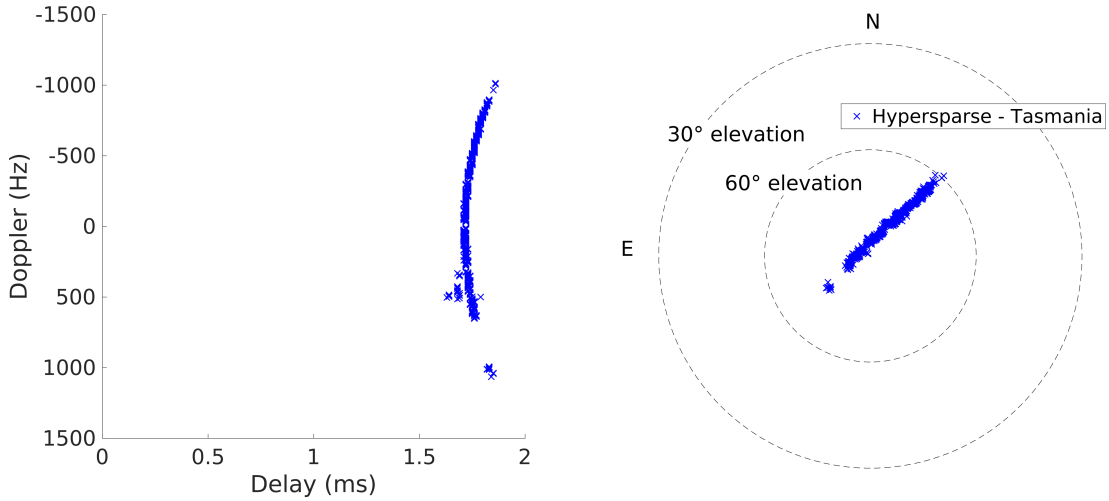


Figure A.11: Detection output of an ISS pass with the hypersparse array, processed using the reference signal from the distant transmitter in Tasmania. The left subplot shows the detected delay and Doppler, the right shows the detections' azimuth and elevation.

### A.5.2 Aircraft Detection

In addition to satellites, the radar also consistently detected aircraft to a maximum distance of 350 km slant range from the receiver. Fig. A.12 highlights some examples with commercial aircraft at ranges 350 km, 300 km and 210 km from the receiver. Note for the target at 350 km, the total reflected path from the transmitter, to the target, to the receiver was 780 km. These large ranges,

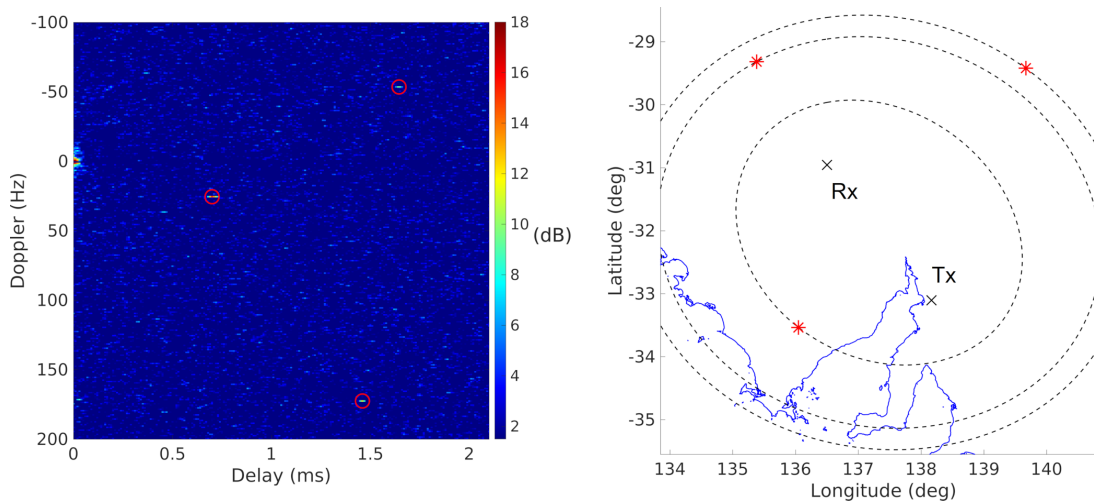


Figure A.12: Three example long-range commercial aircraft detections are shown. The left subplot shows the aggregate delay-Doppler map of three individual highlighted detections. The right subplot is a map of the configuration with the three detections, and their iso-range ellipses, highlighting a large surveillance area.

when combined with the extended baseline result in a vast surveillance volume. This is highlighted by the detection ellipsoids of the targets in Fig. A.12. This result was unexpected given the targets were all well outside the receiving array antennas' main beam.

As shown in Fig. A.12, the largest receiver slant ranges were achieved with targets in directions perpendicular to the baseline. This is due to the large separation, with maximum distances being horizon limited when the targets were at endfire, or *over the shoulder*, from the transmitter-receiver baseline. For example, the endfire target in Fig. A.12 is at the limit of detectability, as it was 500 km from the transmitter and  $2^\circ$  below the horizon.

It should be noted that the spatial ambiguities from the array, when configured for satellite detection, make aircraft localisation unachievable. Even if the elevation is constrained to search close to the horizon, there are still far too many grating lobes causing ambiguities in azimuth. The commercial aircraft detections mentioned here were confirmed by associated ADS-B truth information.

## A.6 Conclusion

A deployable passive radar system designed to operate at a significant standoff distance from the transmitter has been described. The radar has been used in real time to detect and track satellites in orbit, utilising a transmitter 300 km away. The system was able to detect objects the size of small rocket bodies, although the system is scalable to a larger number of elements and increased processing intervals. Additionally, detections of satellites have been generated utilising a separately-collected reference signal from a transmitter 1,600 km away. The system also routinely detected commercial aircraft at significant ranges, with the long baseline resulting in a large surveillance volume.



# Appendix B

## Statement of Contributions

The contents of Chapters 3–6, and Appendix A, is my own work, with the following qualifications.

For Chapter 3 the MWA observations were scheduled and undertaken by Steven Tremblay, with reference collection undertaken by Randall Wayth. Calibration solutions were generated by Paul Hancock. Sam McSweeney assisted with understanding the synthesis filter for inverting the fine polyphase filter bank channelisation, including providing the filter weights. Analysis of the data was undertaken by myself under close supervision of Steven Tingay and Robert Young.

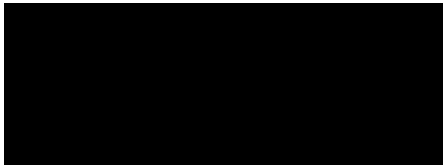
For Chapter 4 useful discussion on astrodynamics and Keplerian orbits were had with Mark Rutten. Analysis of the problem was undertaken by myself under supervision of Mark Rutten, Steven Tingay and Robert Young.

For Chapter 5 the MWA observations were scheduled and undertaken by Marcin Sokolowski, with Brian Crosse undertaking the high time resolution observations. Calibration solutions were generated by Marcin Sokolowski and Paul Hancock. Analysis of the data, including software development, was undertaken by myself under supervision of Mark Rutten, Steven Tingay and Robert Young.

For Chapter 5, the high time resolution observations were undertaken by Brian Crosse and calibration solutions were generated by Marcin Sokolowski. Remote reference collections were undertaken by myself, Brian Crosse, Ashley Summers

and Daniel Gustainis. Mark Rutten provided invaluable guidance for the orbit determination. Robert Young provided guidance generally and contributed to Figure 6.6. Data analysis and processing, including significant software development, was undertaken by myself under supervision of Steven Tingay and Mark Rutten.

For Appendix A, all coauthors assisted with the activity planning, conduct and data collection, under the close supervision of Robert Young. Antenna modelling and array layout was led by Nathan Misaghi. Ben Somers led the remote reference collection. Daniel Gustainis was the lead architect, and developer, for the real-time Praxis software, and also wrote Section A.4..



(Signature of candidate)




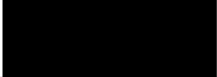


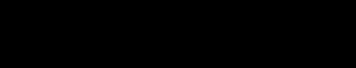
(Signature of supervisor)



## B.1 Attribution Tables

### B.1.1 Chapter 3

	Conception & Design	Acquisition of Data & Method	Data Conditioning & Manipulation	Analysis & Statistical Method	Interpretation & Discussion
S. Tingay	✓				✓
S. Tingay Acknowledgement: I acknowledge that these represent my contribution to the above research output and I have approved the final release: [REDACTED]					
Signed [REDACTED]					
P. Hancock	✓				✓
P. Hancock Acknowledgement: I acknowledge that these represent my contribution to the above research output and I have approved the final release: [REDACTED]					
Signed [REDACTED]					
R. Young	✓				✓
R. Young Acknowledgement: I acknowledge that these represent my contribution to the above research output and I have approved the final release: [REDACTED]					
Signed [REDACTED]					
S. Tremblay	✓	✓			
S. Tremblay Acknowledgement: I acknowledge that these represent my contribution to the above research output and I have approved the final release: [REDACTED]					
Signed [REDACTED]					
R.B. Wayth	✓	✓			
R.B. Wayth Acknowledgement: I acknowledge that these represent my contribution to the above research output and I have approved the final release: [REDACTED]					
Signed [REDACTED]					
J. Morgan	✓				
J. Morgan Acknowledgement: I acknowledge that these represent my contribution to the above research output and I have approved the final release: [REDACTED]					
Signed [REDACTED]					
S. McSweeney	✓				
S. McSweeney Acknowledgement: I acknowledge that these represent my contribution to the above research output and I have approved the final release: [REDACTED]					
Signed [REDACTED]					

B. Crosse	✓	✓			
B. Crosse Acknowledgement: I acknowledge that these represent my contribution to the above research output and I have approved the final release: Signed 					
M Johnston-Hollitt	✓				
M Johnston-Hollitt Acknowledgement: I acknowledge that these represent my contribution to the above research output and I have approved the final release: Signed 					
D.L. Kaplan	✓				
D.L. Kaplan Acknowledgement: I acknowledge that these represent my contribution to the above research output and I have approved the final release: Signed 					
D. Pallot	✓				
D. Pallot Acknowledgement: I acknowledge that these represent my contribution to the above research output and I have approved the final release: Signed 					
M. Walker	✓				
M. Walker Acknowledgement: I acknowledge that these represent my contribution to the above research output and I have approved the final release: Signed 					

## B.1.2 Chapter 4

	Conception & Design	Acquisition of Data & Method	Data Conditioning & Manipulation	Analysis & Statistical Method	Interpretation & Discussion
M. Rutten	✓				✓
M. Rutten Acknowledgement: I acknowledge that these represent my contribution to the above research output and I have approved the final release: [REDACTED]					
Signed [REDACTED]					
S. Tingay	✓				✓
S. Tingay Acknowledgement: I acknowledge that these represent my contribution to the above research output and I have approved the final release: [REDACTED]					
Signed [REDACTED]					
R. Young	✓				✓
R. Young Acknowledgement: I acknowledge that these represent my contribution to the above research output and I have approved the final release: [REDACTED]					
Signed [REDACTED]					

### B.1.3 Chapter 5

	Conception & Design	Acquisition of Data & Method	Data Conditioning & Manipulation	Analysis & Statistical Method	Interpretation & Discussion
S. Tingay	✓				✓
S. Tingay Acknowledgement: I acknowledge that these represent my contribution to the above research output and I have approved the final release: Signed [Redacted]					
R. Young	✓				✓
R. Young Acknowledgement: I acknowledge that these represent my contribution to the above research output and I have approved the final release: Signed [Redacted]					
M. Rutten	✓				✓
M. Rutten Acknowledgement: I acknowledge that these represent my contribution to the above research output and I have approved the final release: Signed [Redacted]					
B. Crosse	✓	✓			
B. Crosse Acknowledgement: I acknowledge that these represent my contribution to the above research output and I have approved the final release: Signed [Redacted]					
P. Hancock	✓				✓
S. Tremblay Acknowledgement: I acknowledge that these represent my contribution to the above research output and I have approved the final release: Signed [Redacted]					
M. Sokolowski		✓			
M. Sokolowski Acknowledgement: I acknowledge that these represent my contribution to the above research output and I have approved the final release: Signed [Redacted]					
M Johnston-Hollitt	✓				
M Johnston-Hollitt Acknowledgement: I acknowledge that these represent my contribution to the above research output and I have approved the final release: Signed [Redacted]					
D.L. Kaplan	✓				
D.L. Kaplan Acknowledgement: I acknowledge that these represent my contribution to the above research output and I have approved the final release: Signed [Redacted]					

## B.1.4 Chapter 6

	Conception & Design	Acquisition of Data & Method	Data Conditioning & Manipulation	Analysis & Statistical Method	Interpretation & Discussion
M. Rutten	✓				✓
M. Rutten Acknowledgement: I acknowledge that these represent my contribution to the above research output and I have approved the final release: Signed [REDACTED]					
R. Young	✓			✓	✓
R. Young Acknowledgement: I acknowledge that these represent my contribution to the above research output and I have approved the final release: Signed [REDACTED]					
S. Tingay	✓				✓
S. Tingay Acknowledgement: I acknowledge that these represent my contribution to the above research output and I have approved the final release: Signed [REDACTED]					
A. Summers		✓			✓
A. Summers Acknowledgement: I acknowledge that these represent my contribution to the above research output and I have approved the final release: Signed [REDACTED]					
D. Gustainis		✓			✓
D. Gustainis Acknowledgement: I acknowledge that these represent my contribution to the above research output and I have approved the final release: Signed [REDACTED]					
B. Crosse		✓			
B. Crosse Acknowledgement: I acknowledge that these represent my contribution to the above research output and I have approved the final release: Signed [REDACTED]					
M. Sokolowski		✓			
M. Sokolowski Acknowledgement: I acknowledge that these represent my contribution to the above research output and I have approved the final release: Signed [REDACTED]					

## B.1.5 Appendix A

	Conception & Design	Acquisition of Data & Method	Data Conditioning & Manipulation	Analysis & Statistical Method	Interpretation & Discussion
D. Gustainis	✓	✓			✓
D. Gustainis Acknowledgement: I acknowledge that these represent my contribution to the above research output and I have approved the final release: [REDACTED]					
Signed [REDACTED]					
N. Misaghi	✓	✓			✓
N. Misaghi Acknowledgement: I acknowledge that these represent my contribution to the above research output and I have approved the final release: [REDACTED]					
Signed [REDACTED]					
R. Young	✓	✓			✓
R. Young Acknowledgement: I acknowledge that these represent my contribution to the above research output and I have approved the final release: [REDACTED]					
Signed [REDACTED]					
B. Somers	✓	✓			✓
B. Somers Acknowledgement: I acknowledge that these represent my contribution to the above research output and I have approved the final release: [REDACTED]					
Signed [REDACTED]					

# Bibliography

- T. J. Abatzoglou (1986). ‘Fast Maximum Likelihood Joint Estimation of Frequency and Frequency Rate’. *IEEE Transactions on Aerospace and Electronic Systems* **AES-22**(6):708–715.
- T. J. Abatzoglou & G. O. Gheen (1998). ‘Range, radial velocity, and acceleration MLE using radar LFM pulse train’. *IEEE Transactions on Aerospace and Electronic Systems* **34**(4):1070–1083.
- R. Altes (1990). ‘Radar/sonar acceleration estimation with linear-period modulated waveforms’. *IEEE Transactions on Aerospace and Electronic Systems* **26**(6):914–924.
- R. Awadhiya & R. Vehmas (2021). ‘Analyzing the Effective Coherent Integration Time for Space Surveillance Radar Processing’. In *2021 IEEE Radar Conference (RadarConf21)*, pp. 1–6.
- J. Baniak, et al. (1999). ‘Silent Sentry passive surveillance’. *Aviation week and space technology* **7**:134–139.
- S. Barbarossa & V. Petrone (1997). ‘Analysis of polynomial-phase signals by the integrated generalized ambiguity function’. *IEEE Transactions on Signal Processing* **45**(2):316–327.
- S. Barbarossa, et al. (1998). ‘Product high-order ambiguity function for multi-component polynomial-phase signal modeling’. *IEEE Transactions on Signal Processing* **46**(3):691–708.

- R. R. Bate, et al. (2020). *Fundamentals of astrodynamics*. Courier Dover Publications.
- A. P. Beardsley, et al. (2019). ‘Science with the Murchison Widefield Array: Phase I results and Phase II opportunities’. *Publications of the Astronomical Society of Australia* **36**.
- V. S. Beley, et al. (1995). ‘Traveling ionospheric disturbance diagnostics using HF signal trajectory parameter variations’. *Radio Science* **30**(6):1739–1752.
- P. Bello (1960). ‘Joint estimation of delay, Doppler, and Doppler rate’. *IRE Transactions on Information Theory* **6**(3):330–341.
- C. R. Benson (2014). ‘Enhancing Space Situational Awareness using Passive Radar from Space Based Emitters of Opportunity’. In *2014 Military Communications and Information Systems Conference (MilCIS)*, pp. 1–5.
- V. Bezrukovs, et al. (2023). ‘The forward scatter radar method for detecting space objects using emission of extraterrestrial radio sources’. In *2nd ESA NEO and Debris Detection Conference (2023)*.
- N. R. Bhat, et al. (2014). ‘High time resolution radio astronomy with low-frequency interferometric arrays’. In *2014 XXXIth URSI General Assembly and Scientific Symposium (URSI GASS)*, pp. 1–4. IEEE.
- B. Boashash (1992). ‘Estimating and interpreting the instantaneous frequency of a signal. I. Fundamentals’. *Proceedings of the IEEE* **80**(4):520–538.
- B. Boashash (2016). *Time-Frequency Signal Analysis and Processing (Second Edition)*. Academic Press, Oxford.
- B. Boashash, et al. (1990). ‘Algorithms for instantaneous frequency estimation: A comparative study’. In *Advanced Signal Processing Algorithms, Architectures, and Implementations*, vol. 1348, pp. 126–148. SPIE.



- D. Boeringer, et al. (2005). ‘A simultaneous parameter adaptation scheme for genetic algorithms with application to phased array synthesis’. *IEEE Transactions on Antennas and Propagation* **53**(1):356–371.
- K. Borowiec & M. Malanowski (2016). ‘Accelerating Rocket Detection using Passive Bistatic Radar’. In *2016 17th International Radar Symposium (IRS)*, pp. 1–5.
- J. D. Bowman, et al. (2013). ‘Science with the Murchison Widefield Array’. *Publications of the Astronomical Society of Australia* **30**:e031.
- R. Braun (2015). ‘The Square Kilometre Array: Current Status and Science Prospects’. *IAU General Assembly* **22**:2252814.
- D. Cataldo, et al. (2020). ‘Multibistatic radar for space surveillance and tracking’. *IEEE Aerospace and Electronic Systems Magazine* **35**(8):14–30.
- J. Christian, et al. (2022). ‘Doppler-only initial orbit determination for an orbiting transmitter’. In *AIAA SCITECH 2022 Forum*, p. 1000.
- J. M. Christiansen, et al. (2014). ‘Coherent range and Doppler-walk compensation in PBR applications’. In *2014 15th International Radar Symposium (IRS)*, pp. 1–4.
- V. Clarkson & J. Palmer (2019). ‘New frontiers in passive radar’. *IEEE Potentials* **38**(4):9–15.
- C. Coleman & H. Yardley (2008). ‘Passive bistatic radar based on target illuminations by digital audio broadcasting’. *IET Radar, Sonar & Navigation* **2**(5):366–375.
- S. Crawshaw & J. Maxey (2022). ‘Hitchhiking radar and its potential contribution to ballistic missile defence’. In *International Conference on Radar Systems (RADAR 2022)*, vol. 2022, pp. 306–311.

- D. Cristallini, et al. (2010). ‘Space-based passive radar enabled by the new generation of geostationary broadcast satellites’. In *2010 IEEE Aerospace Conference*, pp. 1–11.
- D. Cristallini, et al. (2018). ‘Multi-band passive radar imaging using satellite illumination’. In *2018 International Conference on Radar (RADAR)*, pp. 1–6.
- K. DeMars & M. Jah (2014). ‘Probabilistic initial orbit determination using radar returns’. *Advances in the Astronautical Sciences* **150**:35–54.
- A. Dhondea & M. Inggs (2019). ‘Mission planning tool for space debris detection and tracking with the MeerKAT Radar’. In *2019 IEEE Radar Conference (RadarConf)*, pp. 1–6. IEEE.
- P. M. Djuric & S. M. Kay (1990). ‘Parameter estimation of chirp signals’. *IEEE Transactions on Acoustics, Speech, and Signal Processing* **38**(12):2118–2126.
- A. Droszcz, et al. (2021). ‘Beamforming of LOFAR Radio-Telescope for passive radiolocation purposes’. *Remote Sensing* **13**(4):810.
- C. D’Souza & R. Zanetti (2023). ‘The Initial Orbit Determination (IOD) Problem with Range, Range-Rate and Angles’. In *Proceedings of the 2023 AAS/AIAA Spaceflight Mechanics Meeting*. American Astronautical Society. Paper Number AAS 23-304.
- P. Escobal (1965). *Methods of Orbit Determination*. J. Wiley.
- G. Fabrizio, et al. (2008). ‘Passive radar in the high frequency band’. In *2008 IEEE Radar Conference*, pp. 1–6. IEEE.
- D. Finch, et al. (2022). ‘Assessing passive radar for LEO SSA’.
- T. Flohrer, et al. (2008). ‘Assessment and categorization of TLE orbit errors for the US SSN catalogue’. *Advanced Maui Optical and Space Surveillance Technologies Conference* p. E53.

- V. L. Foreman, et al. (2017). ‘Large satellite constellation orbital debris impacts: Case studies of OneWeb and SpaceX proposals’. In *AIAA SPACE and Astronautics Forum and Exposition*, p. 5200.
- G. Frazer, et al. (2013a). ‘Orbit determination using a decametric line-of-sight radar’. In *Advanced Maui Optical and Space Surveillance Technologies Conference (AMOS)*.
- G. Frazer & C. Williams (2019). ‘Decametric radar for missile defence’. In *2019 IEEE Radar Conference (RadarConf)*, pp. 1–6. IEEE.
- G. Frazer, et al. (2016). ‘Energy-budget analysis of a 2-D high-frequency radar incorporating optimum beamforming’. In *2016 IEEE Radar Conference (RadarConf)*, pp. 1–6. IEEE.
- G. J. Frazer, et al. (2013b). ‘Decametric measurements of the ISS using an experimental HF line-of-sight radar’. In *2013 International Conference on Radar*, pp. 173–178.
- J. Geul, et al. (2017). ‘Modelling and assessment of the current and future space surveillance network’. In *Proceedings of the 7th European Conference on Space Debris (ECSD), Darmstadt, Germany*, pp. 18–21.
- R. Gomez, et al. (2019). ‘Initial operations of the breakthrough Spanish space surveillance and tracking radar (S3TSR) in the European context’. In *Proceedings of the 1st NEO and Debris Detection Conference, Darmstadt, Germany*.
- B. Gong, et al. (2023). ‘Deep-neural-network-based angles-only relative orbit determination for space non-cooperative target’. *Acta Astronautica* **204**:552–567.
- R. Gooding (1993). ‘A new procedure for orbit determination based on three lines of sight (angles only)’. Tech. rep., Defence Research Agency Farnborough (UK).

- W. M. Goss, et al. (2023). *Joe Pawsey and the Founding of Australian Radio Astronomy: Early Discoveries, from the Sun to the Cosmos*. Springer Nature.
- W. M. Goss & R. X. McGee (2010). *Under the radar: the first woman in radio astronomy: Ruby Payne-Scott*. Springer.
- D. R. Griffin, et al. (1960). ‘The echolocation of flying insects by bats’. *Animal behaviour* **8**(3-4):141–154.
- H. Griffiths & N. Long (1986). ‘Television-based bistatic radar’. In *IEE Proceedings F: Communications Radar and Signal Processing*, vol. 133, pp. 649–657.
- H. Griffiths & N. Willis (2010). ‘Klein Heidelberg—the first modern bistatic radar system’. *IEEE Transactions on Aerospace and Electronic Systems* **46**(4):1571–1588.
- W. H. Guier & G. C. Weiffenbach (1959). ‘The Doppler determination of orbits’. Tech. rep., Johns Hopkins University Applied Physics Laboratory.
- J. A. Haimerl & G. P. Fonder (2015). ‘Space Fence system overview’. In *Proceedings of the Advanced Maui Optical and Space Surveillance Technology Conference*. Curran Associates, Inc.
- M. Hapgood (2010). ‘Ionospheric correction of space radar data’. *Acta Geophysica* **58**(3):453–467.
- E. Heading, et al. (2022). ‘Analysis of RF signatures for space domain awareness using VHF radar’. In *2022 IEEE Radar Conference (RadarConf22)*, pp. 1–6. IEEE.
- B. Hennessy, et al. (2022a). ‘Deployable long range passive radar for space surveillance’. In *2022 IEEE Radar Conference (RadarConf22)*, pp. 01–06. IEEE.
- B. Hennessy, et al. (2023a). ‘Effects of range Doppler-rate coupling on high frequency chirp radar for accelerating targets’. In *2023 International Conference on Radar*.

- B. Hennessy, et al. (2020). ‘Orbit determination before detect: orbital parameter matched filtering for uncued detection’. In *2020 IEEE International Radar Conference (RADAR)*, pp. 889–894.
- B. Hennessy, et al. (2022b). ‘Establishing the capabilities of the Murchison Widefield Array as a passive radar for the surveillance of space’. *Remote Sensing* **14**(11):2571.
- B. Hennessy, et al. (2019). ‘Improved techniques for the surveillance of the near Earth space environment with the Murchison Widefield Array’. In *2019 IEEE Radar Conference (RadarConf)*, pp. 1–6.
- B. Hennessy, et al. (2021). ‘Uncued detection and initial orbit determination from short observations with the Murchison Widefield Array’. *IEEE Aerospace and Electronic Systems Magazine* **36**(10):16–30.
- B. Hennessy, et al. (2023b). ‘Velocity ambiguity resolution using opposite chirprates with LFM radar’. In *2023 International Conference on Radar*.
- R. Hoffmann, et al. (2019). ‘Performance evaluation of a distributed radar system for space surveillance’. In *2019 IEEE Radar Conference (RadarConf)*, pp. 1–6. IEEE.
- D. A. Holdsworth, et al. (2020). ‘Low Earth orbit object observations using the Buckland Park VHF radar’. *Radio Science* **55**(2):1–19.
- J. H. Holland (1992). ‘Genetic algorithms’. *Scientific american* **267**(1):66–73.
- P. Howland (1999). ‘Target tracking using television-based bistatic radar’. *IEE Proceedings-Radar, Sonar and Navigation* **146**(3):166–174.
- P. E. Howland, et al. (2005). ‘FM radio based bistatic radar’. *IEE Proceedings - Radar, Sonar and Navigation* **152**(3):107–115.

- S. Imamura, et al. (2021). ‘Attitude and orbit control result of super low altitude test satellite “TSUBAME” (SLATS)’. *Journal of the Japan Society for Aeronautical and Space Sciences*. **69**(1):35–41.
- M. Inggs, et al. (2014). ‘Planning and design phases of a commensal radar system in the FM broadcast band’. *IEEE Aerospace and Electronic Systems Magazine* **29**(7):50–63.
- D. Izzo (2015). ‘Revisiting Lambert’s problem’. *Celestial Mechanics and Dynamical Astronomy* **121**:1–15.
- K. Jędrzejewski, et al. (2022a). ‘Experimental trials of space object detection using LOFAR Radio Telescope as a receiver in passive radar’. In *2022 IEEE Radar Conference (RadarConf22)*, pp. 1–6.
- K. Jędrzejewski, et al. (2021). ‘Field trials of passive radiolocation using LOFAR Radio Telescope and external reference receiver’. In *2021 Signal Processing Symposium (SPSymposium)*, pp. 103–106. IEEE.
- K. Jędrzejewski, et al. (2022b). ‘Passive space object observation using LOFAR Radio Telescope and software-defined radio receiver’. In *2022 19th European Radar Conference (EuRAD)*, pp. 1–4. IEEE.
- K. Jędrzejewski, et al. (2022c). ‘First experimental trials of passive DVB-T based space object detection with a single LOFAR Radio Telescope’ .
- G. Jensen & J. McGeogh (1963). ‘Development of an acceleration gate system for the improvement of the Madre radar. Part 1-system theory, calculations and planning’. Tech. rep., Naval Research Laboratory, Washington DC.
- M. Y. Jin & C. Wu (1984). ‘A SAR correlation algorithm which accommodates large-range migration’. *IEEE Transactions on Geoscience and Remote Sensing* (6):592–597.

- T. Johnsen & K. Olsen (2007). ‘Hitchhiking bistatic radar: principles, processing and experimental findings’. In *2007 IEEE Radar Conference*, pp. 518–523. IEEE.
- N. L. Johnson (1993). ‘US space surveillance’. *Advances in Space Research* **13**(8):5–20.
- W. Joubert & S. Tingay (2021). ‘Simulations of orbital debris clouds due to breakup events and their characterisation using the Murchison Widefield Array radio telescope’. *Experimental Astronomy* **51**:61–75.
- K. Jędrzejewski, et al. (2023). ‘Long-distance bistatic measurements of space object motion using LOFAR Radio Telescope and non-cooperative radar illuminator’. In *2023 IEEE Radar Conference (RadarConf23)*, pp. 1–6.
- S. Kay & G. Boudreaux-Bartels (1985). ‘On the optimality of the Wigner distribution for detection’. In *ICASSP ’85. IEEE International Conference on Acoustics, Speech, and Signal Processing*, vol. 10, pp. 1017–1020.
- E. J. Kelly (1961). ‘The radar measurement of range, velocity and acceleration’. *IRE Transactions on Military Electronics* **MIL-5**(2):51–57.
- F. Kerr (1984). ‘Early days in radio and radar astronomy in Australia’. *The Early Years of Radio Astronomy-Reflections Fifty Years after Jansky’s Discovery* p. 133.
- F. Kerr & C. Shain (1951). ‘Moon echoes and transmission through the ionosphere’. *Proceedings of the IRE* **39**(3):230–242.
- F. Kerr, et al. (1949). ‘Moon echoes and penetration of the ionosphere’. *Nature* **163**(4139):310–313.
- F. J. Kerr (1952). ‘On the possibility of obtaining radar echoes from the sun and planets’. *Proceedings of the IRE* **40**(6):660–666.

- J. Kłos, et al. (2020). ‘On the possibility of using LOFAR Radio Telescope for passive radiolocation’. In *2020 21st International Radar Symposium (IRS)*, pp. 73–76. IEEE.
- E. F. Knott, et al. (2004). *Radar cross section*. SciTech Publishing.
- S. Kodituwakku & R. Melino (2014). ‘Detection of fast moving and accelerating targets compensating range and Doppler migration’. *Research report Defence Science and Technology Organisation (Australia) DSTO-TR-2978* .
- R. Kohlleppel (2018). ‘Extent of observation parameters in space surveillance by radar’. In *2018 19th International Radar Symposium (IRS)*, pp. 1–7.
- K. S. Kulpa & J. Misiurewicz (2006). ‘Stretch processing for long integration time passive covert radar’. In *2006 CIE International Conference on Radar*, pp. 1–4.
- H. Kuschel (2013). ‘Approaching 80 years of passive radar’. In *2013 International Conference on Radar*, pp. 213–217. IEEE.
- F. Laghezza, et al. (2010). ‘Italian bistatic radar system for surveillance of space debris in low Earth orbit’. In *2010 IEEE Radar Conference*, pp. 220–224.
- J. Li, et al. (2019). ‘The capability analysis of the bistatic radar system based on Tianlai radio array for space debris detection’. *Advances in Space Research* **64**(9):1652–1661.
- Z. Li, et al. (2017). ‘Multi-frame fractional Fourier transform technique for moving target detection with space-based passive radar’. *IET Radar, Sonar Navigation* **11**(5):822–828.
- F. D. Lind (2006). ‘Passive radar and ionospheric irregularities’. In *Solar Heliospheric and Ionospheric Workshop for the MWA*.



- P. Lombardo, et al. (2012). ‘Advanced processing methods for passive bistatic radar systems’. In *Principles of modern radar: advanced radar techniques*, pp. 739–821. SciTech Publishing.
- M. Losacco, et al. (2023). ‘Robust initial orbit determination for surveillance Doppler-only radars’. *IEEE Transactions on Aerospace and Electronic Systems* pp. 1–12.
- M. Losacco, et al. (2019). ‘The multibeam radar sensor BIRALES: performance assessment for space surveillance and tracking’. In *2019 IEEE Aerospace Conference*, pp. 1–13.
- M. Losacco, et al. (2020). ‘Initial orbit determination with the multibeam radar sensor BIRALES’. *Acta Astronautica* **167**:374–390.
- A. C. B. Lovell (1964). ‘Joseph Lade Pawsey, 1908-1962’.
- B. Lovell (1990). ‘Astronomer by chance’. *New York: Basic Books, c1990*. .
- D. Ly, et al. (2020). ‘Correcting TLEs at epoch: Application to the GPS constellation’. *Journal of Space Safety Engineering* **7**(3):302–306.
- K. Madsen, et al. (2004). ‘Methods for non-linear least squares problems’ .
- M. S. Mahmud, et al. (2016). ‘Affordable processing for long coherent integration of weak debris-scattered GNSS signals with inconsistent Doppler’. In *2016 Annual IEEE Systems Conference (SysCon)*, pp. 1–6.
- M. Malanowski (2012). ‘Detection and parameter estimation of manoeuvring targets with passive bistatic radar’. *IET Radar, Sonar & Navigation* **6**(8):739–745.
- M. Malanowski (2019). *Signal processing for passive bistatic radar*. Artech House.

- M. Malanowski, et al. (2018a). ‘Rocket detection using passive radar-challenges and solutions’. In *2018 International Conference on Radar (RADAR)*, pp. 1–5. IEEE.
- M. Malanowski, et al. (2018b). ‘Detection of supersonic rockets using passive bistatic radar’. *IEEE Aerospace and Electronic Systems Magazine* **33**(1):24–33.
- M. Malanowski, et al. (2021a). ‘Passive radar based on LOFAR Radio Telescope for air and space target detection’. In *2021 IEEE Radar Conference (RadarConf21)*, pp. 1–6. IEEE.
- M. Malanowski, et al. (2021b). ‘Passive radar based on LOFAR Radio Telescope for air and space target detection’. In *2021 IEEE Radar Conference (RadarConf21)*, pp. 1–6.
- M. Malanowski, et al. (2023). ‘Satellite orbit refinement based on passive bistatic radar measurements’. In *2023 IEEE Radar Conference (RadarConf23)*, pp. 1–6.
- M. Malanowski & K. Kulpa (2008). ‘Analysis of integration gain in passive radar’. In *2008 International Conference on Radar*, pp. 323–328.
- M. Malanowski, et al. (2020). ‘Noise vs. deterministic waveform radar — possibilities and limitations’. *IEEE Aerospace and Electronic Systems Magazine* **35**(10):8–19.
- M. Malanowski, et al. (2014). ‘Analysis of detection range of FM-based passive radar’. *IET Radar, Sonar Navigation* **8**(2):153–159.
- M. Malanowski, et al. (2012). ‘Long range FM-based passive radar’. In *IET International Conference on Radar Systems (Radar 2012)*, pp. 1–4.
- J. Markkanen, et al. (2005). ‘Real-time space debris monitoring with EISCAT’. *Advances in space research* **35**(7):1197–1209.

- J. C. McDowell (2020). ‘The low Earth orbit satellite population and impacts of the SpaceX Starlink constellation’. *The Astrophysical Journal Letters* **892**(2):L36.
- J. McGeogh & G. Jensen (1967). ‘Acceleration and velocity processing of HF radar signals’. Tech. rep., Naval Research Laboratory, Washington DC.
- B. McKinley, et al. (2013). ‘Low-frequency Observations of the Moon with the Murchison Widefield Array’. *The Astronomical Journal* **145**.
- J. McMullin, et al. (2020). ‘The Square Kilometre Array project’. In *Society of Photo-Optical Instrumentation Engineers (SPIE) Conference Series*, vol. 11445 of *Society of Photo-Optical Instrumentation Engineers (SPIE) Conference Series*, p. 1144512.
- S. McSweeney, et al. (2020). ‘MWA tied-array processing III: Microsecond time resolution via a polyphase synthesis filter’. *Publications of the Astronomical Society of Australia* **37**.
- R. Melino & H. T. Tran (2011). ‘Application of the Fractional Fourier Transform in the detection of accelerating targets in clutter’. *Research report Defence Science and Technology Organisation (Australia) DSTO-RR-0365* .
- T. Michal, et al. (2005). ‘GRAVES: the new French system for space surveillance’ .
- A. Milani, et al. (2004). ‘Orbit determination with very short arcs. I admissible regions’. *Celestial Mechanics and Dynamical Astronomy* **90**(1):57–85.
- O. Montenbruck, et al. (2002). ‘Satellite orbits: models, methods, and applications’. *Appl. Mech. Rev.* **55**(2):B27–B28.
- B. Morreale, et al. (2017). ‘Australian space situational awareness capability demonstrations’. In *Advanced Maui Optical and Space Surveillance (AMOS) Technologies Conference*, p. 63.

- I. Morrison, et al. (2023). ‘MWAX: A new correlator for the Murchison Widefield Array’. *Publications of the Astronomical Society of Australia* **40**:e019.
- C. A. Muller & J. H. Oort (1951). ‘Observation of a line in the galactic radio spectrum: the interstellar hydrogen line at 1,420 Mc./sec., and an estimate of galactic rotation’. *Nature* **168**(4270):357–358.
- J. Murray & F. Jenet (2022). ‘The Arecibo Observatory as an instrument for investigating orbital debris: legacy and next generation performance’. *The Planetary Science Journal* **3**(3):52.
- National Research Council (2012). *Continuing Kepler’s Quest: Assessing Air Force Space Command’s Astrodynamics Standards*. The National Academies Press, Washington, DC.
- B. Neale (1985). ‘CH—the first operational radar’. *GEC journal of research* **3**(2):73–83.
- N. Neuberger, et al. (2023). ‘GESTRA: first results of LEO object parameter estimation’ .
- H. Nosrati, et al. (2022). ‘Bi-static radar interferometric localization of MEO and GEO space debris using the Australia Telescope Compact Array’ .
- D. W. O’Hagan & C. J. Baker (2008). ‘Passive Bistatic Radar (PBR) using FM radio illuminators of opportunity’. In *2008 New Trends for Environmental Monitoring Using Passive Systems*, pp. 1–6.
- D. W. O’Hagan, et al. (2017). ‘Elevation Pattern Analysis of Common Passive Bistatic Radar Illuminators of Opportunity’. *IEEE Transactions on Aerospace and Electronic Systems* **53**(6):3008–3019.
- S. Ord, et al. (2019). ‘MWA tied-array processing I: calibration and beamformation’. *Publications of the Astronomical Society of Australia* **36**:e030.

- P. O'shea (2002). 'A new technique for instantaneous frequency rate estimation'. *IEEE Signal Processing Letters* **9**(8):251–252.
- S. J. Ostro (1993). 'Planetary radar astronomy'. *Reviews of Modern Physics* **65**(4):1235.
- J. Palmer (2015). 'A Signal Processing Scheme for a Multichannel Passive Radar System'. In *2015 IEEE International Conference on Acoustics, Speech and Signal Processing (ICASSP)*, pp. 5575–5579.
- J. Palmer, et al. (2008). 'Illuminator of opportunity bistatic radar research at DSTO'. In *2008 International Conference on Radar*, pp. 701–705.
- J. Palmer, et al. (2009). 'DSTO's experimental geosynchronous satellite based PBR' pp. 1–6.
- J. Palmer, et al. (2011). 'An overview of an illuminator of opportunity passive radar research project and its signal processing research directions'. *Digit. Signal Process.* **21**(5):593–599.
- J. E. Palmer, et al. (2017). 'Surveillance of space using passive radar and the Murchison Widefield Array'. In *2017 IEEE Radar Conference (RadarConf)*, pp. 1715–1720.
- J. E. Palmer & S. J. Searle (2012). 'Evaluation of adaptive filter algorithms for clutter cancellation in passive bistatic radar'. In *2012 IEEE Radar Conference*, pp. 0493–0498. IEEE.
- N. V. Patel (2015). 'Averting space doom [News]'. *IEEE Spectrum* **52**(2):16–17.
- R. B. Patton (1960). 'Orbit Determination from single pass Doppler observations'. *IRE Transactions on Military Electronics* **MIL-4**(2/3):336–344.
- J. Pawsey (1953). 'Radio astronomy in Australia'. *Journal of the Royal Astronomical Society of Canada* **47**:137.

- S. Peleg & B. Friedlander (1995). ‘The discrete polynomial-phase transform’. *IEEE Transactions on Signal Processing* **43**(8):1901–1914.
- S. Peleg & B. Porat (1991a). ‘Estimation and classification of polynomial-phase signals’. *IEEE Transactions on Information Theory* **37**(2):422–430.
- S. Peleg & B. Porat (1991b). ‘Linear FM signal parameter estimation from discrete-time observations’. *IEEE Transactions on Aerospace and Electronic Systems* **27**(4):607–616.
- R. P. Perry, et al. (1999). ‘SAR imaging of moving targets’. *IEEE Transactions on Aerospace and Electronic Systems* **35**(1):188–200.
- R. P. Perry, et al. (2007). ‘Coherent integration with range migration using keystone formatting’. In *2007 IEEE Radar Conference*, pp. 863–868.
- A. R. Persico, et al. (2018). ‘Cubesat-based passive bistatic radar for space situational awareness: a feasibility study’. *IEEE Transactions on Aerospace and Electronic Systems* **55**(1):476–485.
- S. Peters, et al. (2021). ‘Glaciological monitoring using the Sun as a radio source for echo detection’. *Geophysical Research Letters* **48**(14):e2021GL092450.
- F. Pignol, et al. (2018). ‘Lagrange-polynomial-interpolation-based Keystone Transform for a passive radar’. *IEEE Transactions on Aerospace and Electronic Systems* **54**(3):1151–1167.
- T. Pisanu, et al. (2020). ‘The Italian BIRALET Radar System to perform range And range rate measurements in the EUSST European Space Surveillance And Tracking Program’. In *Proc. 71th International Astronautical Congress (IAC)*.
- D. Poullin (2005). ‘Passive detection using digital broadcasters (DAB, DVB) with COFDM modulation’. *IEE Proceedings-Radar, Sonar and Navigation* **152**(3):143–152.

- S. Prabu, et al. (2023). ‘Demonstration of Orbit Determination for LEO Objects using the Murchison Widefield Array’. *arXiv preprint arXiv:2308.04640* .
- S. Prabu, et al. (2020a). ‘A low-frequency blind survey of the low Earth orbit environment using non-coherent passive radar with the Murchison Widefield Array’. *Publications of the Astronomical Society of Australia* **37**.
- S. Prabu, et al. (2022). ‘Improved sensitivity for space domain awareness observations with the Murchison Widefield Array’. *Advances in Space Research* .
- S. Prabu, et al. (2020b). ‘The development of non-coherent passive radar techniques for space situational awareness with the Murchison Widefield Array’. *Publications of the Astronomical Society of Australia* **37**:e010.
- S. R. Prabu (2021). *Advantages and limitations of using the Murchison Widefield Array for space surveillance: a feasibility study*. Ph.D. thesis, Curtin University.
- J. Qu, et al. (2022a). ‘Initial orbit determination method for low Earth orbit objects using too-short arc based on bistatic radar’. *IEEE Access* **10**:76766–76779.
- J. Qu, et al. (2022b). ‘An analytical initial orbit determination method using two observations from a bistatic radar’. *Advances in Space Research* .
- H. Riebeek (2009). ‘Catalog of Earth satellite orbits: feature articles’ .
- M. Ringer, et al. (1999). ‘Waveform analysis of transmissions of opportunity for Passive Radar’. *Research report Defence Science and Technology Organisation (Australia) DSTO-TR-0809* .
- A. Rossi, et al. (2017). ‘A quantitative evaluation of the environmental impact of the mega constellations’ .
- J. Rowland, et al. (2021). ‘A worldwide network of radars for space domain awareness in low Earth orbit’ .

- S. Rzewuski, et al. (2015). ‘Supersonic target detection in passive radar’. In *2015 16th International Radar Symposium (IRS)*, pp. 89–94. IEEE.
- J. D. Sahr (2007). ‘Lossy compression of voltage level samples before detection in distributed passive bistatic radar systems’. In *2007 IET International Conference on Radar Systems*, pp. 1–4. IET.
- J. D. Sahr & F. D. Lind (1997). ‘The Manastash Ridge radar: A passive bistatic radar for upper atmospheric radio science’. *Radio Science* **32**(6):2345–2358.
- J. D. Sahr & F. D. Lind (1998). ‘Passive radio remote sensing of the atmosphere using transmitters of opportunity’. *Radio Science Bulletin* (284):4–7.
- S. Saillant (2016). ‘Bistatic space-debris surveillance radar’. In *2016 IEEE Radar Conference (RadarConf)*, pp. 1–4.
- P. Samczynski, et al. (2015). ‘Passive radars utilizing pulse radars as illuminators of opportunity’. In *2015 IEEE Radar Conference*, pp. 168–173. IEEE.
- A. V. Schaeperkoetter (2012). *A comprehensive comparison between angles-only initial orbit determination techniques*. Ph.D. thesis, Texas A & M University.
- H. Schily, et al. (2022). ‘State representation of eccentricity-limited targets for bistatic space surveillance radar design’. In *2022 IEEE Radar Conference (RadarConf22)*, pp. 01–06. IEEE.
- D. Schwab, et al. (2022). ‘Angles-only initial orbit determination via multivariate gaussian process regression’. *Electronics* **11**(4):588.
- K. M. Scott, et al. (2015). ‘The keystone transform: Practical limits and extension to second order corrections’. In *2015 IEEE Radar Conference (RadarCon)*, pp. 1264–1269.
- S. Searle, et al. (2018). ‘Cancelling strong Doppler shifted returns in OFDM based passive radar’. In *2018 IEEE Radar Conference (RadarConf18)*, pp. 0359–0354.



- S. Sirianunpiboon, et al. (2019). ‘Fast direct detection of accelerating radar targets’. In *2019 27th European Signal Processing Conference (EUSIPCO)*, pp. 1–5.
- M. I. Skolnik (1970). *Radar handbook*. McGraw-Hill, New York, NY.
- F. G. Smith (1951). ‘An accurate determination of the positions of four radio stars’. *Nature* **168**(4274):555–555.
- R. Sridharan & A. F. Pensa (1998). ‘US Space Surveillance Network capabilities’. In *Image Intensifiers and Applications; and Characteristics and Consequences of Space Debris and Near-Earth Objects*, vol. 3434, pp. 88–100. SPIE.
- S. Stein (1981). ‘Algorithms for ambiguity function processing’. *IEEE Transactions on Acoustics, Speech, and Signal Processing* **29**(3):588–599.
- A. G. Stove (2013). ‘Radar considered as a fine art’. In *2013 International Conference on Radar*, pp. 542–547.
- S. Strømøy (2013). ‘Hitchhiking bistatic radar’. Master’s thesis.
- S. Tingay, et al. (2020). ‘A survey of spatially and temporally resolved radio frequency interference in the FM band at the Murchison Radio-astronomy Observatory’. *Publications of the Astronomical Society of Australia* **37**.
- S. J. Tingay, et al. (2013a). ‘The Murchison Widefield Array: The Square Kilometre Array Precursor at Low Radio Frequencies’. *Publications of the Astronomical Society of Australia* **30**:e007.
- S. J. Tingay, et al. (2013b). ‘On the Detection and Tracking of Space Debris Using the Murchison Widefield Array. I. Simulations and Test Observations Demonstrate Feasibility’. *The Astronomical Journal* **146**:103.
- G. Tommei, et al. (2007). ‘Orbit determination of space debris: admissible regions’. *Celestial Mechanics and Dynamical Astronomy* **97**:289–304.

- H. T. Tran, et al. (2014). ‘Detection of accelerating targets in clutter using a de-chirping technique’. *Research report Defence Science and Technology Organisation (Australia) DSTO-RR-0399* .
- S. Tremblay, et al. (2015). ‘The high time and frequency resolution capabilities of the Murchison widefield array’. *Publications of the Astronomical Society of Australia* **32**.
- USSPACECOM (2023). ‘Space-Track’.
- D. Vallado & W. McClain (2001). *Fundamentals of Astrodynamics and Applications*. Space Technology Library. Springer Netherlands.
- D. A. Vallado, et al. (2006). ‘Revisiting spacetrack report# 3’. *AIAA* **6753**(2006):446.
- M. P. van Haarlem, et al. (2013). ‘LOFAR: The low-frequency array’. *Astronomy & astrophysics* **556**:A2.
- J. Vierinen, et al. (2019). ‘2018 beam-park observations of space debris with the EISCAT radars’ .
- J. Vierinen, et al. (2017). ‘Use of EISCAT 3D for observations of space debris’ .
- J. Wang, et al. (2022). ‘Simulation and observational evaluation of space debris detection by Sanya incoherent scatter radar’. *Radio Science* **57**(10):e2022RS007472.
- G. Watts, et al. (2015). ‘Space situational awareness applications for radio astronomy assets’. In *Sensors and Systems for Space Applications VIII*, vol. 9469, p. 94690N. International Society for Optics and Photonics.
- R. Wayth, et al. (2022). ‘A portable many-element coherent receiver system for passive radar and space domain awareness’ .

- R. B. Wayth, et al. (2018). ‘The Phase II Murchison Widefield Array: Design overview’. *Publications of the Astronomical Society of Australia* **35**:e033.
- B. Weeden, et al. (2010). ‘Global space situational awareness sensors’. In *AMOS Conference*.
- S. Welch, et al. (2022). ‘Long baseline radar bistatic measurements of geostationary satellites’. In *2022 19th European Radar Conference (EuRAD)*, pp. 1–4.
- H. Wilden, et al. (2019). ‘GESTRA - recent progress, mode design and signal processing’. In *2019 IEEE International Symposium on Phased Array System Technology (PAST)*, pp. 1–8.
- H. Wilden, et al. (2016). ‘GESTRA — a phased-array based surveillance and tracking radar for space situational awareness’. In *2016 IEEE International Symposium on Phased Array Systems and Technology (PAST)*, pp. 1–5. IEEE.
- A. Wilkins (2011). ‘The birth of British radar’. *DEHS/RSGB*.
- A. Williamson, et al. (2021). ‘An ultra-high time resolution cosmic-ray detection mode for the Murchison Widefield Array’. *Journal of Astronomical Instrumentation* **10**(01).
- N. Willis & H. Griffiths (2007). *Advances in bistatic radar*. The Institution of Engineering and Technology.
- N. J. Willis (2005). *Bistatic radar*, vol. 2. SciTech Publishing.
- P. M. Woodward (1953). ‘Probability and information theory: with applications to radar’.
- X.-G. Xia (2000). ‘Discrete chirp-Fourier transform and its application to chirp rate estimation’. *IEEE Transactions on Signal processing* **48**(11):3122–3133.

- C. Yanez, et al. (2017). ‘A novel initial orbit determination algorithm from Doppler and angular observations’. In *7th European Conference on Space Debris*.
- H. J. Yardley (2007). ‘Bistatic radar based on DAB illuminators: the evolution of a practical system’. In *2007 IEEE Radar Conference*, pp. 688–692. IEEE.
- A. Yasotharan & T. Thayaparan (2002). ‘Strengths and limitations of the Fourier method for detecting accelerating targets by pulse Doppler radar’. *IEE Proceedings-Radar, Sonar and Navigation* **149**(2):83–88.
- M. Zatman (2022). ‘How many photons does a radar engineer need?’. Remarks by Michael Zatman during his plenary talk at the 2022 IEEE Radar Conference, New York, 21-25 March 2022.
- V. U. Zavorotny, et al. (2014). ‘Tutorial on remote sensing using GNSS bistatic radar of opportunity’. *IEEE Geoscience and Remote Sensing Magazine* **2**(4):8–45.
- S. Zhang, et al. (2019). ‘An initial orbit determination method using single-site very short arc radar observations’. *IEEE Transactions on Aerospace and Electronic Systems* **56**(3):1856–1872.
- F. Zhou, et al. (2007). ‘Approach for single channel SAR ground moving target imaging and motion parameter estimation’. *IET Radar, Sonar & Navigation* **1**(1):59–66.

Every reasonable effort has been made to acknowledge the owners of copyright material. I would be pleased to hear from any copyright owner who has been omitted or incorrectly acknowledged.